Insights of the Nanoscale Compositional Variations in Dental Enamel Revealed by Statistical Atom Probe Tomography

Jack R. Grimm

A dissertation

submitted in partial fulfillment of the

requirements for the degree of

Doctor of Philosophy

University of Washington

2025

Reading Committee:

Dwayne Arola, Chair

Arun Devaraj, Co-Chair

Lara Gamble

Program Authorized to Offer Degree:

Materials Science and Engineering

University of Washington

Abstract

Insights of the Nanoscale Compositional Variations in Dental Enamel Revealed by Statistical Atom Probe Tomography

Jack R. Grimm

Chair of the Supervisory Committee:

Dwayne Arola

Department of Materials Science and Engineering

Dental enamel is a critical tissue in the body, acting as the primary surface for mastication as well as serving an aesthetic role in a smile. Enamel is also an inspirational material from a materials science perspective, as it endures decades in a challenging and complex oral environment whilst being subjected to cyclic loads. For these reasons, it is worthwhile to develop a thorough understanding of the microstructural and compositional features that provide this tissue its longevity, and how those features can be altered as a function of location within the tooth, age, or external factors such as disease or lifestyle choices. This dissertation is concerned with exploring the composition of the hydroxyapatite nanocrystals that constitute enamel at the smallest scale, elucidating where changes take place at a nanometric level and providing a perspective as to how those changes occur.

Atom probe tomography (APT) is a powerful tool that is well suited to this investigation. Over the past decade, APT has had a significant impact on the study of enamel structure, however small sample sizes and inconsistent use of parameters have limited its ability to make rigorous comparisons between samples from distinct locations, age groups, or conditions. To address these issues, we have developed a routine for atom probe data analysis which enables more granular and robust statistical tests to provide a measure of confidence when comparing multiple groups. The routine is strengthened by complimentary analysis with other techniques such as TEM and Raman spectroscopy. Applied to human enamel from young and senior age groups, this routine reveals an enrichment of fluorine with age in the outer shell of nanocrystals, but not in the nanocrystal core or the intergranular space between nanocrystals. This reflects the culmination of decades of cyclical de- and re-mineralization during which fluorine is incorporated into the nanocrystal shells, though the nanocrystals themselves become slightly smaller and the separation between them slightly larger. The routine described above was also applied to "aprismatic" crocodilian enamel (i.e. without rods), complimenting a broader investigation of the sharp gradient in mechanical properties, composition, and nanocrystal morphology that arises at the outermost enamel surface.

Parameter selection during atom probe experimentation and choices made during analysis can have a substantial impact on the reported results. In pursuit of improved accuracy, precision, and repeatability for these and future experiments, this dissertation also includes a systematic exploration of the parameter space for atom probe experiments on synthetic hydroxyapatite. As part of this, we present a facile and automated approach to ranging of the mass-to-charge spectrum, from which the composition is derived. The significance of the wavelength of the laser pulse used during APT is also studied, with evidence indicating that hydroxyapatite is photoionized by the

deep ultraviolet wavelength laser which comes equipped on the newest generation of commercial laser pulsed atom probe systems.

Finally, this dissertation incorporates the developments described above to compare inner enamel from primary, young, and senior age groups, with a particular focus on the presence of nanoscale organic precipitates that reside between some nanocrystals. Statistical analysis of these precipitates allows for the confident differentiation between organic (e.g., CO) and inorganic (e.g., CO_2H) carbon-containing signals in atom probe reconstructions, which can then be applied to better understand the variations in both mineral and organic components between age groups. Additionally, retention of some precipitates after exposure of the enamel to a prolonged bleaching solution indicates that these organic features can be occluded by mineral and thus can be resistant to change under attack by external threats.

Altogether, this research advances both our understanding of dental enamel as well as the measurement science required to explore nanoscale features in this and other material systems. We envision that future investigations will be able to delve deeper into specific conditions of global and clinical concern, such as aging populations, environmental exposures, caries, molar-incisal hypomineralization, and amelogenesis imperfecta.

Table of Contents

Table of Figures

Some passages have been quoted verbatim from the following sources:

Grimm JR, Renteria C, Mukhopadhyay S, Devaraj A, Arola DD. Stratification of fluoride uptake among enamel crystals with age elucidated by atom probe tomography. *Commun Mater* 2024;**5**:270. https://doi.org/10.1038/s43246-024-00709-8.

Grimm JR, Tao J, Ginovska B, Devaraj A, Taylor SD. Stoichiometric Measurement of Hydroxyapatite by Atom Probe Tomography: Effects of UV and Deep UV Laser-assisted Analytical Conditions. *Microsc Microanal* 2025;**31**:ozaf105. https://doi.org/10.1093/mam/ozaf105.

Acknowledgements

Nothing is done in isolation, least of all this work, and there are many people to whom I owe my thanks. At the top of that list are my advisors, Prof. Dwayne Arola and Dr. Arun Devaraj. Thank you both for your years of support, guidance, and encouragement, and for allowing me the freedom to explore this subject and the many rabbit holes I stuck my nose in along the way. I am grateful for the plentiful opportunities to engage with new groups and research questions that you have connected me with, starting with the DGRP before I even accepted the offer to study at UW and continuing to today. I also extend my deepest thanks to the members of my committee, Prof. Lara Gamble, Prof. Eleftheria Roumeli, and Prof. Tracy Popowics. I appreciate the time you spend to help me and countless other students as we enter into this career. A big thank you as well to Bojana Ginovska and Peter Sushko for letting me be involved in their projects and supporting me at PNNL.

This research wouldn't have been possible without the support of my group mates, both at UW and PNNL. Dr. Cameron Renteria taught me several times how to perform nanoindentation and Raman spectroscopy, and showed me the magic of a properly focused SEM. Katie Tang has provided me with the best prepped and documented samples I could ask for, not to mention many fruitful discussions and her willingness to make "just one quick little figure," again and again. I am eternally grateful to Dr. Sandy Taylor for not just patiently walking me through my early days of making and running APT samples, but also for her thorough and constructive feedback and her organizing of regular atom prober get-togethers. I always look forward to the next! I could likely write a chapter just on the ways Semanti Mukhopadhyay has helped me grow to be a better researcher, but for now we'll settle with featuring the stellar STEM images in Chapter 2. I have launched volleys of APT-related questions and received floods of insight in return from Danny

Perea, Mark Wirth, Dallin Barton, Kayla Yano, Christian Roach, Dan Schrieber, and Sten Lambeets. Similarly, Tanvi Ajantiwalay, Odeta Qafoku, and Alan Schemer-Kohrn helped with countless rounds of FIB troubleshooting. I also have to shout out Bhuvana Vukkum and Francelia Sanchez for the great discussions and for keeping 1160 the best and most communicative lab in ESC. Thank you to all, and I can't wait to see what we work on together next!

Turns out there are not many crocodiles or alligators in the Pacific northwest, but that was no issue thanks to samples provided by Ruth Elseley of the Louisiana Department of Wildlife and Fisheries and Terry Philip and Tom Lang at Reptile Garden in South Dakota.

Outside of lab, I've been exceedingly fortunate to enjoy lifelong friendships old and new. Cheers to my esteemed day-one Dakotans Alex, Brian, Warren, and Adam for all our adventures past and future. Rick, you're a scholar and a gentleman, and the kind of roommate that usually only exists in wholesome sitcoms (read: perfect). To my WA friends, Zane, Benjamin, Eliot, Ashley, Lorenz, Mike, and Annie, thanks for all the good wine and great times. I'm still a bit shocked that Sam and Brandon actually made the 1000+ mile trek to central WA just to watch a season finale together (and Sam did it twice!). Talking about nothing is never nothing with you. I have a special three-part gratitude towards Mallory for (i) being the best commiserator, that most essential friend during grad school, (ii) finding the best restaurants to commiserate/celebrate at, and (iii) going to the coolest shows to make sure there's always something exciting to look forward to outside of lab. I hope your next couch is as surfable so we can keep up the trend.

Last but far from least, I can't say thank you enough to my family for their love and enthusiasm throughout this whole process. Anything I've achieved is only possible because of your support and the great examples you have set.

1. Introduction

1.1. Motivation

Dental enamel is of great interest to biomimetic engineers, materials scientists, and of course, dental professionals. Biomimetic engineers and materials scientists study this biomineral because enamel is a highly mineralized tissue that employs a complex hierarchical structure to achieve a high degree of damage tolerance [1, 2], a challenging feat for many synthetic materials [3]. Dentists are interested because enamel is the outermost layer of the tooth and is thus subject to dissolution by dietary acids and caries [4]. What design elements allow a hypermineralized material to exhibit such remarkable damage tolerance? Which features are necessary to produce accurate biomimetic structures? How do environmental factors alter the structure, composition, and properties of enamel over time? Materials science is concerned with the relationships between material composition, structure, processing and properties, a perspective which can be applied to answer these and other questions.

The microstructure of enamel consists of hierarchical levels that confer impressive properties: nanocrystals build into rods that assemble into decussation bands [5, 6]. Additionally, there are functional gradients in structure, composition, and mechanical properties that further improve damage tolerance, increase wear resistance, and decrease solubility [7-9]. This dissertation focuses primarily on furthering understanding of enamel structure and composition at the nanoscale through the use of atom probe tomography (APT). Findings from these and future studies will be critical for the design of materials and dental therapies to enhance, restore, and maintain the function of teeth for patients globally [10].

The nanocrystals of enamel have recently gained attention as new studies have revealed that even at this scale, there is evidence of structural and compositional hierarchies that contribute to the overall tissue properties [11, 12]. As enamel is an acellular tissue that does not undergo remodeling [5], any compositional changes that occur over time take place and potentially accumulate at the nanoscale. This could include the competing processes of demineralization by biofilm activity and/or ingestion of acidic dietary components [13] and remineralization promoted by saliva or dental treatments [4, 14]. Changes to the composition can alter the mechanical properties or resistance to dissolution, making an understanding of the nanocrystal composition an essential factor in oral health and longevity. Additionally, nanocrystals are the product of ameloblast cell activity during amelogenesis (the process of enamel tissue formation and development) [15]. Enamel, similar to most biomineralized tissues, is formed under physiological conditions, i.e. at low temperatures and supersaturations relative to typical industrial processes. The control that biology has over these mineralization processes is remarkable, and replication through artificial means will surely unlock new possibilities for material design. Clearly, there are many benefits to studying enamel nanocrystals, and APT is a powerful tool that is well positioned to explore this space.

The first studies of mouse enamel nanocrystals by APT were published by Gordon et al. in 2015 [16]. However, Gordon had previously published a study on chiton teeth in 2011 [17], revealing organic-rich volumes buried within the primarily magnetite tissue. A perennial challenge in the field of APT research is the fragmentation of a material into ions or molecular ions, which may not always intuitively reflect the local bonding environment or expected stoichiometry of the material [18-21]. Recognizing this, Gordon performed a systematic study of synthetic hydroxyapatite, fluorapatite, and chlorapatite along with geological hydroxyapatite to identify

parameters that improved the compositional accuracy of APT [22]. Further research of the field evaporation mechanisms for hydroxyapatite, enamel, and other calcium phosphates have followed in recent years [23, 24]. These earlier studies provide a strong foundation that this dissertation expands upon.

1.1.1. Overview of this dissertation

A frequent shortcoming of APT studies across all material classes is a lack of statistical evaluations involving multiple samples or numerical comparisons between sample conditions. This is understandable to an extent, as considerable time from a well-trained operator must be invested to prepare specimens, perform APT measurements, and analyze datasets. Each APT measurement produces a 3-dimensional point cloud which can then be segmented into smaller regions of interest to extract the composition. In Chapter 2, we segment APT data from young (<35 years old) and senior (>55 years old) enamel into three distinct phases identified as nanocrystal core, nanocrystal shell, and intergranular amorphous calcium phosphate. The numerous regions of interest associated with each phase are then aggregated into one composition each per APT measurement, enabling more reliable averaging of the composition across multiple measurements. Furthermore, this treatment of the data permits statistical comparison between enamel from young and senior age groups, providing insight into what compositional changes accrue in the outer enamel over decades.

The statistical approach used in Chapter 2 is also applied in evaluations of the aprismatic enamel of the saltwater crocodile in Chapter 3. However, rather than comparing between age groups, the comparison is made within one tooth sampling across the enamel thickness,

complimented by through-thickness evaluations of mechanical properties by nanoindentation and bulk mineral composition by Raman spectroscopy. We find that the outer layer is significantly harder and has a significantly lesser degree of carbonate substitutions than the remainder of the enamel thickness. This is an interesting difference from the relatively smooth gradients in composition and properties that have been recorded in mammalian enamel. One particularly useful finding from this study is that the sharp gradient enables comparisons between certain molecular ions in the APT data, such as CO and CO_2. These molecular ions can then be corroborated with the data from Raman spectroscopy to better understand what these molecular ions reflect.

The data presented in Chapters 2 and 3 were collected on an atom probe system employing an ultraviolet 355 nm wavelength laser pulse to assist with field evaporation. This has been the standard laser system for previous studies of enamel as well (e.g., [11, 25-27]). However, the newest generation of commercial atom probe systems has shifted to a deep ultraviolet 257.5 nm wavelength laser, which has been reported to induce photoionization for a number of materials [28, 29]. We find that this is also the case for hydroxyapatite as explored in Chapter 4, a systematic study of how varying experimental parameters such as laser pulse energy on both the 355 nm and 257.5 nm wavelength systems alters the measured composition. This study also explores the effect of choices made during analysis on measured composition, such as definition of ranges on the mass-to-charge spectra. An algorithmic approach to automate range adjustment is developed and employed to reduce operator bias.

Chapter 5 presents a unique evaluation of human enamel supported by the advancements achieved in the previous chapters. We again return to evaluating enamel from distinct age groups, in this case from primary, young, and senior donors. However, this study investigates the inner

enamel near the dentin-enamel junction, where organic components are expected to be in greater abundance. It was hypothesized that by sampling from the inner enamel, there would be minimal compositional differences between the age groups, yet the APT measurements reveal some subtle variations which may be associated with age. Additionally, the 257.5 nm laser system was used, with parameter selection and interpretation informed by the results of Chapter 4. One objective of this study was to remove any organic components from the enamel by subjecting the tissues to a bleaching treatment in order to more confidently identify which signals belonged to organic or inorganic sources. Surprisingly, the bleaching treatment did not remove the organic components as expected, but the signals could still be identified by careful examination of organic precipitates trapped between nanocrystals. Several conclusions regarding the fluid permeability and ion diffusion of enamel at the nanoscale can be inferred from these results, which are discussed at length.

Finally, Chapter 6 provides conclusions and prospective outlooks for future research directions sparked by the findings of these studies. The remainder of this chapter provides an overview of the microstructure, composition, and formation of enamel, as well as a brief summary of the literature regarding de- and re-mineralization and a review of previous studies of enamel by APT.

1.2. Microstructure of Enamel

Enamel microstructure consists of four hierarchical levels. The smallest fundamental unit is the hydroxyapatite (HA) nanocrystal (Figure 1.1a) with a cross section of approximately 50×150 nm and up to 100 μm in length [4, 11, 30]. The nanocrystals tend to have a hexagonal morphology,

as might be expected from the hexagonal lattice structure of apatite ($P6_3/m$) [31]. A layer of amorphous mineral [11, 16] and occasional organic-rich precipitates [25, 26, 32] separate the nanocrystals.

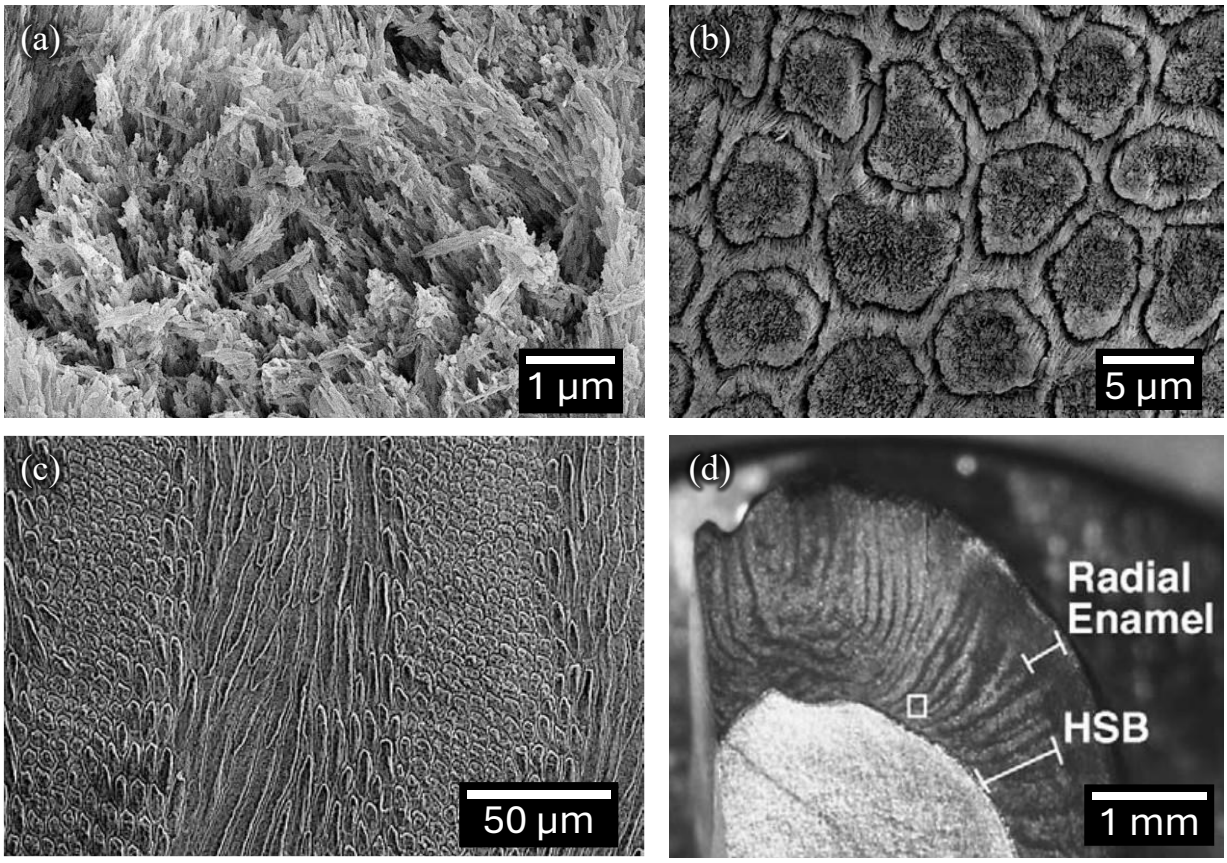

Figure 1.1. Hierarchical microstructure of enamel revealed by scanning electron microscopy. *(a) Hydroxyapatite nanocrystals constitute the fundamental mineral unit of enamel. (b) ~10^4 nanocrystals are bundled into each rod. Rods are surrounded by an organic-rich sheath separated from other rods by a layer of interrod enamel consisting of HA nanocrystals with a distinct orientation. (c) Bands of rods cross each other to form decussation patterns. (d) Decussation bands, also called Hunter-Schreger bands (HSB) give way to radially-aligned rods near the outer enamel surface. Additionally, decussation bands form a more complex "gnarled" pattern at cusps. (a-c) Courtesy of C. Renteria. (d) reproduced from [33] with permission from Elsevier.*

Nanocrystals sharing a common alignment are bundled together into rods, the next hierarchical level with an approximate diameter of 3-5 μm (Figure 1.1b). There are on the order of 0.5—1×10^4 nanocrystals per rod, based on the measurements of average rod [34] and nanocrystal [35] cross sectional areas in human enamel. The rods extend continuously through almost the entirety of the enamel thickness [5]. Adjacent rods are separated by a layer of nanocrystals with an opposing direction to that of the rods referred to as interrod enamel. A finger-like protrusion on the ameloblast cells that produce enamel called a Tomes' process secretes the mineral that becomes the rods, while the basal portion of the cell secretes the interrod [15]. Each rod and some portion of the immediately surrounding interrod enamel is templated by an individual ameloblast as the cell progresses from the dentin enamel junction (DEJ) to what will eventually become the outer enamel surface (OES). The interrod enamel and the interface between rod and interrod regions are mechanically weaker, providing a preferred path for crack extension and guiding cracks to the DEJ where they can be arrested without causing major spalling or chipping of the enamel.

Ameloblast cells make systematic variations in their secretion paths that are reflected in the final microstructure of the rods, yielding the third hierarchical level regarded as decussation (Figure 1.1c). When measuring the out-of-plane angle of rods in a line from one band to the next, a sinusoidal pattern emerges [36-38]. Decussation bands constrain the crack to a localized region and guide it along a tortuous route, minimizing damage and increasing the crack growth resistance [1, 39].

The final hierarchal layer concerns the variation of decussation patterns, rods, and nanocrystals with respect to position within the tooth (Figure 1.1d). Decussation bands in the cervical region tend to be relatively parallel with a slight curvature. Near the cusps of many molars,

the bands become more gnarled [2, 33, 37, 40, 41]. Decussation generally extends within the innermost ~80% of the enamel thickness in many mammals, with the outmost layer consisting of radially aligned rods [9, 36, 42]. Additionally, because the area of the outer enamel surface is greater than that of the inner, but the number of rods is presumed to remain constant (i.e. all rods start at the DEJ and end at the OES), variations of the rod and/or interrod enamel dimensions with respect to distance from the DEJ can also be present.

One of the primary motivations for studying biominerals is to identify patterns that can be exploited and replicated in modern materials [6, 43]. Natural selection over millions of years optimizes structures and properties for their specific functions. Specifically, there is evidence that the microstructure of a given species either adapts to or enables their diet. Guatelli-Steinberg et al. recently compared enamel from three primate species: one that almost exclusively consumes hard foodstuffs, one that consumes exclusively soft food, and one that seasonally consumes hard food as a fallback when soft alternatives are not available [37]. The enamel rods of the species that exclusively eats hard food had a greater range in their rod angles when sectioned mesial-distally. Rods with a more tortuous path cause cracks to deflect further, increasing the energy expended for the crack to progress through the enamel thickness. A similar result was found when comparing the microstructure of enamel from a group of mammals across a large range in bite force quotients (bite force normalized by body mass) [36]. The maximum out-of-plane rod angle (termed "pitch" in that paper) increased with increasing bite force quotient, whereas the width of the decussation bands decreased. Both factors synergize to better constrain cracks that might be generated under high bite force.

If the decussation of rods or similar fibers could be emulated in synthetic materials, through e.g., continuous fiber composite additive manufacturing or direct ink writing of ceramic additive manufacturing, the remarkable damage tolerance of enamel could be replicated on the micro- to macro-scale. As such, the role of decussation and decussation patterns has received considerable attention [1, 2, 39, 44]. The author acknowledges the importance of this level of hierarchy for overall damage tolerance, but this dissertation will instead be focused on the hydroxyapatite nanocrystals. Nanocrystals have recently begun to receive increased attention from a materials science perspective [12, 45], reinforcing that the complexities of the hierarchical enamel structure continue to the smallest scale. Furthermore, nanocrystals are the foundation for enamel formation [15], demineralization [13], and remineralization [4], as well as the interaction of proteins and organics with the mineral phase both during enamel formation and daily use [46].

Crocodilian enamel contrasts the complexities of mammalian enamel. Despite being apex predators in their ecosystem and having the highest bite force of any terrestrial animal [47], crocodilians have only a relatively thin layer of enamel which does not possess rods (Figure 1.2) [48-50]. This is possible because crocodilians continuously regenerate new teeth throughout their lifespan [51-53]. Aprismatic enamel is often called "primitive" because of the resemblance to fossil records of ancient teeth before the evolution of rods [49], though this may be somewhat of a misnomer. There is evidence that the nanocrystals in modern crocodilian enamel have become more aligned than those from a Cretaceous crocodylomorph [54], suggesting some evolutionary change has taken place. Regardless, the nanocrystals in aprismatic enamel still show subtle patterns [49]. However, because they lack the clear organization into rod and interrod regions, the ability of those patterns to improve the crack growth resistance remains limited [48, 55].

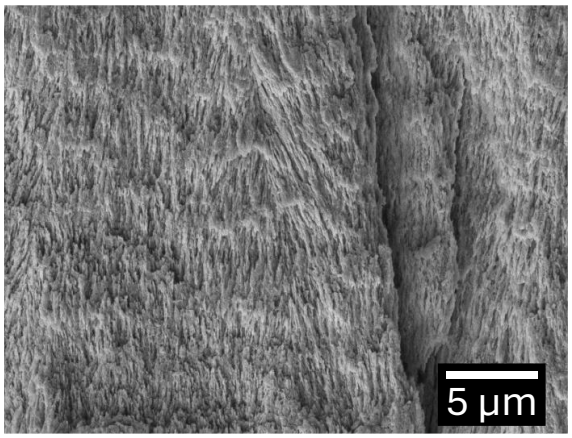

Figure 1.2. Scanning electron micrograph of *Alligator mississippiensis.* *Crocodilian enamel lacks rod structure, it is instead comprised only of nanocrystals that extended radially from the dentin enamel junction towards the outer enamel surface*.

While it lacks the inspiring microstructural features of decussated enamel, investigation of the aprismatic crocodilian enamel is still valuable for at least two reasons. The first is that it offers a unique opportunity to explore composition and properties of a less evolutionary complex micro- and nanostructure in the absence of higher hierarchical levels. Secondly, certain phenotypes of the family of genetic diseases called amelogenesis imperfecta result in malformed enamel with microstructures similar to that of crocodilians [15]. Studying the aprismatic enamel of crocodilians thus not only provides a perspective of the diverse niches across the tree of life but may also serve as a useful point of reference when evaluating defective enamel in humans.

In order to appreciate the composition, morphology, and structure of enamel nanocrystals, it is important to understand how they are formed. There is a rich literature investigating the complex process of amelogenesis, which will be briefly summarized in the following section.

1.3. Amelogenesis

A major facet of enamel research is focused on the biomineralization pathway that produces the tissue. While the damage tolerance of enamel is inspirational, building a fundamental understanding of how the enamel structure is constructed will have applications in biomaterial development [56], studies of and treatments for amelogenesis imperfecta, and the recent push for products that deposit new hydroxyapatite on the enamel surface in vivo [57, 58].

1.3.1. Stages of Amelogenesis

The process of enamel formation and development is termed amelogenesis ("amel" stemming from *esmal*, the same obsolete root word of enamel). Amelogenesis is commonly divided into three stages: pre-secretory, secretory, and maturation [15, 59]. The pre-secretory stage primarily involves the development of the ameloblast cells along with changes at the pre-dentin surface where the enamel attaches. Secretory and maturation are the stages during which mineral nucleation and growth occur. As these latter two stages are the most relevant to this study, they will be discussed here in more detail.

During the secretory stage, ameloblasts depart from the basement membrane separating the pre-enamel from the maturing dentin and proceed as a unified front. In most mammals, each ameloblast develops a protruding feature termed a Tomes' process (TP) that extends from the cell towards the DEJ [60]. The TP does not fill the full area of the cell, and there is a small "shoulder" at the base of the cell. Both the end of the TP and the shoulder membrane secrete the proteins, enzymes, and ions necessary for mineralization simultaneously, and are referred to as the distal (disTP) and proximal (proxTP) Tomes' processes, respectively. The role of disTP and proxTP have been experimentally revealed by removing the cells from artificially interrupted enamel, after

which the mineral associated with the proxTP is more prominent and resembles a continuous honeycomb-like structure with discrete recesses where the TPs had been situated [61]. The secretions of the disTP eventually become a rod – each TP is associated with one rod – while the concurrent secretions of the proxTP produce the interrod enamel (Figure 1.3).

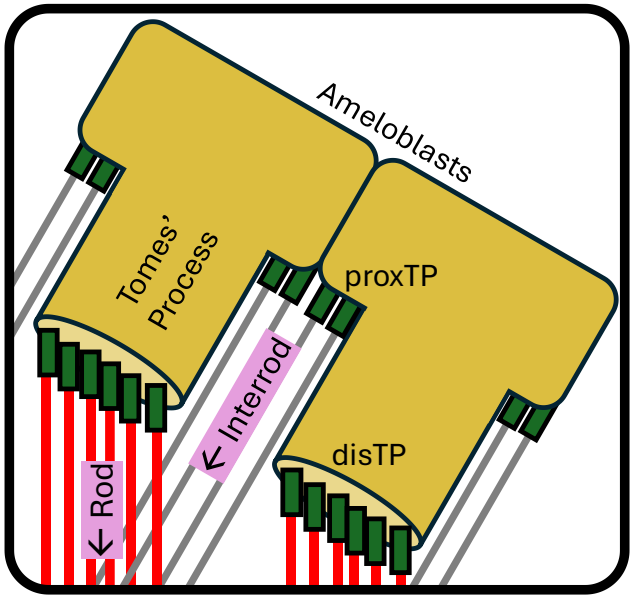

Figure 1.3. Schematic of the secretory Tomes' processes (TP) of ameloblasts. *The proximal "shoulder" of the TP (proxTP) produces mineral that becomes the interrod enamel, whereas the distal end of the TP (disTP) leads to the formation of an individual rod.*

Ameloblasts do not secrete minerals directly but instead produce an extracellular matrix (ECM) that templates mineralization. Many proteins and enzymes contribute to the formation of the ECM, including amelogenin (Amel), ameloblastin (Ambn), enamelin (Enam), tuftelin (Tuft), matrix metalloproteinase 20 (MMP20, also known as enamelysin), kallikrein 4 (KLK-4), FAM20A Golgi associated secretory pathway pseudo kinase (FAM20A), among others [15, 62, 63]. Amel is the most plentiful of these components and is cleaved by MMP20 immediately following secretion

[64, 65]. The cleavage products are then able to assemble into nanospheres or nanoribbons which are thought to provide the template scaffold upon which the mineral forms [66-69]. Knockout mouse models have shown that the absence of MMP20 results in enamel that is notably thinner, less mineralized, and lacks the typical rod structure because the Amel was not cleaved [70, 71].

The protein-mediated nucleation and early growth of the calcium phosphate phase also occur during the secretory stage. Mineralization begins by the nucleation of an amorphous calcium phosphate (ACP), templated by the ECM [59, 66, 67, 72, 73]. A 32 kDa cleavage product of Enam promotes mineral nucleation, with the Enam:Amel ratio of ~2:50 being found to be most effective in vitro [74]. ACP is an unstable phase that is driven to transform to the stable HA [75]. However, if it is allowed to transform as soon as possible, the resultant nanocrystals will be rather short, which apparently impedes their organization into rods at longer length scales [76]. Thus, the transformation must be inhibited to achieve the remarkable aspect ratio of the eventual nanocrystals. The presence of Mg ions [77], Amel phosphorylation [76], and the ratio of Enam:Amel [74] have all been shown to stabilize the ACP until it can form ribbon structures. Ambn regulates the signaling, matrix adhesion, and polarization of the ameloblast cells throughout this stage [78-80]. Ambn is also cleaved by MMP20, and cleavage products concentrate in the so-called "sheath" region between rod and interrod enamel [79]. Several micrometers removed from the ameloblast, the transformation to apatite and crystal growth begins [81], but the nanocrystals are still much narrower than their final dimensions and the developing tissue is still rich in organic components: only ~40% of the total amount of mineral forms during the secretory stage [82].

It is during the maturation stage that the nanocrystals grow and densify [15, 59]. Once the ameloblasts have reached the end of their path (the final thickness of the enamel), approximately

25% of the ameloblasts undergo apoptosis while the remainder initiate morphological changes [82]. TPs are retracted, and the main body of the cells expand to form a new basement membrane on the surface of the nascent enamel. Maturation-stage ameloblasts then cyclically alternate between ruffle-ended and smooth-ended morphologies [62, 83]. Mineralization, now realized as crystal growth, happens primarily during the ruffle-ended portions of the cycle [84]. The deposition of mineral ions causes the local environment to decrease to pH ~6, which is counterbalanced by a shorter cycle when the smooth-ended configuration secretes carbonate to balance the pH back to ~7.2 [59, 83].

Enzymatic degradation of the enamel matrix proteins is necessary to make room for the growing mineral phase. KLK-4 is the dominant protease that achieves this and is secreted near the outermost surface of the developing tissue and diffuses inwards. That leads to a gradient in the efficacy of the protease and thus a gradient in the residual organic content in the final tissue [15, 59]. Where more organic matrix is removed, the nanocrystals can grow larger. This diffusion-induced gradient of KLK-4 activity is the mechanism behind the gradients in stiffness, hardness (measured by nanoindentation), and degree of crystallinity (from Raman spectroscopy) [7, 9, 85]. The ameloblast cells secreting KLK-4 remain on the outermost surface of the developing enamel, causing that layer to be the most completely deproteinized and thus most mineralized.

In humans, the maturation stage lasts 4-5 years. Considering that the primary dentition starts to erupt in infants around 4-7 months old, the tissue has not yet had sufficient time to completely develop, leading to a markedly lower stiffness and hardness in primary enamel compared to permanent enamel of adults [86]. It seems likely that the diphyodont nature of most mammals is

an evolutionary adaptation that provides a functional tooth as early as possible, providing a temporary dentition for childhood while permanent teeth fully mature.

A schematic flowchart highlighting the various changes and processes that take place during amelogenesis is presented in Figure 1.4, including some of the factors that the enamel is exposed to during regular function after it has erupted. It should be noted that this is a short and simplified description of a highly complex process, with many other relevant components, that is at the center of ongoing discussions and debate in the community.

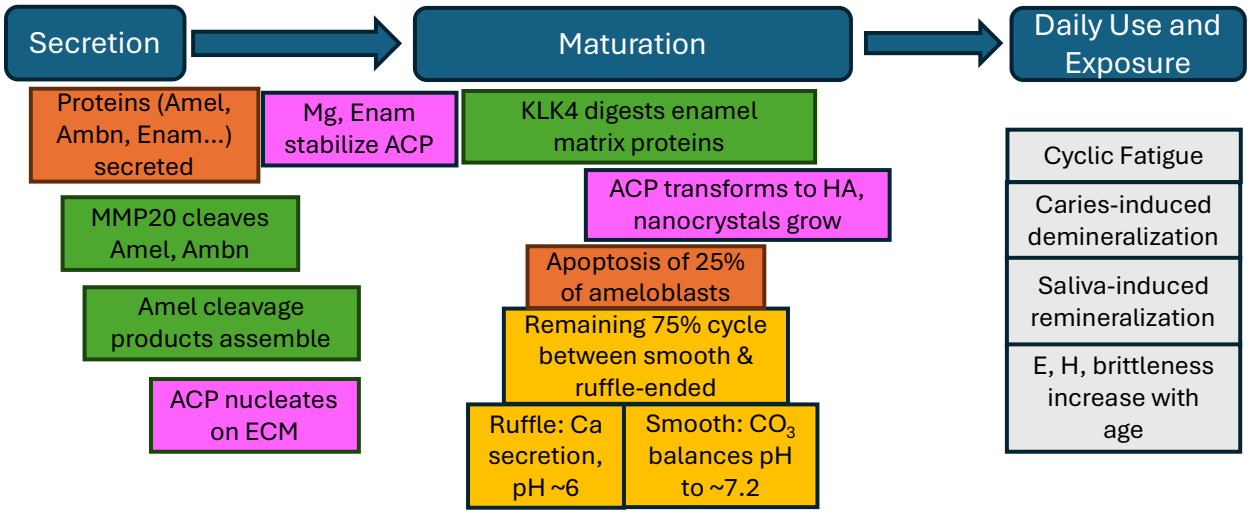

Figure 1.4. Simplified schematic timeline of enamel tissue lifespan, including amelogenesis and regular use of the fully developed tissue. *Boxes with orange or yellow backgrounds relate to the activity of ameloblast cells, green relates to proteins, pink to the developing mineral phase, and gray to environmental factors during regular use. Abbreviations: Amel = amelogenin, Ambn = ameloblastin, Enam = enamelin, MMP20 = matrix metalloproteinase 20, ACP = amorphous calcium phosphate, ECM = extracellular matrix, HA = hydroxyapatite, E = elastic modulus, H = hardness.*

1.4. Composition of Enamel

The mineral hydroxyapatite ($Ca_{10}(PO_4)_6(OH)_2$) comprises ~95 wt.% of enamel, with ~2 wt.% residual organic components and the remaining balance comprised of water. All three of these components are interwoven at the nanometer scale: organics and water occupy the space between mineral nanocrystals [25, 26]. The composition and structure of the nanocrystals are similar between rod and interrod regions, though the sheath regions surrounding rods have somewhat higher organic content relative to the rods themselves [79].

Apatites are a group of calcium phosphate minerals. Chlorine, fluorine, or hydroxyl ions can be interchanged to form chlor-, fluor-, and hydroxyapatites, respectively, but only hydroxyapatite is relevant to enamel. Partially fluoridated hydroxyapatite is of particular interest because it reduces the solubility of the mineral, which in turn reduces the susceptibility of the enamel tissue to dissolution from carious attack [87]. Hence, fluoride is added to many toothpastes and water supplies as a public service to reduce caries prevalence [88].

The organic portion of enamel consists of cleavage fragments of the proteins used in the extracellular matrix during amelogenesis. Similar to many other biocomposite systems used for bioinspiration (e.g. nacre [89, 90], dactyl shrimp club [91, 92], fish scales [93, 94]), the organic component serves as a plasticizer to improve toughening through plastic deformation and crack bridging [95, 96]. There may also be a size effect, where the nanometer-scale constraint of the organic layer separating hard mineral crystals provides additional toughness to the material [97], but this has not yet been confirmed in enamel.

Throughout the enamel thickness, there are gradients in the composition and mechanical properties [85]. There is good consensus in the literature that the outermost enamel is the hardest and has the highest elastic modulus, a key to the wear resistant surface, while the inner enamel is

softer and has lower stiffness to improve crack growth resistance [1, 7, 98, 99]. The outer layer also exhibits a higher degree of crystallinity and fewer carbonate substitutions in the HA lattice [8, 86]. These trends in mechanical properties and composition appear to be consistent for a variety of mammals and primates [9, 37, 100].

1.5. De- and Re-mineralization

Of the myriad problems that are encountered in a dental clinic, there are two recurrent ones that are most common, namely caries and fractures. Caries has an estimated incidence of 7.2 billion people worldwide [101], and impacts both the primary and permanent dentition [57, 102, 103]. In addition, as mortality rates continue to decline, the global population is aging. Like any material, enamel is susceptible to fatigue as daily cyclical stresses and other threats from the chemical environment accumulate and reduce the effective fracture resistance of the tissue [104, 105]. Both caries and aging directly involve the de- and re-mineralization of enamel.

Caries is the localized demineralization of enamel that results from acidic secretions of biofilm bacteria. The bacterial digestion of sugars produces organic acids, such as lactic acid, that can accumulate in the enamel and cause a sufficient decrease in pH to demineralize the tissue [106]. A biofilm on the enamel surface is inevitable in the oral environment, but it becomes pathological when the culmination of dietary, lifestyle, developmental, and medical factors favor those bacteria that secrete excessive acids [5]. By demineralizing the enamel, the tooth becomes sensitive and more prone to mechanical failure [107], which may require removal of the affected region and replacement with a filling.

While caries effects an overwhelming majority of the population, chronological aging is even more universal. In studies comparing the mechanical properties of enamel from young (<35 years old) and senior (>55 years old) age groups, the enamel of seniors is harder and has a higher elastic modulus, but most important to lifelong oral health, it has increased brittleness [86, 98, 108, 109]. Dentin also becomes embrittled in a similar fashion but due to different driving forces [110]. The precise origin of such age-related degradation remains an open question, but loss of organic content between nanocrystals and changes to nanocrystal composition over time are suspected to be key factors. This is where advanced methods of characterization are needed.

Saliva is the body's first defense against demineralization as it balances the pH to stop further mineral loss, while also providing calcium and phosphate ions necessary to rebuild lost mineral [14]. Within a given age group, there are statistically significant correlations between certain characteristics of an individual's saliva (e.g. "frothiness" caused by unusually high protein content) and likelihood of caries [111]. However, the correlation between saliva characteristics and caries is different for each age group, reinforcing that chronological age is a major contributor to enamel health.

1.6. Characterization of Enamel by Atom Probe Tomography

Building an understanding of any material requires characterization across length scales. Because the rod-interrod interfaces of enamel and their complex three-dimensional arrangement guide cracks and confer a large degree of the crack growth resistance, much of the literature has focused on the micrometer – millimeter scale [2, 39, 42, 44, 112, 113]. However, recent studies have revealed that there is considerable complexity at the nanometer scale as well [11, 12, 16, 26,

27, 32, 45]. Additionally, any compositional change produced by de- and re-mineralization cycles will necessarily take place at the irregular interfaces between the nanocrystals and the amorphous intergranular phase that separates them [4, 13]. Atom probe tomography (APT) is uniquely capable of resolving the chemical distribution with ppm-level sensitivity and nanometer resolution for a volume of hundreds of cubic nanometers.

In APT, a three-dimensional reconstruction of atom positions within a sample is achieved by subjecting a sharp needle to intense electric fields (10s of V/nm at the surface) [45, 114]. A femtosecond laser pulse induces field evaporation of ions towards a two-dimensional detector [18]. The needle-shaped samples of non-conductive materials are often prepared by a focused ion beam liftout approach (Figure 1.5) that allows for precise site selection. Time-of-flight and hit location on the detector are recorded for each evaporated ion, which enables the physical position of each ion to be reconstructed with sub-nanometer resolution. The resultant reconstruction is then interrogated to discern nanoscale chemical gradients and distinct crystallographic and other structural features in materials.

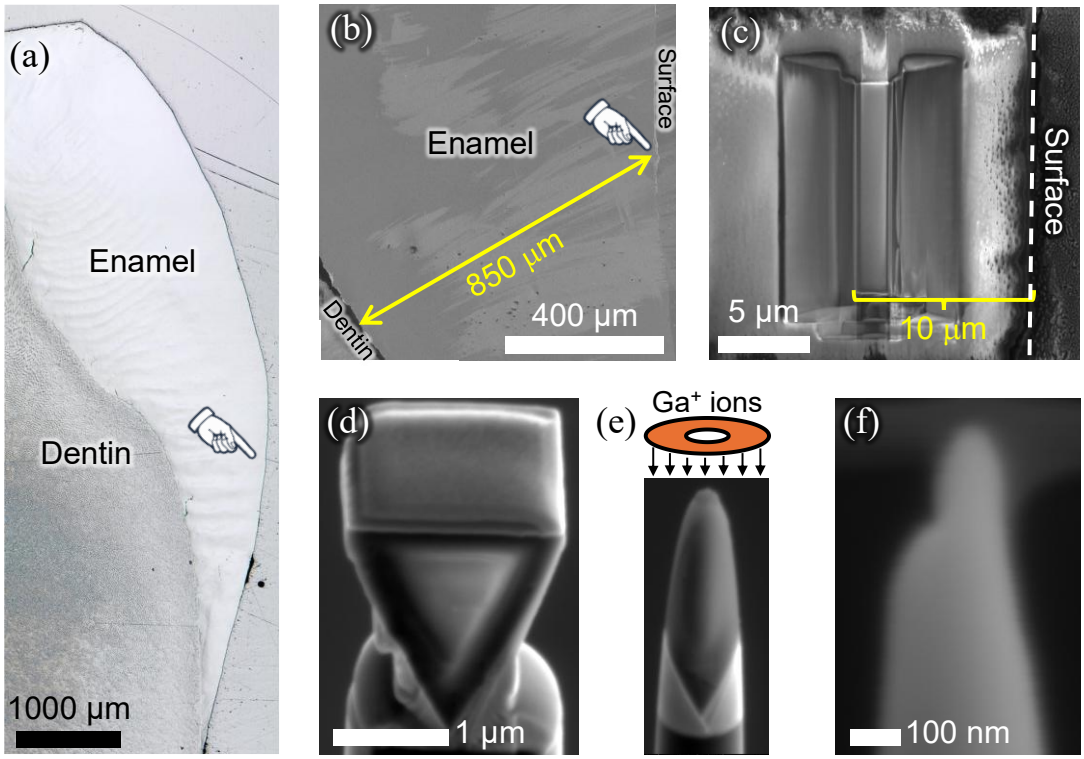

Figure 1.5. Preparation of samples for atom probe tomography. *(a) Optical micrograph of polished cross section of a young molar with enamel and dentin noted for clarity. (b) Scanning electron micrograph of cervical enamel from a young molar. The sample was taken from a location approximately 850 µm from the dentin-enamel junction, and (c) approximately 10 µm from the outer enamel surface. (d) A cantilever with triangular cross section was produced in situ using focused ion beam milling to be lifted out. (e) A segment of the liftout was attached to a Si micropost then milled with progressively smaller annular ion beam patterns to shape the needle before a final low-kV polishing step was used to achieve a tip diameter <100 nm (f).*

APT has been used to reveal the distribution of elements and impurities in mature enamel [11, 16, 25-27, 32, 115]. In a study of murine incisors, Gordon et al. showed that distinct HA nanocrystals can be identified by an amorphous calcium phosphate (ACP) intergranular phase rich in Mg, organic residues, and other impurities [16, 25]. This aligns with expectations from the post-

classical theory of amelogenesis, wherein enamel maturation is thought to occur by transformation of ACP precursor nanoribbons into HA [59, 75]. Mg initially serves to stabilize ACP, allowing the nanoribbons to grow in length before transforming to HA [59, 116]. The HA crystal lattice has lower solubility for Mg [116]; as amelogenesis progresses and the nanocrystals transform and grow, Mg and residual organics are pushed to the intergranular spaces and concentrated there. Interestingly, in human molars, Mg is additionally enriched in the core of the nanocrystals [11], a notable departure from the prior studies of murine enamel [16]. The Mg-rich core is believed to be an artifact of the early stages of mineral nucleation and growth, though it may also serve to induce residual compressive stresses through lattice distortion which improve the mechanical properties [11].

2. Stratification of fluoride uptake among enamel crystals with age elucidated by atom probe tomography

2.1. Synopsis

Dental enamel is subjected to a lifetime of de- and re-mineralization cycles in the oral environment, the cumulative effects of which contribute to embrittlement with age. However, the understanding of atomic scale mechanisms of dental enamel aging is still at its infancy, particularly regarding where compositional differences exist in the hydroxyapatite nanocrystals and what underlying mechanisms might be responsible. Here, we use atom probe tomography to compare enamel from a young (22 years old) and a senior (56 years old) adult donor tooth. The three-dimensional spatial resolution of atom probe tomography enables segmentation of the enamel into distinct phases corresponding to the mineral nanocrystal shell, nanocrystal core, and the intergranular space between adjacent nanocrystals. Statistical tests are then applied to resolve compositional differences between the two enamels with increased confidence. Findings reveal that the concentration of fluorine is elevated in the shells of senior nanocrystals relative to young, with less significant differences between the cores or intergranular phases. It is proposed that the embrittlement of enamel may be driven, at least in part, by the infusion of fluorine into the nanocrystals and that the principal mechanism is de- and re-mineralization cycles that preferentially erode and rebuild the nanocrystals shells.

2.2. Introduction

Due to the diphyodont nature of humans and the acellular nature of enamel, an increasing life expectancy subjects the permanent dentition to more physical (i.e., cyclic contact) and chemical (i.e., demineralization) damage. To this end, there is an expanding effort to develop therapeutic approaches that can counteract the effects of aging and preserve the function of natural enamel. Such treatments will necessarily interface with the hydroxyapatite (HA, $Ca_{10}(PO_4)_6(OH)_2$) nanocrystals that constitute the fundamental unit of enamel. However, there is limited atomic scale understanding of the morphological and chemical changes that the HA nanocrystals undergo with age. The present study applies atom probe tomography (APT) to compare the composition of HA nanocrystals and the surrounding intergranular amorphous phase from young (< 35 years of age) and senior (> 55 years of age) adult human molar enamel.

Enamel, like many other mineralized tissues, has a complex hierarchical microstructure [1, 2]. Optical microscopy on a polished cross section of enamel reveals light and dark bands approximately 50 μm wide (Figure 1.1a), which correspond to decussated assemblies of enamel rods with diameters of ~5 μm. The rods are in turn constituted of HA nanocrystals with a cross section of ~50 x ~120 nm and up to 100 μm in length [4, 11, 30]. The nanocrystal interfaces consist of several nanometers of amorphous mineral and organic residues [11, 16, 26, 45]. Though small in size, even the HA nanocrystals appear to have been optimized through natural selection to improve the durability of enamel. For example, adjacent nanocrystals are reported to have distinct crystal lattice alignments, which increases the energy required for an incident crack tip to proceed from one nanocrystal to the next [12]. There is also evidence that compositional gradients within a single nanocrystal result in a residual compressive strain on the surface that improves both the

mechanical and chemical properties [11]. A key knowledge gap is the influence of changes to the nanoscale composition of these nanocrystals with aging towards enhancing or diminishing the performance and longevity of the enamel tissue.

Chronological aging is a universal process which induces detrimental changes to the properties and performance of enamel. Specifically, it becomes harder, stiffer, more brittle, and thus more prone to mechanical failure, particularly near the outer enamel surface [86, 98, 108, 117]. A pathway by which these changes are realized is the ion exchange induced by extended exposure to a dynamic oral environment. Demineralization by dietary choices with low pH and biofilm activity is counteracted by salivary action and regular dental care to balance the pH and introduce e.g. calcium and phosphate ions to remineralize the tissue [14]. The intergranular phase between nanocrystals is a known channel for the introduction of ions into enamel [13, 105, 118], exposing the nanocrystal shell to etchants and remineralizing agents alike and rendering it a prime location where ion exchanges may accumulate with age. While there is no shortage of studies motivated to understand enamel dissolution by caries or dietary choices [13, 119, 120], how chronological aging in otherwise healthy enamel produces variations in the nanocrystal composition remains an open question.

There is no doubt that the composition is critically important, as evidenced by the well-known examples of fluoridated drinking water as a public service and fluoride-laden dental treatments to combat caries [88]. Partially fluoridated apatite has a lower solubility than pure hydroxyapatite [87]. Excess fluoridation, however, is detrimental to the damage tolerant properties of enamel that are so critical to function, and in the extreme case, can be pathological (fluorosis) [121, 122]. Various spectroscopy methods (e.g. energy dispersive, Raman, Fourier-transformed

infrared) have been applied to enamel at the micron to millimeter scale to measure such compositional changes in bulk, e.g. references [8, 116, 123-125]. However, the introduction and exchange of ions will necessarily take place at the atomic level, presumably at curved nanoscale interfaces. Thus, in order to accurately observe compositional changes associated with age, 3D sub-nanometer scale resolution characterization techniques such as atom probe tomography (APT) are needed.

In APT, a three-dimensional reconstruction of atom positions within a sample is achieved by subjecting a sharp needle to intense electric fields (10s of V nm^{-1}) along with a femtosecond laser pulse to induce field evaporation of ions towards a two-dimensional detector [45, 114]. The needle samples of non-conductive materials are often prepared by a focused ion beam liftout approach (Figure 1.5c-f) that allows for precise site selection. Time-of-flight and hit location on the detector are recorded for each evaporated ion, which enables the physical position of each ion to be reconstructed with sub-nanometer resolution. The resultant reconstruction is then interrogated to discern nanoscale chemical gradients and features in materials.

APT has been used to reveal the distribution of elements and impurities in mature enamel [11, 16, 25, 26, 32]. In a study of murine incisors, Gordon et al. showed that distinct HA nanocrystals can be identified by an amorphous calcium phosphate (ACP) intergranular phase, rich in Mg, organic residues, and other impurities [16, 25]. This aligns with expectations from the post-classical theory of amelogenesis, wherein enamel maturation is thought to occur by transformation of ACP precursor nanoribbons into HA [59, 75]. Mg initially serves to stabilize ACP, allowing the nanoribbons to grow in length before transforming to HA [59, 116]. The HA crystal lattice has lower solubility for Mg [116]; as amelogenesis progresses and the nanocrystals transform and

grow, Mg and residual organics are pushed to the intergranular spaces and concentrated there. Interestingly, in human molars, Mg is additionally enriched in the core of the nanocrystals [11], a notable departure from the prior studies of murine enamel [16]. The Mg segregation can thus be used to visually distinguish core, shell, and intergranular phases in enamel, enabling further analysis and comparison between phases in ex vivo samples.

To assess the nanoscale compositional modification that could potentially occur in human enamel with aging, we conducted APT analysis of the outer cervical enamel of young and senior adult molars. The APT results revealed that the concentration of fluorine was elevated in the shell regions of senior enamel nanocrystals relative to the young, providing evidence of the mechanism by which ion concentrations accumulate with age with 3D nanometer resolution.

2.3. Methods

Anonymous human third molars were obtained for this investigation from the Dental School at the University of Washington in Seattle, WA, under an institutional review board (IRB) exemption for STUDY00014724 from the University of Washington IRB. The young and senior third molars were free of fillings or carious lesions and were obtained from a 22 year old and a 56 year old donor, respectively. Upon receipt, the teeth and tissue waste were sterilized using a freshly prepared 1:10 dilution of 0.5% sodium hypochlorite. The teeth were sectioned buccal-lingually along the midline of the tooth using a wire saw (STX-202A, MTI Corporation) with copious water as coolant. Each tooth was allowed to dry at room conditions, then one half was stored while the other was mounted in a two-part epoxy (EpoFix resin and hardener, Struers). The mounted sections were ground with a sequence of SiC papers (ISO numbers 800, 1200, 2400, 4000), ultrasonicated,

and polished with diamond suspensions (particle sizes 3, 0.5 µm; Struers) on separate polishing cloths (MD-Dac, Struers). Polished samples were stored in a desiccator for at least 48 hours to release unbound water, then sputter coated with 10 nm of Pt for conductivity (ACE600, Leica).

Samples were prepared for APT using a typical liftout procedure in a dual-beam focused ion beam scanning electron microscope (FIB-SEM; Helios and/or Quanta, both manufactured by Thermo Fisher Scientific). A protective Pt coating was deposited on a region of interest that was ~10 µm from the outer enamel surface (OES) and ~850 µm from the dentin-enamel junction (DEJ). Trenches were then milled on either side and one edge of the coated strip at a 30° incidence angle using a 30 kV 1 nA ion beam and cleaned of redeposited material with a second pass. The cantilever was attached to a nanomanipulator (Omniprobe) by a Pt weld then freed from the bulk material with a thin ion beam cut. The liftout was attached to a coupon of prepared Si microposts designed for APT (M22 array, Cameca) with Pt welds. To produce a sharp needle for APT, each sample was polished using annular ion beam milling. Final polishing of the needle was completed at 5 kV to remove the Ga-implanted region (~30-200 nm of enamel).

Experiments were run in a local electrode atom probe (LEAP 4000 XHR, Cameca) pulsing a 355 nm wavelength laser with a laser pulse energy of 60 pJ, a pulse frequency of 125 kHz, a base temperature of 40 K, and a target detection rate of 0.5%. This resulted in a charge state ratio for $^{40}Ca^{2+}$:$^{40}Ca^{+}$ of ~1400.

Reconstructions of the APT data were performed using the integrated visualization and analysis software (IVAS version 3.8.10, Cameca). Ranges were drawn to include those portions of the peak that had a signal with twice as many counts as the surrounding background. Voltage-based tip evolution was used to drive the reconstruction, assigning Ca with a field evaporation of

18 V nm^{-1} as the primary element, with default element specific atomic volumes, a detector efficiency of 0.36, k factor of 3.30, and an image compression factor of 1.650.

Regions of interest (ROIs) were generated by first rotating the reconstruction with only Mg ions visualized until the displayed ions aligned and the core-shell structures and intergranular areas became clear. The approximate boundaries of each nanocrystal were traced (see Figure 2.2a,c and Supplementary Figure 2a,c,e,g), and then segmented with rectangular ROIs drawn on each phase (Figure 2.2b,d and Supplementary Figure 2b,d,f,h). The size of the ROIs associated with the intergranular and core phases was adjusted to encapsulate the region of highest Mg concentration, whereas those associated with shell phase were sized to fill the spaces between core and intergranular ROIs. An effort was made to encapsulate as much of the reconstruction as possible, but without any overlapping of adjacent ROIs. Additionally, as the length of HA nanocrystals in enamel is many times longer than their cross section, each nanocrystal observed in the APT dataset was assumed to extend well beyond the reconstructed volume, and so the ROIs extend through the whole width of the reconstruction (into/out of the page in Figure 2.2b,d, Supplementary Figure 2b,d,f,h).

A frequency distribution analysis with 10-ion blocks was exported from each ROI as .csv files then loaded into a custom Python (version 3.11) script for analysis. The background-subtracted mass-to-charge spectra from each ROI (10s of ROIs per dataset) were ranged using the same .rrng file as the overall reconstruction they belong too, then the count of each ranged ion summed in a custom jupyter notebook by phase (3 phases per dataset). This condensed the composition of each dataset into just three compositions, one for each phase, rather than one for each ROI. The statistical strength of comparisons between the three phases and the two age groups

were evaluated using the scipy package for one-way ANOVA (`scipy.stats.anova`) and unequal variance t-test (`scipy.stats.t`), respectively.

Samples for scanning transmission electron microscopy (STEM) were prepared using a plasma FIB (PFIB, Helios Hydra, Thermo Fisher) using a typical liftout approach, full details can be found in the Supplementary information. Briefly, a protective Pt cap was first deposited over the region of interest, which was then milled using the Xe ion beam and attached to a nanomanipulator (EZLift, Thermo Fisher). Foils were attached to a 5-post Cu TEM Grid (Ted Pella) and thinned to a thickness of approximately 100 nm using a rocking polish technique. The foils were extracted from the same teeth used for the APT data collection at a location < 50 μm from the site of the APT liftout and 10 μm from the outer enamel surface.

STEM was performed on a Thermo Fischer Scientific Themis Z 30-300 kV monochromated aberration corrected S/TEM, operated at 300 kV with spot size of 9. Imaging was performed with a 70 μm probe forming aperture, 29 pA screen current, and camera length of 185 mm.

Nanocrystal size measurement was conducted in ImageJ version 1.54g (National Institutes of Health, USA). After setting the scale of the image, the freehand tool was used to outline individual nanocrystals from STEM micrographs collected at 165,000× magnification. Only nanocrystals for which the edges could be clearly defined were measured. The area of the enclosed nanocrystal as well as the major and minor axes of the fit ellipse around the drawn shape were recorded. An unequal variance t-test (`scipy.stats.t` in python v3.11) was used to evaluate significance of comparisons.

2.4. Results

2.4.1. Atom Probe Tomography

Three APT datasets large enough to capture multiple HA nanocrystals (between 8.5×10^6—19×10^6 ions per dataset) were obtained for both the young (total = 37.2×10^6 ions) and senior enamel (total = 36.9×10^6 ions). Samples were collected within 10 μm of the outer enamel surface (Figure 1.5a-c) as this region is most severely embrittled in senior enamel [86, 98]. Enamel from the cervical portion of the tooth was utilized in this study as it is not directly subjected to the mechanical wear imposed by mastication, allowing for improved consistency between samples from different individuals or age groups.

The mass-to-charge spectra from each APT dataset exhibited on the order of 100 peaks, due to the complex field evaporation phenomena that take place. It is noted that the largest molecular ions primarily featured covalently bonded groups, from PO at 46.969 Da to P_4O_{10} at 283.846 Da A segment of a representative spectra from 0 – 50 Da comparing the young and senior age groups and the chemical identity of each peak is presented in Figure 2.1. The full version of the spectral comparison is presented in Supplementary Figure 1. The most prominent peak in each spectra was the $^{40}Ca^{2+}$ peak at 19.982 Da.

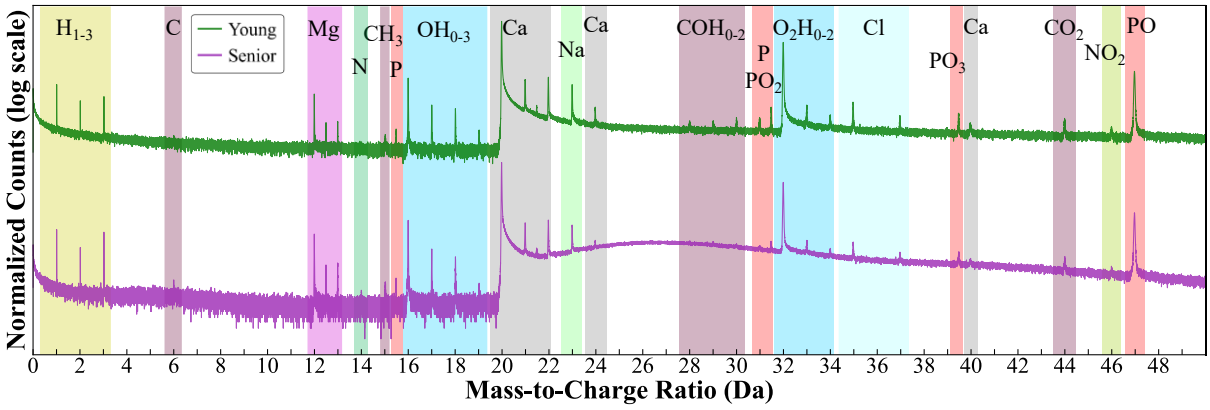

Figure 2.1. Labeled segment of representative mass-to charge spectra from young and senior enamel.

APT reconstruction of the enamel nanostructures (Figure 2.2) shows that independent of age, Mg is segregated to the core of each nanocrystal as well as the intergranular space between them, which agrees with the findings of another recent study [11]. The core of each nanocrystal is visible as an ovular, nearly linear region with a relatively high density of Mg ions surrounded by a Mg-depleted shell. Between shell regions the Mg density increases again, forming a continuous intergranular phase separating each nanocrystal. The shell thickness is not uniform; the cores are not evenly centered, and in many crystals, the core is observed to nearly contact the intergranular phase. The thickness of the intergranular phase is likewise nonuniform as some nanocrystals appear to almost impinge on each other while others are separated by tens of nm. As there is no definitive way to determine the edge of the nanocrystals based on ion concentrations, it is difficult to make a truly quantitative measure of the intergranular separation from APT alone. However, from approximate measures taken between the dashed lines in Figure 2.2 and Supplementary Figure 2, the average distance separating adjacent nanocrystals in the young enamel is ~3.9 nm, while that in the senior enamel is ~6.4 nm.

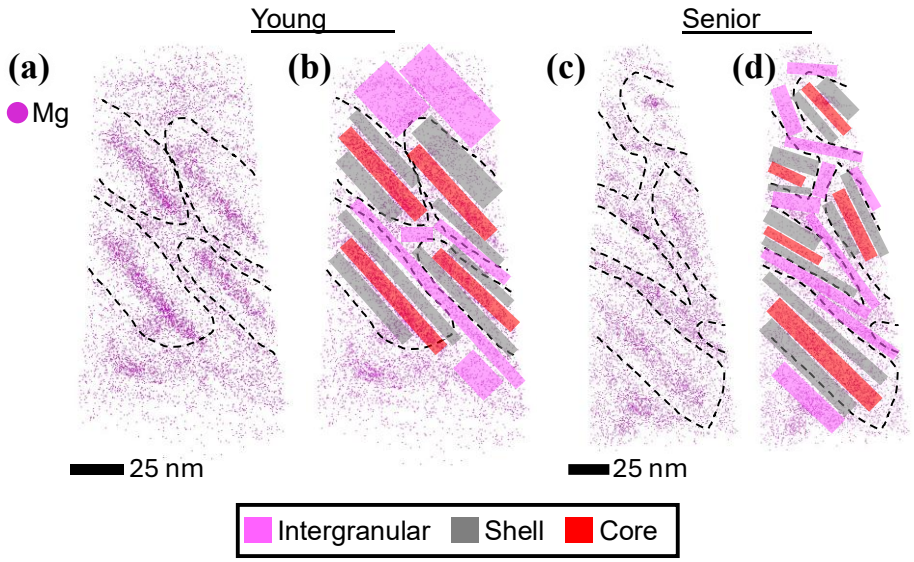

Figure 2.2. Representative APT reconstructions for young and senior enamel. Only the Mg ions are visible. *(a, c) Properly aligned reconstructions show the Mg-enriched core of each nanocrystal surrounded by a Mg-depleted shell. The intergranular space between nanocrystals also has a relatively high Mg concentration. The boundaries of each nanocrystal are outlined. (b, d) Rectangular ROIs are drawn and assigned to the intergranular, shell, or core phase.*

A two-tailed unequal variance t-test was performed to evaluate the strength of evidence for differences between the age groups, presented in Figure 2.3. There is moderate evidence that the senior enamel (0.136 ± 0.0064 at.% Mg, mean ± standard deviation) had a higher bulk concentration of Mg than the young (0.113 ± 0.0035 at.% Mg) enamel (p = 0.019), though there is no evidence of significant differences for any specific phase (Figure 2.3b). However, there are highly significant differences in the F concentration. In particular, the shells of nanocrystals in senior enamel (0.113 ± 0.0066 at.% F) show significantly higher F relative to those in young enamel (0.096 ± 0.0049 at.% F, p = 0.000595). There is additionally strong evidence that the bulk concentration of F is higher in senior enamel (p = 0.00263). This trend also appears true for the

intergranular and core phases, though the evidence is weaker ($p = 0.054$ and $p = 0.060$, respectively). In addition, the mean concentration of Na is higher in the young enamel for all phases, but there is no statistical evidence to support this trend (lowest $p = 0.117$ for bulk-bulk comparison, Figure 2.3d). Interestingly, the concentration of C, including both organic and inorganic contributions, is almost identical between young and senior enamel for the bulk as well as each phase. The mean concentration of C in the intergranular phase appears slightly lower than that in the young enamel, but there is no evidence to support this difference ($p = 0.659$, Figure 2.3e).

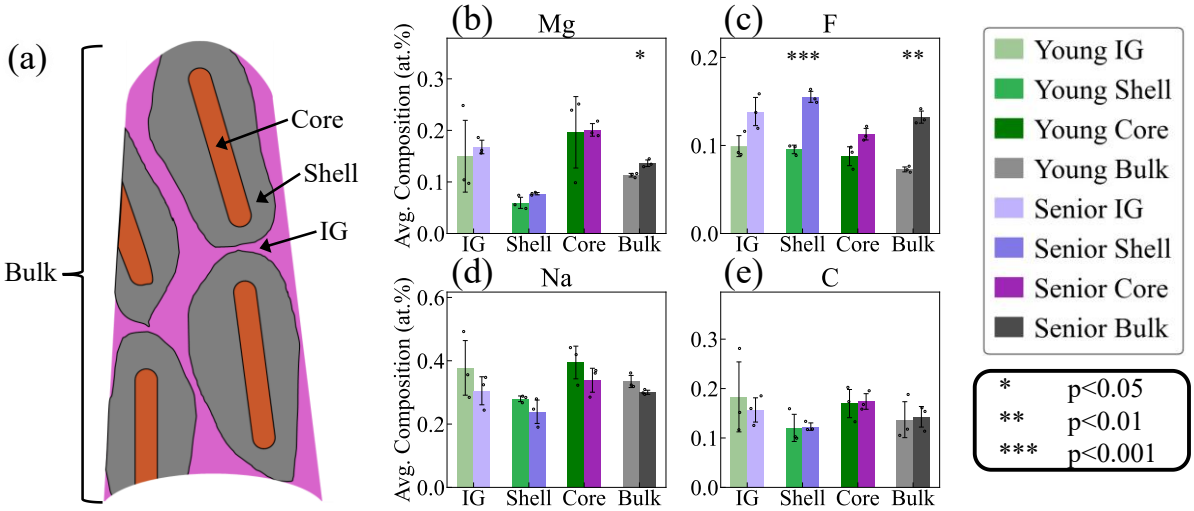

Figure 2.3. Comparison of minor element concentrations by nanocrystal phase. *(a) Schematic of an APT reconstruction that has captured several hydroxyapatite nanocrystals, with phases labeled. (b-e) Average composition in atomic% of Mg, F, Na, and C, respectively. For each phase, data from the young sample is on the left, senior is on the right. Error bars represent one standard deviation, each dataset is represented as a point. These concentrations are measured after molecular ions (e.g. CaF) have been decomposed into their constituent elements.*

Nitrogen is another signal which was expected to correlate with the residual organic components in enamel. This notion is supported by the fact that for the young enamel, the concentration of N is slightly but significantly greater (p = 0.0055) in the IG phase than in the shell. However, no significant difference was observed between phases for the Senior enamel, or between young and senior for any phase (Figure 2.4a).

Chlorine, like fluorine, can also substitute the OH groups in HA to form chlorapatite. Exposure of enamel to chlorine is exceedingly prevalent through dietary NaCl, yet no difference in Cl concentration was observed between young and senior enamel (Figure 2.4b). This is most likely because substitution of OH^- groups with Cl^- ions in HA is energetically challenging, especially at biological conditions [126]. Another complicating factor is that the spatial accuracy of Cl within the reconstruction is reduced due to the relatively high thermal background at the mass-to-charge ratios for Cl ions (Figure 2.1); it is challenging to determine whether a given ion is genuine Cl signal (spatially accurate) or an unintended evaporated event (limited chemical or spatial accuracy).

The molecular ions CO and CO_2 (Figure 2.4c,d) have also been identified as corresponding to proteins in APT reconstructions [46], with the complication that the latter has also been identified as associating with the carbonate substitutions in the HA lattice [26]. We hypothesized that the senior enamel would have a lower organic content in the IG phase, which could contribute to the increased brittleness [86]. However, in this data, it appears that the senior enamel has a slightly higher concentration of CO and CO_2 molecular ions, but these differences are not significant ($p > 0.05$ for each phase comparison).

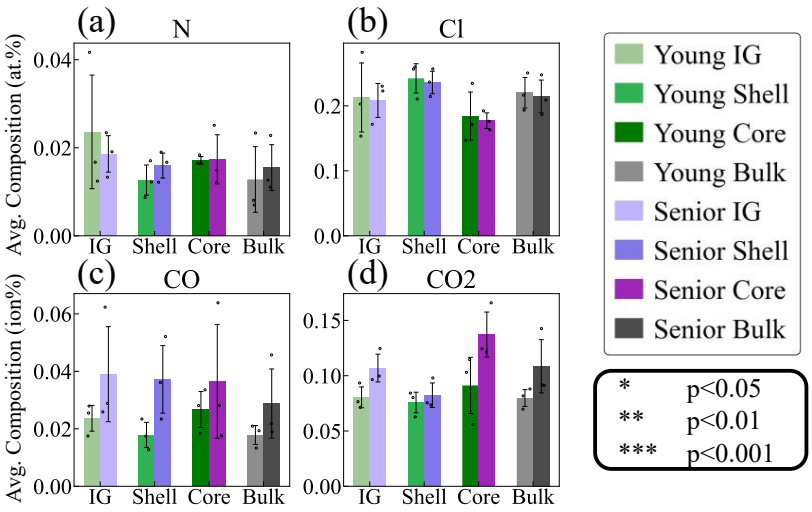

Figure 2.4. Comparison of additional ion concentrations between young and senior enamel by APT. *(a) N, (b) Cl, (c) CO molecular ions, (d) CO_2 molecular ions. Error bars represent one standard deviation, each data is represented as a point. Note that for a-b, the composition is taken after deconvolution of all ions, whereas for c-d, the composition is reflective of only that molecular ionic species against all ranged ions.*

2.4.2. Evaluation of ROI Accuracy

APT analysis software includes several powerful tools for automatically identifying volumes of interest. One of the most commonly employed is the iso-concentration surface (isosurface), whereby a 3-D surface is generated to enclose volumes of the reconstruction that have a concentration of the specified ion/element above a defined threshold. Unfortunately, this approach has limited success in enamel. A species that can be used to "trace" the phases (namely Mg) does not segregate with sufficient concentration or spatial clarity to generate a clean and continuous isosurface (see for example [26]), though it still aids in identifying grain boundaries [32]. However, when visually inspecting the reconstruction with only Mg ions visible, the viewing direction can be relatively easily aligned with the long axis of the HA nanocrystals as outlined by the Mg ions.

Because the HA nanocrystals are much longer than the diameter of the reconstruction, each dataset captures the cross sections of several nanocrystals in parallel, and the chances of capturing the end of a nanocrystal is very small. It is then both possible and essential to align ROIs to specific phases (core, shell, intergranular) so that the volumes enclosed can be used for further compositional analysis.

Figure 2.5a presents a histogram of the Mg concentration within each ROI, separated by phase. The cores and shells for both the young and senior enamel samples show good separation with distinctive high (>0.17 at.% Mg) and low (<0.13 at.% Mg) concentrations, respectively, which is expected given the visually guided definition in the reconstruction. ROIs associated with the intergranular phase have intermediate Mg concentrations between ~0.13 – 0.21 at.%, generally lower than in the cores but higher than the shells.

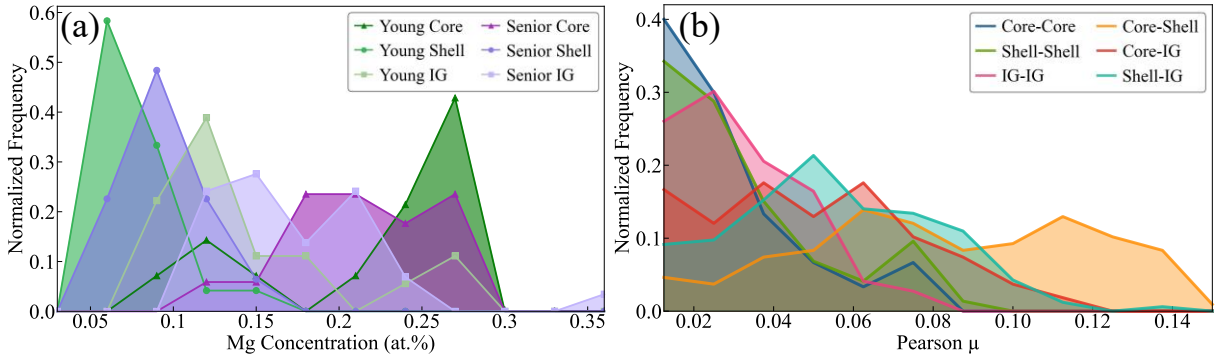

Figure 2.5. Validation of ROI phase assignments in APT data from young and senior adult enamels. *(a) Normalized frequency histogram of the Mg concentration (in at.%) of ROIs belonging to each phase. Cores and shells (triangle and circle markers, respectively) have good separation for both young and senior enamel samples, while the intergranular phase (square markers) is intermediate. (b) Normalized frequency histogram of the Pearson contingency coefficient μ calculated from pairwise comparisons of Mg frequency distribution between ROIs. Pairs of the type A-A have low μ values, whereas A-B pairs*

trend towards higher μ. Note that a given ROI is only compared against the other ROIs from the same APT dataset reconstruction.

A frequency distribution analysis (FDA) was performed on each ROI in Young Dataset 2 (Supplementary Figure 1a-b) and Senior Dataset 1 (Figure 2.2c-d) to provide an additional measure of the similarity between any two ROIs. A block size of 10 ions was chosen when exporting the distribution. The Pearson contingency coefficient μ was then calculated for each pair of ROIs within one dataset (i.e. each ROI was only paired against other ROIs from that same dataset). The interested reader is directed to reference [127] for additional description of μ; briefly, μ values range from 0 to +1 for highly similar to highly dissimilar distributions, respectively. The distribution of μ values for each type of pairs are presented in Figure 2.5b, separated by the phases being compared. Pairs of the type A-A (where A is core, shell, or intergranular phase) tend towards low values of μ around 0.02, though intergranular-intergranular pairs skew towards slightly higher μ of around 0.04. This is indicative that the distribution of Mg within the intergranular phase is somewhat heterogenous, agreeing with the observed spread of Mg concentration for intergranular ROIs in Figure 2.5a. Pairs of ROIs associated with different phases (e.g. A-B pairs) exhibited much higher μ values. Core-Shell pairs had the largest μ values, with most above ~0.05. This matches expectation as cores and shells have the largest difference in Mg concentration. The μ values for core-intergranular and shell-intergranular still tend to be larger than those for the A-A pairs but less than the core-shell pairs. This is due to the overlap in Mg concentration of intergranular ROIs with both cores and shells; a high-Mg intergranular and a low-Mg shell may appear similar and thus yield a low μ.

It is noted that the values of μ presented for the Mg distribution in Figure 2.5b may be somewhat lower than expected, despite the relatively obvious differences seen in the reconstruction visualization (Figure 2.2, Supplementary Figure 2). This is due to the concentration of Mg ions being quite low, and the block size being only 10 ions. The frequency distribution of an ROI with a relatively high concentration of Mg (e.g. 0.3 at%) will still be dominated by blocks that contain no Mg, and thus it can only vary so much from an ROI with low Mg concentration. That is under the assumption that each ROI follows a similar distribution (e.g. no clustering, which is validated by the low μ when comparing an Mg concentration in an ROI to its binomial). Because μ is a measure of similarity between two distributions, for ROIs with a similar degree of clustering, μ is constrained by the difference in composition. Finally, it must be critically noted that μ is not used here not to evaluate the compositional differences between ROIs or phases, but rather it is a tool that can help validate that the ROIs have been drawn accurately. If the phase of a given ROI cannot be confidently determined visually, the smallest μ value resulting from pairwise comparisons to known representative ROIs from each phase will indicate which phase the unknown ROI is most similar to.

2.4.3. Scanning Transmission Electron Microscopy

STEM was used to compare the relative morphology and nanocrystal size between the young and senior enamel samples by extracting cross sections from locations near where the APT samples were taken. Representative high-angle annular dark field (HAADF)-STEM micrographs were obtained at high camera length to reveal locations of higher strain, as presented in Figure 2.6. Nanocrystals with the expected elongated hexagonal cross section morphology and a core with darker contrast are readily seen in both samples. In the senior sample (Figure 2.6b), the nanocrystal

boundaries generally have good contrast, and the nanocrystals themselves are relatively well aligned and closely packed, though there are some gaps between misaligned nanocrystals. Nanocrystals that have a substantially brighter contrast may indicate higher lattice strain within these crystals. These bright crystals were observed far more frequently in the FIB lamella prepared from the senior enamel (Supplementary Figure 3). In comparison, nanocrystals in the young enamel sample are not as closely packed, with gaps being somewhat larger and more frequent. Additionally, there are mineralized regions that do not conform to the expected morphology, appearing more equiaxed, globular, or fragmented. Several such regions are highlighted by arrows in Figure 2.6a.

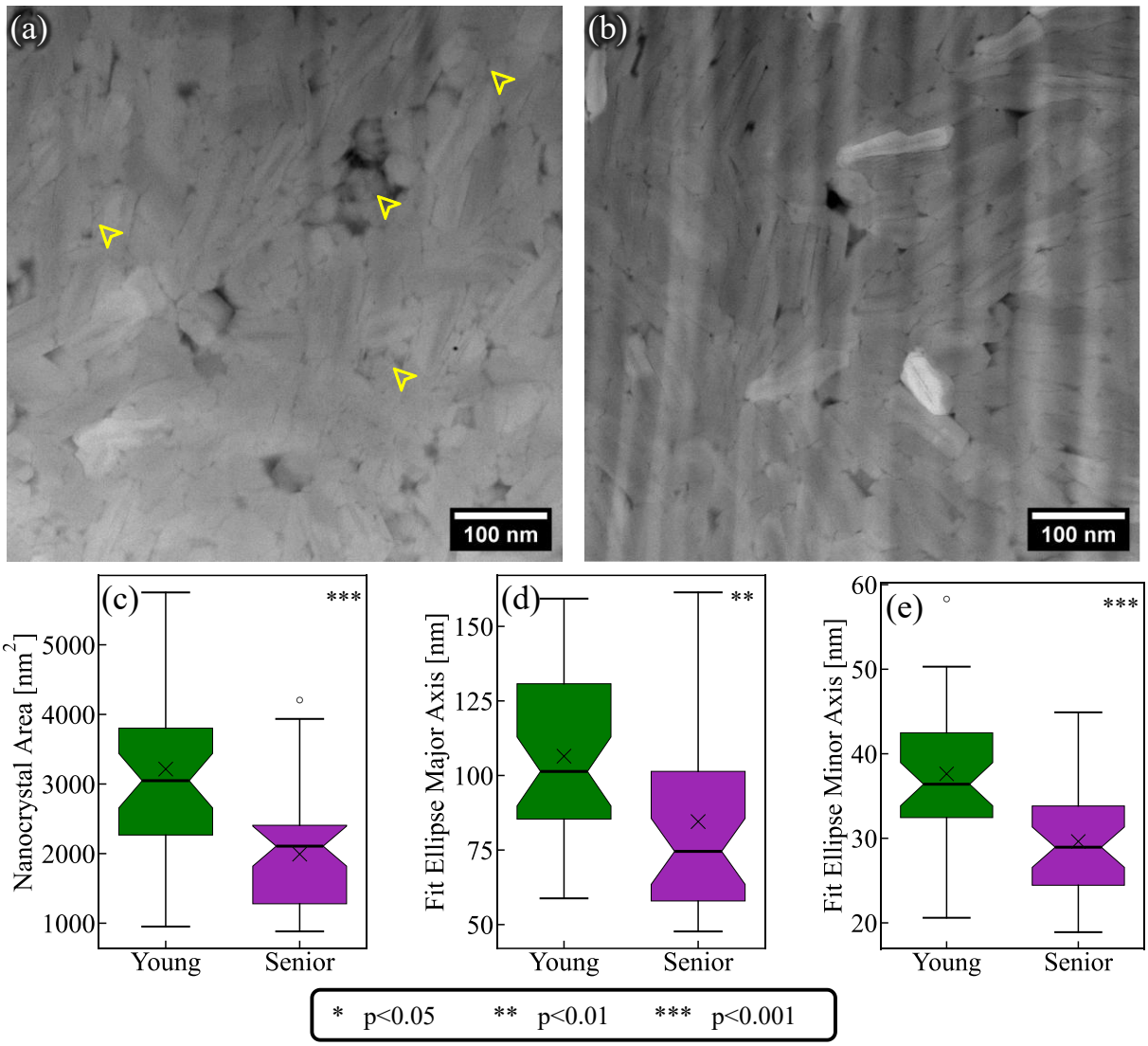

Figure 2.6. Comparison of nanocrystal dimensions and morphology by STEM high-angle annular dark field (HAADF). *(a) Young enamel. The yellow pointers highlight several regions where the mineral domain appears equiaxed, globular, or fragmented. (b) Senior enamel. (c-d) Box-and-whisker plots summarizing the distribution of (c) nanocrystal area, (d) fit ellipse major axis length, and (e) fit ellipse minor axis length for individual nanocrystals measured by STEM. Asterisks in the upper right corner denote the p value from an unequal variance t-test. In each plot, the box encloses the second and third quartile, the line represents the median, the notch is the 95% confidence interval for the median, the x marks the mean, and the whiskers stretch beyond the box by 1.5 times the inter-quartile range.*

Dimensional comparisons reveal that the average nanocrystal dimensions (in cross sectional area, and major and minor axis lengths) are smaller for the senior enamel sample relative to the young (Figure 2.6c-e). The nanocrystal cross sectional area is significantly different (p = 5.3E-6, unequal variances t-test) between the young (mean ± std = 3214 ± 1256 nm^2, n = 38) and senior (1993 ± 853 nm^2, n = 38) enamel samples. Similarly, the minor axis length of a fit ellipse drawn around each measured nanocrystal is significantly different (p = 4.6E-6, young = 38 ± 8 nm, senior = 30 ± 6 nm). There is also a difference in the long axis dimension between nanocrystals in the young (106 ± 28 nm) and senior (85 ± 30 nm) samples, though the statistical significance is not as strong (p = 0.0015).

2.5. Discussion

The mass-to-charge spectra were primarily dominated by Ca, O, and P-containing species. Smaller concentrations of impurity elements, such as Cl, Na, F, Mg, and C were also observed. In laser-pulsed APT of materials with low thermal conductivity, residual thermal energy from the laser pulse can cause mistimed evaporation events, which present as a thermal tail after prominent peaks. The senior enamel appears to have higher thermal tails after the Ca and O_2 peaks relative to the young samples (Figure 2.1). This may suggest that the senior enamel has physical features such as cracks or porosity that hinder thermal dissipation. The presence of bright nanocrystals in the senior enamel of our STEM analyses (Figure 2.6b, Supplementary Figure 3) may reflect nanocrystals with lattice strain that could impede thermal diffusivity. However, this is speculative and should be corroborated by measurements of thermal conductivity from other techniques (e.g. scanning thermal microscopy [128] or infrared measurements [129]) before making any firm conclusions.

The nanocrystal shape, as outlined by the intergranular regions enriched in Mg (Figure 2.2), agreed well with expectations from previous reports on enamel from APT, transmission electron microscopy, and atomic force microscopy in the literature [4, 11, 16, 25, 32, 130, 131]. It also agrees well with our own STEM analyses on these samples. Furthermore, the Mg-enriched core that has been previously reported in human enamel nanocrystals [11] was observed here as well. These regions of Mg enrichment served as the basis by which ROIs belonging to the core, shell, and intergranular phases were assigned. While it is challenging to measure the borders of the nanocrystals with certainty from APT data alone, using the dashed outlines as in Figure 2.2a,c, the intergranular thickness between nanocrystals is lower in the young samples. Measurements from STEM present a complimentary observation: the nanocrystals in young enamel are significantly larger (Figure 2.6), which has also been observed by atomic force microscopy [131]. A size decrease of HA nanocrystals in dentin tubules with increasing age has been reported [132, 133]. Assuming that the number density of nanocrystals does not change with age for a given volume of enamel, it follows that some volume of the nanocrystal shell is replaced by the intergranular phase over time. Such a pathway may also be responsible for the absence of the small mineral domains noted in the young enamel sample (Figure 2.6a yellow pointers) in the senior enamel, but more dedicated study is required.

A probable mechanism for the higher F content in the nanocrystal shells of senior enamel relative to young (Figure 2.3c) is the introduction and diffusion of F through the intergranular phase during the de- and re-mineralization cycles. When the enamel surface is exposed to an acid, it permeates through the intergranular spaces and reduces the diameter of the nanocrystals [13]. In the same vein, treatment with NaF solution results in strong segregation of both Na and F concentrations to the intergranular phase [11]. The outer enamel is exposed to both acidic and

remineralizing agents cyclically on a daily basis, and it is during these remineralization cycles that F ions can be incorporated into the HA lattice structure [4, 134].

Additionally, F substitutions within the HA lattice may diffuse further into the shell towards the core over time. Within the crystal structure of (hydroxy-, fluor- or chlor-) apatite, the interchangeable ion (OH^-, F^-, Cl^-) positions lie in a column along the vertical 6-fold screw c-axis [31]. The columnar alignment of the lattice points eligible for substitution makes the c-axis the fastest channel for ion diffusion. It has been conventional knowledge that the hexagonal crystal structure is aligned with the approximately hexagonal nanocrystal morphology [130], but there is recent evidence that the crystal directions of two adjacent nanocrystals can be misaligned by several 10s of degrees, even though the nanocrystals themselves appear well aligned [12]. This implies that the relatively fast-diffusing c-axis can be exposed to the intergranular phase, thereby enabling ion diffusion somewhat further into the nanocrystal.

The APT reconstructions showed only weak statistical evidence that the F concentrations of the intergranular and core phases were different between age groups (Figure 2.3c). Because the intergranular phase is the channel by which acids and remineralizing agents permeate the enamel, it is in a state of constant flux and long-term changes are unable to accumulate. Conversely, because the core is not directly exposed to the intergranular phase, it is unlikely to be directly affected by de- and re-mineralization cycles. The F concentration gradient between shell and core provides a driving force for diffusion. However, F^- substitutions in a HA lattice interact with the neighboring OH^- groups through hydrogen bonds, which can limit the rate of diffusion, even along the c-axis [135]. Thus, the composition of the core is relatively stable over time.

The fluoride concentration is of considerable importance because it enhances the dissolution resistance of the mineral. Partially fluoridated HA has substantially lower solubility relative to pure hydroxyapatite, with minimum solubility at ~2.4 at.% F [87]. This is an order of magnitude greater than the F concentration observed via APT. However, the gradient of F concentration against distance from the enamel surface is very sharp, even within just the first 5 μm [136], so the nanocrystals surveyed here are expected to have less F than those at the surface. It has also been shown that the difference in F concentration between young and senior enamel is more pronounced near the outer enamel surface [137]. Hence, a repeat of this study performed with tissue obtained closer to the enamel surface (perhaps even directly on the surface) would be expected to show similar trends, but with even greater difference between young and senior enamel.

Residual organic content between nanocrystals is a key component of crack growth resistance in enamel [138]. We hypothesize that residual organic content is leached out over time and replaced by mineral, contributing to the increase in brittleness, but there are challenges to assessing this with APT. From this data, a reliable method for determining whether a carbon-containing molecular ion is of organic (proteins and protein cleavage products) or inorganic (CO_3 substitutions in the HA lattice) origin could not be determined. Additionally, none of the datasets collected for this study exhibited the organic- and Mg-rich precipitates that other groups have reported in enamel [26, 32]. This is expected to be partly due to taking samples near the outer surface, where protein content is lowest [7, 86, 98]. It has been proposed that the CO^+ signal at 28 Da is associated with both organics and inorganics while CO_2^+ at 44 Da is only associated with inorganics based on their segregation within or outside of organic precipitates [26, 46]. As shown in Figure 2.4, there was little to no statistical evidence in this case that the concentration of CO or CO_2 showed any trend with age between the young and senior enamel (Figure 2.4c-d). The same

is true for N (Figure 2.4a), which would be expected to be associated with organics. This question is explored systematically and in greater detail in Chapter 5.

Admittedly, a higher F concentration in the outer enamel of seniors could be expected [86, 108, 137]. However, the spatial evaluations of F across individual crystal domains between individuals enabled by recent advances in APT provides a new perspective of the mechanisms at play. It is proposed that the intergranular amorphous mineral phase that separates the hydroxyapatite nanocrystals is the primary channel by which the de- and re-mineralization cycles of enamel occur. Fluorine (from e.g. fluoridated drinking water and other F-enriched dental products) is incorporated into the shells of nanocrystals during remineralization. While some diffusion of F ions through the nanocrystal surely occurs, the accumulation of F is largely restricted to the nanocrystal shell, suggesting that ion replacement during remineralization is the dominant mechanism.

There are recognized limitations to the present study that are important to consider. The primary limitation is the relatively small number of samples. Only one donor tooth from each age group was considered, and only three datasets were collected for each tooth. A small sample size cannot account for intrinsic variation between individuals owing to their lifestyle, diet, upbringing (i.e. exposure to fluoridated water in adolescence during permanent molar formation), or genetic predisposition. These are equally interesting topics that merit future evaluation. Nevertheless, we believe that the proposed model is a likely mechanism for the increased fluoride concentration in seniors that has been observed for some time with larger datasets [86, 137]. Topical treatment by NaF (250 mM, pH 8.4, 37°C, 24 hrs) shows that the captured F from exposure at this time scale is restricted to the intergranular phase [11]. Our interpretation of this is that the fluoride is unable to

significantly diffuse and incorporate into the nanocrystal shells by direct exposure only. Here, we did not see a strong difference in the fluoride concentration in the intergranular space; it is unlikely that this is what drives the elevated F content in seniors. That leaves incorporation during de-/re-mineralization cycles as a likely mechanism by which F can accumulate over time.

One could question the clinical relevance of the research. We envision that the findings could help guide the development of clinical approaches to improve the efficacy of fluoride treatments in tooth protection. Key would be understanding the placement and degree of accumulation of fluorine within crystals. Clearly, APT could serve as a valuable resource in this effort. With regards to the accumulation of fluorine with age, the findings establish one aspect of change in the structure-composition-properties relationship that could be responsible for the increased hardness and embrittlement of enamel in older patients [86, 109, 139]. Modulating tooth protection and age-related embrittlement simultaneously has the potential for substantial clinical impact and the status of lifelong oral health.

Regrettably, APT is not easily applied to large sample sizes because access to the required instrumentation is costly, and it is time-intensive from sample preparation through data collection and analysis. However, the statistical methods employed herein identified highly significant differences in composition and can be readily applied to larger datasets as automation capabilities for both data collection and analysis continue to improve. Furthermore, although this study was focused primarily on fluorine, there are other components, including carbonate substitutions, organic residues, and nanocrystal morphology, that undoubtedly contribute to the degradation in mechanical properties of senior enamel as well, and warrant further investigation. The findings emphasize that compositional modifications that accompany aging accumulate with the

chronological clock. Key to mitigating the age-induced degradation of enamel will be identifying those nanoscale factors that accelerate the aging process, the underlying mechanisms, and the most appropriate avenues for therapeutic treatment.

2.6. Conclusion

A statistical approach for comparing APT datasets is developed and applied to the samples taken near the outer surface for young and senior enamels. The nanometer-scale resolution of APT enables a breakdown of the composition tissue into three distinct phases which can be visually and numerically distinguished by the presence of Mg ions: nanocrystal core, nanocrystal shell, and amorphous intergranular phase. We report a significantly elevated fluorine concentration in the shell portion of senior nanocrystals relative to young, which is likely incorporated into the hydroxyapatite lattice during cyclical de- and re-mineralization. Through STEM imaging, we also observe that the cross-sectional size of the mineral nanocrystals is significantly smaller for the senior enamel, which may be attributed to erosion and replacement by amorphous intergranular phase during de-/re-mineralization cycles.

This chapter investigated samples taken from near the outer enamel surface, where the influence of external factors in the oral environment are most likely to be exerted. However, gradients in the composition and mechanical properties as a function of distance through the enamel thickness are well documented. Thus, there may be additional merit in sampling multiple locations through the enamel thickness, a topic which is explored further in Chapters 3 and 5. Additionally, there is limited characterization of non-human—and especially non-mammalian—enamel at this scale. Other species have developed different methods of enamel formation to suit

their evolutionary niche, such as the rapidly replaced teeth of crocodilians which experience extreme loading due to high bite force. This is the subject of Chapter 3 below.

3. Sharp gradients in composition, properties, and nanostructure of the surface layer of crocodilian enamel

3.1. Synopsis

Crocodilian enamel is evolutionarily much older and less structurally complex than most mammalian enamels. To accommodate exceptionally strong bite forces without microstructural features to guide and arrest crack growth, crocodilians instead rapidly regenerate and replace their teeth. However, this is not to say that there are no features which might confer improved performance in the enamel layer. A difference in composition (i.e., carbonate substitutions in the hydroxyapatite lattice) and mechanical properties (i.e., hardness and reduced modulus) between inner and outer enamel are reported here for samples from the American alligator (*Alligator mississippiensis*) and saltwater crocodile (*Crocodylus porosus*). In contrast to the gradual or continuous gradient through the thickness observed in many mammals, crocodilian enamel exhibits a relatively thin outermost region, which is considerably harder, stiffer, and contains fewer carbonate substitutions.

The statistical approach developed in Chapter 2 is applied to APT data here to compare the composition of nanocrystals and the intergranular phase between inner and outer enamel of *Crocodylus porosus*. The most significant differences are found for the concentrations of Na, H, and CO_2, with the outer enamel having a lower concentration for all three. Interestingly, the correlation of the carbonate content from Raman spectroscopy and the concentration of CO_2 molecular ions in atom probe tomography lends additional evidence that this ion is a product of inorganic sources. In addition to compositional information, the APT reconstructions indicate that

the smaller nanocrystals of the outer enamel layer are separated by a greater thickness of the amorphous intergranular phase. However, it is not clear at this time whether the composition and structure of the outermost layer is a feature of amelogenesis or a consequence of the environmental exposures experienced by crocodilians.

3.2. Introduction

The structural complexity of most mammalian enamels, as with many specialized biological tissues, is due to iterative improvements introduced as responses to selective pressures over millions of years of evolution [6]. Hierarchical microstructures are evidently a viable answer to the challenge presented when using a relatively hard, stiff material in a chemically challenging oral environment subjected to frequent cyclical loading without the ability to remodel for decades. However, complex decussation patterns are only one answer to the challenges of evolutionary pressures, and other responses have emerged to fill other niches. For instance, the incisors of many species in the order Rodentia grow continuously and exhibit a uniserial decussation pattern (i.e. each layer of rods exhibits an alternating direction, rather than bands of multiple rods) which facilitates a self-sharpening mechanism [42]. Consulting the fossil record and enamel of other extant species reveals another response, the so-called "primitive" enamel of crocodilians and other reptilians [49].

Crocodilian enamel has remained relatively unchanged over millions of years [54], and thus relatively simple in microstructural design, despite the saltwater crocodile (*Crocodylus porosus*) having the highest recorded bite force of any terrestrial species [47]. The microstructure of the enamel consists merely of relatively well-aligned radial nanocrystals that are not arranged into

rods or comparable multi-micrometer-scale features [48, 49]. Instead of relying on robust enamel that can last years, crocodilians rely on a strategy of rapid tooth replacement [140] on a roughly annual schedule [52] to support dietary changes with increasing individual maturity [141] or to replace damaged teeth as long as the alveola is still operational [53], facilitated by stem cell differentiation [51].

The combination of high loading forces with relatively simple microstructure renders crocodilian enamel an interesting subject for study. Extant reptilian enamel provides a comparative model for understanding the most fundamental mechanical and compositional properties of enamel nanocrystals without the higher levels of hierarchical structure. Various properties of the dentin, enamel, and cementum of *C. porosus* teeth have been characterized by Enax et al. [48], but whether or not there are gradients in composition or properties through the enamel thickness—a well-documented feature in mammalian enamel (e.g., [7, 9])—has not been reported to the author's knowledge. Additionally, application of APT to enamel has revealed compositional gradients at the nanocrystal scale which may improve the mechanical properties of the overall tooth [11]. Are such gradients present in crocodilian enamel, or is this a unique feature in humans/mammals? An additional potential point of comparison could be to certain phenotypes of amelogenesis imperfecta in mammals, where genetic defects can result in enamel that lacks the critical rod structure [15]. Understanding the nanocrystals for a "control" system (i.e. not genetically defective) may provide useful context for studies of mature enamel afflicted by amelogenesis imperfecta [115].

In this chapter, we characterize the through-thickness properties and composition using nanoindentation and Raman spectroscopy of enamel from two crocodilian species: *C. porosus* and

Alligator mississippiensis. Additionally, we statistically compare the composition of nanocrystals and intergranular space between outer and inner *C. porosus* enamel using APT. We find that the outermost layer of enamel in both species is substantially more mineralized and harder yet has a markedly smaller and less well-organized nanocrystal structure. We anticipate that the findings will be relevant for future studies of the mechanisms of crocodilian amelogenesis as well as the evolution of micro- and nanostructural complexity in enamel across the tree of life.

3.3. Methods

3.3.1. Sample sourcing and preparation

Teeth were collected for experimental studies from a variety of sources. A human molar for comparison of through-thickness composition and property gradients was obtained from the Dental School at the University of Washington in Seattle, WA, under an IRB exemption for STUDY00014724. Molariform *A. mississippiensis* teeth were extracted from a frozen cadaver of a ~2.5 m long female captured by a nuisance trapper in the Rockefeller Wildlife Refuge in Louisiana. Molariform *C. porosus* teeth were naturally exfoliated during regular use by numerous individuals in a shared enclosure at the Reptile Gardens reptile zoo in Rapid City, South Dakota.

Upon receipt, the teeth and tissue waste were sterilized using a freshly prepared 1:10 dilution of 0.5% sodium hypochlorite. The teeth were sectioned buccal-lingually along the midline of the tooth using a diamond wire saw (STX-202A, MTI Corporation) with copious water as coolant. Each tooth was allowed to dry at room conditions, then one half was mounted in a 2-part epoxy (EpoFix resin and hardener, Struers). The mounted sections were ground with a sequence of SiC

papers (ISO numbers 800, 1200, 2400, 4000), ultrasonicated, and polished with diamond suspensions (particle sizes 3, 0.5 μm; Struers) on separate polishing cloths (MD-Dac, Struers).

3.3.2. Nanoindentation

Gradients in mechanical properties were evaluated using nanoindentation performed on a Hysitron Triboindenter TI 980 (Bruker) equipped with a Berkovich pyramid indenter. Arrays of 3×3 indents were performed on the polished buccal-lingual section at six equally spaced locations across the enamel thickness along a given trajectory perpendicular to the DEJ. These locations are reported as normalized distance (ND) from DEJ to OES. The first and last locations were ~20 μm from the DEJ or OES, respectively. A load of 5 mN with a 5 s hold time and loading and unloading rate of 1 mNs^{-1} were used for each indent. Three trajectories were analyzed for each tooth, yielding a total of 162 indents per tooth (9 indents x 6 normalized distances x 3 trajectories = 162). The hardness and reduced modulus were calculated for each indent from the unloading force-displacement curve following the method described by Oliver and Pharr [142]. Averages and standard deviations were calculated for each of the six normalized distances including measures taken from all three trajectories. Before starting indents on each tooth, the instrument was calibrated by performing an air indent and the tip-area function was validated by indenting a fused quartz reference sample. In an effort to maintain tooth hydration, the enamel was stored in Hank's balanced salt solution until just before testing, wiped dry with a lab wipe, then a droplet of ethylene glycol was smeared on the surface to delay evaporation of bound water in the tissue during testing.

3.3.3. Raman Spectroscopy

To measure compositional characteristics of the enamel mineral component as a function of distance from the DEJ, Raman spectroscopy was performed at six equally spaced distances through the enamel thickness of the polished B-L section along three trajectories (18 scans per tooth), similar to the procedure described for nanoindentation. The trajectories used for Raman spectroscopy were not the same as those for nanoindentation, though the same polished buccal-lingual section was used. As a reference, spectra were also collected from synthetic HA (Clarkson Chromatography Products, Inc.). Scans were performed using a 785 nm laser over a spectral range of 300 – 1200 cm^{-1} on a confocal Raman microscope (InVia, Renishaw) with a 50x objective lens (Leica Microsystems), yielding a spot size of ~10x50 μm. Each scan was run at 50% laser power and with a scan time of 10 s. A calibration scan was performed on Si before each sample.

Spectra were processed including background subtraction and analyzed using Windows-based Raman Environment software v3.4 (WiRE, Renishaw). Peak fitting curves were used to extract the position, full width at half maximum (FWHM), and integrated area of the phosphate ν_1 peak at ~960 cm^{-1}, as well as the integrated area of the carbonate ν_1 peak at ~1069 cm^{-1}.

3.3.4. Scanning Electron Microscopy

Polished samples were stored in a desiccator for at least 48 hours to release unbound water before being etched with 10% HCl for 6 s then sputter coated with ~15 nm of Au/Pd. A strip of carbon tape was used to provide a conductive pathway from the coated surface of the epoxy puck to the sample stage. Imaging was performed on a FIB-SEM (XL380 Dualbeam, FEI Company). Accelerating voltages of 3-5 kV and a spot setting of 2 were used.

3.3.5. Atom Probe Tomography

Samples were prepared for APT using a typical liftout procedure in a FIB-SEM (Helios Nanolab 600i and/or Quanta, Thermo Fisher Scientific), as described in Chapter 2. Samples were first sputter coated with 10 nm of Pt to improve conductivity (Leica ACE600). A localized protective Pt cap was deposited on regions in the inner and outer enamel of a sectioned *C. porosus* tooth by decomposing organometallic gas with the electron and ion beams, sequentially. The outer enamel liftout was taken from a location near the cusp of the tooth within 10 μm of the outer enamel surface. The middle enamel liftout was taken from the same tooth along a line extending perpendicularly from the DEJ to the location of the outer enamel liftout, at an ND of approximately 0.6 (Supplementary Figure 4). Trenches were then milled on either side of the Pt cap and one edge of the coated strip at a 30° incidence angle using a 30 kV 1 nA ion beam then cleaned of redeposited material with a second pass (Figure 1.5c). The cantilever was attached to a nanomanipulator (Omniprobe) by a Pt weld then freed from the bulk material with a thin ion beam cut. The liftout was attached to a coupon of prepared Si microposts designed for atom probe tomography (M22 array, Cameca) with Pt welds (Figure 1.5d). To produce a sharp needle for APT, each sample was polished using annular ion beam milling (Figure 1.5e). Final polishing of the needle was completed at 5 kV to remove the Ga-implanted region (~30-200 nm of enamel, Figure 1.5f).

APT data collection, reconstruction, and segmentation were performed in the same fashion as described for human outer enamel in Section 2.4.1. The only difference is that due to a lack of Mg-rich cores, *C. porosus* APT reconstructions were only segmented into crystal and intergranular (IG) phases, again through visual alignment of the Mg-rich regions.

3.3.6. Statistics

Following the procedure established in Chapter 2, the background-subtracted mass-to-charge spectra from each ROI (10s of ROIs per dataset) were ranged using the same .rrng file as the overall reconstruction they belong to, then the count of each ranged ion was summed in a custom jupyter notebook (Python 3.11) by phase. This treatment condensed the composition of each dataset into just two compositions, one for each phase, rather than one for each ROI. The statistical strength of comparisons between the phases and the age groups/locations were evaluated using the scipy package for one-way ANOVA (`scipy.stats.anova`) and unequal variance t-test (`scipy.stats.t`), respectively.

3.4. Results

The through-thickness change in nanocrystal morphology in crocodilian enamel imaged by SEM is presented in Figure 3.1, which shows the gradient in microstructure from the DEJ to the OES. Throughout, the nanocrystals are well aligned, extending radially from the DEJ to the OES as expected from the B-L section presented in Figure 1.2. The nanocrystals near the DEJ (Figure 3.1b) have a "fanning" pattern consisting of sheets of nanocrystals overlapping. In the middle enamel (Figure 3.1c), the nanocrystals are somewhat more aligned and more densely packed while the nanocrystal size and shape are consistent with those near the DEJ. However, near the outer enamel surface (Figure 3.1d), there is a sharp gradient where the nanocrystal size and the contrast between nanocrystals decrease. This gradient takes place in the outermost ~30 μm of the enamel thickness, notably the outermost ~10 μm appears more as a cuticle-like layer with very low contrast between adjacent nanocrystals. While contrast between nanocrystals in the outer layer is

generally reduced on the section plane, the exposed ends of the nanocrystals on the OES (upper right corner of Figure 3.1d) are still visible. The oblique angle of the exposed ends makes quantitative measurements challenging, but it is apparent that the nanocrystals that intersect the OES are substantially smaller than those in the inner and middle enamel.

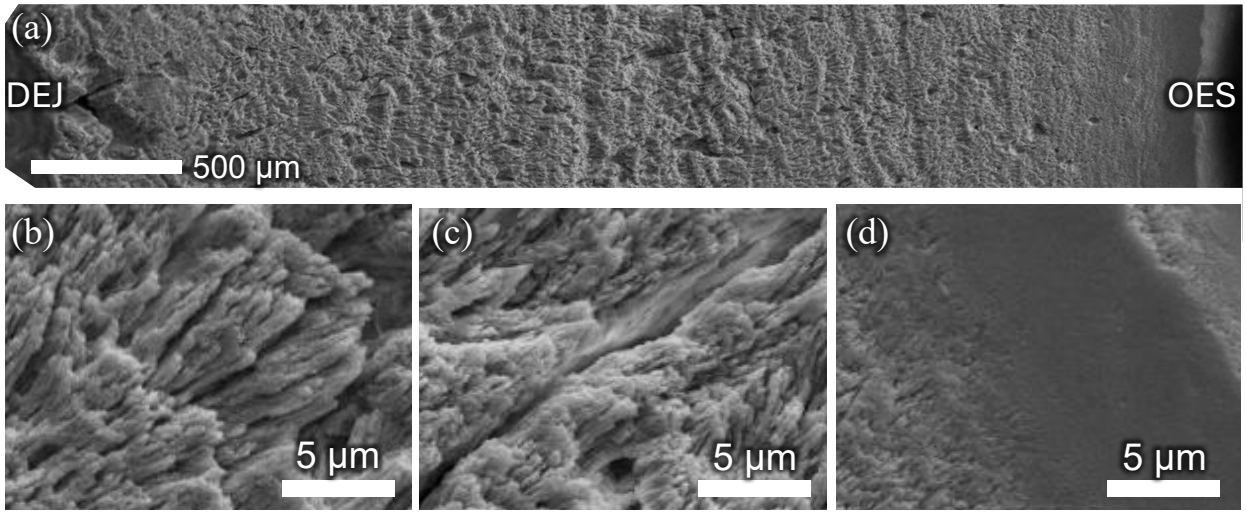

Figure 3.1. SEM of an Alligator mississippiensis tooth sectioned transversely after etching with EDTA for 20 min to reveal the microstructure. *(a) Composite SEM of the full thickness from dentin-enamel junction (DEJ) to the outer enamel surface (OES). (b-d) High magnification images of the (b) inner, (c) middle, and (d) outer enamel layers. The size and distribution of nanocrystals is relatively consistent throughout the inner and middle layers of the enamel, but near the OES, the nanocrystal size rapidly diminishes. There is low contrast between nanocrystals near the OES on the section plane, but the ends of nanocrystals can still be observed on the outermost surface (upper right corner of (d)).*

Raman spectroscopy (Figure 3.2) also revealed a substantial change in the outermost layer of enamel relative to the rest of the thickness. Similar to the nanocrystal morphology, the position and width of the P-O ν_1 symmetric stretching peak at ~961 cm^{-1} ($PO_4\nu_1$), as well as the integrated ratio of the $CO_3\nu_1$:$PO_4\nu_1$ peaks, are consistent throughout the inner and middle enamel with a

sudden change near the OES. Additionally, both the *C. porosus* and *A. mississippiensis* enamels showed highly similar trends, as indicated by the overlapping shaded 95% confidence interval bands in Figure 3.2. Considering the *C. porosus* enamel, the mean $PO_4\nu_1$ position increased from 959.69 cm^{-1} (standard deviation ± 0.07 cm^{-1}, n = 12 spectra) in the middle enamel (normalized distance between 0.33 – 0.66) to 960.08 cm^{-1} (± 0.12 cm^{-1}, n = 6) at the OES (Figure 3.2a). Similarly, the full width at half max (FWHM) of the $PO_4\nu_1$ peak decreased from 15.37 (± 0.08) cm^{-1} in the middle to 13.43 (± 0.26) cm^{-1} at the OES (Figure 3.2b). Lastly, the ratio of the integrated area of the $CO_3\nu_1$ peak at ~1069 cm^{-1} decreased from 0.167 (± 0.013) in middle enamel to 0.101 (± 0.077) at the OES (Figure 3.2c). As a reference, synthetic hydroxyapatite has an average $PO_4\nu_1$ peak position of 962.80 (± 0.08) cm^{-1}, $PO_4\nu_1$ peak FWHM of 5.72 (± 0.09) cm^{-1}, and $CO_3\nu_1$:$PO_4\nu_1$ ratio of 0.025 (± 0.006).

Human enamel showed the same trends in measurements from Raman spectroscopy, though the gradient in each property is much more gradual and continuous between the DEJ and OES and the values are closer to that of pure synthetic hydroxyapatite. For human enamel, the $PO_4\nu_1$ peak position ranged from 960.02 (± 0.08, n = 6) cm^{-1} at the DEJ to 960.54 (± 0.13, n = 5) cm^{-1} at the OES. The $PO_4\nu_1$ FWHM near the DEJ is 14.75 (± 0.19) cm^{-1}, decreasing to 10.42 (± 0.17) cm^{-1} at the OES. Lastly, the $CO_3\nu_1$:$PO_4\nu_1$ ratio decreases from 0.150 (± 0.013) near the DEJ to 0.068 (± 0.004) at the OES.

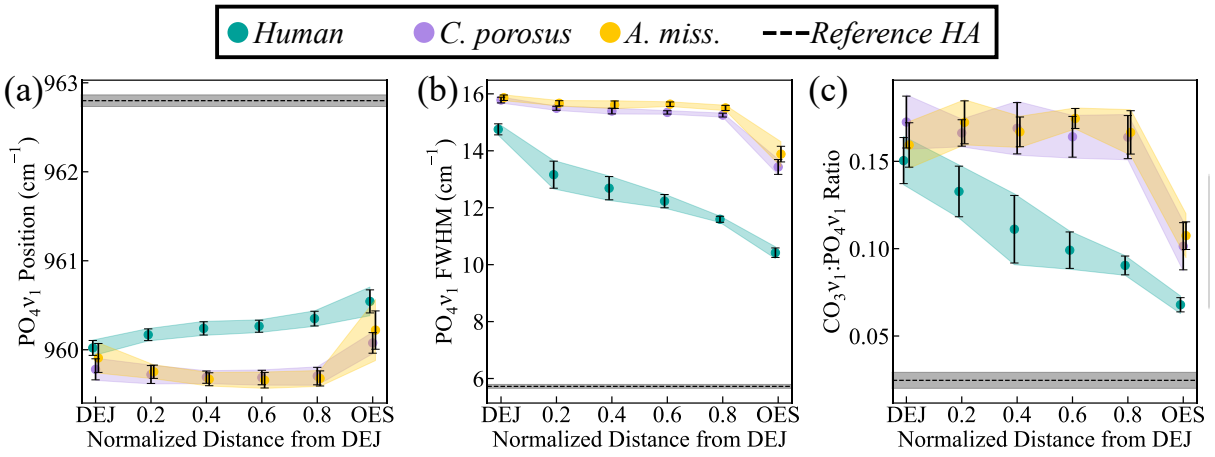

Figure 3.2. Summary of Raman spectroscopy results for synthetic hydroxyapatite (HA) and enamel from Human , *C. porosus*, and *A. mississippiensis*. *Data from enamel samples are plotted against distance from the dentin-enamel junction (DEJ) towards the outer enamel surface (OES) normalized by the enamel thickness. Each point represents the mean of 4-6 measurements, error bars one standard deviation, and shaded bands the 95% confidence interval. (a) Wavenumber of the center of the $PO_4\nu_1$ peak. (b) Full width at half maximum of the $PO_4\nu_1$ peak. (c) Ratio of the integrated areas of the $CO_3\nu_1$:PO4v1 peaks after peak fitting.*

Gradients in the mechanical properties of human and crocodilian enamels measured by nanoindentation as a function of normalized distance from the DEJ are presented in Figure 3.3. Human enamel has a considerably higher reduced modulus (between 75.2 ± 5.5 – 94.6 ± 5.1 GPa) than either of the crocodilian species (between 63.4 ± 8.4 – 70.6 ± 3.6 GPa for both species). Additionally, the trend of increasing reduced modulus with increased distance from the DEJ is only apparent for the human enamel. Considering the substantial change observed in the mineral characteristics measured by Raman spectroscopy, there is only a slight increase in the reduced modulus between the middle enamel (67.0 ± 3.4 GPa, n = 107 indents) and the outermost layer (70.6 ± 3.6 GPa, n = 54) in *C. porosus* (Figure 3.3a). Similar trends are noted for the *A.*

mississippiensis, though there is a deviation near the DEJ where the *C. porosus* enamel shows relatively elevated stiffness (69.8 ± 4.6 GPa), while the *A. mississippiensis* enamel is somewhat lower (63.4 ± 8.4 GPa).

By contrast, both crocodilian species show an elevated hardness near the DEJ and the OES relative to the middle enamel. For *C. porosus*, the middle enamel had a hardness of 3.65 (± 0.55, n = 107) GPa, while the indents nearest the DEJ measured 3.93 (± 0.83, n = 54) GPa and those near the OES measured 4.08 (± 0.57, n = 54) GPa (Figure 3.3b). In comparison, the hardness gradient in the human enamel is continuous and nearly linear, increasing from 3.70 (± 0.43, n = 54) GPa to 4.79 (± 0.51, n = 53) GPa between DEJ and OES regions, respectively.

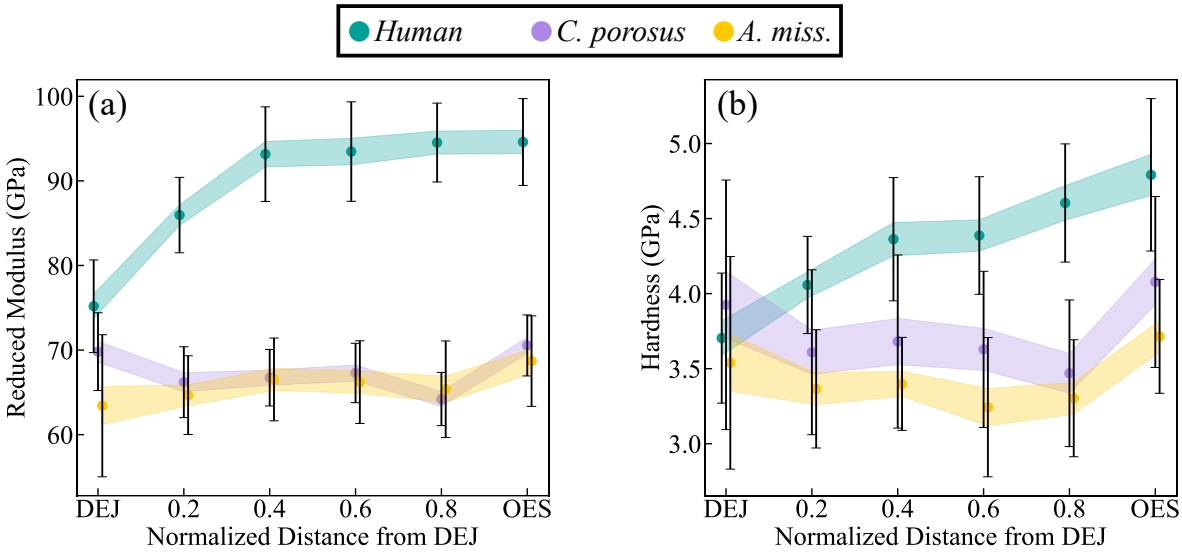

Figure 3.3. Summary of nanoindentation results on enamel from Human, C. porosus, and A. mississippiensis. *Results are plotted as a function of distance from the dentin-enamel junction (DEJ) towards the outer enamel surface (OES) normalized by the enamel thickness. Each point is the mean of 45-54 indentations, the error bar is one standard deviation, and the shaded area the 95% confidence interval. (a) Reduced modulus. (b) Hardness.*

Six APT datasets each containing between 1.2×10^6 – 7.2×10^6 ions were collected from the middle (n = 3 samples, 15.1×10^6 ions total) and outer (n = 3, 11×10^6 ions) enamel of *C. porosus*. Reconstructions of the Mg concentration from representative APT reconstructions from these regions are presented in Figure 3.4. As in human enamel, the Mg is segregated to the intergranular phase between nanocrystals, enabling visualization of the nanocrystals, though *C. porosus* enamel lacks the Mg-enriched nanocrystal cores. The intergranular regions in the middle enamel are relatively thin (~7 nm), and separate nanocrystals of ~11–16 nm thick. Interestingly, the nanocrystals appear to curve, but due to the limited volume captured by APT it is impossible to resolve the full morphology of whole nanocrystals without correlative techniques such as STEM or atomic force microscopy. In the outer enamel, the nanocrystals appear to be somewhat smaller and are separated by a more continuous intergranular phase (Figure 3.4b). Regions of interest were manually defined based on the Mg concentration (Figure 3.4c-d) to separate the reconstruction into crystal and intergranular phases.

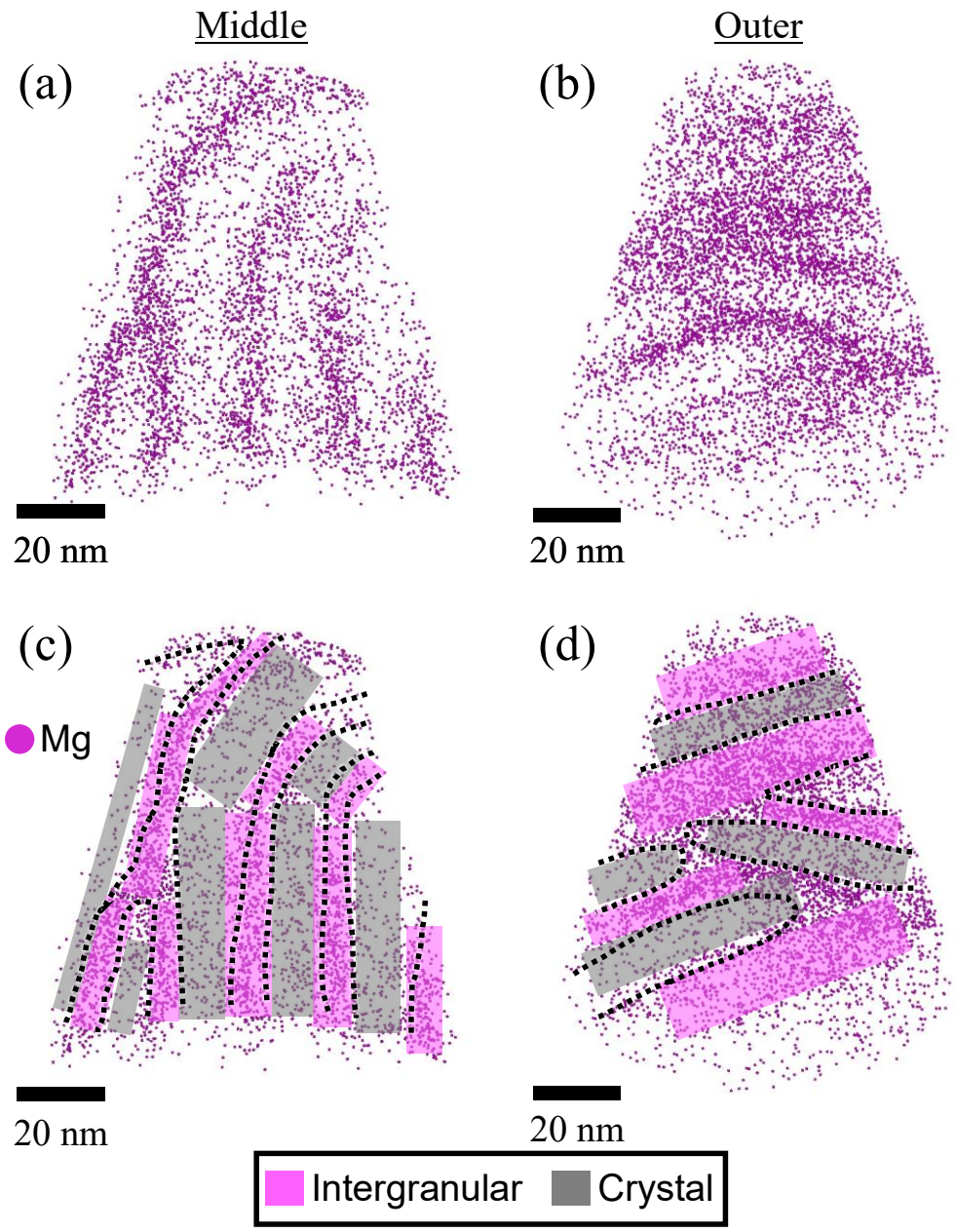

Figure 3.4. APT reconstructions of (a, c) middle and (b, d) outer enamel from C. porosus. *(a, b) Reconstructions with only Mg enabled were used to identify intergranular (high Mg) and crystal (low Mg) phases. (c, d) Rectangular regions of interest were then defined to capture the intergranular and crystal phases.*

The composition of H, C, Na, Cl, CO, CO_2, and Mg for the intergranular and crystal regions of the APT reconstructions are presented in Figure 3.5. ROIs were labeled as crystal or intergranular based on the concentration of Mg, which is reflected in Figure 3.5a. There is no significant difference in the Mg concentration between the middle and outer enamel for either intergranular or crystal phases, which implies that the utilization of Mg remains relatively constant throughout crocodilian amelogenesis. However, there is statistically significant evidence ($p = 0.0435$) that the middle enamel contains a higher bulk concentration of Na (1.17 ± 0.07 at.%) than the outer enamel (0.94 ± 0.08 at.%, Figure 3.5b). It appears the crystal phase could be most responsible for this difference, though the t-test produces a p statistic of 0.0899 when comparing middle crystal to outer crystal, which is above the commonly used threshold for significance of 0.05. The H concentration was also higher in the middle enamel (Figure 3.5c), though in this case the strongest statistical difference came when comparing the intergranular phase ($p = 0.0337$). Carbon in enamel can come from both inorganic (CO_3 substitutions in the mineral phase) and organic (protein residues), and when considering the decomposed C signal (Figure 3.5d), no difference between the middle and outer enamel can be determined. For these samples, the CO molecular ion concentration was similar between middle and outer enamel (Figure 3.5e). However, when considering the signal from CO_2 molecular ions (Figure 3.5f), there are significant differences between both crystal ($p = 0.0063$) and intergranular ($p = 0.0219$) phases, which translates to a difference in the bulk composition as well ($p = 0.0626$).

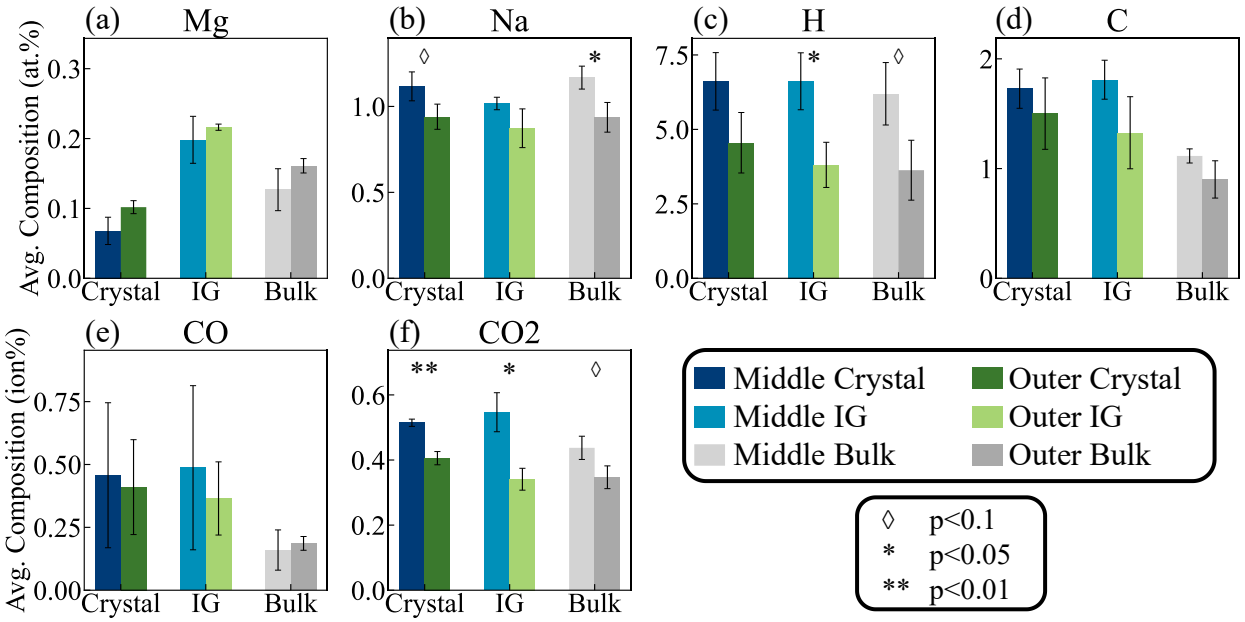

Figure 3.5. Composition of intergranular and crystalline regions of middle and outer C. porosus enamel. *(a) Mg, (b) Na, (c) H, and (d) C show the average composition after molecular ions are deconvoluted, whereas the concentration of the (e) CO and (f) CO_2 molecular ions are in ion%. Markings indicate the p statistic from a two-tailed t-test with unequal variances between middle and outer enamel.*

3.5. Discussion

Gradients in enamel composition, structure, and properties from the outer to the inner enamel are a well-documented phenomenon [99]. Results from Raman and nanoindentation showed that crocodilian enamel is unique; the gradient is constrained to only the outermost < 20% of the enamel thickness, with the rest of the tissue having more similar properties. As such, this discussion will focus primarily on the outer layer, how it is distinguished from the rest of the tissue and what advantages it might confer or degradation it might experience over time.

X-ray diffraction has been used to measure the size of the crystalline domains in *C. porosus* enamel and was reported to be 8 nm [48]. However, no spatial information was reported as those samples were powderized and not divided into inner, middle, or outer enamel. In contrast, X-ray diffraction of human enamel reports a domain size of 26-28 nm [143], emphasizing the small size of crocodilian nanocrystals. The use of powders for these past X-ray diffraction studies make it challenging to identify gradients in nanocrystal size throughout the enamel, though the SEM images presented here (Figure 3.1) make it clear that such gradients can exist. Techniques such as transmission electron microscopy or atomic force microscopy can be used in the future to enable quantitative measurements. Considering the morphology of the crystals observed by SEM and APT in this study, those near the outer enamel surface are much smaller than those in the inner and middle regions.

Raman spectroscopy has been used to describe the degree of crystallization in enamel by monitoring the full width at half maximum of the dominant P-O ν_1 symmetric stretch signal at ~960 cm^{-1}, and occasionally comparing to a reference crystal [9, 85, 144]. As can be seen in Figure 3.2b, the synthetic HA reference has a narrower peak width than any of the enamels, which is generally taken to indicate a higher degree of crystallinity. Using this metric to assess results from Raman spectroscopy, it would appear that the outer layer of crocodilian enamel has a higher degree of crystallinity (Figure 3.2b), but this conclusion is disputed by the apparent increased intergranular thickness observed in APT (Figure 3.4). However, PO_4 ν_1 peak width reflects factors beyond just the degree of crystallinity; an increase in the carbonate concentration also causes the $PO_4\nu_1$ peak to broaden [145]. Thus the narrower peak in outer enamel is caused by the decreased CO_3 concentration as measured by both the carbonate ratio from Raman spectroscopy (Figure 3.2c) and the concentration of CO_2 molecular ions from APT (Figure 3.5f).

The position of the $PO_4\nu_1$ peak reveals additional information about the composition. Increased carbonate content in HA causes the peak to shift to lower wavenumbers (redshift), while increasing fluoride concentration causes a shift to higher wavenumbers (blueshift) [145]. Thus, the blueshift of the $PO_4\nu_1$ peak position to higher wavenumbers near the OES for both human and crocodilian enamels (Figure 3.2a) could reflect increased fluoride concentration, decreased carbonate content, or both, as a function of distance from the DEJ. However, fluorine was not detected in crocodilian enamel by APT, as would be expected given that neither *A. miss.* or *C. porosus* were not exposed to fluoridated water or dental care products. Therefore, the blueshift of the $PO_4\nu_1$ peak position in the outer enamel of crocodilians is due to decreased carbonate content. Additionally, the $CO_3\nu_1$:$PO_4\nu_1$ peak area ratio also directly shows that the outer enamel has a lower carbonate content (Figure 3.2c).

The APT data agrees with the conclusion from Raman spectroscopy that the HA in the outer enamel contains less carbonate than that in the middle enamel. This is reflected in the concentration of CO_2 molecular ions (Figure 3.5f) where there is strong statistical evidence that the crystals in the middle enamel contain more CO_2^+ than in the outer region ($p = 0.0063$, two tailed t-test with unequal variances). The intergranular phase and the bulk compositions of the samples also show the same trend, though the significance of those observations is not as strong ($p = 0.0219$ and $p = 0.0626$, respectively). It has been suggested that CO molecular ions in enamel are associated with organics or inorganic sources, while CO_2 molecular ions primarily have inorganic origins [26]. There have also been controlled examples of protein adsorbed to synthetic, non-carbonated HA where both CO and CO_2 were highly constrained to the organic layer [46]. In this study, we find that the concentration of CO_2 molecular ions is associated with carbonate content, as the molecular ion concentration shows the trend as the carbonate content measured by Raman spectroscopy. The

decreased CO_2 concentration in outer enamel is strongest for the HA nanocrystals, supporting the association of that species with inorganic sources. However, this does not rule out the notion that CO_2 can be generated by organic species as well. The weaker difference in CO_2 concentration between middle and outer intergranular phases could be partially due to less carbonate, but also less organic content, as is suggested by the hydrogen concentration (Figure 3.5c).

Hydrogen in APT can be difficult to quantify on an absolute scale due to contamination from the atmosphere in the analysis chamber [146]. However, when characterizing organic materials, the H signal can become quite significant [147], well exceeding what could be expected as the background level and allowing it to be used to compare samples semi-quantitatively. The intergranular phase of the outer crocodilian enamel in this study has a significantly lower amount of H relative to the middle enamel ($p = 0.0337$). This suggests that the outer layer of the crocodilian enamel retains less organic residues from amelogenesis, despite having a somewhat higher volume fraction of amorphous intergranular phase (Figure 3.4).

Why is the outer layer of crocodilian enamel less carbonated? The demand for a harder and stiffer surface layer to resist wear during feeding is surely a factor. Carbonated synthetic HA has a reduced elastic modulus and bending strength, particularly in wet environments [148], and so there is a direct benefit to having a lower carbonate concentration in the surface layer. This is confirmed by the moderate increase in the hardness and reduced modulus in the outer layer measured via nanoindentation (Figure 3.3). Another major consideration is that the solubility of hydroxyapatite increases with increasing carbonate substitutions [149]. Thus, the reduced carbonate content near the OES serves to improve the solubility resistance. This is a critical feature for species that spend a considerable portion of their time with their teeth submerged in rivers, lakes, or other wetlands.

Unfortunately, there is scant literature regarding crocodilian amelogenesis that can be used to describe how carbonate levels are controlled during enamel development. In mammals, carbonate ions are introduced during the maturation stage by smooth-ended ameloblasts to balance the pH after the mineralization cycle of ruffle-ended ameloblasts [59, 83]. Ameloblasts are in the ruffle-ended form most of the time in rodents [150], but perhaps the smooth-ended configuration is more effusive or persists longer in crocodilians, if they do indeed undergo a similar process of amelogenesis as outlined in Figure 1.4.

The smooth gradient in composition and properties through the enamel thickness that are commonly seen in humans and other mammals [99] is not present in crocodilians. In mammalian enamel, the initial compositional gradient is likely a result of the final maturation stage of amelogenesis. The protease KLK4 is secreted by the ameloblasts on the outer enamel surface, inducing a gradient in the concentration of the protease and thus its efficacy to extract organic content from between mineral fibers [15]. Crocodilian teeth are replaced every ~3-6 months [52, 151]. Perhaps that is not enough time for ameloblasts to remain on the surface of the enamel and undergo complete maturation subsequent to secretion, and instead they simply cease to deposit enamel when the tooth erupts. The dramatic decrease in nanocrystal size in the outermost ~10 μm supports this notion: the nanocrystals are initially small near the ameloblast surface just after secretion then grow as Ca and PO_4 ions are incorporated at greater distances from the cell [81]. It would be expected that if enamel development were interrupted in this way that the organic content would be highest in the outer layer, as presumably the extraction of organic residues would be incomplete, but there is evidence to the opposite from the APT measurement of H concentration (Figure 3.5c). However, the *C. porosus* tooth used in this study had been naturally exfoliated, indicating that it had been erupted and in use for at least several months to a year. This provides

ample opportunity for environmentally induced changes to the morphology and composition that could explain the low organic content. This could be tested relatively easily in the future by determining whether the outer surface of unerupted or very recently erupted crocodilian enamel exhibits a hard outer layer.

Demineralization is an additional factor that could be responsible for the reduction in nanocrystal size near the OES. The comparison between young and senior human enamel (Figure 2.6) provides evidence that nanocrystals are replaced by the intergranular phase over decades of de- and re-mineralization. It is likely that organic contents are also removed from the amorphous intergranular phase during these cycles. In the case of crocodilians that have their teeth frequently exposed to an external aqueous environment, demineralization may be favored over remineralization, causing the nanocrystal morphology to be significantly impacted even in the relatively short time period during which the teeth are in use. There remains a question of how much remineralization is possible in a crocodilian mouth where the teeth are not immersed in saliva as they are in a human oral cavity. Additional data regarding the salivary characteristics of crocodilians and how much their teeth are exposed to saliva would be necessary before the potency of de-/re-mineralization cycles could be fully understood.

Besides CO_2 molecular ions and H, the only other ion to show a significant difference between middle and outer enamel from the APT data was Na (Figure 3.5b). The bulk composition of Na was lower in the outer enamel ($p = 0.0435$), but the difference between the crystal phase was less significant ($p = 0.0899$). One function of Na in enamel is to remedy the charge imbalance of carbonate substitutions in HA (i.e., Na^+ and CO_3^{2-} in place of Ca^{2+} and PO_4^{3-}) [152]. The correlation of Na with carbonate is supported by the CO_2 molecular ion concentration (Figure 3.5f) and Raman

data (Figure 3.2c). Na is likely incorporated into enamel during amelogenesis: it is a prevalent ion in physiological fluids, and certain transport mechanisms involved in ameloblast activity (in murine enamel) depend on Na [153].

It is worth noting that the *A. mississippiensis* teeth used in this study were extracted from a wild-caught cadaver, whereas the *C. porosus* teeth were shed naturally during tooth replacement by individuals in captivity. Yet the composition and properties between the two species were remarkably similar, which implies that the gradient in carbonate content near the OES is a "designed" feature, and not a product of the environment that the individual was in during the generation of the tooth in question. Even if extrinsic demineralization is responsible for the change in nanocrystal morphology and reduction in carbonate content, these are desirable changes that improve the mechanical properties and decrease the solubility of the outer layer. Perhaps anticipating environmental contributions is a critical part of the "design" of natural selection.

The connection between the CO_2 molecular ion and inorganic carbonate in APT data has been proposed before, based on the distinct spatial location of CO_2 and CO ions in the 3D reconstruction [26]. However, this report is the first to the author's knowledge that uses multiple samples from different locations in the same tooth alongside Raman spectroscopy to corroborate that claim. The application of APT to biominerals is still quite recent [17, 45], and using correlative tools at multiple hierarchical scales is essential to better understand the mass-to-charge spectra and improve reconstruction accuracy. However, it is also imperative to comprehensively understand how parameter selection during an atom probe experiment can impact the measured compositional accuracy.

The results presented in this chapter and Chapter 2 were collected on the same LEAP instrument using comparable experimental parameters in an effort to minimize instrument-induced variations. Specifically, this was achieved by using a constant laser pulse energy throughout the run, which is standard practice in the field, but does not necessarily guarantee that the field evaporation conditions experienced by the sample are consistent. Nevertheless, the technique proved sufficiently sensitive to identify significant differences between sample groups. This raises the question: can the experimental parameter selection be optimized further to enhance both overall accuracy and sensitivity to subtle composition measurements? Additionally, a new generation of commercial APT systems is now available (LEAP 6000 XR and Invizo 6000, Cameca), boasting improved detection efficiency and a shift to a shorter wavelength laser for the laser pulse used to induce field evaporation. The next chapter uses synthetic hydroxyapatite as a reference material to both identify optimal parameters for future data acquisition, as well as to understand the impact on measured results caused by the shift to a shorter wavelength laser.

3.6. Conclusion

The existence of sharp gradients in composition, structure, and properties of crocodilian enamel between the outermost layer and the inner and middle enamel were reported in this chapter and discussed. The direction of the trend (i.e., the outer layer being harder and having less carbonate substitutions relative to the inner enamel) is the same as the gradual gradients present in human and other mammalian enamels, but constrained to the outermost <20% of enamel thickness, rather than throughout the full thickness.

Atom probe tomography experiments were carried out to investigate the composition and structural features of the outer and middle enamel at the nanocrystal scale. Notably, the nanocrystals lacked the Mg-rich cores which have been reported in human enamel. Additionally, the nanocrystals of the outer enamel appeared significantly smaller and separated by a greater thickness of the Mg-rich amorphous intergranular phase than those from the middle enamel. Segmentation of the reconstructions into nanocrystal and intergranular phases enabled a statistical comparison, revealing reduced Na, organics (i.e., H signal), and carbonate (i.e., CO_2 molecular ions) concentrations in the outer enamel. The trend in carbonate is particularly interesting as it is corroborated by the results from Raman spectroscopy, improving confidence in the conclusions drawn.

At present, there are relatively few published reports in the literature surrounding crocodilian amelogenesis and compositional changes that accumulate over time due to environmental exposure. Consequently, it is not possible to determine from this study alone whether the outermost hard layer of crocodilian enamel is a "feature" imparted by amelogenesis to improve tooth function or a consequence of the formation, eruption, and exposure lifecycle of the tissue. However, we envision that these results will serve as a foundation for future investigations into the evolution and development of nanostructural complexity across the tree of life.

4. Stoichiometric Measurement of Hydroxyapatite by Atom Probe Tomography: Effects of UV and Deep UV Laser-assisted Analytical Conditions

4.1. Synopsis

Application of atom probe tomography to electrically non-conductive materials is typically enabled by pulsing a laser onto a sample under strong electric fields to induce field evaporation. The measured composition depends on the laser-material interaction, necessitating systematic optimization experiments. This is particularly important for hydroxyapatite ($Ca_{10}(PO_4)_6(OH)_2$), a biologically and geologically relevant mineral for which subtle compositional changes can have significant implications. Therefore, we perform a series of experiments on synthetic hydroxyapatite to systematically assess how the laser pulse energy, definition of ranges in the mass-to-charge state spectrum, and calcium charge state ratio impact the measured calcium to phosphorous ratio and mechanism of field evaporation on separate atom probe systems equipped with ultraviolet (355 nm wavelength) and deep ultraviolet (257.5 nm) lasers. We also evaluate the stoichiometric accuracy of the simultaneous voltage pulsing mode on the deep ultraviolet system, which both reduces the background of and introduces artifacts into the mass-to-charge state spectrum. Correlations between the calcium-to-phosphorus ratio and the charge state ratio and fraction of ions ranged are identified. In turn, these analyses provide guidance for improving measurement accuracy of hydroxyapatite and other insulating materials using atom probe tomography.

4.2. Introduction

Atom probe tomography (APT) is a burgeoning analytical microscopy technique that provides three-dimensional (3D) elemental and isotopic mapping within materials at the nanometer scale. Widespread use across a broad range of materials, particularly electrically non-conductive ones, has been enabled through recent developments of laser-assisted field evaporation technologies [154-158]. For instance, decreasing laser wavelengths in commercially produced local electrode atom probes (LEAP, manufactured by Cameca) over time have anecdotally led to improved data quality, sample yield, and enabled analyses of more challenging non-conductive samples [29]. Over the years, the wavelength of the laser pulses has decreased from near infrared 788 nm [154], to green 532 nm (LEAP 3000) [159], to ultraviolet (UV) 355 nm (LEAP 4000 & 5000) [160], and now to deep ultraviolet (DUV) 257.5 nm (LEAP 6000 and Invizo 6000) [161]. While advances in the focusing optics have led to improved performances in each generation of laser systems, fundamental changes in sample-laser interactions, such as photoionization phenomena as observed in an extreme UV 28 – 50 nm laser system [162, 163], must also be considered and thus require further study.

Additional advancements to the control software and hardware have been made, unlocking new experimental parameters. One such feature is the ability to dynamically vary laser pulse energy (LPE) to maintain a target charge state ratio (CSR), i.e., the ratio of a given ionic species at charge state A to the same ion at charge state B, throughout an experiment. As the CSR reflects the field strength at the specimen surface [164, 165], control of this parameter provides higher consistency in the evaporation field throughout the APT acquisition by normalizing the electric field. Lastly, the most recent development of simultaneous voltage pulsing (SVP) in laser mode

has been shown to improve mass resolving power in metallic and semiconductor systems [166, 167]. The utility of these new capabilities to compositional analyses across a broad range of materials, such as minerals, is yet to be explored.

Advances in APT instrumentation have, however, significantly outpaced the measurement science, hindering the realization of the technique's full potential. New field evaporation physics unique to each laser wavelength will naturally cause deviations across a number of variables, including the field ionization potential among elements and compounds, thermal dissipation, single or multiple ion emission by elements and compounds (on a per pulse basis), specimen shape evolution, and detection- and analysis-related artifacts [168]. Careful study over the past decade has built a stronger understanding of how these variables result in compositional deviations, particularly for oxides with the widely-used UV laser systems [19, 169-171]. By comparison, there are relatively few studies that evaluate the accuracy with the DUV laser, though significant strides are being made [29, 172]. Given that multiple generations of atom probe systems with differing laser wavelengths are currently in use, a thorough and systematic investigation of the effects of these variables on compositional analyses is of broad significance to the APT community.

At the user level, accurate chemical quantification dependent on mass spectral analyses is a long-standing challenge, and there is a drive to develop tools that can improve and automate the analysis [173, 174]. APT is based on time-of-flight (ToF) mass spectrometry, and ionic species are identifiable as peaks at distinct values in the mass-to-charge state (m/z) spectrum [18, 175]. The peak shape for each ionic species and the mass resolving power are described by the leading edge and trailing tail of the peak, which are governed by the detector system response, evaporation physics, material properties, and, for laser-assisted APT, dissipation of thermal energy [176-179].

Ultimately, each ionic peak within the mass spectrum is ranged, analyzing select areas under each peak, to quantify the material's elemental and/or isotopic composition. However, there is not a single model peak shape that can be universally applied to all peaks within a single spectrum or between data sets of a given material, as the peak shape for each ion species in a single spectrum can vary significantly. This has led to various and oftentimes arbitrary ranging approaches, e.g., from ranging the full peak width, to specifying ranges for each peak based on a certain full-width at some fraction of the maximum value [174], or to use machine-learning to adapt and fit specific peak forms [168]. Additionally, compositional accuracy may be improved by ranging the tails after major peaks as well as the peak itself, as has been demonstrated for ß-tricalcium phosphates using UV laser pulsed APT [24].

In this study, we systematically assess the effect of various laser-pulsing conditions on stoichiometric measurements for the mineral hydroxyapatite ($Ca_{10}(PO_4)_6(OH)_2$; HA). HA serves as a model system, as previous studies have demonstrated its potential for accurate stoichiometric analyses during laser-induced evaporation [16, 17, 26, 32] compared to oxide materials, for instance [19, 169, 180-183]. This mineral is also of broad significance, from biological to industrial applications [35, 45, 46, 184, 185]. However, a reliable protocol for achieving stoichiometrically accurate measurements has yet to be established, and understanding of the impact of DUV laser [186, 187] and new experimental techniques (i.e., controlling LPE via CSR, or SVP mode) is a presently limited but growing area of research.

Specifically, we compare the effects of laser wavelength and LPE on the m/z spectra quality and measured composition on synthesized pure HA samples, providing some insight into the mechanisms of field evaporation on the UV and DUV laser systems. Secondly, we assess HA

stoichiometry relative to the $^{40}Ca^{2+}$:$^{40}Ca^{+}$ CSR using the DUV system. Lastly, we explore the effect of SVP with varying voltage pulse amplitudes on the m/z spectra of HA, an insulator. To facilitate these comparisons of stoichiometry across multiple parameter variations, we also developed a simple mass-ranging protocol called the "elbow" ranging approach that could be automatically applied to all peaks without analyst bias, which revealed clear compositional trends. Ultimately, this study presents fundamental insight into analytical protocols and conditions influencing stoichiometric analyses of minerals. These approaches and results can be broadly extended to probe a wide range of materials, improving compositional analyses at the nanoscale.

4.3. Materials and Methods

Micrometer-sized hydroxyapatite single crystals (e.g.,~20 μm long × 5 μm wide) were prepared using a potassium sulfate molten salt synthesis technique, described in detail in [188]. Samples were coated with approximately 5 nm of Pt (ion beam sputter/etch system, South Bay Technology, Inc.) to improve conductivity, and analyzed by energy dispersive spectroscopy (EDS; X-Max^{N} 80 detector, Oxford Instruments) in a focused ion beam scanning electron microscope (FIB-SEM; Helios NanoLab 600i, Thermo Fisher Scientific) to determine the Ca:P ratio of the crystals (at 10 kV, 1.4 nA electron beam). Spectra were collected from two independent microcrystals (three points each) and the results were exported as atomic fractions, reported in Supplementary Table 1 in Appendix 0. The Ca:P ratio for the HA sample here was measured to be 1.54 (± 0.20) by EDS; the ratio deviates from the nominal stoichiometric value of 1.67 due to K substitutions during synthesis.

APT specimens were prepared from the HA sample using conventional FIB techniques (Helios NanoLab 600i or Helios Hydra plasma FIB-SEM, Thermo Fisher Scientific) (Supplementary Figure 5) [18, 114]. Additional details can be found in Appendix 0.

APT analyses were conducted using a LEAP 4000 X-HR equipped with a UV laser (wavelength of 355 nm) and a LEAP 6000 X-HR equipped with a DUV laser (257.5 nm) (hereafter referred to as UV and DUV systems, respectively). For all analyses, the base temperature was held at 40 K and the target detection rate (DR) was set to 0.005 ions per pulse. On the UV system, LPE was varied from 20 – 200 pJ with a pulse frequency of 125 kHz, collecting ~ 5×10^5 ions at each LPE setting. On the DUV system, the LPE was varied from 15 – 150 pJ with a pulse frequency of 100 kHz, collecting ~1×10^6 ions per setting.

To evaluate the active mechanisms of field evaporation on the UV and DUV systems, comparisons of the DR versus LPE for both instruments were performed on HA and pre-sharpened silicon microtips following a similar protocol to that described in [28]. This involved incrementally increasing the LPE while holding the standing voltage constant. Data was collected for approximately 2 minutes at each LPE setting. This process was immediately repeated at a higher standing voltage for both samples on both instruments. A constant pulse rate of 100 kHz (for HA) or 200 kHz (for silicon), and a stage temperature of 40 K were used.

The LEAP 6000 control software (Acquisition Control Center, version 6.3.2, Cameca) allows the user to control the LPE to maintain a target peak ratio. Experiments were performed targeting a $^{40}Ca^{2+}$:$^{40}Ca^{+}$ CSR of 30, 100, 200, or 300 using the ranges [19.913, 20.065] Da for $^{40}Ca^{2+}$ and [39.914, 40.077] Da for $^{40}Ca^{+}$.

SVP experiments were conducted using the LEAP 6000, with a base temperature of 40 K, target DR of 0.005 ions per pulse, pulse frequency of 100 kHz, and target $^{40}Ca^{2+}$:$^{40}Ca^{+}$ CSR of 200, with the voltage pulse fraction of 0.02, 0.10, or 0.20. Additional details regarding the SVP experiment parameters are included in Appendix 0.

Atom Probe Suite (APS, version 6.3.3.7, Cameca) was used for APT data analysis, evaluating only ions which were collected after the final stage motion during sample alignment (typically discarding $< 1 \times 10^4$ ions). Details of peaks used for the peak fitting step of the reconstruction wizard are included in the SI.

Peaks in the m/z spectra with a maximum signal approximately greater than double the surrounding background were identified and assigned a chemical identity. While this approach was suitable for the datasets and purposes of this study, this criteria may vary in other circumstances; for instance, the compositional accuracy of smaller datasets or those with higher noise may benefit from selecting peaks with higher signals. For the "elbow"-ranging method, a Python script was used to systematically adjust the bounds of each range for each dataset to the inflection point ("elbow") on either side of the peak (described further in the Results section). As an illustrative counterpoint, ranges that include the thermal tail ("tail ranges") were made by extending the upper bound of the range for $^{40}Ca^{2+}$, O_2^{+}, and all P_xO_y peaks to an m/z value after the peak with counts comparable to the background before the initial peak, deleting any overlapping ranges which belonged to $^{41–44}Ca^{2+}$ or hydrogen-containing peaks (e.g., $O_2H_{1\text{-}3}^{+}$ or $PO_2H_{1\text{-}3}^{+}$) originating from the mineral itself or resulting from specimen preparation and/or ionization of ambient H in the analysis chamber [146]. Copies of typical .rrng files, the Python script used for adjusting ranges, and the raw APT data are uploaded to the Zenodo repository at doi.org/10.5281/zenodo.15319905.

Except when describing a specific ion (e.g., $^{40}Ca^{2+}$) or ratio of ions, all compositions are reported after background subtraction and decomposition of molecular ions.

4.4. Results

4.4.1. Effect of laser wavelength and LPE

We first studied the fundamental impact of laser wavelength (i.e., UV vs. DUV) and LPE on apparent elemental concentrations within HA. Figure 4.1 shows the m/z spectra for HA collected at different conditions (i.e., UV-60 pJ vs. DUV-15 pJ and DUV-60 pJ). Ionic species were assigned to each peak based on previous studies [22, 24, 46]. Major ionic species include Ca^{2+} at 20 – 24 Da as well as O_2^+ and PO_x^+ ionic species. A complete spectrum with elbow ranges overlaid is provided in Supplementary Figure 6.

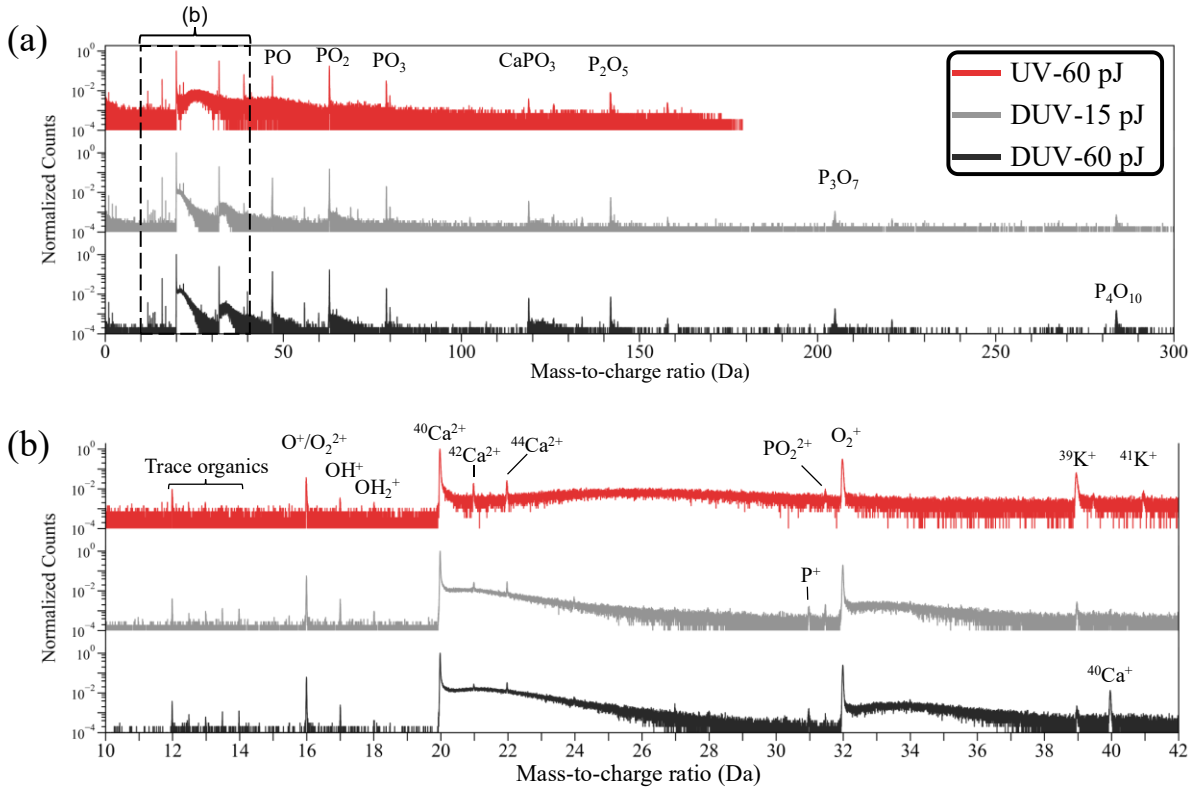

Figure 4.1. Example mass-to-charge state ratio (m/z) spectra for HA. *(a) Full spectra from 0 – 300 Da. (b) Magnified view of 10 – 41 Da highlights the differences in background and thermal tails. Bin width is set to 0.001 Da for both (a) and (b).*

Qualitatively, considerable differences in thermal tails and background levels for distinct peaks are observed at the different conditions, which ultimately impact accurate quantification of elemental concentrations. Two features of particular interest are the baseline background and the tails, exemplified as the regions before and after the $^{40}Ca^{2+}$ peak, respectively (Figure 4.1b). Tails can also be seen after other prominent peaks, e.g., O_2^+, PO^+, etc. The lowest baseline background is observed with relatively high LPE on the DUV system (e.g., DUV-60 pJ). Meanwhile, lower LPE (DUV-15 pJ) or larger wavelength (UV-60 pJ) results in moderately higher baseline backgrounds. In contrast, the thermal tails of the DUV-60 pJ and DUV-15 pJ spectra contain more

counts, obscuring the $^{42}Ca^{2+}$ and $^{44}Ca^{2+}$ peaks more than the UV-60 pJ condition. A lower baseline background and greater tail together suggest that a LPE of 60 pJ on the DUV system transfers a greater amount of energy to the HA specimen than an equivalent LPE on the UV system.

4.4.2. Evidence of photoionization by DUV laser pulse

The shift in laser wavelength from UV to DUV may also activate different mechanisms of field evaporation. The general interpretation of laser-assisted APT is that the laser briefly increases the temperature of the specimen, reducing the threshold field required to evaporate ions [176], though photoionization has been observed in semiconductors [189] and, more recently on a DUV system, chromia [28]. Here, we perform a similar experiment to that described in [28] by measuring the DR as we incrementally increased the LPE while holding the voltage constant for Si and HA on both the UV (Figure 4.2a) and DUV (Figure 4.2b) systems.

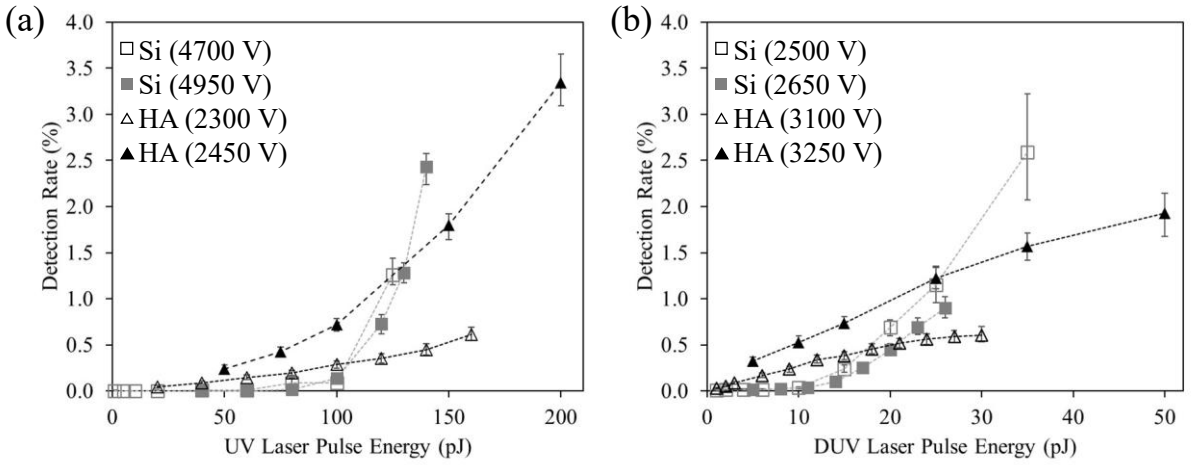

Figure 4.2. DR versus LPE at constant DC voltages for silicon and hydroxyapatite specimens measured with the (a) UV and (b) DUV laser systems. *Each point denotes the median measured DR within the 2-minute data collection interval, while the error bars denote the interquartile range.*

On both laser systems, Si showed an exponential increase in DR with increasing LPE. For the UV system, the trend between DR and LPE can be fit to an Arrhenius equation of the form DR = LPE^2 * *exp(A*/LPE*)* where *A* is a constant. This equation is a simplification and adaptation of the Fowler-Nordheim type equation, which links temperature (e.g., LPE) to the current of the electron tunneling in an electrostatic field; the interested reader is directed to [28] for a more rigorous discussion. The interpretation here is that the exponential increase in DR with increasing LPE is indicative of primarily thermally activated field evaporation. Thus, we believe that thermal activation is the dominant mechanism for Si on both UV and DUV systems.

HA on the UV system also exhibits a somewhat exponential increase in DR with increasing LPE but does not fit the Arrhenius equation mentioned above, apparently due to convolution with a more linear trend. The linear trend is more pronounced in the data collected at a lower field (hollow points in Figure 4.2a) when the DR is lower. The linear portion may indicate that some evaporation is occurring by photoionization: greater photon flux (higher LPE) directly corresponds to greater rates of evaporation. Combined, the trends of HA on the UV system are similar to the behavior observed in chromia on a DUV system, a combination of photoionization at low LPE and photofield tunneling (including both thermal and photonic contributions) at higher LPE [28].

In contrast, the trend between DR and LPE for HA on the DUV system (Figure 4.2b) is decidedly linear at both low and high LPE, suggesting that photoionization is the dominant mechanism of field evaporation. During typical APT acquisitions, the target detection rate is maintained by increasing the voltage to compensate for the increasing tip-electrode distance and the evolving tip radius. However, as the voltage was fixed for each experiment here, a slight reduction in the field experienced by the specimen can be expected as the specimen evaporates,

causing the measured DR at higher LPE to be slightly less than it otherwise would be. This seems to be the most likely explanation for why the measurements taken at higher LPE have a slightly lower DR than expected from the linear trend established at lower LPE. Comparison with the data collected on the UV system provides strong evidence that the application of a DUV laser causes photoionization in HA. It is worth noting that the DUV laser still results in tails in the m/z spectrum (Figure 4.1). However, for strong dielectric materials, it is possible for photoionization to be followed by delayed, thermally activated desorption [162], providing a mechanism for tail development that does not imply a substantial temperature increase and is compatible with the other evidence of photoionization shown in Figure 4.2b.

4.4.3. Elbow-ranging approach of m/z spectra

As mentioned above, the ranging approach is imperative for elemental and isotopic quantification, and is a chief source of variance between analysts. Generally, each ionic peak is ranged to maximize inclusion of peak area while minimizing contributions from background and/or tails. One ambiguity during this process across analysts is to what extent tails should be included. That is, if the entirety of the tail signal is thought to be due to late evaporation events of the leading peak, then an apparent solution to improve accurate compositional measurement is to define ranges that capture the entire tail, as explored in depth by [24]. An illustrative example of such "tail-inclusive" ranging is presented in Figure 4.3a. However, this may inadvertently misidentify or obscure the background, minor elements, or isotopes in the tail.

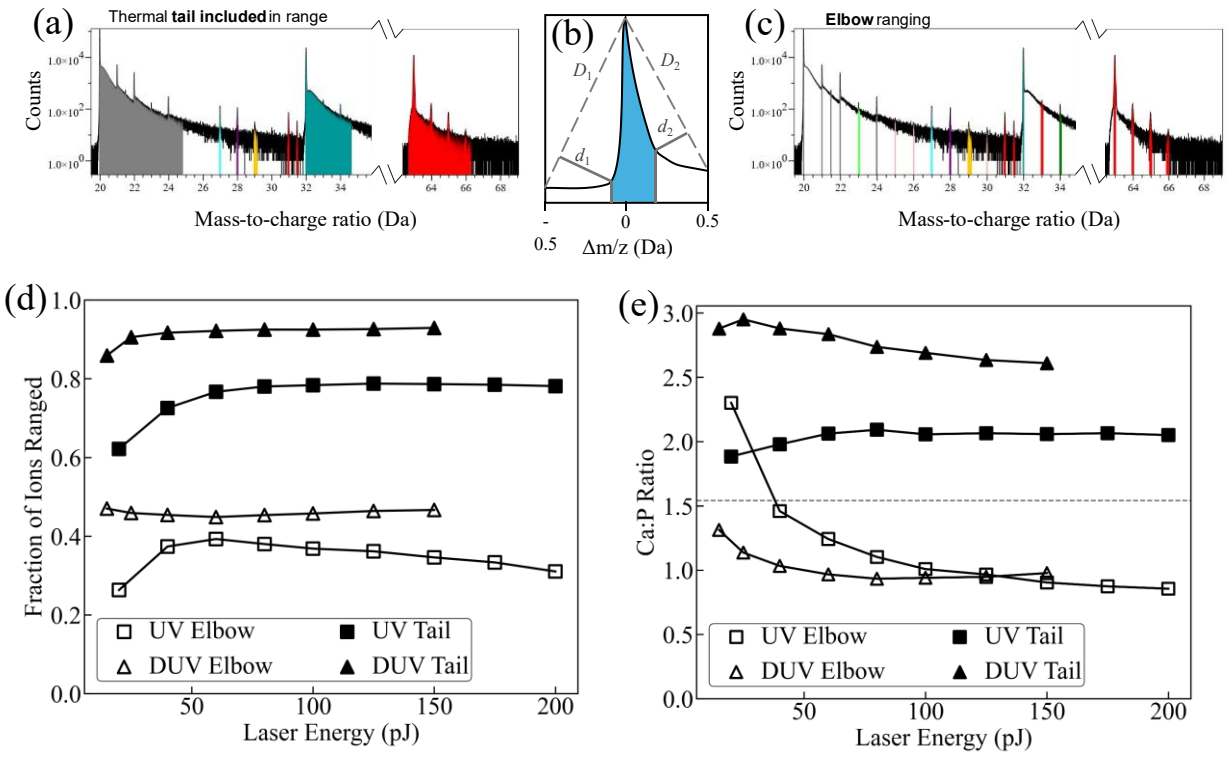

Figure 4.3. Effect of tail- vs. elbow-ranging approaches on compositional analyses. *a) Examples of ranges that include thermal tails on a m/z spectrum of HA. b) Schematic illustration of "elbow" definition. Lines D_1 and D_2 are drawn from the peak to the spectrum value 0.5 Da away, and a perpendicular line d_1 or d_2 is connected to the spectra. The start and stop of the range are set to be the x-coordinates for which d_1 and d_2 are maximized, respectively. c) Examples of elbow-ranging on the same spectrum presented in (a). d) Fraction of ions included in ranges and e) measured Ca:P ratio using the tail- and elbow ranging approaches as a function of LPE on the UV and DUV systems. Error bars from counting statistics are smaller than the plotted points for (d-e).*

To contrast, we developed a ranging approach defined by the peak "elbows," illustrated in Figure 4.3b, reducing inclusion of the thermal tails, as well as presenting a consistent and automated procedure for ranging different peak forms (provided as part of the supplementary dataset on Zenodo). Lines D_1 and D_2 are first defined by connecting the peak maximum to the

spectrum some distance away, for instance 0.5 Da or half the distance to the nearest peak, whichever is less, as shown on Figure 4.3b. The elbow point on each side of the peak is then defined as the point on the spectrum that maximizes the perpendicular distance *d* to line *D*. Figure 4.3c shows ranges systematically defined to start and stop at the elbows of various peaks and peak forms. In general, it can be seen that ranging peaks to the elbow points leads to relatively narrower ranges that capture the most intense portions of each peak while being responsive to the different forms of the leading and tailing ends.

In Figure 4.3d and Figure 4.3e, we show how the inclusion or exclusion of thermal tails during peak ranging can affect compositional measurements by comparing the tail- vs. elbow-ranging approaches. To do so, we conducted conventional LPE series experiments on both the UV and DUV systems, which involved assessing compositional measurements against LPE [22, 190]. We then applied both the tail- and elbow-ranges to the spectra from each LPE setting to compare the fraction of ions included in the ranges and the measured Ca:P ratio.

By comparing the total fraction of ions included by each ranging approach, we can estimate the magnitude of the thermal tails. Figure 4.3d presents the fraction of ions ranged as a function of LPE for both UV and DUV systems. For both instruments and both ranging approaches, the ranged fraction initially increases with increasing LPE as the baseline background is reduced. On the UV system, 60 pJ is a notable point, as this yields the maximum ranged fraction of 0.39 by the elbow-ranging approach. Above an LPE of 60 pJ, the thermal tails become more dominant, causing a decrease in signal captured by elbow-ranging, but only a slight change in the fraction captured by tail-ranging (0.77 at 60 pJ to 0.79 at 200 pJ).

Conversely, there is virtually no decrease in ranged fraction when using elbow ranging on the DUV system. The ranged fraction only varies from 0.45 – 0.47 between LPEs of 15 to 150 pJ. Similarly, there is negligible change when including tails: above 25 pJ the ranged fraction only varies between 0.91 – 0.93. The lack of change with either ranging approach provides quantitative evidence that the proportion of signal that is attributed to thermal tails is constant regardless of the LPE for HA on the DUV system.

We assessed the accuracy of each ranging approach in reproducing the Ca:P ratio for our synthetic HA sample, measured to be 1.54 (± 0.20) by EDS (Supplementary Table 1). Here the impact of tails on the measured stoichiometry becomes apparent (Figure 4.3e, Supplementary Figure 7). For both the UV and DUV systems, ranging the tails overestimates the Ca:P ratio, driven by the increased counts in the tail after the $^{40}Ca^{2+}$ peak. On the UV system specifically, the Ca:P ratio increases from 1.88 (± 0.01) at 20 pJ to a plateau around 2.05 – 2.09 (0.01) from 60 – 200 pJ. The plateau in the Ca:P ratio at moderate to high LPE mirrors that of the fraction of ions ranged (Figure 4.3d). Exclusion of the tails (elbow ranges) conversely causes the measured Ca signal to decrease with increasing LPE (Supplementary Figure 7), reducing the Ca:P ratio from 2.30 (0.02) at 20 pJ to 0.86 (0.01) at 200 pJ. Of the measured UV LPE settings, the closest measured Ca:P ratio to the expected was 1.46 (0.01) with the 40 pJ LPE.

On the DUV system, while inclusion of the tails still leads to an overestimated Ca:P ratio, there is less variation as a function of LPE, decreasing from a maximum of 3.00 (0.01) at 25 pJ to 2.68 (0.01) at 150 pJ. Using the elbow ranges causes a similar trend, decreasing from 1.31 (0.01) at 15 pJ to a minimum of 0.93 (0.01) at 80 pJ before increasing slightly to 0.98 (0.01) at 150 pJ. The trend implies that an LPE less than 15 pJ would be required to achieve the expected Ca:P

value. As the amount of signal in the tail is consistent between LPE settings (Figure 4.3d), the change in measured Ca:P ratio is due to variations in which peaks are visible and their relative intensity, implying changes in the electric field during evaporation.

4.4.4. Charge state ratio (CSR) as a control parameter

As described above, conventional protocols for optimizing elemental analyses have involved conducting LPE series experiments [22, 190], where composition is measured and optimized against incremental changes of the LPE. This can result in variations in peak forms or intensities in the m/z spectra over time, as the field changes due to increasing specimen-electrode distance and apex shape evolutions. Further complicating matters, the delivered LPE can vary from instrument to instrument with the same wavelength or from one point in time to another on the same instrument due to slight differences in hardware, assembly, or wear/uptime of components. (One way to address this is using the "tool matching" protocol, which can be performed automatically in AP Suite [191], where a pre-sharpened silicon microtip with a known composition and geometry is used to calibrate the input LPE to match a reference value based on the $^{28}Si^{2+}$:$^{28}Si^{+}$ CSR.) However, these challenges combined suggest that reporting the LPE used for an experiment alone may be of limited value for replicating compositional measurements of a sample between specimens, instruments, or researchers. CSR provides a more realistic estimate of the electric field experienced at the tip [164, 165]. Furthermore, a correlation between CSR and measured composition has been found for several oxides [19, 20, 172], indicating that this is a more reliable parameter that can be tuned to achieve the nominal stoichiometry.

The control software of the 5000 and 6000 generations of LEAP allows the user to dynamically adjust the LPE throughout an acquisition by setting a target peak ratio. Here, we use this approach to evaluate compositional accuracy of HA on the DUV system across multiple individual specimens with target $^{40}Ca^{2+}$:$^{40}Ca^{+}$ CSRs of 30, 100, 200, or 300 using consistent ranges of [19.913, 20.065] for $^{40}Ca^{2+}$ and [39.914, 40.077] for $^{40}Ca^{+}$ (i.e. not adapted per dataset). It is worth noting that these ranges do not include significant portions of the tail behind the $^{40}Ca^{2+}$ peak and the $^{40}Ca^{+}$ peak has no significant tail, and so a disproportionate amount of $^{40}Ca^{2+}$ counts may be discarded. One could alternatively use a different ionic species with multiple charge states that have smaller tails, such as PO_3^{2+}:PO_3^{+} as in [24], but this is not explored in this study. Examples of the variation in CSR and LPE as a function of ion sequence number are provided in Supplementary Figure 8, and Figure 4.4a plots the LPE as a function of DC voltage. For each specimen, the LPE is highest at the start of the experiment, when the specimen is sharpest and the voltage required for field evaporation is lowest. As the specimen blunts and the voltage increases, the LPE decreases to maintain the target CSR, with the magnitude of LPE change being inversely correlated to the CSR (e.g., higher CSR requires less change in LPE). Notably, two specimens (target CSR = 30 and 300) were interrupted and resumed on a later date, the break is denoted by the green circles in Figure 4.4a. In both cases, the LPE versus voltage curve continued the trajectory established from the first experiment. Lastly, we note that lower target CSRs (e.g., increased $^{40}Ca^{+}$ signal) required higher LPEs.

The consistency in compositional measurements for three CSR conditions (30, 100, and 300) is presented as Ca:P ratio as a function of ion sequence number in Figure 4.4b and Table 4.1. Each dataset consisted of 10×10^6 ions, which were subdivided into blocks of 2×10^6 ions. It was expected that the implementation of the CSR as a control parameter would minimize variation in the

measured Ca:P ratio, which is partially true. Each of the CSR controls selected resulted in a range of Ca:P ratios, with the value at the start of the experiment (e.g., 0 – 2×10^6 ions) being the most dissimilar from the rest of the experiment. The fact that the initial segment has the most dissimilar composition for each CSR setting suggests that compositional accuracy can be improved by discarding some of the initial data, a common practice in APT analysis to avoid artifacts such as FIB-induced ion implantation or surface oxidation [18]. However, doing so may also discard features of interest near the surface, particularly for small or fragile samples that may not collect large numbers of ions. Here, we note that the range of Ca:P ratio is decreased with decreasing CSR, with a range of 0.44 for the 300 CSR condition, 0.12 for the 100 CSR, and 0.09 for the 30 CSR. These variations are presumably caused by the different magnitudes of the electric field at each CSR, and the ability of the LPE to adjust rapidly to better maintain the target CSR. That is, there is less variation in CSR when targeting a lower CSR rather than a higher one. Numerically, the mean absolute percent error between the measured CSR and target CSR ranges from 8% for 30 CSR to 18% for 300 CSR (Supplementary Figure 8). It is reasonable then that tighter control of the CSR during the experiment leads to tighter control of the electric field, which in turn results in less variability in the measured Ca:P ratio.

Table 4.1. Measured $^{40}Ca^{2+}$:$^{40}Ca^{+}$ CSR and Ca:P ratio from segments of experiments using various target CSR as controls

Ion Sequence No. (×10^6 ion)	0 – 2	2 – 4	4 – 6	6 – 8	8 – 10	0 – 10
Target CSR	30	30	30	30	30	30
Measured CSR (s.d.)	26.9 (0.2)	27.0 (0.2)	26.6 (0.2)	26.1 (0.2)	26.3 (0.2)	26.6 (0.1)
Ca:P Ratio (s.d.)	1.603 (0.004)	1.522 (0.003)	1.516 (0.003)	1.525 (0.003)	1.537 (0.004)	1.540 (0.002)
Target CSR	100	100	100	100	100	100
Measured CSR (s.d.)	99 (2)	99 (2)	94 (1)	100 (1)	99 (1)	98.3 (0.7)
Ca:P Ratio (s.d.)	1.473 (0.004)	1.529 (0.004)	1.541 (0.004)	1.576 (0.004)	1.595 (0.004)	1.546 (0.002)
Target CSR	300	300	300	300	300	300
Measured CSR (s.d.)	370 (9)	430 (12)	480 (14)	480 (14)	500 (15)	446 (6)
Ca:P Ratio (s.d.)	2.339 (0.005)	2.072 (0.005)	1.979 (0.004)	1.93 (0.004)	1.904 (0.004)	2.04 (0.002)

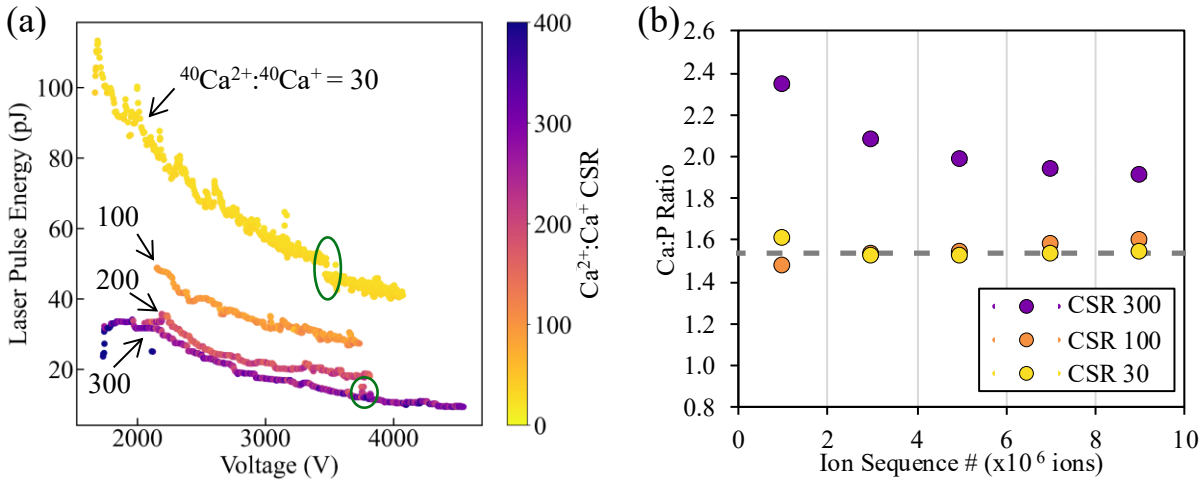

Figure 4.4. Laser pulse energy versus standing DC voltage curves at target CSR. *a) The color scale reports the measured $^{40}Ca^{2+}$:$^{40}Ca^{+}$ ratio sampled during the experiment. Green circles indicate points where an experiment was stopped and started again on a later date with the same sample and same conditions. b) Experiments were divided into segments*

of 2×10^6 ions to calculate the decomposed Ca:P ratio. Error bars of the Ca:P ratio from counting statistics are smaller than the points.

Considering the whole 10×10^6 ion dataset, a consistent trend of increasing Ca:P ratio with increasing CSR is revealed (Table 4.1). This data suggests that an intermediate CSR between 30 – 100 could achieve the expected Ca:P ratio of 1.54, although it should be cautioned that some variation in the Ca:P ratio between the start and end of the acquisition could be expected (Figure 4.4b). Furthermore, when thinking of how to extend these observations to materials which may or may not have a uniform, stoichiometric compositions, we speculate that being able to maintain consistency in experimental conditions would be essential; for instance, in biominerals with nano-scale compositional gradients [11, 35], a lower CSR could help minimize parameter-driven compositional variance—as opposed to actual gradients—throughout the duration of the APT data acquisition.

4.4.5. Effect of pulse fraction in simultaneous voltage pulsing

SVP, also known as voltage-plus-laser mode [192], is a recently developed capability [166] that was commercially introduced on the LEAP 6000 system [161]. It is meant to reduce the background level in the m/z spectrum caused by stochastic field evaporation events by applying an approximately 11 ns voltage pulse to the local electrode as the femtosecond laser pulse hits the specimen apex [193]. Because the field experienced by the APT specimen is a function of the potential difference between the specimen and the local electrode, the standing field is lower between pulses, reducing the likelihood of random "white noise" background detection events. The operator can adjust the timing and magnitude of the voltage pulse, determined as a fraction of

the standing voltage (called "pulse fraction", PF). The schematic in Figure 4.5a represents the cumulative effects of standing voltage, voltage pulsing, and laser pulsing that contribute to field evaporation, with the stacked height of all concurrent effects corresponding to the likelihood of an evaporation event. SVP has been shown to improve the resolving power when applied to metals [166], semiconductors [167], and chromia [172].

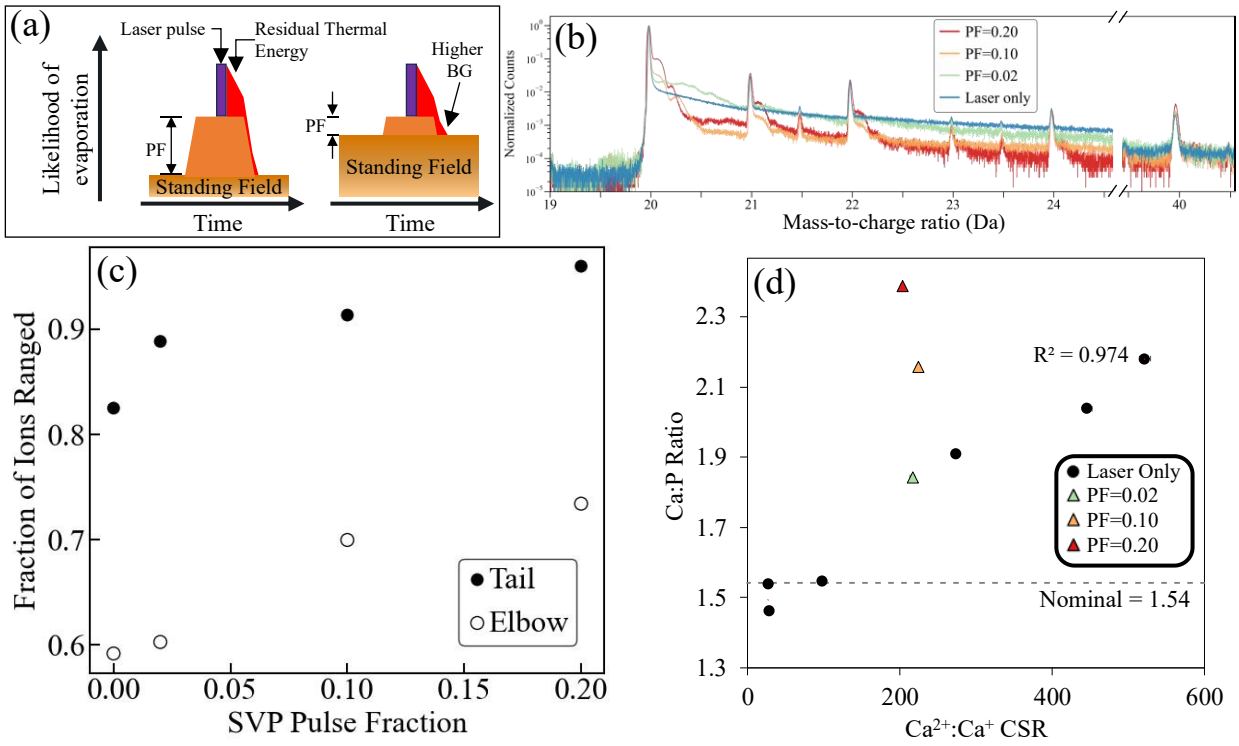

Figure 4.5. Simultaneous voltage pulsing applied to HA with a target CSR of 200. *a) Schematic illustrating the cumulative effects of the variables studied that contribute to field evaporation over time at the per-pulse scale. The vertical axis represents the generic input energy from the standing field, the laser pulse, residual thermal energy from the laser pulse, and varying pulse fractions (PF) of the simultaneous voltage pulse; the likelihood of an evaporation event occurring at a moment in time is reflected by the stacked height of all generic input energy factors. b) Comparison of mass-to-charge spectra for experiments with pulse fractions of 0.02, 0.10, and 0.20, as well as that of an experiment using laser only with a target CSR of 200. c) Fractions of ions included in thermal or elbow ranges for*

each of the experiments presented in (b). d) Decomposed Ca:P ratio against CSR. The trendline and associated R^2 are for the laser-only data. The error bars derived from counting statistics are smaller than the data points.

Here, we evaluated the effect of varying PF (between 0.02 – 0.20) on the m/z spectrum and measured composition during SVP mode using three separate HA specimens, controlling the LPE to maintain a target $^{40}Ca^{2+}$:$^{40}Ca^{+}$ CSR of 200. As expected, application of the SVP mode reduced the background measured during each experiment from an average of 23 (standard deviation ± 3) ppm/ns in laser-only mode to 16 (± 3), 16 (± 2), and 9 (± 1) ppm/ns for PF of 0.02, 0.10, and 0.20, respectively (Supplementary Figure 9). It is also worth noting that the standing voltage required for field evaporation of the same number of ions decreased with increasing PF (Supplementary Figure 10). The tail following the $^{40}Ca^{2+}$ peak shows considerably different behavior depending on the PF utilized. In the case of the 0.10 and 0.20 PF spectra, the background of the tail is considerably reduced relative to the laser-only spectrum, enabling easier identification of minor isotopes $^{42}Ca^{2+}$, $^{43}Ca^{2+}$, $^{44}Ca^{2+}$, and $^{48}Ca^{2+}$. However, following each Ca^{2+} peak, "shoulder peaks" cause an increase in the signal for ~0.4 Da (e.g., 20 – 20.4 Da). A somewhat different behavior is seen in the 0.02 PF spectrum, where the tail is considerably larger than the laser-only spectrum, with a periodic rise and fall in the signal intensity, which is most readily observed following the $^{40}Ca^{2+}$ peak (e.g., 20 – 20.6 Da). For both cases, these features are believed to be artifacts of the SVP mode caused by application of the voltage pulse to an electrically insulating material with high impedance, and not genuine peaks that merit identification. In other words, they can be considered as mistimed evaporation events and treated in the same fashion as tails of laser-only spectra (Figure 4.6).

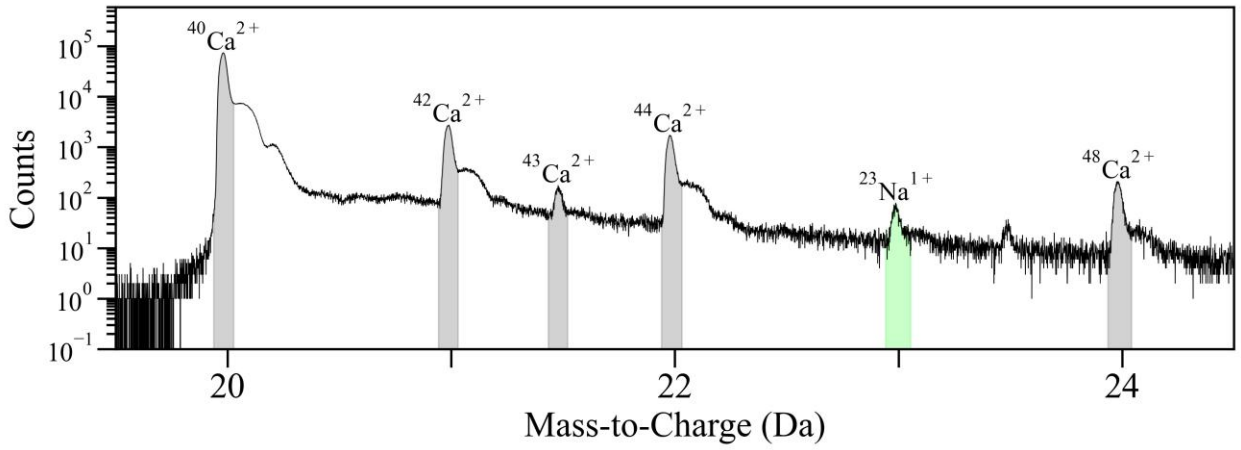

Figure 4.6. Segment of the m/z spectrum of the 0.20 PF SVP experiment from 19.5 – 24.5 Da overlaid with the systematically adjusted elbow ranges. *Note that the elbow ranges do not capture the secondary shoulder peaks*.

Increasing the PF increases the ranged fraction, whether using elbow or tail-inclusive ranges, owing to a reduction in the standing field between pulses and the reduction in stochastic evaporation events (Figure 4.5c). The improvement in the elbow ranging is particularly notable: at 0.10 and 0.20 PF, the ranged fractions were 0.70 and 0.73, respectively, whereas the laser-only (i.e., 0 PF) and 0.02 PF experiments had ranged fractions of 0.59 and 0.60, respectively. As before, increasing the range width to include the tails dramatically increases the ranged fraction, from a minimum of 0.82 to a maximum of 0.96 for the laser only and 0.20 PF spectra, respectively. The continuous increase in ranged fraction with increasing PF, at least up to a PF of 0.20, provides evidence that the SVP mode successfully reduces the background during APT experiments on insulative materials.

In this study, the SVP experiments were performed on three specimens that had been previously run (i.e. "polished") in APT to make their starting conditions as similar as possible. The prior runs were all conducted with a laser pulse energy of 20 pJ and ended at 2.6 kV, with the

intention being to achieve a congruent tip radius for each. The SVP experiments then proceeded with only the PF varying, with a stop point of 3.3 kV. The larger the PF, the longer the experiment proceeded, as the stop voltage is determined by the DC standing voltage, not the combined effect of the standing and pulsed potentials (Supplementary Figure 10) All SVP experiments were conducted with a target $^{40}Ca^{2+}$:$^{40}Ca^{+}$ CSR of 200.

The Ca:P ratio is plotted as a function of the measured $^{40}Ca^{2+}$:$^{40}Ca^{+}$ CSR for both laser-only CSR-controlled and SVP experiments in Figure 4.5d. This presentation reveals two notable trends. First, considering the laser-only data, there is a linear trend of increasing Ca:P ratio with increasing CSR, as was qualitatively noted when assessing the consistency of compositional measurements when using CSR as an experimental control (Figure 4.4b). A linear equation can be fit to this trend using (Eq 4.1).

$$\text{Ca:P Ratio} = 0.0014 * (CSR) + 1.456 \qquad \text{(Eq 4.1)}$$

with an $R^2 = 0.974$, which predicts that the Ca:P ratio of 1.54 measured by EDS can be obtained at a CSR of 60. The second observation is that the Ca:P ratio also increases with increasing PF in SVP mode, with the measured composition deviating considerably from the trendline established by the laser-only data. Indeed, the Ca:P ratio of the 0.20 PF experiment was 2.39 (± 0.01), well above the highest Ca:P ratio obtained during the laser-only experiments (2.04 ± 0.01 at a CSR of 440). The fact that there are two distinct trends connecting the Ca:P ratio to either the CSR or the SVP PF suggests that a more unifying parameter ought to form a more reliable predictor, which can be found in the ranged fraction.

4.4.6. Ranged fraction as a predictor of Ca:P ratio

Compiling data from all the experiments reported in this study, a striking trend between the Ca:P ratio and the fraction of ions ranged is revealed (Figure 4.7). Across both UV and DUV systems, increasing the ranged fraction through experimental conditions (e.g., using DUV, using SVP with higher PF) or ranging approach (e.g., including tails) results in a higher Ca:P ratio. Excluding one datapoint from the UV system (ranged fraction = 0.26, Ca:P = 2.30, corresponding to an LPE of 20 pJ), a strong linear trend between the Ca:P ratio and ranged fraction RF can be described using (Eq 4.2)

$$\text{Ca:P Ratio} = 3.290 * (RF) - 0.230 \qquad \text{(Eq 4.2)}$$

with an R^2 = 0.918. From this, we can estimate that if all ions were ranged (RF = 1.0), the Ca:P ratio would be 3.06. This reflects a systematic underrepresentation of P, presumably due to the formation of neutral species, which do not generate a detection event.

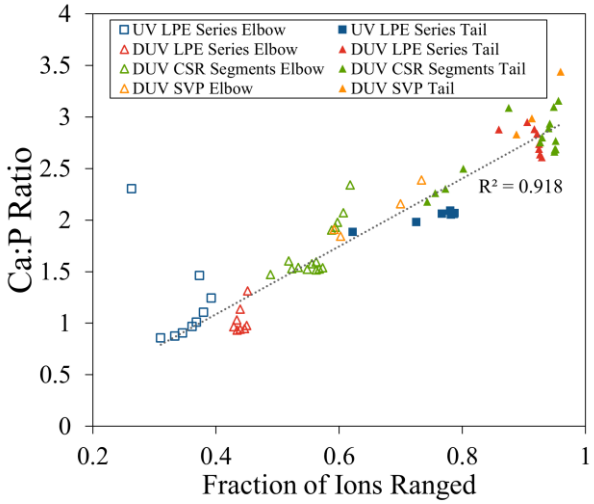

Figure 4.7. Ca:P ratio as a function of ranged fraction across all experiments in this study on both UV and DUV laser systems, using elbow and tail-inclusive ranging approaches. *The line of best fit (Eq 4.2) and associated R^2 value exclude the outlying point at (ranged fraction = 0.26, Ca:P = 2.30).*

ToF correlation histograms can be used to infer the formation of neutral species by post-evaporation dissociation, so long as one of the daughter molecules is ionically charged and generates a detection event [194]. This approach has been applied to synthetic HA by DeRocher, who reported that several molecular ions could produce a neutral daughter molecule (e.g. $P_4O_{12}^{2+} \rightarrow P_4O_{10}^{2+} + O_2$), though in each case, the neutral daughter was O_2 [23]. This does not alleviate the discrepancy in P concentration, suggesting that a considerable amount of P-containing ions were not detected, which will be addressed in the Discussion section.

Conversely, the trend in Figure 4.7 suggests that a ranged fraction of 0.53 will yield an accurate measurement of the composition, which is in the range of experiments that were performed with a target CSR of 30 – 100 with elbow ranges; another visualization of the trend of Ca:P ratio as a function of CSR presented in Figure 4.5d. While this interpretation obviously sacrifices some fidelity by discarding signal, it yields the most accurate measurement of stoichiometry, providing a solid foundation on which measures of inherent compositional discrepancies in more complex samples (e.g., biominerals with nanoscale compositional gradients [11]) can be built. Furthermore, these conditions take advantage of the instrument-independent CSR as a control parameter, and the application of elbow-ranging reduces the risk of analyst bias, improving the reliability and repeatability of results between researchers.

4.5. Discussion

With the introduction of commercial LEAPs equipped with DUV laser systems to the APT community, it is imperative to understand how the change in laser energy will impact the field evaporation and compositional measurements of samples. This is especially relevant when

assessing the same or similar materials between UV and DUV systems. The evidence presented in this study points to a fundamental change in the mechanism of field evaporation, at least for HA. However, it also enables parameter selection that improves the reliability and repeatability of compositional measurements on a reference sample (e.g., HA) that can be applied across multiple instruments and analysts.

One of the simpler optimizations available is to determine what LPE setting results in the most accurate composition. This is particularly true if the APT instrument at hand does not have the software necessary to control LPE to maintain a target CSR, as is the case on the UV system in this study. On the UV system, a LPE of 40 pJ yielded the closest Ca:P ratio to the expected value when using elbow ranges (Figure 4.3e). Higher LPE both increases the tail size and decreases the measured Ca:P ratio, indicating that a moderate LPE is preferable to a very high LPE. On the DUV system, the trend suggests that the target Ca:P ratio would be measured using an LPE below 15 pJ, though notably, increasing the LPE does not significantly change the tail.

All experiments performed in this study were conducted with a base temperature of 40 K, but temperature plays an important role in the field evaporation process for both metallic [195] and nonmetallic samples [172, 196]. In the case of the DUV laser where it seems that minimal temperature increase occurs for HA, it may be particularly rewarding to evaluate peak shape, tail prominence, and compositional accuracy as a function of base temperature in future studies.

Due to differences in laser-specimen interactions, LPE alone is not a reliable metric to compare between instruments, and to a lesser extent, between specimens. The electric field that the sample experiences during field evaporation, which can be correlated to CSR [164, 165], is a repeatable parameter that can be used to make comparisons across LPE [19, 197] and laser

wavelength [163, 170]. Unfortunately, $^{40}Ca^{+}$ was not detected using the UV system within the 20 – 200 pJ range, so CSR could not be used to make comparisons between instruments. However, $^{40}Ca^{+}$ was readily detectable on the DUV system with an LPE as low as 25 pJ, indicating a shift in laser-specimen interactions and field evaporation mechanisms has occurred.

Additional evidence that the DUV laser causes direct photoionization of HA can be found by considering the m/z spectra (Figure 4.1) and the proportion of the tails (Figure 4.3d). Whereas the UV system shows increasingly larger tails with increasing LPE due to increased thermal energy causing delayed evaporation events, the tails on the DUV system do not significantly change as a function of LPE. The presence of tails in the DUV spectra is probably due to delayed desorption of ions generated by photoionization and is less likely to represent a substantial temperature change, similar to observations of tails in the spectra of Si using an extreme UV system [162]. The reduction of tail intensity by moderate PF in SVP mode (Figure 4.5b), suggests that the rate of delayed desorption is also influenced by the field strength. Perhaps field-dependent desorption could also provide an explanation for the secondary peaks observed at high PF conditions in SVP, but this question requires further study.

The emergence of photoionization of HA using the DUV system may be explained by considering the work function of HA and the photon energy of the UV and DUV systems. A laser wavelength of 257.5 nm can be equivalently expressed (via the Planck equation) as a photon energy of 4.8 eV, while 355 nm is 3.5 eV. The work function of HA has been experimentally reported to be between 4.7 – 5.1 eV, with the lower values being measured on 20 – 60 nm nanoparticles [198]. Therefore, the DUV photon energy likely exceeds the electron work function of HA for ultra-sharp APT specimens, leading to photoionization and field evaporation.

Meanwhile, the UV photons have insufficient energy to ionize HA and instead contribute to a temperature increase, allowing thermal mechanisms to dominate. Additionally, absorption at particular wavelengths may correspond to excitations of certain electronic states, e.g., reports for ultraviolet-visible spectroscopy of pure HA describe an approximately two-to-three-fold increase in absorption at a wavelength of ~257.5 nm relative to that at ~355 nm [199, 200]. In the context of APT experiments this may increase the likelihood of ionization, though further research which considers factors such as high electric field and ultrahigh vacuum is needed to confirm this. In contrast, the work function of Si (001) is reported as 4.9 – 5.1 eV [201, 202], leading to thermally-driven evaporation on both the UV and DUV systems as neither has sufficient photon energy for photoionization (Figure 4.2). This explanation is consistent with similar observations from chromia [28] and strontium titanium oxide [29]. A full mechanistic explanation of photoionization of HA is beyond the scope of this paper, but we anticipate the evidence for and understanding of photoionization for certain materials caused by DUV laser pulsing will grow as the breadth and depth of materials studied on DUV systems grows in the coming years.

Irrespective of the means of field evaporation, the analyst ultimately must tune parameters to yield the most accurate spatial and compositional measurements. Optimization of the former is reserved for other work comparing reconstruction dimensions to empirically measured evaporated lengths, as outlined by [203]. Here, we focus on the compositional accuracy, specifically the Ca:P ratio, as different calcium phosphate phases relevant to biomineralization and geochemistry have distinct Ca:P ratios (e.g., 1.67 for HA; 1.33 for octacalcium phosphate, $Ca_8H_2(PO_4)_6$; 1.00 for brushite, $CaHPO_4$). There are two components to accurate measurements: the experimental parameters that affect the relative intensity of certain signals, and the ranging approach applied to the m/z spectrum. We find that dynamically changing the LPE to maintain a $^{40}Ca^{2+}$:$^{40}Ca^{+}$ CSR of

60 and using the elbow-ranging approach described in Figure 4.3b results in the most accurate composition (Figure 4.5d). Critically, the specific value of the "optimal" CSR is dependent upon the ranging approach applied – e.g., one may arrive at a different optimal CSR for compositional accuracy if one utilizes an alternative ranging protocol such as the full width at 9/10 maximum approach described in [174] or the ranging of the elevated background above 20 Da as Ca^{2+} described in [24], though the link between ranged fraction and Ca:P ratio (Figure 4.7) would still provide a reasonable guide.

One concern that initially arises from using a target CSR to control the LPE is that it can result in high LPE, particularly at the start of an experiment (Figure 4.4a), which could then cause significant changes to the tail [24]. Fortunately, this problem was avoided in this study, as the tail intensity does not substantially increase with increasing LPE on the DUV system used for the CSR-controlled experiments (Figure 4.3d), and the UV system did not result in a $^{40}Ca^{+}$ peak that could be used for the $^{40}Ca^{2+}$:$^{40}Ca^{+}$ CSR controls. However, if one were to use a different peak ratio (e.g., PO_3^{2+}:PO_3^{+} as in [24]), then perhaps it would be necessary to set a maximum allowable LPE or to discard the early portion of the run until tails are at an acceptable level.

It is important to acknowledge that the elbow ranging procedure discards a considerable amount of collected data, only ranging ~54% of the detected ions (Figure 4.7, Supplementary Equation S2). However, as the fraction of ions ranged increases, whether by ranging the tails or reducing the tail intensity (i.e., SVP mode), the Ca:P ratio shifts further and further in favor of Ca. Both approaches disproportionately result in a greater number of ions attributed to Ca, with relatively modest gains to P-containing peaks. Post-evaporation neutralization of phosphate ions seems the most likely explanation for this discrepancy. ToF correlation histograms have inferred

that neutral O_2 daughters can be generated from HA by dissociation of ions after evaporation [23], but no evidence was found for neutral P-containing species. Critically, ToF correlation histograms are most successful when using straight-flight path instruments, whereas both the UV and DUV systems in this study had energy-compensating reflectron designs. If neutralization of P-containing molecular ions occurs near the specimen surface, or before exiting the reflectron, then they will not reach the detector. Furthermore, even for a straight-flight instrument, Saxey notes that if formation of neutrals occurs near the specimen surface, the resultant molecule may not have sufficient energy to trigger the detector, and the signal may be substantially displaced from the expected time of flight [194]. The linear correlation between the Ca:P ratio and CSR (Figure 4.5d) suggests that we may be able to exert some control over the formation of neutral species through the electric field.

Unfortunately, this data loss to neutral formation is inevitable, so to achieve an accurate Ca:P ratio we are relegated to finding parameters that repeatably, though indirectly, discard the appropriate portions of the appropriate signals across multiple specimens. The elbow-ranging approach is our solution to this problem, as it is a simple algorithmic procedure that does not rely on the analyst to draw the ranges consistently. While advanced methods to discern the composition from the m/z spectrum are being developed [168, 204], here we present a facile and versatile approach to achieve accurate compositional measurements through combining CSR controls and systematic peak ranging, i.e., the elbow-ranging approach.

4.6. Conclusions

This study had three primary objectives, united by the aim to improve the quality and reproducibility of APT data. The experiments were performed on synthetic HA with a known composition as a model system of broad significance from biological to industrial applications. The first objective was to evaluate the differences in mass-to-charge spectra quality, measured composition, and mechanisms of field evaporation between the UV and DUV laser systems of LEAP 4000X-HR and 6000 XR systems, respectively. On the UV system, laser pulses increase the temperature of the specimen, reducing the threshold for field evaporation, while the DUV laser induces photoionization of HA. While increasing the LPE on the UV system increases the proportion of delayed evaporation events (i.e., tails), the tails are more consistent across LPE on the DUV system.

Secondly, we evaluated the performance of the recently developed SVP mode for HA, a non-conductive material. Generally, the background and thermal tails were reduced when using SVP with moderate (≥ 0.10) voltage pulse fractions. However, unexpected shoulder features were introduced after major peaks, possibly a result of the high impedance of HA. The results are promising, though additional work is required to fully understand how field evaporation is impacted for this and other non-conductive materials

Lastly, we determined that a systematic approach to ranging and the use of the $^{40}Ca^{2+}$:$^{40}Ca^{+}$ CSR as a control on the DUV system more consistently reproduced the mineral stoichiometry. Specifically, using range bounds defined at the elbows on each peak, the trendline indicated that a CSR of 60 yielded the expected Ca:P ratio of 1.54.

HA is a biologically, geologically, and industrially relevant material. This is also a crucial foundation upon which to build future studies of the complex nanometer-scale structures and compositional gradients that are inherent to many HA systems (e.g., biominerals), improving the confidence with which APT can be used to probe these materials. This is specifically applied in the next Chapter to human inner enamel from three distinct age groups. More generally, we argue that HA can serve as a reference material for APT analyses of electrical insulators, as conditions have been identified to achieve the stoichiometric Ca:P ratio while mitigating sources of analyst and operator error.

5. Exploration of Nanoscale Organic and Mineral Compositions in Human Primary and Permanent Inner Enamel

5.1. Synopsis

Chapters 2 and 3 established a statistical approach for segmenting enamel into distinct phases which can then be compared. A systematic evaluation of HA by APT was conducted in Chapter 4, showing that the best measurement precision can be achieved by setting a target $^{40}Ca^{2+}$:$^{40}Ca^{+}$ charge state ratio during experiments and using automatically adjusted ranges during analysis. This chapter leverages the gains in confidence and precision from these approaches to perform a robust evaluation of inner human enamel from donors of three age groups, namely primary, young permanent, and senior permanent. The primary focus is the residual organic content that resides between nanocrystals. This evaluation is divided into three assessments. (I) Firstly, a comparison of the composition of each phase within each tooth allows a confident identification of signature molecular ions that can be associated with the HA mineral (e.g., OH^{+}, CO_2H^{+}) or organic (e.g., CO^{+}, N) components. (II) A comparison of the phases between age groups was performed to search for signs of compositional change that might be due to tooth maturity or individual age. Minimal changes were expected at the sampled location from the inner enamel, as de-/re-mineralization cycling is thought to be prevalent only near the outer surface. Nonetheless, an increased concentration of e.g., K was noted in senior enamel, while the young enamel had the lowest concentration of OH^{+}, which may reflect that the tissue was not fully matured yet. (III) Lastly, samples were exposed to a bleaching solution for 15 days with the goal of removing the organic

precipitates. However, complete removal was not achieved, indicating that the precipitates are thoroughly occluded by mineral and thus resistant to alteration by external factors.

5.2. Introduction

Enamel is a highly mineralized composite material composed of ~95 wt.% calcium-deficient carbonated hydroxyapatite mineral, ~2 wt.% residual organic compounds, and ~3 wt.% water. The organic component purportedly contributes to the mechanical properties of the tissue, and most notably in the resistance to fracture [138]. Thus, knowledge of changes to the organic component is of critical importance to understanding tooth maturation or degradation associated with increasing age [86, 98]. While much of this organic content is believed to be located at the rod-interrod interface, where it can contribute to crack bridging [1], APT studies have also reported nanoscale organic precipitates between some of the hydroxyapatite nanocrystals [25, 26]. It is also important to note that the nanocrystals that constitute enamel are not tightly packed [62]. Gaps can be found between adjacent nanocrystals that do not perfectly tessellate, which is presumably where organic residues are displaced by growing mineral nanocrystals during the maturation stage of amelogenesis due to their insolubility in the HA crystal. As such, these organic-filled spaces can be considered as precipitates.

These organic-rich precipitates have received limited focus to date, leaving many questions unanswered. One such question that is relevant to the mechanical and optical properties of teeth is whether the quantity or quality of organic precipitates is affected by environmental exposure and age. Here, we apply a statistical APT analysis to explore and compare the composition of organic precipitates, as well as the surrounding mineral, from the inner enamel of primary, young

permanent, and senior permanent age groups. Inner enamel is softer and has a lower reduced modulus than outer enamel [7], a gradient that results from the diffusion-limited efficacy of protein removal during maturation [62], i.e., the enzymes and proteases used to remove organic content are supplied from the outer surface of the enamel after it has reached its full thickness. Thus, sampling from the inner enamel was expected to yield higher likelihood of encountering organic precipitates or higher intergranular and interrod organic content in APT datasets. However, there is some ambiguity as to the origin of the fragmented molecular ions that are generated during APT experiments. For instance, carbonated mineral and organics can both generate CO_2^+ molecular ions [26, 46]. Similarly, it can be expected that H will be abundant in both the hydroxyapatite mineral as well as the amino acids that constitute the organic phase.

Precipitates are separate from the amorphous intergranular matrix phase that surrounds each nanocrystal [11, 16]. The intergranular phase has been shown to be a relatively fast diffusion pathway for ions or solutions to permeate into the enamel tissue. One example is the infiltration of topically applied 250 mM NaF over 24 hours, which created the stark compositional contrast of Na and F ions to the intergranular phase in APT experiments [11]. Another example is reduction in nanocrystal diameter when enamel was subjected to 1.27 mM citric acid for 1 min, indicating that the solution permeated through the intergranular space and attacked the (100) and (110) faces of the HA crystals [13].

We hypothesized that the presence of precipitates and the permeability of the intergranular phase could serve as tools that would allow for an improved identification of which ionic signals in APT experiments correspond to the organic residues or inorganic carbonate substitutions in enamel. Identification of such ions is the first step in being able to quantitatively compare the

composition of organic content at the nanoscale. Our analysis is split into three assessments. In the first, we evaluate the composition of nanocrystal, intergranular, and precipitate phases. By comparing the composition of the organic-rich precipitate to that of the inorganic nanocrystals, we are able to confidently identify signature molecular ions for each phase. Then, we compare the control data across age groups. As the inner enamel is relatively insulated from the oral environment and thus less likely to experience substantial de-/re-mineralization cycling, minimal variations associated with age were expected, though several differences are noted. Lastly, we consider the effect of a bleaching treatment relative to a control on the presence and composition of enamel. Precipitates can still be found readily after treatment and the composition is not significantly impacted, evidence that they are fully occluded by mineral. The findings provide an unprecedented nanoscale perspective of the organic content in enamel and will be support future investigations focused on the effects of age, disease, or lifestyle choices on enamel composition, microstructure, and properties.

5.3. Methods

Samples used for APT were taken from matching halves of one molar each for primary, young, and senior age groups, anonymously extracted for orthodontic reasons with the roots intact under an IRB exemption for STUDY00014724 from the University of Washington. The primary tooth was a second molar (position K) from an 8-year-old female, the young tooth was a third molar (position 1) from a 21-year-old female, and the senior tooth was a third molar (position 16) from a 60-year-old female. After extraction, the samples were stored in Hank's balanced salt solution (HBSS, Hygia Reagents) until ready for preparation. Roots were removed from the teeth, then they were bisected along the buccal-lingual plane using a diamond wire saw (STX-202A,

MTI Corporation) with copious use of water as coolant. One half of each tooth was reserved as a control while the other was submerged in 0.35 M NaOCl solution for 15 days on a vibrating table, exchanging with fresh solution every 3 days. After treatment, each half was embedded in epoxy (EpoFix resin and hardener, Struers), then subsequently the sectioned face was ground with a series of SiC papers from ISO 800 to 4000 grit and finished with a 1 μm diamond polishing suspension on a MD-Dac polishing cloth (Struers). Polished samples were coated with ~5 nm of Pt to enhance conductivity (ACE600, Leica).

The use of a plasma focused ion beam-scanning electron microscope (PFIB) (Helios Hydra, Thermo Fisher) enabled APT samples to be extracted from matching locations on each tooth to minimize the spatial variation in composition or response. This was done by first drawing a 125 μm radius circle centered on the lingual horn of each section, then extending a perpendicular 50 μm line from the intersection of that circle with the DEJ on the cervical side of the tooth; the resultant site is approximately 135 μm from lingual horn (Figure 5.1a-c). A protective 12×3×1 μm Pt capping was deposited parallel to the DEJ at this location using first a 5 kV 1.6 nA electron beam, followed by a 30 kV 0.3 nA Xe ion beam (Figure 5.1d). Trenches were then milled on either side of the protective cap at a 30° incident angle using a 14×4×5 μm rectangular pattern with a 30 kV 1 nA ion beam (Figure 5.1. One end was cut free and attached to a nanomanipulator (EZLift, Thermo Fisher) by a small Pt deposition. The remaining end of the cantilever was cut free from the bulk and the liftout transferred to be sliced and affixed to Si microposts (M22 array, Cameca) using 1.4×1.5×0.5 μm Pt welds deposited by a 30 kV 30 pA ion beam. Each sample was then sharpened into a fine needle with a series of annular ion beam milling patterns at 30 kV, 0.3 nA: 4×1.3 μm (outer diameter × inner diameter) for 180 s, 3.5×1.0 μm for 60 s, 3×0.8 μm for 30 s, 3×0.5 μm for 20 s. This process was followed by polishing at 5 kV 30 pA with a combination of

2×0.4 µm annular pattern and no pattern (i.e., "live imaging") until the final tip diameter was less than 150 nm. A secondary electron image acquired in immersion mode using a 3 kV 0.2 nA electron beam of the final tip shape was captured at a stage tilt of 52° to document the tip profile. An additional sample taken near the outer enamel surface of the young tooth was also extracted following the same protocols. The data from the outer enamel liftout was used to verify that Mg-rich cores could be found with the instrument and sample preparation techniques described, but it was not considered for any of the compositional comparisons featured in this chapter.

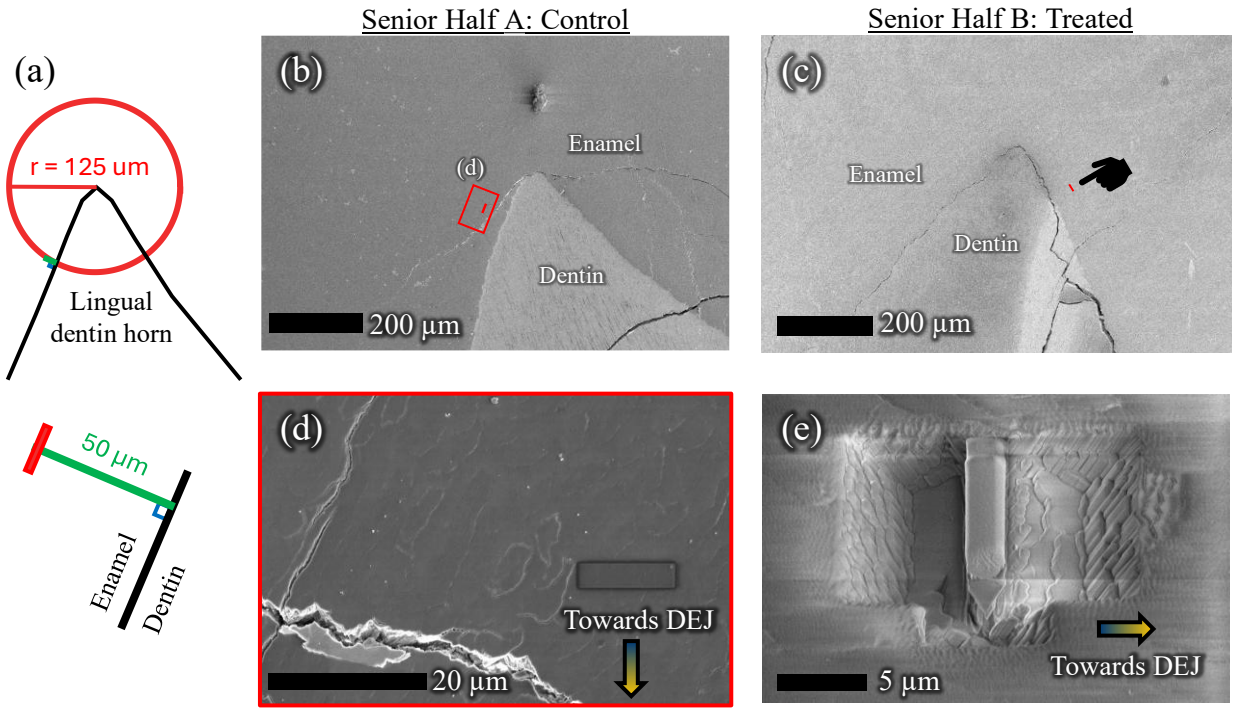

Figure 5.1. Preparation of samples from matching halves. *(a) Schematic showing the location of the liftout relative to the lingual dentin horn. Samples for APT were taken from mirrored locations of the (b) control and (c) NaOCl-treated halves of the same tooth. (d) Higher magnification image of the Pt capping deposited on the target site in a relatively parazone region (rods have a low incidence angle with the section plane). (e) After trenching and polishing, the cantilever can be attached to a nanomanipulator so that segments can be transferred to prepared Si microposts for polishing.*

APT experiments were conducted on a local electrode atom probe (LEAP) 6000 XR (Cameca) equipped with a 257.5 nm wavelength laser in laser pulsing mode at a stage temperature of 30 K and using a 100 kHz pulse frequency. The voltage was automatically adjusted to maintain a target detection rate of 0.003 ions/pulse. The laser pulse energy was simultaneously automatically adjusted to maintain a target $^{40}Ca^{2+}$:$^{40}Ca^{1+}$ charge state ratio of 150, following the guidance for synthetic hydroxyapatite provided in Chapter 4. When possible, experiments were stopped before fracture of the specimen so that they could be imaged using the electron beam (3 kV, 0.2 nA) of the PFIB in immersion mode at a stage tilt of 52° to estimate the length (along the specimen axis) evaporated during the APT experiment.

Note that throughout this chapter, the isotope or charge of an ion or molecular ion is only specified when necessary, otherwise it can be assumed that all isotopic variants and all charge states are being referred to. A full list of the ranges including identity of molecular ions and the charge state for each range is provided in Supplementary Table 2.

Reconstruction of APT datasets was performed using the integrated visual analysis software (IVAS) module of Atom Probe Suite software (v6.3.3.7, Cameca). The following peaks were used during the mass calibration stage of the reconstruction wizard: H_1,$^{25}Mg^{2+}$, $^{16}O^{+}$, $^{40}Ca^{2+}$, Na^{+}, P^{+}, $^{16}O_2^{+}$ (31.99 Da), $^{40}Ca^{+}$, PO^{+} (46.969 Da), PO_2^{+} (62.964 Da), PO_3^{+} (78.959 Da), $CaPO_3^{+}$ (118.922 Da), $P_2O_5^{+}$ (141.923 Da), $P_2O_6^{+}$ (157.918 Da), $P_3O_7^{+}$ (204.887 Da), $P_3O_8^{+}$ (220.882 Da), and $P_4O_{10}^{+}$ (283.846 Da). It was determined that the most accurate reconstructions were achieved by setting the detector efficiency to be 0.52 (nominal detector efficiency) × Ranged ions ÷ Collected ions (yielding a typical value of approximately 0.35), drawing a tip profile, and using the electrostatic reconstruction method in scaled apex mode with 50 spherical apexes, 19 scaling

neighbors, no Z reordering, and a detector back-projection grid size of 200. If no suitable micrograph was available to define the tip profile, then instead the radius evolution was determined by the voltage, setting the evaporation field to 11.8 V/nm (empirically estimated using a procedure similar to [203]), and the atomic volume to be element specific. Preliminary investigations showed both the electrostatic and voltage-driven reconstructions to reasonably match the evaporated length of the sample as measured by SEM images taken before and after the APT experiment.

ROIs were manually defined after first rotating the reconstruction with only Mg ions visible to align the intergranular phases that span through the thickness of the reconstruction. For the phase-based analysis, rectangular ROIs with variable dimensions were arranged first along the $^{25}Mg^{2+}$-rich intergranular (IG) phase, then the $^{12}C^{2+}$-rich precipitates (PR) if present, and finally within the crystals (CR) to fill the remaining space. Mass-to-charge state ratio spectra from 0 – 290 Da were exported from each region of interest with a bin size of 0.005 Da and bins with "negative" counts after background correction truncated to 0 counts. For each reconstruction, the spectra exported from rectangular ROI associated with each phase were combined into a single m/Z spectrum (i.e., one spectrum for CR, IG, and PR per reconstruction) using the custom Python script developed in Chapter 2. A base .RRNG file was developed by assigning a chemical identity to each peak with a maximum intensity exceeding approximately double the surrounding background. This base .RRNG was then applied to at least one dataset from each age-treatment pair (3 ages × 2 conditions = 6 datasets) to ensure any peaks specific to a particular age-treatment combination were included. The ranges from this base .RRNG file were then adjusted to the bulk m/z spectrum for each collected dataset (unique run serial number) using the elbow-ranging approach as described in Chapter 4. Those elbow ranges were then applied to the combined m/z spectra collected by phase. Recalculation of the local range assisted background (LRAB) was

performed for each combined phase m/z spectra using Python. Within the commercial IVAS module, the LRAB is calculated according to a power law defined from the nearest peak with a lower m/z position [205]. The same power law was used in the Python estimates, though additionally, a linear fit and the average signal intensity were checked to identify the fit with the best coefficient of determination calculated using `sklearn.metrics.r2_score` package. The corrected counts used for compositional measurements were then calculated by subtracting the background estimate from the uncorrected counts for bin and integrating across the full range.

Peak deconvolution was performed in Python by applying the proportionality expected from isotopic abundances using the corrected counts of a reference peak at the same change state with no overlapping signals. Three peaks were identified in the m/z spectrum with significant overlaps: $^{24}Mg^{2+}/^{12}C^{+}$ at ~12 Da, $^{26}Mg^{2+}/CN^{2+}$ at ~13 Da, and $^{48}Ca^{2+}/^{24}Mg^{+}$ at ~24 Da, and the reference peaks were $^{25}Mg^{2+}$, $^{25}Mg^{2+}$, and $^{40}Ca^{2+}$, respectively. When applicable, decomposition of molecular ions into their elemental constituents was performed in Python, reported here as atomic percentages (at.%).

Statistical comparisons between the treated and non-treated conditions for each age were evaluated using the scipy package for unequal variances *t*-test in python (`scipy.stats.t`). Comparisons between phases or age groups were conducted using a one-way analysis of variance (ANOVA) followed by Tukey post-hoc tests. The threshold for significance in both cases was set at a p value less than 0.05.

5.4. Results & Discussion

5.4.1. Nanocrystals and the absence of Mg-rich cores

Previous studies of human molar enamel focused near the OES have repeatably found that the hydroxyapatite nanocrystals have a core-shell structure, where the core is defined as a Mg-rich phase separate from the Mg-rich intergranular phase [11, 35] (Figure 5.2a-b). It was posited that the core is connected to the so-called central dark line [11, 206] and that they could be a unique feature of human enamel, as they are not observed in murine enamel [16, 25] or crocodilian enamel (Chapter 3) and it is unclear whether they are present in bovine enamel [27]. It has been proposed that these cores develop in the late secretory stage of amelogenesis, when the nascent mineral is ACP rather than HA and Mg concentrations are elevated [11].

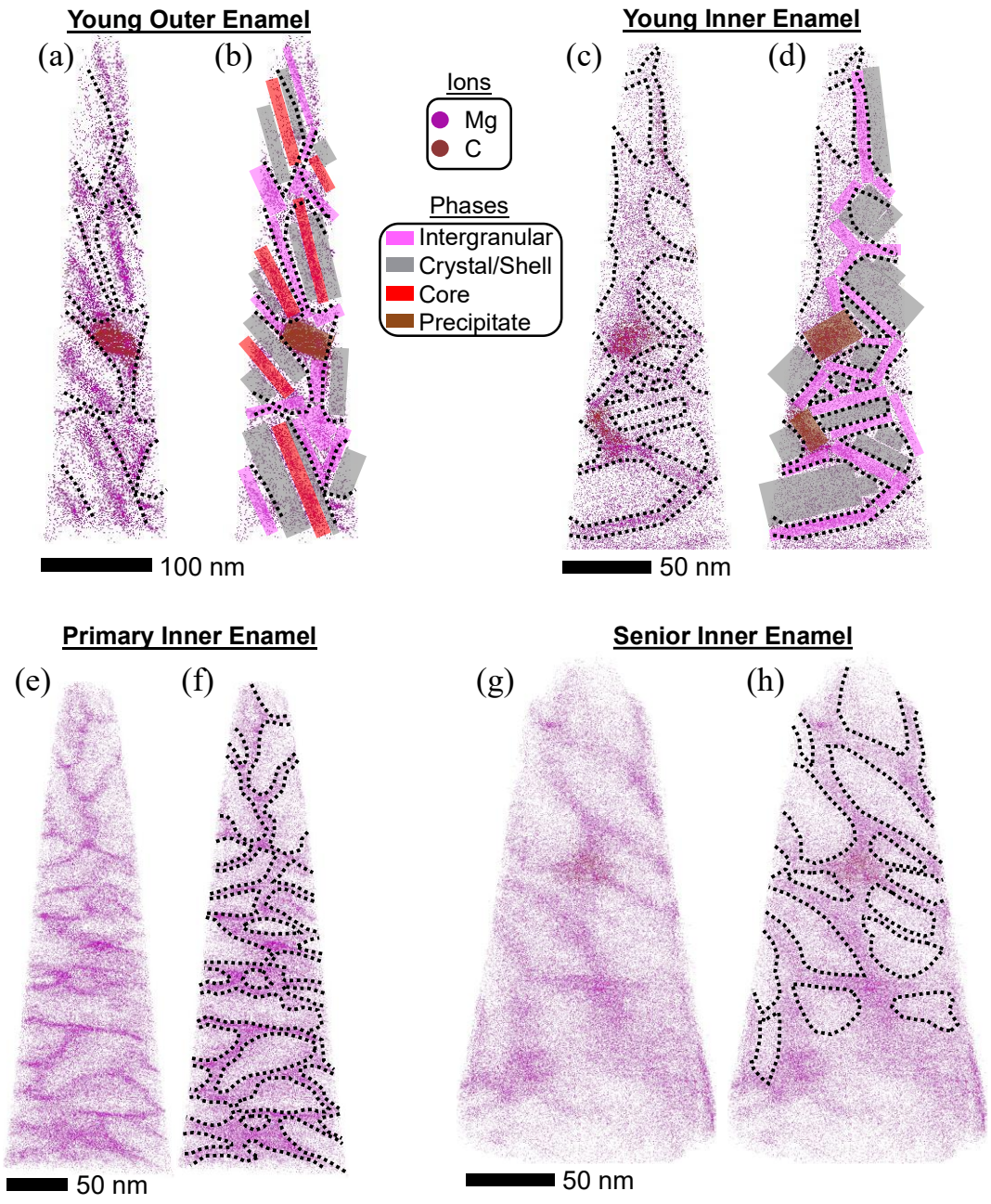

Figure 5.2. APT reconstructions of outer and inner enamel. *Representative reconstructions aligned to the long direction of the HA nanocrystals for (a-b) young outer enamel, (c-d) young inner enamel from the same tooth, (e-f) primary inner enamel, and (g-h) senior inner enamel. Each reconstruction shows the Mg^{2+} and C^{2+} ions which serve as the primary markers used to identify the intergranular, crystal/shell (in inner/outer enamel, respectively), nanocrystal core, and precipitate phases, marked as rectangular ROIs in (b, d). Dashed lines in (a-d, f, h) outline individual nanocrystals.*

However, in the three human teeth sampled here, we were surprised to find that all nanocrystals lacked a Mg-rich core, regardless of age group (Figure 5.2c-h). We hypothesize that the presence of Mg-rich cores may not be solely a species-dependent feature, but rather that it is dependent upon the sampling location within the tooth. Nanocrystals near the OES have Mg-rich cores while those near the DEJ do not, which may imply that Mg-rich cores are a byproduct of the maturation stage of amelogenesis, similar to other functional gradients across the enamel thickness (e.g., mechanical properties [7] or composition [8, 9]).

There is insufficient evidence at this time to definitively identify a mechanism that explains presence of cores in outer enamel but their absence near the DEJ. It can be observed that some adjacent nanocrystals share a common alignment (i.e., are elongated in parallel) and are separated by a Mg-rich IG layer. Perhaps the IG phase can be converted into a core through the fusion of the adjacent nanocrystals. However, this is unlikely to be the origin for Mg-rich cores in most nanocrystals as it would require that every nanocrystal in outer enamel is the product of exactly two smaller adjacent nanocrystals that share a common orientation. Furthermore, if this were the case, there is no apparent force that would restrict more than two nanocrystals from fusing and yielding thick nanocrystals with two or more cores, but only single cores have been documented in APT and TEM studies (Figure 2.2, Figure 2.6) [11].

A somewhat more plausible explanation for the presence of Mg-rich cores in the outer enamel could be due to accumulation of Mg that is insoluble from the inner enamel. During the secretory stage of amelogenesis, the mineralization front follows several micrometers behind the ameloblasts, with the nanocrystal width experiencing greater increases before the width as a function of distance from the Tomes' process [81]. It could be possible for excess Mg to pile up as

deeper nanocrystals grow and eject insoluble Mg. If we assume that the amount of Mg introduced by ameloblasts or extracellular fluid ahead of the mineralizing front per unit time remains constant throughout amelogenesis, then the local concentration of Mg would increase as a function of distance traveled by the ameloblasts (i.e. distance from the DEJ) due to increasing contributions from "old" Mg being pushed towards the mineralizing front. It has been proposed that the Mg-rich cores originate as Mg-rich ACP nanoribbons which then serve as the seed mineral that transforms to HA and grows during maturation [11]. Following this logic, then the cores could be a sort of "snapshot" of the local Mg concentration at a given location within the tooth when mineralization began. In other words, the inner enamel nanocrystals may have a core to them as well, but the Mg concentration was not notably elevated when they were formed.

An additional implication would be that the presence of the Mg-rich core is not specific to humans or any other species insofar as physiological differences are concerned, but rather they are specific to enamel that developed with an elevated Mg concentration due to pileup of Mg ions near the mineralization front during amelogenesis of thicker enamel layers typical of humans. If this hypothesis were the case, then one would expect an increasing gradient in Mg concentration as a function of distance from the DEJ to the OES, but several studies of mature human enamel report the opposite [116, 207, 208]. A rebuttal may be found by considering the aprismatic outer layer of human primary enamel. The aprismatic layer is a commonly observed feature in mature enamel, though it is much thicker in primary enamel than in permanent, possibly a result of incomplete maturation before eruption. Kis and coworkers have measured the concentration of Mg in the aprismatic layer (starting ~0.9 mm from the DEJ) to be approximately three-to-four-fold greater than in the decussated portion of primary enamel [209]. If the aprismatic enamel reflects the structure and composition at an intermediate stage of maturation (i.e., more developed than

secretory, but not completely mature), it provides plausible evidence for the Mg content being elevated at greater distances to the DEJ, and more importantly, that Mg content is decreased during complete maturation, in line with observations on permanent mature enamel [116, 207]. Ultimately, there is insufficient evidence to conclusively determine the origin of the Mg-rich cores, but we propose that they are representative of the local Mg concentration at the time of mineral nucleation. During maturation, the Mg concentration of the matrix is reduced and the ACP nanoribbon transforms to crystalline hydroxyapatite while growing in thickness and to a lesser extent, width [81]. Less Mg is incorporated into the HA nanocrystal during maturation, producing a distinct core-shell structure that is most obviously visible in those nanocrystals which formed in an environment with higher Mg concentration.

A complimentary experiment that could be performed to lend further evidence towards or against this theory would be to measure the Mg concentration within nanocrystals as a function of distance from the DEJ using APT. This can also be corroborated by TEM, in particular searching for evidence of the central dark line that is often noticed in enamel nanocrystals which is believed to be caused by the increased Mg content [11]. Additionally, measurements of the Mg concentration in developing enamel as a function of distance from the DEJ are needed. Murine incisors may serve as a useful tool in this aspect, as one can sample multiple stages of amelogenesis throughout the length of the incisor from apical loop to erupted tissue [73, 210].

5.4.2. Assessment I: Differences in phase composition

For the remainder of this chapter, we only segment the APT data into crystal (CR), intergranular (IG), and organic precipitate (PR) phases, dropping the nanocrystal core phase that

was used in Chapter 2. It is crucial to emphasize that the measured compositions reported here may not represent the true composition in any of the samples or phases, owing to data loss associated with the process of field evaporation. This is particularly true for organic molecules, a class of materials for which the field evaporation mechanics in atom probe are relatively poorly understood [211]. Rather, the statistical method employed here is used to identify with confidence which peaks can be used to discriminate organic-rich regions in biominerals.

One of the primary aims of this study was to determine which signals in the m/z spectrum could be used to reliably differentiate organic and inorganic species in APT reconstructions of enamel. The basic approach consisted of segmenting the reconstruction into phases using Mg as a tracer to highlight the IG and PR phases. The presence of the PR phase in many of the reconstructions provided a relatively straightforward way to determine what species were organic in nature. While first reported in [26], it was only applied visually. In this assessment, our aim is to confirm and bolster those findings with a greater number of samples and to leverage statistics to improve the confidence while identifying other compositional distinctions between the phases.

For each tooth, the concentration of each molecular ion in each phase was compared using a one-way ANOVA and Tukey post-hoc testing resulting in a list of pairwise comparisons. The volume of these comparisons is considerable, and thus only select comparisons with the greatest significance will be presented in detail here. Table 5.1 shows the molecular ions with significant differences (defined here as a p value < 0.05) between CR, IG, and PR phases for each tooth, sorted into columns by the phase with the highest concentration of that species. By comparing the species that are listed in each column between the three ages, we can see that the trends were generally consistent between all three teeth tested.

Table 5.1. Ion signatures for each phase. *Each column lists the ionic species that that are highest in that phase (ANOVA with Tukey post-hoc test $p < 0.05$), repeated for each tooth. For example, the IG and PR phases have significantly higher Mg concentrations than that of the CR. Elements marked with an * indicate that the significant difference was found for the decomposed concentration of that species. The number n of experiments that captured each age-phase combination are listed in each cell.*

Tooth	Crystal (CR)	Intergranular (IG)	Precipitate (PR)
Primary	H*, Ca_1, CO_2H, $OH_{1\text{-}3}$, O_2H n = 5	Mg, CN n = 5	n = 1
Young	H*, H_3, CH_3, CO_2H, $OH_{1\text{-}2}$, O*, O_2 n = 5	Mg, CN, P* n = 5	Mg, C_1, C*, N_1, N*, H_1, CO, CaF, Ca*, Na, Cl, K, NO n = 5
Senior	CO_2H, OH, O_2H n = 6	Mg, CO_2H, CN, O_2H n = 6	Mg, C_1, N_1, N*, H_1, CO, CN, CNH, Cl, NO n = 3

The unique compositional characteristic of each phase is revealed by considering which species consistently have the highest concentration. The CR phase is characterized by having a higher concentration of CO_2H, and $O_{0\text{-}1}H_{1\text{-}3}$ molecular ions (Figure 5.3), which in turn yield a higher decomposed H* signal. These signals reflect the composition of carbonate-substituted hydroxyapatite, a mineral rich in OH groups. For the primary tooth, the CO_2H concentration in the CR phase is 0.12 ± 0.01 (standard deviation) ion%, which is significantly greater than in the IG (0.09 ± 0.01 ion%, $p = 0.0014$) and PR (0.05 ion%) phases, while no significand difference was found between IG and PR phases ($p = 0.0835$). Note that only n = 1 precipitate was captured for the primary control data, so no standard deviation can be provided and the Tukey post-hoc pairwise tests comparing it to CR or IG were not performed. Similar trends are observed in the young tooth, where the concentration of CO_2H is greater in CR (0.12 ± 0.03 ion%) than in PR (0.06 ± 0.02 ion%, $p = 0.009$), though IG is at an intermediate value of 0.09 ± 0.02 ion% and is not significantly

different from either CR or IG. Lastly, in the senior enamel, the CO_2H concentration in the PR (0.08 ± 0.01 ion%) is less than both CR (0.13 ± 0.02 ion%, $p = 0.0009$) and IG (0.11 ± 0.01 ion%, $p = 0.0309$) phases, while the latter two are not significantly different from each other ($p = 0.1999$). The trend amongst all three ages is that the concentration of CO_2H is highest in the CR phase, though the concentration of IG is more intermediate and may be more comparable to the PR (as in primary) or CR (as in senior) phase. This is a pattern which is representative of the other molecular ions listed in Table 5.1: the IG phase tends to have an intermediate composition between PR and CR phases, and the strength of differences between phases varies somewhat for each tooth sampled. For brevity, this dissertation will only detail p values for representative comparisons going forward.

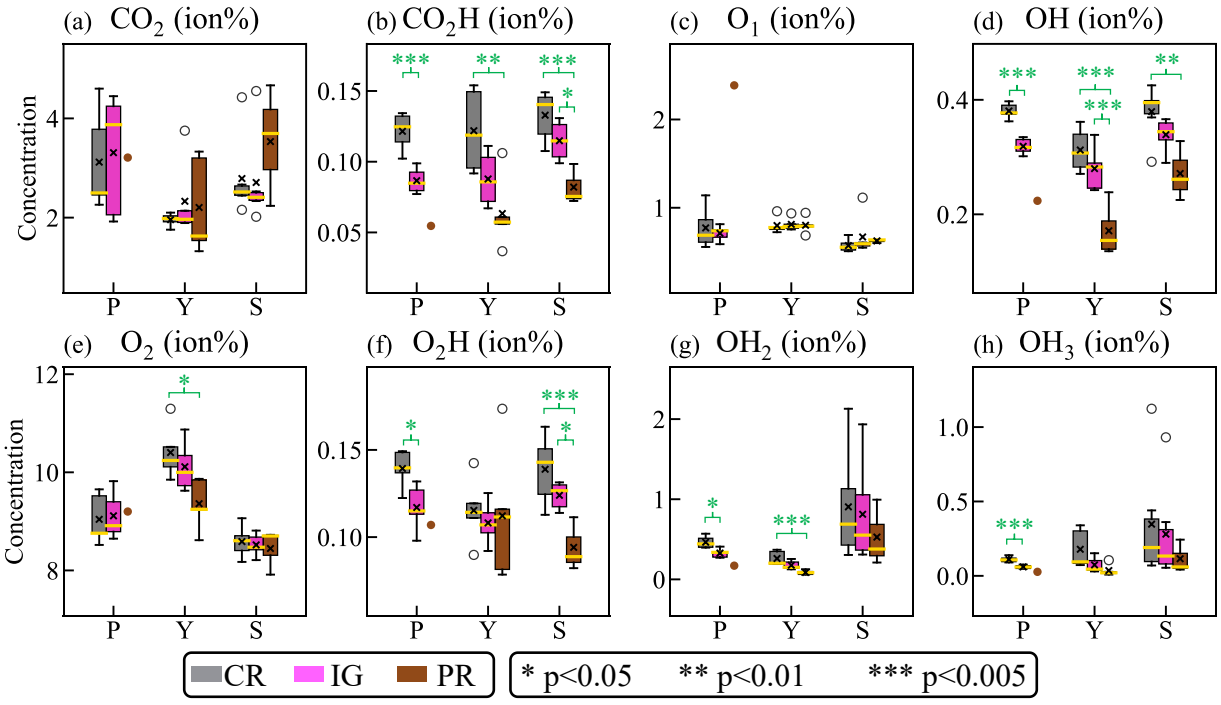

Figure 5.3. Comparison of composition for species which tend to be highest in the crystal phase. *Compositions in ion% are presented for molecular ions (a) CO_2, (b) CO_2H, (c) O_1, (d) OH, (e) O_2, (f) O_2H, (g) OH_2, and (h) OH_3. For each plot, the distribution of compositions for crystal (CR), intergranular (IG), and precipitate (PR) phases are grouped*

according to the tooth they came from: Primary (P), Young (Y), or Senior (S). When n > 2, "x" mark indicates the mean, yellow horizontal bar indicates the mean, the box indicates the interquartile range, whiskers indicate 1.5 times the interquartile range, and outliers are denoted by hollow circles. The level of statistical significance from Tukey post-hoc test is indicated with asterisks and a bracket connecting the two groups being compared. If n ≤ 2, individual data points are shown instead.

Results from this analysis show that we can confidently associate the CO_2H signal with the carbonate substitutions in the HA nanocrystal lattice. Interestingly, there is no significant difference in CO_2 concentration between phases in the primary, young, or senior teeth; the strongest difference was between the IG (2.71 ± 0.84 ion.%) and PR (3.53 ± 1.00 ion%) in Senior enamel. With $p = 0.4771$ (Figure 5.3a), there is no significant difference, but the results appear to resolve a minor conflict in the literature. Taylor et al. successfully used CO_2 molecular ions as a strong indicator of organics (amelogenin protein) adsorbed to the surface of synthetic, non-carbonated HA [46], whereas Fontaine et al. associated CO_2 primarily with carbonate substitutions in the HA of enamel [26]. We propose that CO_2 can have both organic and inorganic origins, while CO_2H is primarily inorganic in nature, at least under the experimental conditions used here (i.e., deep UV laser, target $^{40}Ca^{2+}$:$^{40}Ca^{+}$ CSR of 150). The additional H in the molecular ion is presumably from the abundant hydroxyl groups in HA. But this conflicts somewhat with the conclusion drawn from crocodilian enamel in Chapter 3, where Raman spectroscopy supported the notion that the CO_2 molecular ion could be used to identify inorganic carbonate substitutions. The crocodilian data was collected using an atom probe system equipped with a 355 nm laser wavelength, whereas the present data was collected with a 257.5 nm wavelength. The difference in wavelength can have significant impact on the electric field and thus evaporated ions and measured composition, as illustrated in Chapter 4. Additionally, upon a closer inspection of the

m/z spectra provided in the supplementary information of [26], it appears that peaks at approximately 44 and 45 Da are identified as CO_2, while here they are identified as CO_2 and CO_2H, respectively. Therefore, it is possible that Fontaine's conclusion of CO_2 being associated with inorganic carbonate is due to a hidden contribution from CO_2H.

Of similar behavior, the concentrations of OH and O_2H are generally greatest in the CR phase, as evident in Figure 5.3c-f. Using the senior enamel as an example, the OH concentration in the CR (0.38 ± 0.04 ion%) is significantly greater than in the PR (0.27 ± 0.04 ion%, $p = 0.0062$), while the IG has an intermediate value of 0.34 ± 0.03 ion%. In contrast, there is no significant difference measured in the O_1 concentration between the phases ($p > 0.05$). This relationship mirrors the observation made for CO_2H, namely that the addition of H to a molecular ion (e.g. O_1 or O_2) is more associated with the crystalline HA, presumably due to the abundance of hydroxyl groups in HA.

The IG and PR phases are typically identified as ACP as it is more accommodating of impurity ions (e.g. Mg) [11, 16, 26, 209]. ACP has a variable composition with bound water of the form $Ca_xH_y(PO_4)_z \bullet nH_2O$ ($3 < n < 4.5$) [212]. Therefore, rather than hydroxyl groups, one might expect to see signs of water from molecular ions of OH_2 or OH_3, a common ion associated with water ice in APT [213, 214]. However, OH_2 and OH_3 exhibit trends similar to OH or O_2H, with highest concentration in CR (Figure 5.3g,h). The composition of enamel in vivo includes approximately 3 wt.% water, which would presumably be more likely found in the PR or amorphous IG phases. It is worth noting that the extracted teeth were stored in a vacuum desiccator for a period of several weeks before excising samples, so the presence of unbound water would be expected to be negligible. It could be interesting to study whether OH_2 and OH_3 molecular ions

could be used to measure and locate water content in the IG or PR phase in a hydrated sample. However, in the desiccated samples studied here, OH_2 and OH_3 show a slight tendency to be more prevalent in the mineral CR phase.

We can now turn our attention to those species most prevalent in the organic precipitates, as summarized in Figure 5.4. These will serve as the primary indicator of organic content in Assessments II and III, as well as in future studies. It is envisioned that this knowledge will facilitate interrogations of more thorough and accurate compositional variations related to enamel conditions, disease, or treatments (e.g., aging or caries). In general, the results match expectations from previous APT studies of enamel [26, 115], in particular regarding the elevated concentration of H_1, C_1, N_1, and CO within the precipitate phase (Figure 5.4a-d). The PR phase has significantly greater concentrations of H_1, C_1, and CO molecular ions compared to both the IG and CR phases ($p < 0.005$ for all) in both the young and senior enamel. The same appears true for the primary enamel as well, but falls short of significance. Furthermore, the IG and CR have nearly equivalent average compositions for these species, which are near zero.

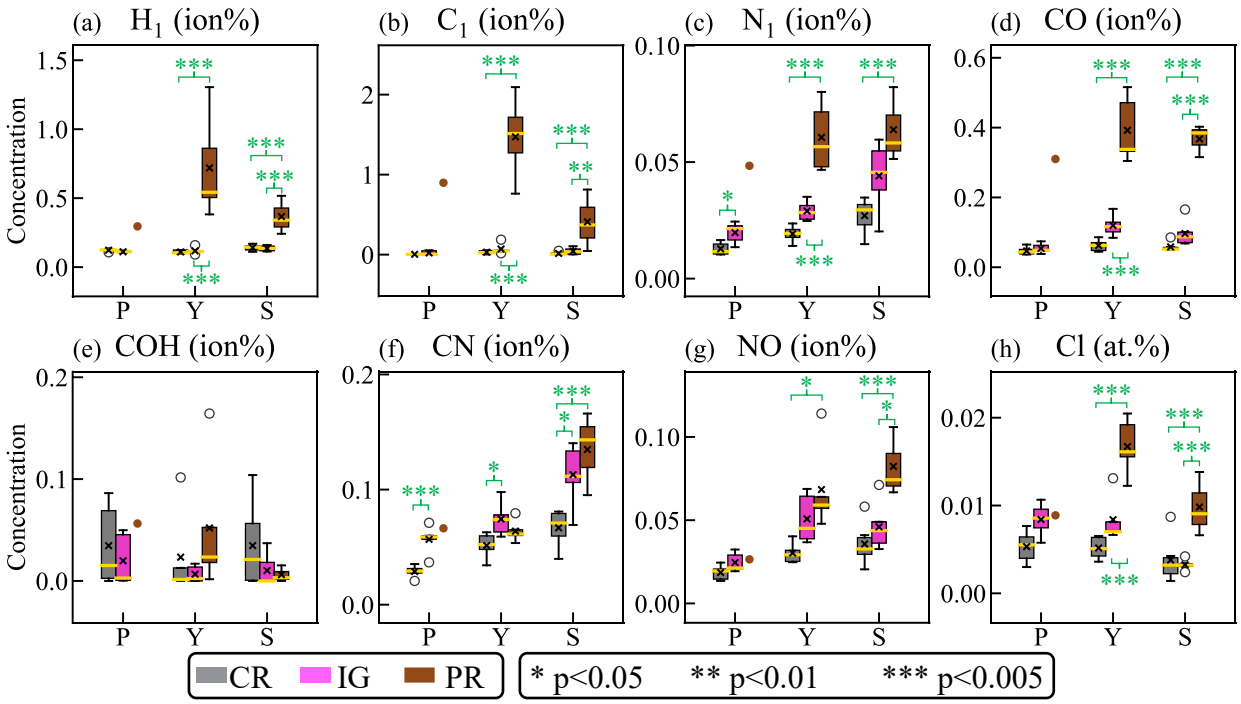

Figure 5.4 Comparison of composition for species which tend to be highest in the precipitate phase. *Compositions are presented in ion% for molecular (a) H_1, (b) C_1, (c) N_1, (d) CO, (e) COH, (f) CN, (g) NO, and in at.% for decomposed counts of (h) Cl. For each plot, the distribution of compositions for crystal (CR), intergranular (IG), and precipitate (PR) phases are grouped according to the tooth they came from: Primary (P), Young (Y), or Senior (S). When n > 2, "x" mark indicates the mean, yellow horizontal bar indicates the mean, the box indicates the interquartile range, whiskers indicate 1.5 times the interquartile range, and outliers are denoted by hollow circles. The level of statistical significance from Tukey post-hoc test is indicated with asterisks and a bracket connecting the two groups being compared. If n ≤ 2, individual data points are shown instead.*

Interestingly, the concentration of COH (m/z ~ 29 Da) was generally low in most measurements, and no significant difference between phases was found (Figure 5.4e). Given that there are plentiful C, O, and H atoms present in proteins, it is surprising that COH is not more abundant in the PR phase. COH is also not significantly elevated in the CR or IG phases, indicating

that it does not represent inorganic carbonate substitutions in the HA lattice as was the case for CO_2H. Fontaine et al. reported that COH molecular ions had a relatively similar spatial distribution to CO and they concluded that both CO and COH could signal both organic and inorganic sources [26]. Our analysis diverges from this conclusion: we find that CO strongly represents the organic precipitate and COH remains inconclusive. Another discrepancy with Fontain et al. is their use of CNO at an m/z of approximately 42 Da as an indicator of the organic phase, whereas here that peak is identified as CaH_2. As mentioned above, differences in electric field experienced by the sample during APT experiments on different instrument setups may be responsible for the disagreement between this work and Fontaine et al. A facile method to compare the evaporation field is through the use of charge state ratios [165]. These experiments were conducted at a $^{40}Ca^{2+}$:$^{40}Ca^{+}$ CSR of 150, while the estimated CSR of the m/z spectra in the supplemental information of Fontaine et al. is ~2100. Hence, the substantial difference in electric fields between the two studies could explain the differing conclusions regarding CO and COH.

Molecular ions containing nitrogen - N_1, CN, and NO - also tend to be elevated in the PR phase, though the tendency is not equally strong or consistent between the three teeth (Figure 5.4c, f, g). In the young tooth, the concentration of N_1 is significantly greater in the PR phase (0.061 ± 0.013 ion%) than in CR (0.019 ± 0.003 ion%, $p < 0.0001$) and IG (0.029 ± 0.004 ion%, $p = 0.0001$) phases. For the senior tooth, the IG has a somewhat elevated concentration of N_1 (0.15 ± 0.03 ion%), meaning the only significant difference is between the PR (0.19 ±0.02 ion%) and CR (0.13 ± 0.03 ion%) phases ($p = 0.0025$). For both young and senior adult enamel, a significant difference is not measured between CR and IG. But in the primary tooth, the IG (0.02 ± 0.01 ion%) has a moderately greater concentration of N_1 than the CR (0.01 ± 0.01 ion%, $p = 0.0359$), although both are considerably less than the value in the PR (0.05 ± 0.01 ion%). Similar

trends are observed for CN and NO (Figure 5.4e, g). Considering N_1, CN, and NO, there is an apparent trend between age groups as well, namely that the senior tooth has a higher nitrogen content than the young and primary teeth, which will be explored in Assessment II.

The molecules in Figure 5.4a-g originate from the carbon-, nitrogen-, and hydrogen-rich residual organic content, which constitutes ~2 wt.% of mature enamel. Presumably, the organic molecules themselves are cleavage products of amelogenin and other enamel matrix proteins that were impinged by surrounding nanocrystals undergoing growth during maturation. Organic molecules in enamel could also have extrinsic origins, introduced by dietary or bacterial secretions, then diffusing into the enamel. However, since these APT samples were extracted near the DEJ, it is less likely for extrinsic organic molecules to have diffused through >1 mm of enamel. Consequently, we consider them to be intrinsic. We speculate that it could be possible to differentiate intrinsic versus extrinsic organic molecules by their composition, but this remains a question for future research and should be performed on samples excised near the OES.

The PR phase also shows a significantly greater concentration of Cl than the CR or IG phases (Figure 5.4h). Cl^- ions serve at least two roles during amelogenesis: (i) they facilitate the modulation of ameloblasts during the maturation stage of amelogenesis; and (ii) they assist in transport of bicarbonate ions to buffer the decreased pH induced by growing HA mineral [83]. Mouse models have shown that a decreased concentration of Cl during amelogenesis results in reduced mineralization of the final tissue [84, 215]. It is also worth noting that the amount of chlorine present in the enamel increases with increasing mineralization [83]. However, Cl incorporation into HA introduces lattice compression, which destabilizes the structure and renders it unfavorable at biological conditions [126]. Thus, the elevated concentration of Cl in the PR

phase reflects that Cl, like residual organic molecules, is insoluble in the growing HA nanocrystals and is driven the same spaces with insoluble precipitates during enamel maturation.

Sodium is another ion which is highly prevalent during amelogenesis, facilitating exchange and transport of Ca into the developing enamel fluid [83]. Thus, it might be expected that it would display similar trends as Cl. However, the only significant difference in Na concentration noted is between the IG (0.83 ± 0.11 ion%) and PR (1.07 ± 0.10 ion%) phases in young enamel ($p = 0.009$). The concentration of Na is relatively high in all three phases for all three teeth (i.e. between 0.75—1.25 ion%) compared to Cl (i.e. between 0.01—0.04 ion%), which provides evidence that HA and the amorphous calcium phosphate have a greater solubility for Na substitutions. In HA, Na^+ substitutes for Ca^{2+}, balancing the charge of CO_3^{2-} substitutions [216]. The increased solubility of Na in HA means less Na would be ejected during mineral growth, resulting in less significant differences between phases.

APT is subject to various sources of error, ranging from the field evaporation physics, to instrument limits, to choices made by the analyst. Regarding field evaporation, post-evaporation ion neutralization [20, 169] can cause signal loss, as the detector is only sensitive to charged ions. The electric field can also play a significant role on which ions are generated and the composition that results (Chapter 4). Additionally, the detector has a detection efficiency < 1 (i.e., 0.52 for the LEAP 6000 XR), which further reduces captured signal. When reconstructing the data, the analyst must define ranges for each peak in the m/z spectrum to ascribe ion identities that are then translated to the reconstruction. How to best define the ranges is a subject of considerable discussion in the APT community [168], though it is generally agreed that a systematic approach to ranging is more precise and accurate than the manual approach. To address these concerns, all

experiments in this study were conducted on the same machine, adjusting the laser pulse energy to maintain a target $^{40}Ca^{2+}$:$^{40}Ca^{+}$ CSR of 150 for each experiment to minimize differences in electric field experienced by different samples [165]. We used an automated "elbow" ranging approach (described in Chapter 4) to adjust a unified base .RRNG file to each m/z spectrum. Nonetheless, the concentration of certain species (i.e., N_1, COH, Cl) is rather low, raising question to the accuracy of comparisons for such dilute species. As described in Appendix 8.4.1, the counting error of a given sample was determined from the Wilson score interval [217], which provides a more realistic estimation of error than the commonly used Poisson counting statistics [218]. When propagated through averaging, the counting error is considerably less than the standard deviation of the samples (Supplementary Figure 11). Therefore, we are confident that the statistical comparisons performed here are robust, even for the low-concentration species. In fact, those species with very low counts in the CR and IG phases (e.g., H_1, N_1, CN, C_1, CO) are made more reliable as they possess nearly negligible concentrations in non-PR phases. Thus, variations in the concentrations of these species should reflect overall changes in the organic content more accurately.

Geometrically, the PR phase can be considered as a subset of the IG phase as both fill the space between nanocrystals. Compositionally, however, the IG presents as more of an intermediate between the organic-rich extreme PR and the nominally fully mineralized CR. For example, the H* concentration of IG and CR are nearly identical (Figure 5.4a), while the concentration of CO_2H is more similar for IG and PR (Figure 5.3b). Furthermore, of the species analyzed, the IG never has a concentration significantly different than both other phases – it is almost always either more similar to one, indeterminate from both, or rarely, significantly different from both but with an intermediate concentration.

One question that remains unanswered is whether the precipitates are relatively constrained (e.g. spherical globules) or extend much further along the length of the nanocrystals. In this study each of the precipitates extended through the width (i.e., field of view) of the APT reconstruction, which is typically on the order of 50 nm. Whether precipitates extend the full length of the adjacent nanocrystals and how they interact with the ends of nanocrystals are reserved for future inquiry.

It is worth mentioning that some amount of $H_{1\text{-}2}$ can be observed in any APT experiment conducted in laser pulsing mode, even if the sample is completely devoid of H. Ambient H_2 gas present in the ultra-high vacuum analysis chamber is readily ionized by the strong electric field near the specimen apex and is registered by the detector as if it had originated from the specimen [219]. However, the strong differences between the phases of enamel suggest that there is real compositional heterogeneity. Furthermore, the presence of H_3 is commonly observed in laser-pulsed APT experiments on hydroxyapatite (Figure 4.1) [22], but not in laser-pulsed experiments of materials without hydrogen (e.g. Si), further emphasizing that the hydrogen signal can serve as a marker of organic content.

5.4.3. Assessment II: Compositional variations associated with tooth age

Armed with an understanding of which molecular ions can be reliably associated with the crystalline and organic phases, we can now compare the three teeth to investigate compositional differences in inner enamel that may be associated with age. Table 5.2 lists the species for which there is a significantly greater amount in that row's phase of that column's tooth than in the same phase for the other teeth tested. It is critical to highlight that the "n = __" values in this table represent the number of APT reconstructions including that phase and that there was only one tooth

each for primary, young, and senior. Therefore, it is impossible to ensure that any differences between teeth are due to age, and not attributable to other factors such as diet, lifestyle, upbringing, ancestry, or inherent biological variation between individuals. Nonetheless, we propose explanations regarding the compositional differences between the three teeth that the statistical analysis enables them to be attributed to age.

Table 5.2. Ion signatures for each age, separated by phase. *Each column lists the ionic species that that are highest in that age (ANOVA with Tukey post-hoc test $p < 0.05$), repeated for each phase. For example, the CR phase in the senior tooth has higher Mg than the CR phase of the young or primary teeth. Elements marked with an * indicate that the significant difference was found for the decomposed concentration of that species. The number n of experiments that captured each age-phase combination are listed in each cell.*

	Primary	Young	Senior
Crystal (CR)	Ca*, Ca_1, OH n = 5	O*, O_2, P*, CH_3, CN, CNH n = 5	OH, H*, H_1, H_2, CH_3, CN, CNH, NO, N_1, Na, Mg, K, CaF, PO_2F n = 6
Intergranular (IG)	Cl n = 5	O_2, P*, Cl, CO, CaF n = 5	OH, H*, H_2, H_3, CH_3, CO_2H, CO_2H_2, N*, CN, CNH, NO, N_1, Na, Mg, K, CaF n = 6
Precipitate (PR)	n = 1	C_1 n = 5	H*, H_3, N*, CN n = 3
Bulk (BU)	Ca_1, Cl, CO_2 n = 5	O*, O_2, P*, C_1, CH_3, CH_5, CO, NO, CaF n = 5	OH, H*, H_2, H_3, C*, CO_2, CH_3, CN, CNH, N*, N_1 Na, Mg, K, CaF n = 6

There are two distinct "ages" that are expected to influence the composition of enamel. The first is the chronological age (CA) of the individuals from whom the teeth came. But perhaps more important is the time since the tooth erupted from the gumline and was directly exposed to the oral cavity, which we will refer to as the "erupted age" of the tooth. We do not have sufficiently detailed

life histories of the donor teeth to definitively evaluate the erupted age for each tooth, but estimates can be made based on typical eruption chronology. The mean eruption time for a North American primary mandibular left second molar is 27 months [220], yielding an erupted age for the primary tooth (CA = 8) of approximately 6 years. Similarly, the mean eruption age for female permanent maxillary third molars has been reported as 18.8 ± 1.8 years, [221]. Rounding to 19 years, this gives an estimated erupted age of 2 years for the young tooth (CA = 21), and 41 for the senior tooth (CA=60). Considering the large spread of potential eruption times, the erupted age for the young tooth could reasonably be between 0 (unerupted) to 4 years. However, given that extraction of unerupted third molars is a common orthodontic procedure to minimize impact with adjacent teeth, and the teeth used for this study were extracted for orthodontic reasons, it is relatively likely that the erupted age of the young tooth is closer to 0. Maturation of human enamel through ameloblast modulation is thought to take as much as four to five years in humans once the enamel thickness is fully defined [62, 222], which could start at approximately 17 years old [221], suggesting that the young tooth may not have fully mineralized by the time of extraction. The primary tooth is also not expected to be fully mineralized, as it erupts long before the requisite maturation time can pass.

Figure 5.5 summarizes a comparison of select element concentrations which are significantly higher in one phase (CR, IG or PR) of a tooth than in the same phase of the other teeth. We begin with signals that are associated with the mineral content. The concentration of CO_2H (Figure 5.5a) is generally consistent for all three teeth, though the concentration in the IG phase of the senior tooth (0.11 ± 0.01 ion%) is significantly greater than that of the young (0.09 ± 0.02 ion%, p = 0.0226) and primary (0.09 ± 0.01 ion%, p = 0.0175) teeth. The difference suggests a higher amount of carbonate groups in the IG phase. A previous study using Raman spectroscopy to compare

primary, young, and senior enamel reported no significant difference in the carbonate content [86], in agreement these APT results. Detection of the slight elevation in the IG phase of the senior tooth requires nanometer-scale resolution, which is far smaller than the laser spot (10s of μm) used in [86]. Indeed, no difference is found when considering the bulk (BU) composition, which includes contributions from all three phases, as assessed by Raman spectroscopy.

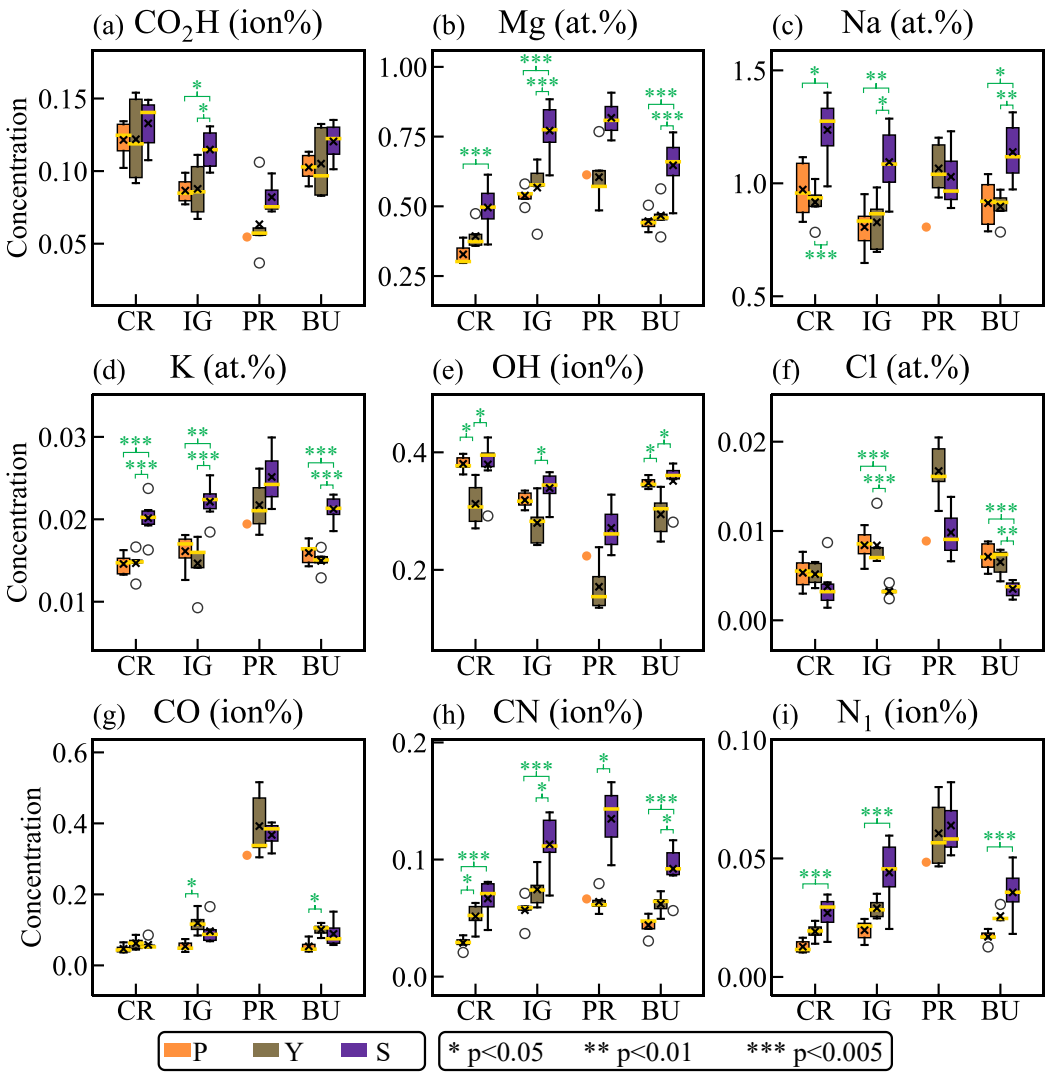

Figure 5.5. Comparison of compositions between teeth, organized by age. *Compositions are presented for (a) CO_2H, (b) Mg, (c) Na, (d) K, (e) OH, (f) Cl, (g) CO, (h)*

CN, and (i) N_1. The vertical axis is in ion% for molecular ions (a, e, g, h, i) and at.% for decomposed species (b, c, d, f) For each plot, the distribution of compositions for crystal (CR), intergranular (IG), and precipitate (PR) phases as well as bulk (BU) are grouped according to the tooth they came from: Primary (P), Young (Y), or Senior (S). When n > 2, "x" mark indicates the mean, yellow horizontal bar indicates the mean, the box indicates the interquartile range, whiskers indicate 1.5 times the interquartile range, and outliers are denoted by hollow circles. The level of statistical significance from Tukey post-hoc test is indicated with asterisks and a bracket connecting the two groups being compared. If n ≤ 2, individual data points are shown instead.

The Mg concentration (Figure 5.5b) is also significantly greater in the senior IG and CR phases relative to the primary, and in the IG phase relative to the young tissue. In Chapter 2, we found that the bulk Mg concentration near the OES was slightly greater for senior enamel than young (Figure 2.3), in agreement with these results near the DEJ. Similarly, the senior enamel has a significantly higher concentration of Na and K (Figure 5.5c-d) than the young and primary enamel in the CR and IG phases as well as in the bulk. These findings suggest an accumulation of Mg, Na, and K occurs over decades. Regarding Na and K, there are two principal paths of incorporation into the lattice: either through surface adsorption and subsequent incorporation into surface sites, or as substitutions during mineral formation [223, 224]. In the former pathway, the concentration of K and Na incorporated into synthetic HA remains relatively constant over time as the hydration layer becomes saturated, with K being slightly less soluble than Na [223]. Observations from *in vitro* reports show that Na can substitute with surface sites of HA, while K does not [224], quite possibly due to the discrepancies in atomic radii between Na (190 pm) and K (243 pm), compared to Ca (194 pm). This trend is also seen in the concentration of K and Na in developing HA: Na is more soluble than K, and furthermore, the developing HA rejects K over

time due to the destabilizing effect [223]. Our data from APT support this, showing typical concentrations of Na at approximately 0.75-1.5 at.% across all three teeth, while K concentration is in the range of 0.01—0.03 at.% (Figure 5.5c-d). As to the origins of these species, both Na and K are essential to amelogenesis [225], providing the opportunity to be incorporated into the developing nanocrystals. However, the tooth is a dynamic environment even after complete maturation and eruption; exposure to additional sources of Na and K is possible through bodily fluids or dietary intake. While Na can exchange with surface sites of HA [224], it could also be possible that de-/re-mineralization cycles facilitate the incorporation of both Na and K into the nanocrystals. Over decades, this process could lead to the elevated levels of Na and K identified in senior inner enamel. However, it is unclear whether the increase in these species is due to inward (i.e., from the oral environment) or outward (i.e., from the pulp chamber) diffusion, and to what extent de-/re-mineralization cycles happen in inner enamel. Investigations of the composition through the thickness of the enamel could reveal the direction of diffusion, as it would be expected to follow an increasing gradient towards the source of the ions. This could in turn help determine the mechanism by which the ions are incorporated.

The concentrations of OH and Cl in Figure 5.5d-e, respectively, convey increasing mineralization over time. For the CR phase, the concentration of OH in both primary (0.38 ± 0.01 ion%) and senior (0.38 ± 0.04) enamel is significantly greater than the young tissue (0.31 ± 0.03 ion%, $p = 0.0285$ and $p = 0.0246$, respectively). The BU measurement shows similar trends, while in the IG, only the senior enamel is significantly greater than the young. Considering that the estimated erupted ages of the primary and senior teeth are 6 and 41 years, respectively, while that of the young tooth is likely between 0-2 years, the OH content could reflect the degree of mineralization. In other words, those teeth which have been erupted for a longer time have more

mineralized nanocrystals, or perhaps nanocrystals with fewer substitutions replacing OH groups. Clearly, additional evidence is necessary to validate the assumption that OH ions detected during APT experiments can indeed be correlated to OH^- ions in the crystal structure. Nonetheless, we have found that the OH molecular ion in APT correlates with the CR phase, suggesting that OH molecular ions do originate from OH^- groups in the crystal.

A compositional change over time can also be inferred from the decreased concentration of Cl in the senior enamel relative to both the young and primary enamel. The bulk concentration of Cl in senior enamel was 0.0035 ± 0.0008 ion%, which is significantly less than that of the young (0.0065 ± 0.0014 ion%, $p = 0.0075$) and primary (0.0071 ± 0.0014 ion%, $p = 0.002$) enamel. In Assessment I, Cl was most strongly associated with the PR phase, so it is tempting to infer that the decrease in Cl reflects removal of organic content overall. However, this is not supported by the concentrations of other organic signatures. As noted earlier, Cl is somewhat soluble in HA, but it destabilizes the crystal structure [126]. One cause for the decreased Cl concentration in senior enamel could be replacement of Cl that is present during development [84] with more favorable groups in the crystal structure, such as OH.

Our initial hypothesis was that the organic content would be diminished in senior enamel relative to both the young and primary enamel, as this would drive the embrittlement of the outermost layer with age [86, 138]. However, when considering CO (Figure 5.5f), the most abundant molecular ion associated with the organic precipitate, there is limited difference between age groups. Only the IG phase of young enamel (0.12 ± 0.03 ion%) has a significantly higher concentration than the primary enamel (0.05 ± 0.01 ion%, $p = 0.0105$), potentially a marker of the young enamel's low erupted age/maturation rather than a loss of organics incurred over decades.

The outer enamel surface is the most exposed to acidic attack and remineralizing solutions, and our results suggest that these cycles have minimal influence on the composition of inner enamel. Further experiments would be needed to estimate the effective depth of de-/re-mineralization cycles.

As evident in Figure 5.4, there were few significant differences in the composition of the PR phase between young and senior permanent enamels. The only molecular ions to exhibit a difference were CN ($p = 0.0114$, Figure 5.5g) and H_3 ($p = 0.0387$); in both cases, the senior enamel had the higher concentration, though only the former is firmly associated with the organic content (from Assessment I, Section 5.4.2). The relative stability of the PR phase between samples across teeth from a wide range of biological and erupted ages suggests that the precipitates are protected by the surrounding densely packed mineral. Hence, they are unable to undergo significant compositional change over time. It is surprising though that the PR composition is so similar for the three teeth. More biological variation would be expected when sampling different individuals, or for the composition of each precipitate to be more unique. However, assuming that formation of the PR phase is due to rejection of insoluble organic compounds from the growing CR and mineralizing IG phases, then the composition of PR is largely controlled by the solubility limits of impurities in HA, which does not rely upon biology. The three teeth sampled in this study were extracted for orthodontic reasons and there was no apparent disease impacting enamel quality. Thus, all three would likely have had nominally similar oral environments during amelogenesis. Furthermore, this model implies that the composition of the PR phase is an artifact of amelogenesis, which reflects the composition of the extracellular organic matrix at the time of mineralization, meaning little variation would be expected over the region of the tissue sampled here across multiple APT measurements (~10 μm). We expect that organic precipitates from teeth

afflicted by abnormal conditions, such as amelogenesis imperfecta, could have distinct compositions reflecting those conditions. Perez-Huerta et al. investigated enamel afflicted by amelogenesis imperfecta using APT [115]. While this article does not describe precipitates, they do report a nearly nine-fold increase in the decomposed C concentration in the amelogenesis imperfecta-afflicted enamel relative to the wild type.

Two organic species of interest remain to discuss, namely CN and N_1 (Figure 5.5h-i). The former was shown in Assessment I to correspond with both the IG and PR phases, while the latter is most strongly associated with PR. When comparing between teeth, it appears that the concentration of both NO and N_1 as well as CO increase with chronological age, particularly in the CR and IG phases, counter to expectations. That the senior CR phase would also show elevated levels of these supposedly organic signals in the CR phase is especially surprising, though the concentrations in CR are still considerably lower than in the PR phase. One potential explanation could be that nitrogen is actually incorporated into HA by substitution of OH^- ions with CN_2^{2-} ions, as has been reported for HA sintered in ammonia gas at 900-1200 °C [226], or incorporation of NO_3^{2-} ions in place of OH^- or PO_4^{3-} as has been achieved by synthetic precipitation [227]. The CN, NO, and N_1 molecular ions detected by APT could then be generated during field evaporation of HA. While it is unclear whether N is significantly incorporated into HA during amelogenesis, an additional route for introduction could be through the cycles of de- and re-mineralization, where N (perhaps as NO_3^{2-} [227]) can be incorporated into new mineral layers. However, the extent to which these cycles play out in the inner enamel, and thus the degree of impurity implantation, seems unlikely to be significant. Yet, it could merit future investigation. Therefore, at this time we are unable to make any definitive explanations regarding the increased N in senior CR.

Our previous study of enamel near the OES described in Chapter 2 found that the IG and shell phases of senior enamel had significantly higher concentrations of F than their young counterparts, an increase attributed to de-/re-mineralization cycles and exposure to fluoride through dental treatments and/or drinking water. While the decomposed concentration of F does not show these trends, the molecular ion CaF does show a slight but significantly higher concentration in senior enamel CR phase than young or primary (Supplementary Figure 12). This could reflect that some F is incorporated over decades even near the DEJ. However, the confidence in this claim would be strengthened by a better understanding of the molecular ions of fluorinated HA under the electric fields achieved in this experiment. Gordon et al., have characterized synthetic and geologic fluorapatite on a LEAP system equipped with a 355 nm wavelength laser [22], which results in considerably different electric fields, as discussed regarding carbonate signals earlier in this chapter. They found CaF to be the most prominent F-containing molecular ion, whereas PO_2F has the highest concentration in the present data. A more systematic study of fluoridated HA would aid in the interpretability of the molecular ions observed in human enamel.

Overall, we find some differences in composition between primary, young, and senior enamel which can be used to infer compositional changes that take place with chronological or erupted age. Most notably, the Mg, Na, and K are elevated in the CR and IG phases of senior enamel, suggesting an accumulation of these substitutional ions in HA over decades. Meanwhile, the OH content is higher for the CR phase of both primary and senior teeth, which were both fully erupted for a longer time than the young enamel, which has a lower OH content. We observe no major compositional differences in the PR phase between age groups, which could be evidence that the organic precipitates are formed from a comparable extracellular environment during amelogenesis, and that they are occluded and remain trapped in the enamel for decades. We observe slight

increases in the concentration of a few N-containing species (e.g., CN, NO, N_1) in senior CR and IG phases, though a definitive explanation for this requires further research.

5.4.4. Assessment III: Attempted removal of organics through NaOCl

To remove organic signals and eliminate ambiguity between molecular ions, we exposed one half of each sample to a 0.35 M NaOCl bleaching solution for 15 days. Our expectation was that it would be straightforward to determine which APT signals belonged to organic material in enamel based on their absence in the treated samples. To minimize variation due to sampling location, APT samples were prepared from the treated half of the tooth at a location directly mirroring the location of samples extracted from the control half (i.e., approximately 125 μm from the lingual dentin horn and 50 μm from the DEJ). The APT datasets were then segmented into CR, IG, and PR phases as before so that the composition of each phase could be compared using an unequal variances t-test within a given tooth to hopefully identify organic species which had been removed. Select comparisons of the control and treated enamel are presented in Figure 5.6.

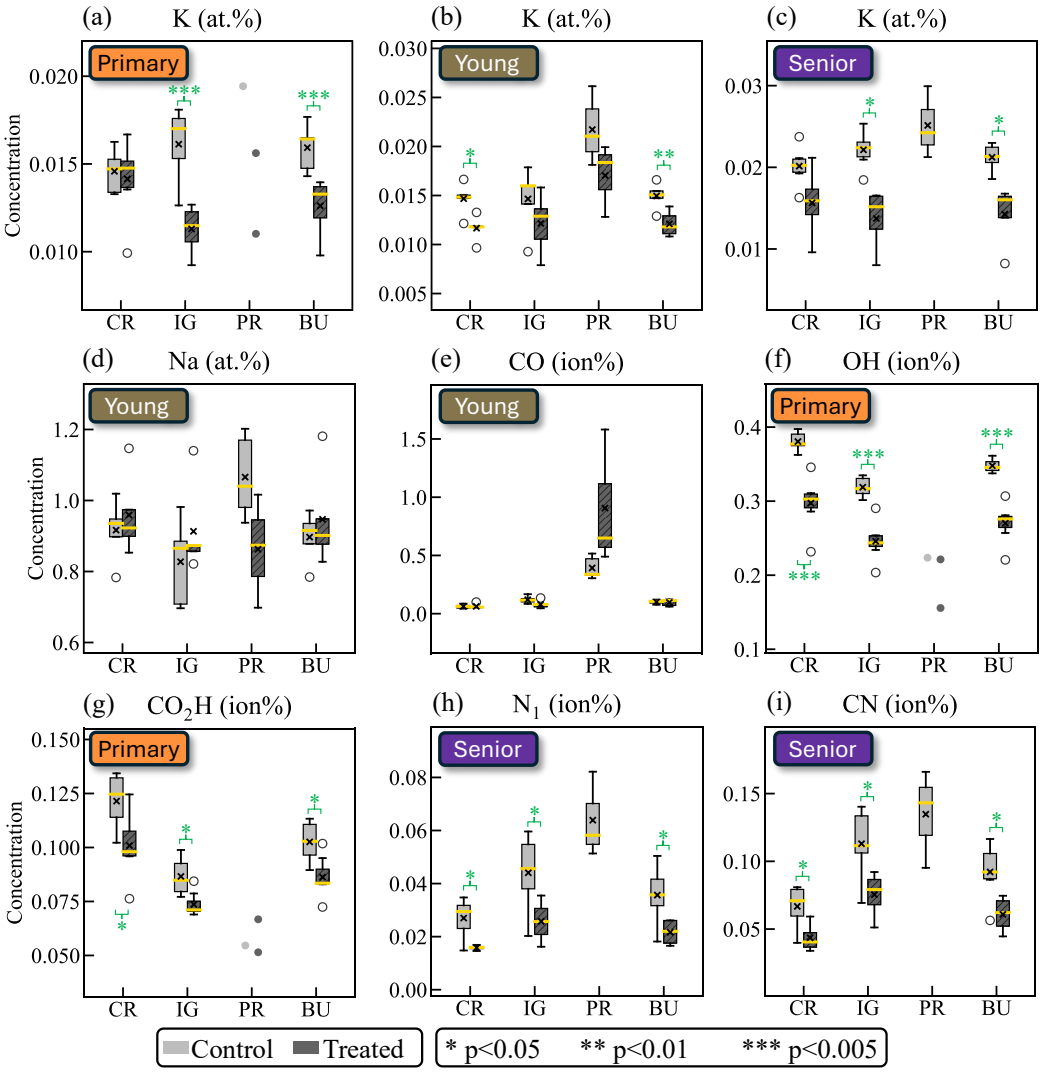

Figure 5.6 Select comparisons of composition between control and NaOCl-treated enamels from primary, young, and senior teeth. *Compositions are presented in at.% for decomposed counts of (a-c) K in primary, young, and senior, (d) Na in young, and in ion% for molecular ions (e) CO in young, (f) OH in primary, (g) CO_2H in primary, (h) N_1 in senior, and (i) CN in senior. For each plot, the distribution of compositions for are grouped by phase: crystal (CR), intergranular (IG), and precipitate (PR), or bulk (BU). When n > 2, "x" mark indicates the mean, yellow horizontal bar indicates the mean, the box indicates the interquartile range, whiskers indicate 1.5 times the interquartile range, and outliers are denoted by hollow circles. The level of statistical significance from Tukey post-hoc test*

is indicated with asterisks and a bracket connecting the two groups being compared. If n ≤ 2, individual data points are shown instead.

As a sanity check of the treatment and its efficacy, we expected the concentration of Na or Cl to increase in the IG and PR phases, as these would be most amenable to impurity ions. However, no significant increase in the Na or Cl concentrations was observed, which could suggest limited flow of the solution through the tissue occurred despite being immersed in the bleaching solution for prolonged period of 15 days (Figure 5.6d). Previous reports of APT performed on outer enamel treated with 0.25 M NaF for 24 hours describe a slight increase in overall Na content between control and treated samples [11], but with two important caveats: (i) it was not reported whether the control and treated data came from the same tooth or same individual and (ii) the range of bulk Na concentrations for treated was 1.4—1.8 at.%, while that for untreated was 0.75—1.6 at.%. Regarding caveat (i), there is presently limited understanding on the degree of variation in enamel composition that can be expected at the nanocrystal scale when comparing between teeth from the same individual or between multiple individuals. And regarding caveat (ii), a wide range of bulk Na concentration in untreated teeth is reported that overlaps with the treated group, and a comparison of the composition in the IG phase specifically is not provided. The range of Na concentrations reported is comparable to that found in the present study. Thus, between [11] and the present study, there are two instances where exposing enamel to an Na-containing solution fails to significantly increase the concentration of Na. A probable explanation is that the enamel was already saturated with Na before exposure to the treatment solution. Considering the control data, the average IG concentration of Na is 0.81—1.09 at.%, which is markedly lower than the ~6 at.% Na expected in the hydration shell of synthetic hydroxyapatite exposed to 80 mM Na, the level present in saliva [228] (calculations presented in Appendix 8.4.2, using data from [224, 228]).

Obviously, nanocrystals in enamel are not exposed to the solution directly but rather are surrounded by the amorphous IG phase. Evidently, this imposes a much lower saturation limit on the amount of Na that can be integrated into the IG phase, and thus even the greatly increased concentration of Na in the bleach solution does not induce a significant change in the Na content of enamel at the nanocrystal scale.

The fact that precipitates are still identified in the primary and young treated teeth, and that there is no significant difference in organic signals (e.g. CO, Figure 5.6e), provides further evidence that the bleaching treatment was ineffective at removing the organic content. Or at the least, if the solution did penetrate the precipitates, there was insufficient flow to extract the organics. Initially, the senior enamel appears to counter this claim, as no precipitates were measured after treatment, implying their complete removal. However, there are two confounding factors. The first is that the datasets of the senior treated enamel were consistently smaller. The average cross-sectional area of the reconstructions once the viewing direction was aligned with the crystal long axis is 0.0168 μm^2 for the treated senior enamel, a 48% reduction from the control (0.0321 μm^2). This results in a smaller total area sampled (0.0670 μm^2 for senior treated compared to 0.1926 μm^2 for control) with less contained per dataset. Precipitates are most easily defined in relation to the context of their local environments, and smaller datasets provide less context.

The second confounding factor is with regards to classification of regions as IG or PR. As illustrated in the reconstruction of senior treated enamel in Figure 5.7, it is not always immediately obvious whether a given region ought to be classified as IG or PR, especially when the region intersects with a boundary of the reconstruction. For example, regions (i), (ii), and (iii) are all considered as IG in this work. Region (i) is the most obvious, as it is rich in Mg and C is relatively

scarce. Region (ii) shows slightly elevated C signal, but it falls between two parallel nanocrystals, rather than strongly concentrated at the junction between three or more nanocrystals as was observed for other precipitates (Figure 5.2b,d,h). Region (iii) could possibly be a precipitate, as it both shows elevated C and is relatively wide, though the full shape and surrounding context were not captured. The morphology alone cannot be relied upon to confidently claim region (iii) as PR, as region (i) has comparable dimensions and is definitively IG. The concentration of C in region (iii) is approximately 0.3 ion%, whereas that of region (ii) is 0.2 ion%, both significantly lower than the range of 0.7-2.0 ion% measured in PR of other samples (Supplementary Figure 11c). For these reasons, region (iii) was also considered as IG in this analysis. However, it remains a possibility that the conditions for classification of a region as PR were too stringent or subjective, showing that unsupervised machine learning algorithms for segmentation of APT datasets hold tremendous potential [229].

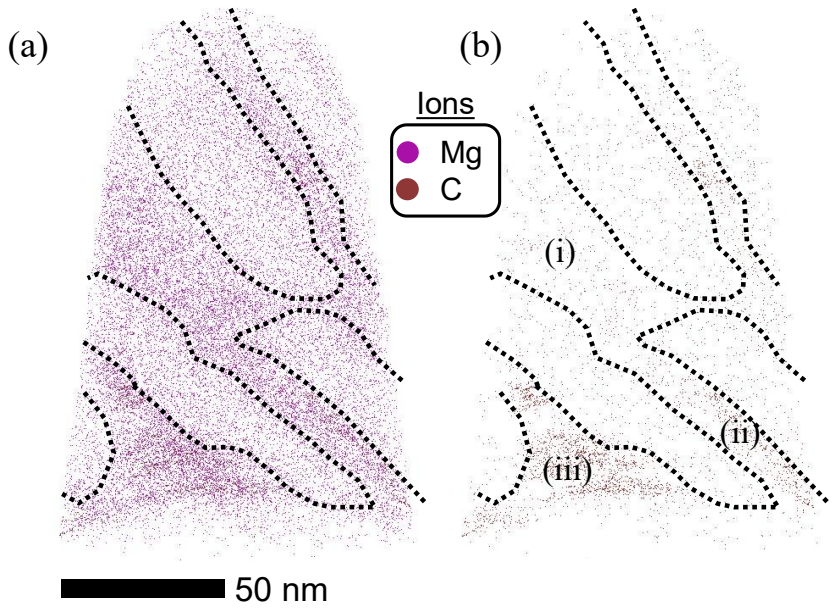

Figure 5.7. Classification of regions in senior treated enamel. *Reconstruction of senior treated enamel with (a) Mg and C ions or (b) only C ions visible. The regions marked with (i), (ii), and (iii) are highlighted and discussed in the text.*

It is worth considering what the frequency of precipitates might be, and whether that can be used as a metric to evaluate treatment efficacy. After all, if organic precipitates were removed by the bleaching treatment, then there would be nothing to compare the composition of. By dividing the number of precipitates captured by the cross sectional (i.e. projected) area for each reconstruction, we can estimate the frequency of precipitate occurrence. These results are presented in Figure 5.8 as number of precipitates per square micrometer, though it is critical to note that due to the small volume of any given reconstruction, it would take approximately 30 – 60 reconstructions to capture a full square micrometer worth of cross sections. Therefore, care must be taken when considering the results. Interestingly, the young control enamel shows a significantly greater frequency (140 ± 45 precipitates/μm^2) than primary control ($p = 0.00132$) or senior control ($p = 0.00341$). This appears to agree with the trend of increased mineralization with

increased erupted age observed when considering the OH concentration (Figure 5.5e). However, this does not necessarily mean that the organic precipitates present in unerupted enamel are lost over time; they might instead coalesce or become dispersed through the IG phase. It is also noteworthy that no significant differences in frequency are found when comparing treated versus control enamel for each tooth, additional evidence that the bleaching treatment did not remove the precipitates.

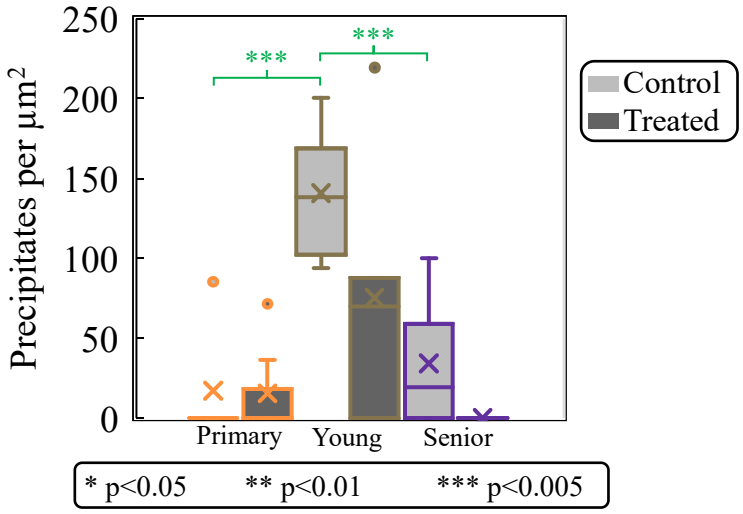

Figure 5.8. Comparison of precipitate frequency in terms of cross-sectional area. *The "x" mark indicates the mean, horizontal bar indicates the mean, the box indicates the interquartile range, whiskers indicate 1.5 times the interquartile range, and outliers are denoted by hollow circles. The level of statistical significance from t-test with unequal variance is indicated with asterisks and a bracket connecting the two groups being compared.*

Potassium was the only element that exhibited a significant decrease in concentration after treatment relative to the control for all three teeth. As discussed in Assessment II, K has a low propensity for substituting into the HA lattice, preferring instead to remain in the hydration layer

[223]. Saliva has a K concentration of 8.9 ± 4.2 mM [228], and after collection at dental clinics, the teeth were stored in Hank's balanced salt solution which contains approximately 5 mM KCl. It is thus likely that the exposure to 0.35 M NaOCl was the first time any of the teeth were exposed to a solution devoid of K for a prolonged time. The adsorption of K in the hydration layer of hydroxyapatite is reversible [224], thus it is plausible that K was removed from the enamel during the solution treatment. A similar decrease in K would be expected if the sample was submerged in distilled water rather than bleach solution, though this has not been tested. It is worth noting that a decrease in K^+ ions ought to be accompanied by an increase in the composition of another cation or a decrease of an anionic species to balance the charge. An increase in Na^+ is a likely candidate, given that it is in great abundance during the bleach treatment, but no significant increase was observed for Na by APT. However, one must consider the magnitude of the concentrations at hand. Using the young enamel BU concentration as an example, K decreased significantly ($p = 0.009$) by 0.0028 at.%, a relative decrease by approximately one-fifth. A corresponding increase of Na concentration (0.90 ± 0.06 at.%) by 0.0028 at.% would be a relative increase by approximately one-thirtieth of the control concentration; that small of a change is an order of magnitude smaller than the standard deviation of the Na concentration and undetectable by the analysis used here. Thus, while it is probable that some additional Na^+ ions are introduced to balance the charge as K^+ is leached from the enamel, this change cannot be detected by the experiments utilized here. Theoretically, isotopically labeled ^{22}Na could be used in the NaOCl solution, to determine whether new Na^+ ions are exchanged into the system, but a competing peak at an m/z = 22 Da from $^{44}Ca^{2+}$ would also present a challenge in detecting this by APT.

While there was only one consistent trend shared by all three teeth, namely the decrease in K concentration, unique trends were found in the changes of each tooth independently. In the case

of the primary tooth, there is a reduction in the BU concentration of OH from 0.35 ± 0.01 to 0.27 ± 0.02 ion% (p = 9.59E-5) and CO_2H from 0.10 ± 0.01 to 0.09 ± 0.01 ion% (p = 0.020). Apart from the BU values, both the CR (p = 0.0004 for OH, p = 0.035 for CO_2H) and IG (p = 0.0001 for OH, p = 0.029 for CO_2H) show the same trend. Based on the findings of Assessment I, these molecular ions are more strongly associated with the hydroxyl and carbonate groups of the mineral phase, suggesting that the bleaching treatment may have partially demineralized the primary enamel. This is apparently possible without direct contact with the fluid, assuming that the IG phase prevents fluid flow around each nanocrystal. However, the amorphous IG phase still permits ion transport [11], which could be sufficient to demineralize the primary enamel. An interesting question is why only the primary enamel is affected in this way, while the permanent enamel (young and senior) does not. Perhaps there is some inherent structural or crystalline difference between primary and permanent enamel that was not captured in the compositional measurements described in Assessment II. Primary enamel is relatively poorly characterized as a materi al relative to the wealth of studies on permanent enamel, so this remains a question for future research.

In the senior enamel, by contrast, there is a reduction in several N-containing molecular ions, particularly N_1 and CN with treatment. As discussed in Assessment II, the exact origin of these molecular ions is not clear, though they are correlated more strongly with the IG and PR phases than the CR which implies they are organic in nature. However, the observed reduction after treatment in both CR and IG phases could indicate an alteration to the mineral phase as well. It is interesting to note that after treatment, the concentration of these N-containing molecular ions becomes more similar to both the control and treated conditions of the young and primary enamel. Specifically, the only dataset with significantly higher concentrations of N-containing molecules is the senior control enamel. That raises to question whether a variable outside of the experiment

could be responsible. Perhaps the data were collected in a short time during which the instrument reported an artificially higher amount of N due to ionization of ambient N in the analysis chamber, which could be caused by a higher pressure in the analysis chamber. Alternatively, perhaps something different was done during sample preparation to introduce more N. As to the first point, Supplementary Figure 13 shows that the background levels, analysis chamber pressure, and date of collection were not anomalous for the senior control or senior treated data relative to the primary and young samples. As to the latter, APT samples were prepared using identical procedures on each half of each tooth, allowing for minor adaptations to ensure each specimen was sharpened to an apex diameter less than 150 nm, all using the same PFIB instrument. As the samples came from spatially matched locations within the same tooth, variations due to sample location should be minimized. We are thus led to believe that the bleaching treatment did cause a real reduction in N concentration in senior enamel. However, the contributing mechanisms are not clear at this time.

There is a peculiar behavior prevalent in the comparisons between the treated and control samples for all three teeth: the strongest compositional trends are equally true for the CR and IG phases, rather than being more pronounced in the IG phase, which is expected to be more amenable to ion transport [11, 13]. A probable explanation for this is that that the constant immersion in NaOCl solution for an extended period of 15 days was sufficient for compositional changes to be realized some depth into the nanocrystal surface as well, which is then captured in the ROIs segmented as CR. Apparently, this is possible through ion exchange with the amorphous calcium phosphate of the IG phase, rather than requiring direct contact between CR and solution. If indeed the IG phase is the mediator for ion exchange, and if the compositional changes in primary (OH, CO_2H) and senior (N_1, CN) enamel are due to said exchange, it could have considerable implications for de-/re-mineralization cycles and the treatment/prevention of caries. As highlighted

by the different responses of primary, young, and senior enamel, composition alone is not the full answer. Structural or crystallographic factors could have an impact on the ability of the IG phase to facilitate ion exchange. The high spatial and compositional resolution of APT has opened the door to begin exploring these research pursuits.

5.4.5. Ca:P ratio

The Ca:P ratio provides another perspective into the mineral composition, with the potential to distinguish mineral phases (e.g., the expected Ca:P for HA is 1.67, while it is 1.33 for octacalcium phosphate, $Ca_8H_2(PO_4)_6$). Of note, systematically understanding the connection between experimental parameters and measured Ca:P ratio was the primary objective of Chapter 4. Yet, the complex field evaporation physics of APT can present a challenge. The lessons learned on synthetic HA can be applied to enamel to improve the accuracy of the Ca:P measurement. The trend line between measured Ca:P ratio and $^{40}Ca^{2+}$:$^{40}Ca^{+}$ CSR (Figure 4.5d, (Eq 4.1)) can be interpreted as a tool to estimate an "error factor" between the known and measured Ca:P ratios by using the experimentally measured CSR to infer what Ca:P ratio would have been measured, then dividing that by the known CSR. For example, a dataset collected with a CSR of 200 would be predicted to yield a Ca:P ratio of 1.736, which can be divided by the empirically measured (by EDS) synthetic HA composition of 1.54 to give an error factor of 1.13 (i.e., a CSR yields a 13% overestimation). The measured Ca:P ratio can then be divided by 1.13 to more accurately estimate the true Ca:P ratio. This approach was applied to each data based on its total $^{40}Ca^{2+}$:$^{40}Ca^{+}$ CSR to produce Figure 5.9.

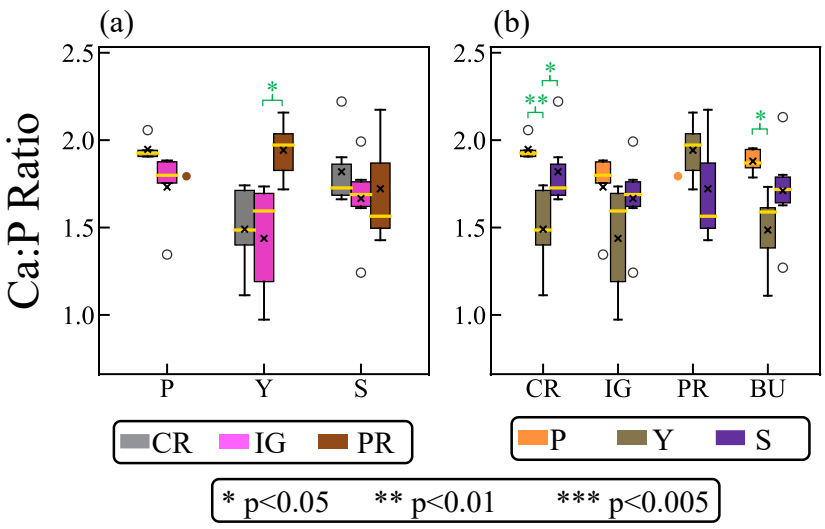

Figure 5.9 Comparison of Ca:P ratio after correction based on CSR. *Comparisons are made (a) between phases within each age and (b) between ages for each phase. When n > 2, "x" mark indicates the mean, yellow horizontal bar indicates the mean, the box indicates the interquartile range, whiskers indicate 1.5 times the interquartile range, and outliers are denoted by hollow circles. The level of statistical significance from Tukey post-hoc test after one-way ANOVA is indicated with asterisks and a bracket connecting the two groups being compared. If n ≤ 2, individual data points are shown instead.*

As evident in Figure 5.9, the mean Ca:P ratios are generally between 1.5 to 2.0, consistent with the expectation that enamel is constituted of HA and not another stoichiometric phase such as octacalcium phosphate or brushite (Ca:P ratio of 1.00). The wide range and higher Ca:P ratios than the stoichiometric 1.67 can be explained by the presence of B-type carbonate substitutions for phosphate groups in the HA lattice [85, 216]. It is expected that the Ca:(P + CO_3) ratio would tend to be closer to 1.67, though this is challenging to achieve as there is no reference APT data for carbonate-substituted HA to calibrate against. The IG phase is believed to be amorphous [16], and as such can have a variable composition. Thus, the estimated Ca:P ratios are deemed

acceptable, but alone are not an effective tool for differentiating between crystalline and amorphous regions.

The average Ca:P ratio was generally consistent between the phases for each tooth, with the only significant difference being between the PR (1.94 ± 0.15) and IG (1.44 ± 0.30) phases for the young enamel (p = 0.0332), shown in Figure 5.9a. Regarding comparisons across teeth and within phases, the CR phase of the young enamel has a significantly lower Ca:P ratio (1.49 ± 0.23) than the primary (1.95 ± 0.06, p = 0.0077) and senior (1.82 ± 0.20, p = 0.0417) enamels (Figure 5.9b). It is challenging to confidently interpret the meaning behind significant differences between the Ca:P ratio between phases or age groups. An elevated Ca:P ratio could be caused by a reduced P concentration due to carbonate substitutions or systematic loss of P during measurement (Figure 4.7). Alternatively, it could be due to increased Ca, which would more likely reflect a decrease in cationic substitutions such as Na, K, or other metals that substitute for Ca in HA. It is interesting that the PR phase has a significantly greater Ca:P ratio than the IG in the young enamel, perhaps reflecting excess Ca ions (or lack of P) trapped in the PR during amelogenesis. However, as the tissue matures, the Ca:P ratio appears to become more homogenous throughout. That could suggest that the precipitate is partially mineralized, though likely it remains amorphous. The fact that the young CR phase has a significantly lower Ca:P ratio than the primary and senior enamels mirrors the observation from OH (Figure 5.5e), potentially reflecting incomplete mineralization due to a lower erupted age. Quantifying the degree of mineralization of individual nanocrystals is a challenging question and pursuit. However, with further controls to better understand the behavior of carbonated HA, these results show that APT could serve as the right tool to provide answers.

5.5. Conclusions

This study presents and analyzes the largest set of APT data from human inner enamel that has been reported to date. Molars from three distinct age groups (primary, young adult, and senior adult) were sectioned into halves along the buccal-lingual plane, subjecting one half of each tooth to a bleaching solution while the other was held as a control. Enamel specimens were then prepared for APT from a spatially matched location in the inner enamel near the lingual dentin horn, where the concentration of organic content was expected to be highest. Employing statistical tests, this dataset provided insight on the crystal morphology, quantitative composition, and properties of inner enamel nanocrystals, assessed in three ways:

- In Assessment I, each APT reconstruction is manually segmented into CR, IG, and PR phases. Signature molecular ions are identified for each phase using one-way analysis of variance to quantify the significance level for each ion. Specifically, OH, O_2H, OH_2, and CO_2H are associated with the CR phase, with the latter reflecting the carbonate substitutions in the HA lattice. Conversely, H_1, C_1, N_1, CO, CN, NO, and Cl ions are found to be most strongly associated with organic precipitates located at some "bad junctions" between nanocrystals. The presence of Cl is evidence that these precipitates originate during the maturation stage of amelogenesis, during which they are rejected from the growing nanocrystals and eventually become encapsulated by adjacent crystals. Lastly, the Mg-rich IG phase generally has an intermediate composition between the CR and IG phases, reinforcing that it is an amorphous phase which can be more accommodating to impurities.
- In Assessment II, comparisons of the phase-specific compositions are instead made between enamel from each age group. Because the samples were extracted from the inner enamel, minimal changes due to extended exposure to the oral environment were expected.

This is indeed the case for most molecular ions. However, the senior enamel was shown to have significantly higher levels of Mg, Na, K, CN, N_1, CO_2H (in the IG phase) and lower levels of Cl. It is possible that ion exchange through the IG phase increases the concentration of these species over decades. However, the possibility that these differences are due to inter-individual variations or lifestyle, rather than only age, cannot be definitively ruled out. Interestingly, the OH concentration of the CR phase is higher in both primary and senior enamels than in young, which is believed to reflect the fact that these teeth would have been erupted for approximately 6 and 40 years respectively, enabling a higher degree of mineralization and maturation than the young enamel, which may have been extracted prior to eruption.

- Finally, in Assessment III, we compare between the treated and control halves of each tooth. The bleaching treatment was hypothesized to fully remove the organic component from the tissue, which would in turn make identification and comparison of inorganic signals simpler. The results did not support this hypothesis, as organic precipitates and molecular ions were still plentiful in the treated enamel; in fact, no significant decrease in organics was consistently observed across all three samples. This suggests that fluid flow did not take place between the nanocrystals, but there is evidence that the amorphous IG phase facilitates ion transport through the enamel. All three teeth showed a decrease in K concentration after exposure to the bleach solution, which is probably a reflection of the fact that the bleach solution did not contain any K and thus did not maintain saturation of K in the tissue. Additionally, a decrease in OH and CO_2H molecular ions could indicate the bleaching solution had a slight demineralizing effect, while a decrease in CN and N_1 in senior enamel highlights that these N-containing molecular ions may be associated with

the mineral rather than solely the organic precipitate. Further research is required to understand why individual teeth were affected in distinct ways; the microstructure, crystal size, properties of the IG phase, or other factors may be responsible.

An additional observation is that none of the nanocrystals sampled near the inner enamel showed Mg-rich cores. This is a surprising departure from previous observations of Mg-rich cores in nanocrystals near the outer surface of human enamel in this work and by others [11]. We hypothesize that the Mg-rich cores become apparent at some point through the enamel thickness, though this, and the question of the significance of the cores, remains a question for future APT and TEM investigations.

In summary, the systematic and statistical approach applied to compositional comparisons here provides nanoscale insight into organic precipitates and mineral in inner enamel and serves as a foundation upon which future investigations can build. With a robust understanding of what each signal reflects, future experiments can quantitatively evaluate the compositional impact of any number of pathologies or treatments applied to enamel specifically, and biominerals in general. Key areas of interest are the fields of amelogenesis imperfecta, where the quality and/or quantity of enamel are deleteriously impacted by genetic mutations which disrupt enamel formation, and caries. The efficacy of certain treatments to e.g. prevent caries or whiten teeth can also be assessed at the nanocrystal level using the approach and results presented here.

6. Conclusions and Future Directions

The primary objective of this dissertation has been to advance the quantitative power of APT for biomineral studies in general and for dental enamel in particular. The efforts have purposefully targeted a common pitfall of studies utilizing APT, namely that few datasets will be reported and limited statistical comparisons will be provided. Reducing uncertainty in APT measurements by employing the methodological and analytical framework developed here to enamel is particularly rewarding, as the feature size of compositional and morphological mineral variations in the tissue are well matched by the resolution and sensitivity of the instrument. Furthermore, careful study of the enamel nanocrystals provides numerous opportunities for better understanding enamel formation, how enamel changes as a function of age or disease, and natural gradients in the enamel structure through the enamel thickness. Knowledge of enamel at this most fundamental scale is essential for developing clinical therapies to promote enamel longevity and oral health as well as for designing biomimetic materials that aim to replicate the impressive properties of enamel. Through development of a protocol to enable statistical comparisons between distinct groups, corroboration with complimentary techniques, and systematic parameter optimization, this dissertation provides new insight into enamel while simultaneously paving the way for future discoveries.

In Chapter 2, APT is used to compare the composition of human outer enamel from young and senior age groups. An analytical protocol is developed whereby 3D APT reconstructions are segmented into three distinct phases corresponding to the cores and shells of hydroxyapatite nanocrystals as well as the amorphous intergranular space separating them. The effort involved meticulously defining ROI volumes in the reconstruction, then combining the m/z spectra from all

the ROIs belonging to the same phase for the same experiment into a single spectrum and analyzing with a custom python script. Additional verification of the phase identity of each ROI is supported by a frequency distribution analysis. Enabled by this effort is a direct application of common statistical tests (i.e., ANOVA and t-test) to lend a degree of quantitative confidence in determining which phases have distinct compositions between the young and senior enamel. The most notable finding here is that the concentration of F was increased in the shell of the senior enamel nanocrystals, which we argue is evidence that cycles of de- and re-mineralization are the primary mechanism for F incorporation in outer enamel over time. Further supporting this notion, we find the senior enamel nanocrystals to be slightly smaller and with a slightly greater separation from each other by the intergranular phase, a result of the imbalance of de-/re-mineralization cycles.

The statistical approach developed in Chapter 2 is also applied to aprismatic crocodilian enamel in Chapter 3, searching for gradients in structure, composition, and properties in conjunction with nanoindentation and Raman spectroscopy. We find that both *C. porosus* and *A. mississippiensis* enamels exhibit a hard, highly mineralized, and less carbonated (i.e., fewer carbonate substitutions in the HA lattice) outermost layer that surrounds a middle and inner enamel, which have virtually no gradient in properties. Those results contrast with mammalian enamel, which tends to show the same overall trend from the outer surface to the DEJ, but as much more gradual and continuous gradients. Interestingly, the complimentary Raman and APT measurements confirm that the CO_2 molecular ion, but not CO, is correlated with carbonate substitutions in the mineral for this system, though CO_2 may also be correlated with organics to some extent.

Chapter 4 describes a systematic exploration of the influence of parameter selection when performing APT on the apparent measured composition for HA. The user-input parameter that arguably has the most direct and important role on field evaporation for electrically insulative materials is the laser pulse, both in terms of the energy delivered per pulse as well as the wavelength of the laser itself. Arguably, the electric field experienced by the sample is the most important parameter, but the laser pulse indirectly controls the field necessary for evaporation through either photoionization or specimen temperature increase. The laser pulse energy can be used to adjust the electric field by targeting a specified charge state ratio. We find that HA undergoes photoionization with the 257.5 nm DUV laser equipped on the newest generation of commercial atom probe systems, whereas it experiences a more "conventional" temperature increase to enable field evaporation under illumination by the 355 nm UV laser. The effect of a simultaneous voltage pulse on the DUV system was also explored, which did somewhat reduce background signal, but also gave rise to unexpected "shoulder" peaks following prominent peaks in the m/z spectra. We conclude that adjusting the laser pulse energy to maintain a target charge state ratio is a reliable and useful method to measure the most consistent and accurate Ca:P ratio. Lastly, we demonstrate how ranging different amounts of the tails behind major peaks in the m/z spectra can have a dramatic effect on the measured composition. We thus present a facile algorithmic approach which adjusts the boundaries of each range to the "elbows" of the peaks, accounting for possible variations in peak form on the leading and tailing sides and mitigating the risk of analyst bias.

The findings and methods developed in the three preceding chapters are applied in Chapter 5, the most thorough assessment of human inner enamel nanocrystals by APT to date. Data was collected using the DUV laser system for which a better understanding of the evaporation and

instrumental errors was established in Chapter 4. APT reconstructions from primary, young, and senior enamels reveal that the inner enamel apparently lacks the Mg-rich nanocrystal cores that have been documented in outer enamel, though organic-rich precipitates at some "bad junctions" between nanocrystals can be observed and quantified. Additionally, the statistical approach developed in Chapter 2 is refined and applied to compare the composition of the nanocrystal, intergranular, and precipitate phases within each tooth as well as between teeth from the distinct age groups. This, combined with a relatively large number of samples, allows confident identification that CO is associated with organic sources, while CO_2H is more strongly associated with inorganic carbonate substitutions in the HA lattice. As the inner enamel is presumably shielded from the most significant effects of de-/re-mineralization cycles, the differences between age groups are subtle. Nonetheless, some trends can be identified, such as the primary and senior enamels exhibit a higher concentration of OH molecular ions in the nanocrystals than young enamel. Based on the erupted age of the teeth used in this study, we interpret the increased OH concentration to reflect a greater degree of mineralization. Similar trends in the Ca:P ratio may support this claim, though further work to understand the significance of the Ca:P ratio for biological carbonated hydroxyapatite is needed to assert such a claim with confidence.

Lastly, we subjected one half of each tooth to an extended bleaching treatment, which did not remove or substantially reduce the organic-rich precipitates and yielded minimal compositional changes except for a reduction in K. We argue that this is a sign that the organic precipitates are fully protected by mineral and that the bleaching solution was unable to flow through the tissue and extract the organics. However, there is evidence that the solution leached K out of the enamel, an interesting sign of ion transport and exchange which is presumably facilitated by the amorphous intergranular phase.

There are a myriad of opportunities for future research, which can expand upon the findings presented in this dissertation and/or apply the techniques developed herein to other questions. Any number of comparative studies between sound enamel and that impacted by disease (e.g., caries, diabetes), lifestyle (e.g., smoking, frequent consumption of acidic beverages), or genetic defects (e.g. amelogenesis imperfecta) can be executed building on the methods described here. One interesting scientific question is regarding the formation of the Mg-rich cores. Apparently, they are present in outer enamel, but not inner enamel (Chapter 5), suggesting that such cores could be developed only after a certain point in the amelogenesis process. A relatively simple study to answer this question would be to extract APT samples from several locations through the enamel thickness along the same trajectory between DEJ to OES to determine at what point the Mg cores appear. The tooth could first be treated with an NaF solution to enhance the contrast between the Mg-rich intergranular phase and the cores of interest.

Another experiment that remains to be performed is an analysis of trace ion diffusion in the outermost few nm or μm of enamel. The outermost enamel is exposed to the most extreme degree of de-/re-mineralization cycling and, therefore, would be expected to have the strongest gradients and most dramatic differences associated with age or oral health conditions. Preliminary APT data shows a measurable decrease in the F concentration in the enamel crystals in just the outermost 1—10 μm. This could be helpful for understanding the formation of subsurface white spot lesions or to design clinical/orthodontic treatments that adhere to the outer surface better.

As shown in this dissertation (particularly Chapters 2 and 3), APT is strongest when it is complimented by other techniques and instruments. Analysis of a large set of data including XRD, SEM, and Raman spectroscopy from the teeth described in Chapter 5 is pending. The results from

that dataset, combined with what is already uncovered by APT in Chapter 5, will improve confidence in the conclusions further.

A final potential application of APT for enamel would be to study the mechanisms and effectiveness of ion transport or co-transport through the mineralized tissue. Enamel is subjected to a large number of trace ionic species every day (e.g., Na, K, Fe, Zn, Sr, etc.), and the presence of the amorphous intergranular phase separating nanocrystals significantly changes how these species interact with and permeate the tissue. Correlation with secondary ion mass spectrometry depth profiling or comparable techniques alongside the nanometer resolution of segmented APT reconstructions is sure to reveal new insights. This also has applications beyond dentistry, as HA is a common host for critical minerals the extraction of which is becoming an increasingly important point of attention globally.

7. References

[1] D. Bajaj and D. D. Arola, "On the R-curve behavior of human tooth enamel," *Biomaterials,* vol. 30, no. 23-24, pp. 4037–4046, 2009, doi: 10.1016/j.biomaterials.2009.04.017.

[2] E. D. Yilmaz, G. A. Schneider, and M. V. Swain, "Influence of structural hierarchy on the fracture behaviour of tooth enamel," *Philosophical Transactions Royal Soc Math Phys Eng Sci,* vol. 373, no. 2038, p. 20140130, 2015, doi: 10.1098/rsta.2014.0130.

[3] R. O. Ritchie, "Toughening materials: enhancing resistance to fracture," *Philosophical Transactions of the Royal Society A,* vol. 379, no. 2203, p. 20200437, 2021, doi: 10.1098/rsta.2020.0437.

[4] T. Yanagisawa and Y. Miake, "High-resolution electron microscopy of enamel-crystal demineralization and remineralization in carious lesions," *Journal of Electron Microscopy,* vol. 52, no. 6, pp. 605–613, 2003, doi: 10.1093/jmicro/52.6.605.

[5] A. Nanci, *Ten Cate's oral histology: development, structure, and function*, 9 ed. Elsevier Inc., 2018.

[6] Z. Liu, Z. Zhang, and R. O. Ritchie, "On the Materials Science of Nature's Arms Race," *Advanced Materials,* vol. 30, no. 32, p. 1705220, 2018, doi: 10.1002/adma.201705220.

[7] J. L. Cuy, A. B. Mann, K. J. Livi, M. F. Teaford, and T. P. Weihs, "Nanoindentation mapping of the mechanical properties of human molar tooth enamel," *Archives of Oral Biology,* vol. 47, no. 4, pp. 281–291, 2002, doi: 10.1016/s0003-9969(02)00006-7.

[8] C. Xu, R. Reed, J. P. Gorski, Y. Wang, and M. P. Walker, "The distribution of carbonate in enamel and its correlation with structure and mechanical properties," *Journal of Materials Science,* vol. 47, no. 23, pp. 8035–8043, 2012, doi: 10.1007/s10853-012-6693-7.

[9] C. Renteria, J. M. Fernández-Arteaga, J. Grimm, E. A. Ossa, and D. Arola, "Mammalian enamel: A universal tissue and diverse source of inspiration," *Acta Biomaterialia,* vol. 136, pp. 402–411, 2021, doi: 10.1016/j.actbio.2021.09.016.

[10] Y. Li *et al.*, "Mechanically Reinforced Artificial Enamel by Mg2+-Induced Amorphous Intergranular Phases," *Acs Nano,* vol. 16, no. 7, pp. 10422–10430, 2022, doi: 10.1021/acsnano.2c00688.

[11] K. A. DeRocher *et al.*, "Chemical gradients in human enamel crystallites," *Nature,* vol. 583, no. 7814, pp. 66–71, 2020, doi: 10.1038/s41586-020-2433-3.

[12] E. Beniash *et al.*, "The hidden structure of human enamel," *Nature Communications,* vol. 10, no. 1, p. 4383, 2019, doi: 10.1038/s41467-019-12185-7.

[13] H. Xiao, J. A. Arsecularatne, J. Zheng, M. J. Hoffman, and Z. Zhou, "Effect of HAP crystallite orientation upon corrosion and tribocorrosion behavior of bovine and human dental enamel," *Corros. Sci.,* vol. 190, p. 109670, 2021, doi: 10.1016/j.corsci.2021.109670.

[14] M. A. R. Buzalaf, A. R. Hannas, and M. T. Kato, "Saliva and dental erosion," *Journal of Applied Oral Science,* vol. 20, no. 5, pp. 493–502, 2012, doi: 10.1590/s1678-77572012000500001.

[15] S. Habelitz, "Materials Engineering by Ameloblasts," *Journal of Dental Research,* vol. 94, no. 6, pp. 759–767, 2015, doi: 10.1177/0022034515577963.

[16] L. M. Gordon, M. J. Cohen, K. W. MacRenaris, J. D. Pasteris, T. Seda, and D. Joester, "Amorphous intergranular phases control the properties of rodent tooth enamel," *Science,* vol. 347, no. 6223, pp. 746–750, 2015, doi: 10.1126/science.1258950.

[17] L. M. Gordon and D. Joester, "Nanoscale chemical tomography of buried organic–inorganic interfaces in the chiton tooth," *Nature,* vol. 469, no. 7329, pp. 194–197, 2011, doi: 10.1038/nature09686.

[18] D. J. Larson, T. J. Prosa, R. M. Ulfig, B. P. Geiser, and T. F. Kelly, "Local Electrode Atom Probe Tomography, A User's Guide," 2013, doi: 10.1007/978-1-4614-8721-0.

[19] A. Devaraj, R. Colby, W. P. Hess, D. E. Perea, and S. Thevuthasan, "Role of Photoexcitation and Field Ionization in the Measurement of Accurate Oxide Stoichiometry by Laser-Assisted Atom Probe Tomography," *The Journal of Physical Chemistry Letters,* vol. 4, no. 6, pp. 993–998, 2013, doi: 10.1021/jz400015h.

[20] D. K. Schreiber, A. N. Chiaramonti, L. M. Gordon, and K. Kruska, "Applicability of post-ionization theory to laser-assisted field evaporation of magnetite," *Applied Physics Letters,* vol. 105, no. 24, p. 244106, 2014, doi: 10.1063/1.4904802.

[21] R. J. H. Morris *et al.*, "Significant Oxygen Underestimation When Quantifying Barium-Doped SrTiO Layers by Atom Probe Tomography," *Microscopy and Microanalysis,* p. ozad144, 2024, doi: 10.1093/micmic/ozad144.

[22] L. M. Gordon, L. Tran, and D. Joester, "Atom Probe Tomography of Apatites and Bone-Type Mineralized Tissues," *Acs Nano,* vol. 6, no. 12, pp. 10667–10675, 2012, doi: 10.1021/nn3049957.

[23] K. A. DeRocher, "The Hierarchical Structure and Graded Chemical Distribution of Human Enamel," 2020. [Online]. Available: https://doi.org/10.21985/n2-1338-nz08

[24] S. Torkornoo, M. Bohner, I. McCarroll, and B. Gault, "Optimization of Parameters for Atom Probe Tomography Analysis of β-Tricalcium Phosphates," *Microscopy and Microanalysis,* vol. 30, no. 6, pp. 1074–1082, 2024, doi: 10.1093/mam/ozae077.

[25] L. M. Gordon and D. Joester, "Mapping residual organics and carbonate at grain boundaries and the amorphous interphase in mouse incisor enamel," *Frontiers in Physiology,* vol. 6, p. 57, 2015, doi: 10.3389/fphys.2015.00057.

[26] A. L. Fontaine, A. Zavgorodniy, H. Liu, R. Zheng, M. Swain, and J. Cairney, "Atomic-scale compositional mapping reveals Mg-rich amorphous calcium phosphate in human dental enamel," *Science Advances,* vol. 2, no. 9, p. e1601145, 2016, doi: 10.1126/sciadv.1601145.

[27] O. Licata, U. Guha, J. D. Poplawsky, N. Aich, and B. Mazumder, "Probing Heterogeneity in Bovine Enamel Composition through Nanoscale Chemical Imaging using Atom Probe Tomography," *Archives of Oral Biology,* vol. 112, p. 104682, 2020, doi: 10.1016/j.archoralbio.2020.104682.

[28] S. Jakob, D. Mayweg, and M. Thuvander, "Ion generation by photoionization and photofield tunneling of electrons during atom probe tomography of thermally grown chromia with deep UV laser light," *Arxiv,* 2024, doi: 10.48550/arxiv.2411.01913.

[29] J. D. Poplawsky, J. Sarker, M. Roldan, and Y. Chen, "Laser Wavelength Dependence on Perovskite Interface Elemental Diffusion During Atom Probe Experiments," *Microscopy and Microanalysis,* vol. 29, no. Supplement_1, pp. 612–613, 2023, doi: 10.1093/micmic/ozad067.297.

[30] G. Daculsi, J. Menanteau, L. M. Kerebel, and D. Mitre, "Length and shape of enamel crystals," *Calcified Tissue International,* vol. 36, no. 1, pp. 550–555, 1984, doi: 10.1007/bf02405364.

[31] M. I. Kay, R. A. Young, and A. S. Posner, "Crystal Structure of Hydroxyapatite," *Nature,* vol. 204, no. 4963, pp. 1050–1052, 1964, doi: 10.1038/2041050a0.

[32] F. Yun *et al.*, "Nanoscale pathways for human tooth decay – Central planar defect, organic-rich precipitate and high-angle grain boundary," *Biomaterials,* vol. 235, p. 119748, 2020, doi: 10.1016/j.biomaterials.2019.119748.

[33] T. E. Popowics, J. M. Rensberger, and S. W. Herring, "Enamel microstructure and microstrain in the fracture of human and pig molar cusps," *Archives of Oral Biology,* vol. 49, no. 8, pp. 595–605, 2004, doi: 10.1016/j.archoralbio.2004.01.016.

[34] C. Renteria, "Structure-Property Relationships in Natural Materials: the Case of Tooth Enamel," PhD, Materials Science and Engineering, Univrsity of Washington, Seattle, WA, 2023. [Online]. Available: http://hdl.handle.net/1773/50858

[35] J. R. Grimm, C. Renteria, S. Mukhopadhyay, A. Devaraj, and D. D. Arola, "Stratification of fluoride uptake among enamel crystals with age elucidated by atom probe tomography," *Commun. Mater.,* vol. 5, no. 1, p. 270, 2024, doi: 10.1038/s43246-024-00709-8.

[36] C. Marsico *et al.*, "Characterizing the Microstructures of Mammalian Enamel by Synchrotron Phase Contrast microCT," *Acta Biomaterialia,* vol. 178, pp. 208–220, 2024, doi: 10.1016/j.actbio.2024.02.038.

[37] D. Guatelli-Steinberg, C. Renteria, J. R. Grimm, I. M. Carpenter, D. D. Arola, and W. S. McGraw, "How mangabey molar form differs under routine vs. fallback hard-object feeding regimes," *PeerJ,* vol. 11, p. e16534, 2023, doi: 10.7717/peerj.16534.

[38] Z. Guo *et al.*, "High Throughput Automated Characterization of Enamel Microstructure using Synchrotron Tomography and Optical Flow Imaging," *Acta Biomaterialia,* vol. 181, pp. 263–271, 2024, doi: 10.1016/j.actbio.2024.04.033.

[39] D. Bajaj and D. Arola, "Role of prism decussation on fatigue crack growth and fracture of human enamel," *Acta Biomaterialia,* vol. 5, no. 8, pp. 3045–3056, 2009, doi: 10.1016/j.actbio.2009.04.013.

[40] N. Zhang, X. Wang, W. Xiang, Y. Zhong, F. Yan, and B. Jiang, "Hierarchy structure and fracture mechanisms of the wild wolf tusk's enamel," *Mater Sci Eng C,* vol. 106, p. 110277, 2019, doi: 10.1016/j.msec.2019.110277.

[41] J. M. Rensberger, "Enamel microstructrual specialization in the canine of the spotted hyena, Crocuta crocuta," *Scanning Microscopy,* vol. 13, no. 2-3, pp. 341–361, 1999.

[42] T. C. Hunt *et al.*, "Microstructurally driven self-sharpening mechanism in beaver incisor enamel facilitates their capacity to fell trees," *Acta Biomaterialia,* 2023, doi: 10.1016/j.actbio.2022.12.051.

[43] A. d. Plessis *et al.*, "Beautiful and Functional: A Review of Biomimetic Design in Additive Manufacturing," *Additive Manufacturing,* vol. 27, pp. 408–427, 2019, doi: 10.1016/j.addma.2019.03.033.

[44] M. Yahyazadehfar, D. Bajaj, and D. D. Arola, "Hidden contributions of the enamel rods on the fracture resistance of human teeth," *Acta Biomaterialia,* vol. 9, no. 1, pp. 4806–4814, 2013, doi: 10.1016/j.actbio.2012.09.020.

[45] K. Grandfield, C. Micheletti, J. Deering, G. Arcuri, T. Tang, and B. Langelier, "Atom Probe Tomography for Biomaterials and Biomineralization," *Acta Biomaterialia,* vol. 148, pp. 44–60, 2022, doi: 10.1016/j.actbio.2022.06.010.

[46] S. D. Taylor *et al.*, "Resolving protein-mineral interfacial interactions during in vitro mineralization by atom probe tomography," *Materials Today Advances,* vol. 18, p. 100378, 2023, doi: 10.1016/j.mtadv.2023.100378.

[47] G. M. Erickson *et al.*, "Insights into the ecology and evolutionary success of crocodilians revealed through bite-force and tooth-pressure experimentation," *PLOS ONE,* vol. 7, no. 3, p. e31781, 2012, doi: 10.1371/journal.pone.0031781.

[48] J. Enax, H.-O. Fabritius, A. Rack, O. Prymak, D. Raabe, and M. Epple, "Characterization of crocodile teeth: Correlation of composition, microstructure, and hardness," *Journal of Structural Biology,* vol. 184, no. 2, pp. 155–163, 2013, doi: 10.1016/j.jsb.2013.09.018.

[49] P. M. Sander, "Development, Function and Evolution of Teeth," pp. 92–106, 2000, doi: 10.1017/cbo9780511542626.007.

[50] K. C. Sellers, A. B. Schmiegelow, and C. M. Holliday, "The significance of enamel thickness in the teeth of Alligator mississippiensis and its diversity among crocodyliforms," *J Zool,* vol. 309, no. 3, pp. 172–181, 2019, doi: 10.1111/jzo.12707.

[51] P. Wu *et al.*, "Specialized stem cell niche enables repetitive renewal of alligator teeth," *Proceedings of the National Academy of Sciences,* vol. 110, no. 22, pp. E2009–E2018, 2013, doi: 10.1073/pnas.1213202110.

[52] J. W. Finger, P. C. Thomson, and S. R. Isberg, "A pilot study to understand tooth replacement in near-harvest farmed saltwater crocodiles (Crocodylus porosus): Implications for blemish induction," *Aquaculture,* vol. 504, pp. 102–106, 2019, doi: 10.1016/j.aquaculture.2019.01.060.

[53] G. M. Erickson, "Toothlessness in American Alligators, Alligator Mississippiensis," *Copeia,* vol. 1996, no. 3, p. 739, 1996, doi: 10.2307/1447542.

[54] O. Vallcorba *et al.*, "Synchrotron X-ray microdiffraction to study dental structures in Cretaceous crocodylomorphs," *Cretaceous Res,* p. 104960, 2021, doi: 10.1016/j.cretres.2021.104960.

[55] E. D. Yilmaz, S. Bechtle, H. Özcoban, J. A. Kieser, M. V. Swain, and G. A. Schneider, "Micromechanical characterization of prismless enamel in the tuatara, Sphenodon punctatus," *Journal of the Mechanical Behavior of Biomedical Materials,* vol. 39, pp. 210–217, 2014, doi: 10.1016/j.jmbbm.2014.07.024.

[56] H. B. Wen and J. Moradian-Oldak, "Modification of calcium–phosphate coatings on titanium by recombinant amelogenin," *Journal of Biomedical Materials Research Part A,* vol. 64A, no. 3, pp. 483–490, 2003, doi: 10.1002/jbm.a.10401.

[57] F. Meyer *et al.*, "Hydroxyapatite as Remineralization Agent for Children's Dental Care," *Front. Dent. Med.,* vol. 3, p. 859560, 2022, doi: 10.3389/fdmed.2022.859560.

[58] H. Zhao, Q. Zhang, and J. Chu, "Effect of phosphate group on remineralization of early enamel caries regulated by amelogenin peptide," *PLOS ONE,* vol. 19, no. 5, p. e0303147, 2024, doi: 10.1371/journal.pone.0303147.

[59] J. P. Simmer, A. S. Richardson, Y.-Y. Hu, C. E. Smith, and J. C.-C. Hu, "A post-classical theory of enamel biomineralization… and why we need one," *International Journal of Oral Science,* vol. 4, no. 3, pp. 129–134, 2012, doi: 10.1038/ijos.2012.59.

[60] D. L. Franklin, N. J. Severs, and E. Katchburian, "Development of the distal end and Tomes' processes of ameloblasts observed by freeze-fracture and ultrathin section electron microscopy," *Journal of anatomy,* vol. 174, pp. 103–14, 1991.

[61] A. Boyde, "The Development of Enamel Structure," *J. R. Soc. Med.,* vol. 60, no. 9, pp. 923–928, 1967, doi: 10.1177/003591576706000965.

[62] C. E. Smith, "Cellular and Chemical Events During Enamel Maturation," *Critical Reviews in Oral Biology & Medicine,* vol. 9, no. 2, pp. 128–161, 1998, doi: 10.1177/10454411980090020101.

[63] J. Moradian-Oldak, "Protein-mediated Enamel Mineralization," *Front. Biosci.,* vol. 17, no. 7, p. 1996, 2012, doi: 10.2741/4034.

[64] V. Uskoković, M. K. Kim, W. Li, and S. Habelitz, "Enzymatic processing of amelogenin during continuous crystallization of apatite," *Journal of Materials Research,* vol. 23, no. 12, pp. 3184–3195, 2008, doi: 10.1557/jmr.2008.0387.

[65] G. W. Buchko, R. J. Arachchige, J. Tao, B. J. Tarasevich, and W. J. Shaw, "Identification of major matrix metalloproteinase-20 proteolytic processing products of murine amelogenin and tyrosine-rich amelogenin peptide using a nuclear magnetic resonance spectroscopy based method," *Archives of Oral Biology,* vol. 93, pp. 187–194, 2018, doi: 10.1016/j.archoralbio.2018.06.001.

[66] S. Akkineni *et al.*, "Amyloid-like amelogenin nanoribbons template mineralization via a low-energy interface of ion binding sites," *Proceedings of the National Academy of Sciences,* vol. 119, no. 19, p. e2106965119, 2022, doi: 10.1073/pnas.2106965119.

[67] A. G. Fincham *et al.*, "Evidence for Amelogenin "Nanospheres" as Functional Components of Secretory-Stage Enamel Matrix," *Journal of Structural Biology,* vol. 115, no. 1, pp. 50–59, 1995, doi: 10.1006/jsbi.1995.1029.

[68] A. G. Fincham *et al.*, "Self-Assembly of a Recombinant Amelogenin Protein Generates Supramolecular Structures," *Journal of Structural Biology,* vol. 112, no. 2, pp. 103–109, 1994, doi: 10.1006/jsbi.1994.1011.

[69] S. T. Mergelsberg, H. Kim, G. W. Buchko, and B. Ginovska, "SAXS of murine amelogenin identifies a persistent dimeric species from pH 5.0 to 8.0," *Journal of Structural Biology,* vol. 216, no. 4, p. 108131, 2024, doi: 10.1016/j.jsb.2024.108131.

[70] A. R. E. Santo, J. D. Bartlett, C. W. Gibson, Y. Li, A. B. Kulkarni, and S. R. P. Line, "Amelogenin- and Enamelysin (Mmp-20)-Deficient Mice Display Altered Birefringence in the Secretory-Stage Enamel Organic Extracellular Matrix," *Connective Tissue Research,* vol. 48, no. 1, pp. 39–45, 2009, doi: 10.1080/03008200601059175.

[71] Y. Hu, C. E. Smith, A. S. Richardson, J. D. Bartlett, J. C. C. Hu, and J. P. Simmer, "MMP20, KLK4, and MMP20/KLK4 double null mice define roles for matrix proteases during dental

enamel formation," *Molecular Genetics & Genomic Medicine,* vol. 4, no. 2, pp. 178–196, 2016, doi: 10.1002/mgg3.194.

[72] Y. Bai *et al.*, "Protein nanoribbons template enamel mineralization," *Proceedings of the National Academy of Sciences,* vol. 117, no. 32, pp. 19201–19208, 2020, doi: 10.1073/pnas.2007838117.

[73] C. E. Smith, Y. Hu, A. S. Richardson, J. D. Bartlett, J. C. C. Hu, and J. P. Simmer, "Relationships between protein and mineral during enamel development in normal and genetically altered mice," *European Journal of Oral Sciences,* vol. 119, no. s1, pp. 125–135, 2011, doi: 10.1111/j.1600-0722.2011.00871.x.

[74] J. Tao *et al.*, "Control of Calcium Phosphate Nucleation and Transformation through Interactions of Enamelin and Amelogenin Exhibits the “Goldilocks Effect”," *Crystal Growth & Design,* vol. 18, no. 12, pp. 7391–7400, 2018, doi: 10.1021/acs.cgd.8b01066.

[75] E. Beniash, R. A. Metzler, R. S. K. Lam, and P. U. P. A. Gilbert, "Transient amorphous calcium phosphate in forming enamel," *Journal of Structural Biology,* vol. 166, no. 2, pp. 133–143, 2009, doi: 10.1016/j.jsb.2009.02.001.

[76] N.-Y. Shin *et al.*, "Amelogenin phosphorylation regulates tooth enamel formation by stabilizing a transient amorphous mineral precursor," *Journal of Biological Chemistry,* vol. 295, no. 7, pp. 1943–1959, 2020, doi: 10.1074/jbc.ra119.010506.

[77] H. Ding, H. Pan, X. Xu, and R. Tang, "Toward a Detailed Understanding of Magnesium Ions on Hydroxyapatite Crystallization Inhibition," *Crystal Growth & Design,* vol. 14, no. 2, pp. 763–769, 2014, doi: 10.1021/cg401619s.

[78] S. Fukumoto *et al.*, "Ameloblastin is a cell adhesion molecule required for maintaining the differentiation state of ameloblasts," *J Cell Biology,* vol. 167, no. 5, pp. 973–983, 2004, doi: 10.1083/jcb.200409077.

[79] N. C. Kegulian, G. Visakan, R. A. Bapat, and J. Moradian-Oldak, "Ameloblastin and its multifunctionality in amelogenesis: a review," *Matrix Biology,* 2024, doi: 10.1016/j.matbio.2024.05.007.

[80] G. Visakan, J. Su, and J. Moradian-Oldak, "Ameloblastin promotes polarization of ameloblast cell lines in a 3-D cell culture system," *Matrix Biology,* 2021, doi: 10.1016/j.matbio.2021.11.002.

[81] G. Daculsi and B. Kerebel, "High-resolution electron microscope study of human enamel crystallites: Size, shape, and growth," *J. Ultrastruct. Res.,* vol. 65, no. 2, pp. 163–172, 1978, doi: 10.1016/s0022-5320(78)90053-9.

[82] C. E. Smith and H. Warshawsky, "Quantitative analysis of cell turnover in the enamel organ of the rat incisor. Evidence for ameloblast death immediately after enamel matrix secretion," *The Anatomical Record,* vol. 187, no. 1, pp. 63–97, 1977, doi: 10.1002/ar.1091870106.

[83] A. L. J. J. Bronckers, "Ion Transport by Ameloblasts during Amelogenesis," *Journal of Dental Research,* vol. 96, no. 3, pp. 243–253, 2017, doi: 10.1177/0022034516681768.

[84] A. L. J. J. Bronckers, D. Lyaruu, R. Jalali, J. F. Medina, B. Zandieh-Doulabi, and P. K. DenBesten, "Ameloblast Modulation and Transport of Cl−, Na+, and K+ during Amelogenesis," *Journal of Dental Research,* vol. 94, no. 12, pp. 1740–1747, 2015, doi: 10.1177/0022034515606900.

[85] P. Wang, E. J. D. Anderson, E. A. Muller, F. Gao, Y. Zhong, and M. B. Raschke, "Hyper-spectral Raman imaging correlating chemical substitution and crystallinity in biogenic hydroxyapatite: Dentin and enamel in normal and hypoplastic human teeth," *J Raman Spectrosc,* vol. 49, no. 9, pp. 1559–1567, 2018, doi: 10.1002/jrs.5419.

[86] C. Renteria, W. Yan, Y. L. Huang, and D. D. Arola, "Contributions to enamel durability with aging: An application of data science tools," *Journal of the Mechanical Behavior of Biomedical Materials,* vol. 129, p. 105147, 2022, doi: 10.1016/j.jmbbm.2022.105147.

[87] E. C. Moreno, M. Kresak, and R. T. Zahradnik, "Fluoridated Hydroxyapatite Solubility and Caries Formation," *Nature,* vol. 247, no. 5435, pp. 64–65, 1974, doi: 10.1038/247064a0.

[88] J. M. t. Cate and M. A. R. Buzalaf, "Fluoride Mode of Action: Once There Was an Observant Dentist," *Journal of Dental Research,* vol. 98, no. 7, pp. 725–730, 2019, doi: 10.1177/0022034519831604.

[89] F. Barthelat, "Nacre from mollusk shells: a model for high-performance structural materials," *Bioinspir Biomim,* vol. 5, no. 3, p. 035001, 2010, doi: 10.1088/1748-3182/5/3/035001.

[90] F. Song, A. K. Soh, and Y. L. Bai, "Structural and mechanical properties of the organic matrix layers of nacre," *Biomaterials,* vol. 24, no. 20, pp. 3623–3631, 2003, doi: 10.1016/s0142-9612(03)00215-1.

[91] J. Q. I. Chua, D. V. Srinivasan, S. Idapalapati, and A. Miserez, "Fracture toughness of the stomatopod dactyl club is enhanced by plastic dissipation: A fracture micromechanics study," *Acta Biomaterialia,* vol. 126, pp. 339–349, 2021, doi: 10.1016/j.actbio.2021.03.025.

[92] J. C. Weaver *et al.*, "The Stomatopod Dactyl Club: A Formidable Damage-Tolerant Biological Hammer," *Science,* vol. 336, no. 6086, pp. 1275–1280, 2012, doi: 10.1126/science.1218764.

[93] S. N. Garner *et al.*, "The role of collagen in the dermal armor of the boxfish," *J Mater Res Technology,* 2020, doi: 10.1016/j.jmrt.2020.09.090.

[94] D. Arola *et al.*, "The limiting layer of fish scales: Structure and properties," *Acta Biomaterialia,* vol. 67, no. Philos. Trans. R. Soc. London A Math. Phys. Eng. Sci. 365 2007, pp. 319–330, 2017, doi: 10.1016/j.actbio.2017.12.011.

[95] M. E. Launey and R. O. Ritchie, "On the Fracture Toughness of Advanced Materials," *Advanced Materials,* vol. 21, no. 20, pp. 2103–2110, 2009, doi: 10.1002/adma.200803322.

[96] E. Munch, M. E. Launey, D. H. Alsem, E. Saiz, A. P. Tomsia, and R. O. Ritchie, "Tough, Bio-Inspired Hybrid Materials," *Science,* vol. 322, no. 5907, pp. 1516–1520, 2008, doi: 10.1126/science.1164865.

[97] W. Huang *et al.*, "Multiscale Toughening Mechanisms in Biological Materials and Bioinspired Designs," *Advanced Materials,* vol. 31, no. 43, p. 1901561, 2019, doi: 10.1002/adma.201901561.

[98] S. Park, D. H. Wang, D. Zhang, E. Romberg, and D. Arola, "Mechanical properties of human enamel as a function of age and location in the tooth," *Journal of Materials Science: Materials in Medicine,* vol. 19, no. 6, pp. 2317–2324, 2008, doi: 10.1007/s10856-007-3340-y.

[99] L.-H. He, Z.-H. Yin, L. J. v. Vuuren, E. A. Carter, and X.-W. Liang, "A natural functionally graded biocomposite coating – Human enamel," *Acta Biomaterialia,* vol. 9, no. 5, pp. 6330–6337, 2013, doi: 10.1016/j.actbio.2012.12.029.

[100] X. Wang, N. Zhang, Y. Zhong, F. Yan, and B. Jiang, "Wild boar's tusk enamel: Structure and mechanical behavior," *Mater Sci Eng C,* vol. 100, no. J. Am. Ceram. Soc. 73 2005, pp. 354–362, 2019, doi: 10.1016/j.msec.2019.03.017.

[101] G. B. D. D. Collaborators *et al.*, "Global, regional, and national incidence, prevalence, and years lived with disability for 328 diseases and injuries for 195 countries, 1990–2016: a systematic analysis for the Global Burden of Disease Study 2016," *Lancet,* vol. 390, no. 10100, pp. 1211–1259, 2017, doi: 10.1016/s0140-6736(17)32154-2.

[102] F. Meyer and J. Enax, "Early Childhood Caries: Epidemiology, Aetiology, and Prevention," *International Journal of Dentistry,* vol. 2018, p. 1415873, 2018, doi: 10.1155/2018/1415873.

[103] A. K. Y. Chan, M. Tamrakar, C. M. Jiang, E. C. M. Lo, K. C. M. Leung, and C. H. Chu, "A Systematic Review on Caries Status of Older Adults," *Int. J. Environ. Res. Public Heal.,* vol. 18, no. 20, p. 10662, 2021, doi: 10.3390/ijerph182010662.

[104] D. Bajaj, A. Nazari, N. Eidelman, and D. D. Arola, "A comparison of fatigue crack growth in human enamel and hydroxyapatite," *Biomaterials,* vol. 29, no. 36, pp. 4847–4854, 2008, doi: 10.1016/j.biomaterials.2008.08.019.

[105] J. J. Kruzic, M. Hoffman, and J. A. Arsecularatne, "Fatigue and wear of human tooth enamel: A review," *Journal of the Mechanical Behavior of Biomedical Materials,* vol. 138, p. 105574, 2022, doi: 10.1016/j.jmbbm.2022.105574.

[106] N. B. Pitts *et al.*, "Dental caries," *Nat. Rev. Dis. Prim.,* vol. 3, no. 1, p. 17030, 2017, doi: 10.1038/nrdp.2017.30.

[107] M. Shahmoradi, B. Wan, Z. Zhang, M. Swain, and Q. Li, "Mechanical failure of posterior teeth due to caries and occlusal wear- A modelling study," *Journal of the Mechanical Behavior of Biomedical Materials,* vol. 125, p. 104942, 2022, doi: 10.1016/j.jmbbm.2021.104942.

[108] W. Yan, C. Renteria, Y. Huang, and D. D. Arola, "A machine learning approach to investigate the materials science of enamel aging," *Dental Materials,* vol. 37, no. 12, pp. 1761–1771, 2021, doi: 10.1016/j.dental.2021.09.006.

[109] M. Yahyazadehfar, D. Zhang, and D. Arola, "On the importance of aging to the crack growth resistance of human enamel," *Acta Biomaterialia,* vol. 32, pp. 264–274, 2016, doi: 10.1016/j.actbio.2015.12.038.

[110] J. W. Ager *et al.*, "On the Increasing Fragility of Human Teeth With Age: A Deep-UV Resonance Raman Study," *J Bone Miner Res,* vol. 21, no. 12, pp. 1879–1887, 2006, doi: 10.1359/jbmr.060816.

[111] J. Cunha-Cruz *et al.*, "Salivary characteristics and dental caries Evidence from general dental practices," *J Am Dent Assoc,* vol. 144, no. 5, pp. e31–e40, 2013, doi: 10.14219/jada.archive.2013.0159.

[112] M. Yahyazadehfar, J. Ivancik, H. Majd, B. An, D. Zhang, and D. Arola, "On the Mechanics of Fatigue and Fracture in Teeth," *Appl Mech Rev,* vol. 66, no. 3, p. 030803, 2014, doi: 10.1115/1.4027431.

[113] P. M. Gignac and G. M. Erickson, "Ontogenetic changes in dental form and tooth pressures facilitate developmental niche shifts in American alligators," *J Zool,* vol. 295, no. 2, pp. 132–142, 2015, doi: 10.1111/jzo.12187.

[114] A. Devaraj *et al.*, "Three-dimensional nanoscale characterisation of materials by atom probe tomography," *Int Mater Rev,* vol. 63, no. 2, pp. 1–34, 2017, doi: 10.1080/09506608.2016.1270728.

[115] A. Perez-Huerta, P. Alvarez-Lloret, M. Yamauti, E. Samajpati, L. D. Lanza, and C. Cappelli, "Characterization of tooth with amelogenesis imperfecta (AI) by atom probe tomography," *MRS Adv.,* pp. 1–12, 2024, doi: 10.1557/s43580-024-00914-0.

[116] R. Z. Legeros, T. Sakae, C. Bautista, M. Retino, and J. P. Legeros, "Magnesium and Carbonate in Enamel and Synthetic Apatites," *Advances in Dental Research,* vol. 10, no. 2, pp. 225–231, 1996, doi: 10.1177/08959374960100021801.

[117] B. He *et al.*, "Mineral densities and elemental content in different layers of healthy human enamel with varying teeth age," *Archives of Oral Biology,* vol. 56, no. 10, pp. 997–1004, 2011, doi: 10.1016/j.archoralbio.2011.02.015.

[118] C. A. Hemingway, D. M. Parker, M. Addy, and M. E. Barbour, "Erosion of enamel by non-carbonated soft drinks with and without toothbrushing abrasion," *Br. Dent. J.,* vol. 201, no. 7, pp. 447–450, 2006, doi: 10.1038/sj.bdj.4814073.

[119] R. Free, K. DeRocher, R. Xu, D. Joester, and S. R. Stock, "A method for mapping submicron-scale crystallographic order/disorder applied to human tooth enamel," *Powder Diffr.,* vol. 35, no. 2, pp. 117–123, 2020, doi: 10.1017/s0885715620000251.

[120] A. Arafa, S. S. Filfilan, and H. A. Fansa, "Erosive effect of beverages on surface hardness and ultra-structure of deciduous teeth enamel," *Pediatric Dent J,* vol. 32, no. 3, pp. 186–192, 2022, doi: 10.1016/j.pdj.2022.08.001.

[121] J. Min *et al.*, "Investigation on the Gradient Nanomechanical Behavior of Dental Fluorosis Enamel," *Nanoscale Res Lett,* vol. 13, no. 1, p. 347, 2018, doi: 10.1186/s11671-018-2768-y.

[122] S. Houari *et al.*, "Multi-scale characterization of Developmental Defects of Enamel and their clinical significance for diagnosis and treatment," *Acta Biomaterialia,* vol. 169, pp. 155–167, 2023, doi: 10.1016/j.actbio.2023.08.011.

[123] Y. Sa *et al.*, "Compositional, structural and mechanical comparisons of normal enamel and hypomaturation enamel," *Acta Biomaterialia,* vol. 10, no. 12, pp. 5169–5177, 2014, doi: 10.1016/j.actbio.2014.08.023.

[124] C. d. C. A. Lopes, P. H. J. O. Limirio, V. R. Novais, and P. Dechichi, "Fourier transform infrared spectroscopy (FTIR) application chemical characterization of enamel, dentin and bone," *Appl. Spectrosc. Rev.,* vol. 53, no. 9, pp. 747–769, 2018, doi: 10.1080/05704928.2018.1431923.

[125] J. Chen *et al.*, "Effects of fluorine on the structure of fluorohydroxyapatite: a study by XRD, solid-state NMR and Raman spectroscopy," *Journal of Materials Chemistry B,* vol. 3, no. 1, pp. 34–38, 2014, doi: 10.1039/c4tb01561d.

[126] G. C. Maiti and F. Freund, "Incorporation of chlorine into hydroxy-apatite," *J. Inorg. Nucl. Chem.,* vol. 43, no. 11, pp. 2633–2637, 1981, doi: 10.1016/0022-1902(81)80589-1.

[127] M. P. Moody, L. T. Stephenson, A. V. Ceguerra, and S. P. Ringer, "Quantitative binomial distribution analyses of nanoscale like-solute atom clustering and segregation in atom probe tomography data," *Microscopy Research and Technique,* vol. 71, no. 7, pp. 542–550, 2008, doi: 10.1002/jemt.20582.

[128] Y. Zhang, W. Zhu, F. Hui, M. Lanza, T. Borca-Tasciuc, and M. M. Rojo, "A Review on Principles and Applications of Scanning Thermal Microscopy (SThM)," *Advanced Functional Materials,* vol. 30, no. 18, p. 1900892, 2020, doi: 10.1002/adfm.201900892.

[129] M. Lin, Q. D. Liu, T. Kim, F. Xu, B. F. Bai, and T. J. Lu, "A new method for characterization of thermal properties of human enamel and dentine: Influence of microstructure," *Infrared Phys. Technol.,* vol. 53, no. 6, pp. 457–463, 2010, doi: 10.1016/j.infrared.2010.09.004.

[130] B. Kerebel, G. Daculsi, and L. M. Kerebel, "Ultrastructural Studies of Enamel Crystallites," *Journal of Dental Research,* vol. 58, no. 2_suppl, pp. 844–851, 1979, doi: 10.1177/00220345790580023701.

[131] C. Leiva-Sabadini, C. M. A. P. Schuh, N. P. Barrera, and S. Aguayo, "Ultrastructural characterisation of young and aged dental enamel by atomic force microscopy," *Journal of Microscopy,* vol. 288, no. 3, pp. 185–192, 2022, doi: 10.1111/jmi.13126.

[132] A. E. Porter *et al.*, "A transmission electron microscopy study of mineralization in age-induced transparent dentin," *Biomaterials,* vol. 26, no. 36, pp. 7650–7660, 2005, doi: 10.1016/j.biomaterials.2005.05.059.

[133] J. H. Kinney, R. K. Nalla, J. A. Pople, T. M. Breunig, and R. O. Ritchie, "Age-related transparent root dentin: mineral concentration, crystallite size, and mechanical properties," *Biomaterials,* vol. 26, no. 16, pp. 3363–3376, 2005, doi: 10.1016/j.biomaterials.2004.09.004.

[134] Y. Miake, Y. Saeki, M. Takahashi, and T. Yanagisawa, "Remineralization effects of xylitol on demineralized enamel," *Journal of Electron Microscopy,* vol. 52, no. 5, pp. 471–476, 2003, doi: 10.1093/jmicro/52.5.471.

[135] R. A. Young, W. V. d. Lugt, and J. C. Elliott, "Mechanism for Fluorine Inhibition of Diffusion in Hydroxyapatite," *Nature,* vol. 223, no. 5207, pp. 729–730, 1969, doi: 10.1038/223729a0.

[136] E. C. Munksgaard and C. Bruun, "Determination of fluoride in superficial enamel biopsies from human teeth by means of gas chromatography," *Archives of Oral Biology,* vol. 18, no. 6, pp. 735–743, 1973, doi: 10.1016/0003-9969(73)90009-5.

[137] S. Isaac, F. Brudevold, F. A. Smith, and D. E. Gardner, "The Relation of Fluoride in the Drinking Water to the Distribution of Fluoride in Enamel," *Journal of Dental Research,* vol. 37, no. 2, pp. 318–325, 1958, doi: 10.1177/00220345580370021801.

[138] M. Yahyazadehfar and D. Arola, "The role of organic proteins on the crack growth resistance of human enamel," *Acta Biomaterialia,* vol. 19, pp. 33–45, 2015, doi: 10.1016/j.actbio.2015.03.011.

[139] S. Park, J. B. Quinn, E. Romberg, and D. Arola, "On the brittleness of enamel and selected dental materials," *Dental Materials,* vol. 24, no. 11, pp. 1477–1485, 2008, doi: 10.1016/j.dental.2008.03.007.

[140] J. W. Osborn, "On the control of tooth replacement in reptiles and its relationship to growth," *J Theor Biol,* vol. 46, no. 2, pp. 509–527, 1974, doi: 10.1016/0022-5193(74)90012-5.

[141] G. M. Erickson, A. K. Lappin, and K. A. Vliet, "The ontogeny of bite-force performance in American alligator (Alligator mississippiensis)," *J Zool,* vol. 260, no. 3, pp. 317–327, 2003, doi: 10.1017/s0952836903003819.

[142] W. C. Oliver and G. M. Pharr, "An improved technique for determining hardness and elastic modulus using load and displacement sensing indentation experiments," *Journal of Materials Research,* vol. 7, no. 6, pp. 1564–1583, 1992, doi: 10.1557/jmr.1992.1564.

[143] N. Vargas-Becerril, R. García-García, and J. Reyes-Gasga, "Structural Changes in Human Teeth after Heating up to 1200°C in Argon Atmosphere," *Mater Sci Appl,* vol. 09, no. 07, pp. 637–656, 2018, doi: 10.4236/msa.2018.97046.

[144] E. Pucéat, B. Reynard, and C. Lécuyer, "Can crystallinity be used to determine the degree of chemical alteration of biogenic apatites?," *Chem Geol,* vol. 205, no. 1-2, pp. 83–97, 2004, doi: 10.1016/j.chemgeo.2003.12.014.

[145] L. Zhang *et al.*, "Raman spectral, elemental, crystallinity, and oxygen-isotope variations in conodont apatite during diagenesis," *Geochimica et Cosmochimica Acta,* vol. 210, pp. 184–207, 2017, doi: 10.1016/j.gca.2017.04.036.

[146] P. Felfer *et al.*, "An Atom Probe with Ultra-Low Hydrogen Background," *Microscopy and Microanalysis,* vol. 28, no. 4, pp. 1255–1263, 2022, doi: 10.1017/s1431927621013702.

[147] D. E. Perea *et al.*, "Atom Probe Tomographic Mapping Directly Reveals the Atomic Distribution of Phosphorus in Resin Embedded Ferritin," *Scientific Reports,* vol. 6, no. 1, p. 22321, 2016, doi: 10.1038/srep22321.

[148] K. Teraoka, A. Ito, K. Maekawa, K. Onuma, T. Tateishi, and S. Tsutsumi, "Mechanical Properties of Hydroxyapatite and OH-carbonated Hydroxyapatite Single Crystals," *Journal of Dental Research,* vol. 77, no. 7, pp. 1560–1568, 1998, doi: 10.1177/00220345980770071201.

[149] H. Pan and B. W. Darvell, "Effect of Carbonate on Hydroxyapatite Solubility," *Crystal Growth & Design,* vol. 10, no. 2, pp. 845–850, 2010, doi: 10.1021/cg901199h.

[150] C. E. Smith, M. D. McKee, and A. Nanci, "Cyclic Induction and Rapid Movement of Sequential Waves of New Smooth-Ended Ameloblast Modulation Bands in Rat Incisors as Visualized By Polychrome Fluorescent Labeling and Gbha-Staining of Maturing Enamel," *Advances in Dental Research,* vol. 1, no. 2, pp. 162–175, 1987, doi: 10.1177/08959374870010020401.

[151] G. M. Erickson, "Daily deposition of dentine in juvenile Alligator and assessment of tooth replacement rates using incremental line counts," *Journal of Morphology,* vol. 228, no. 2, pp. 189–194, 1996, doi: 10.1002/(sici)1097-4687(199605)228:2<189::aid-jmor7>3.0.co;2-0.

[152] C. Robinson, J. Kirkham, S. J. Brookes, W. A. Bonass, and R. C. Shore, "The chemistry of enamel development," *Int J Dev Biology,* vol. 39, no. 1, pp. 145–52, 1995.

[153] H. Ida-Yonemochi, K. Otsu, H. Harada, and H. Ohshima, "Functional Expression of Sodium-Dependent Glucose Transporter in Amelogenesis," *Journal of Dental Research,* vol. 99, no. 8, pp. 977–986, 2020, doi: 10.1177/0022034520916130.

[154] B. Gault *et al.*, "Design of a femtosecond laser assisted tomographic atom probe," *Rev. Sci. Instrum.,* vol. 77, no. 4, p. 043705, 2006, doi: 10.1063/1.2194089.

[155] T. F. Kelly and J. A. Panitz, "The First Fifty Years of Atom Probe," *Microscopy Today,* vol. 25, no. 3, pp. 12–17, 2017, doi: 10.1017/s155192951700044x.

[156] G. L. Kellogg and T. T. Tsong, "Pulsed-laser atom-probe field-ion microscopy," *Journal of Applied Physics,* vol. 51, no. 2, pp. 1184–1193, 1980, doi: 10.1063/1.327686.

[157] S. M. Reddy *et al.*, "Atom Probe Tomography: Development and Application to the Geosciences," *Geostand. Geoanalytical Res.,* vol. 44, no. 1, pp. 5–50, 2020, doi: 10.1111/ggr.12313.

[158] A. Cerezo, C. R. M. Grovenor, and G. D. W. Smith, "Pulsed laser atom probe analysis of semiconductor materials," *Journal of Microscopy,* vol. 141, no. 2, pp. 155–170, 1986, doi: 10.1111/j.1365-2818.1986.tb02712.x.

[159] T. F. Kelly, K. Thompson, E. A. Marquis, and D. J. Larson, "Atom Probe Tomography Defines Mainstream Microscopy at the Atomic Scale," *Microscopy Today,* vol. 14, no. 4, pp. 34–41, 2006, doi: 10.1017/s1551929500050264.

[160] J. Bunton, J. Olson, D. Lenz, D. J. Larson, and T. F. Kelly, "Optimized Laser Thermal Pulsing of Atom Probe Tomography: LEAP 4000X™," *Microscopy and Microanalysis,* vol. 16, no. S2, pp. 10–11, 2010, doi: 10.1017/s1431927610060241.

[161] R. Ulfig *et al.*, "New Product Announcement – LEAP 6000XR, New Applications, New Performance," *Microscopy and Microanalysis,* vol. 28, no. S1, pp. 3190–3191, 2022, doi: 10.1017/s1431927622011849.

[162] A. N. Chiaramonti *et al.*, "Field Ion Emission in an Atom Probe Microscope Triggered by Femtosecond-Pulsed Coherent Extreme Ultraviolet Light," *Microscopy and Microanalysis,* vol. 26, no. 2, pp. 258–266, 2020, doi: 10.1017/s1431927620000203.

[163] B. W. Caplins, A. N. Chiaramonti, J. M. Garcia, N. A. Sanford, and L. Miaja-Avila, "Atom probe tomography using an extreme ultraviolet trigger pulse," *Rev. Sci. Instrum.,* vol. 94, no. 9, p. 093704, 2023, doi: 10.1063/5.0160797.

[164] D. R. Kingham, "The post-ionization of field evaporated ions: A theoretical explanation of multiple charge states," *Surface Science,* vol. 116, no. 2, pp. 273–301, 1982, doi: 10.1016/0039-6028(82)90434-4.

[165] L. Tegg, L. T. Stephenson, and J. M. Cairney, "Estimation of the Electric Field in Atom Probe Tomography Experiments Using Charge State Ratios," *Microscopy and Microanalysis,* vol. 30, no. 3, pp. 466–475, 2024, doi: 10.1093/mam/ozae047.

[166] L. Zhao *et al.*, "Optimizing Atom Probe Analysis with Synchronous Laser Pulsing and Voltage Pulsing," *Microscopy and Microanalysis,* vol. 23, no. 2, pp. 221–226, 2017, doi: 10.1017/s1431927616012666.

[167] D. J. Larson, T. J. Prosa, D. Reinhard, R. M. Ulfig, M. Holman, and D. Lenz, "Simultaneous Voltage and Laser Pulsing in Atom Probe Tomography," *Microscopy and Microanalysis,* vol. 28, no. S1, pp. 718–720, 2022, doi: 10.1017/s1431927622003336.

[168] F. Meisenkothen, D. V. Samarov, I. Kalish, and E. B. Steel, "Exploring the accuracy of isotopic analyses in atom probe mass spectrometry," *Ultramicroscopy,* vol. 216, p. 113018, 2020, doi: 10.1016/j.ultramic.2020.113018.

[169] B. Gault *et al.*, "Behavior of molecules and molecular ions near a field emitter," *New Journal of Physics,* vol. 18, no. 3, p. 033031, 2016, doi: 10.1088/1367-2630/18/3/033031.

[170] D. Santhanagopalan *et al.*, "Effects of laser energy and wavelength on the analysis of LiFePO4 using laser assisted atom probe tomography," *Ultramicroscopy,* vol. 148, pp. 57–66, 2015, doi: 10.1016/j.ultramic.2014.09.004.

[171] P. Parikh, H. Chung, E. Vo, A. Banerjee, Y. S. Meng, and A. Devaraj, "Nanoscale Compositional Mapping of Commercial LiNi0.8Co0.15Al0.05O2 Cathodes Using Atom Probe Tomography," *The Journal of Physical Chemistry C,* vol. 126, no. 34, pp. 14380–14388, 2022, doi: 10.1021/acs.jpcc.2c01217.

[172] S. Jakob, A. Fazi, and M. Thuvander, "Laser-Assisted Field Evaporation of Chromia with Deep Ultraviolet Laser Light," *Microscopy and Microanalysis,* p. ozae111, 2024, doi: 10.1093/mam/ozae111.

[173] M. Kühbach *et al.*, "Community-Driven Methods for Open and Reproducible Software Tools for Analyzing Datasets from Atom Probe Microscopy," *Microscopy and Microanalysis,* vol. 28, no. 4, pp. 1038–1053, 2022, doi: 10.1017/s1431927621012241.

[174] D. Hudson, G. D. W. Smith, and B. Gault, "Optimisation of mass ranging for atom probe microanalysis and application to the corrosion processes in Zr alloys," *Ultramicroscopy,* vol. 111, no. 6, pp. 480–486, 2011, doi: 10.1016/j.ultramic.2010.11.007.

[175] B. Gault *et al.*, "Atom probe tomography," *Nature Reviews Methods Primers,* vol. 1, no. 1, p. 51, 2021, doi: 10.1038/s43586-021-00047-w.

[176] A. Vella, "On the interaction of an ultra-fast laser with a nanometric tip by laser assisted atom probe tomography: A review," *Ultramicroscopy,* vol. 132, pp. 5–18, 2013, doi: 10.1016/j.ultramic.2013.05.016.

[177] Y. Xia, J. Liu, X. Zhang, and R. Zhou, "Theoretical Insights into Energy Absorption and Charge Draining during Field Evaporation Assisted by Femtosecond Laser Pulses," *The Journal of Physical Chemistry A,* vol. 125, no. 42, pp. 9338–9345, 2021, doi: 10.1021/acs.jpca.1c06523.

[178] A. Vella *et al.*, "High-resolution terahertz-driven atom probe tomography," *Science Advances,* vol. 7, no. 7, p. eabd7259, 2021, doi: 10.1126/sciadv.abd7259.

[179] A. J. London, "Quantifying Uncertainty from Mass-Peak Overlaps in Atom Probe Microscopy," *Microscopy and Microanalysis,* vol. 25, no. 2, pp. 378–388, 2019, doi: 10.1017/s1431927618016276.

[180] S. D. Taylor *et al.*, "Visualizing the iron atom exchange front in the Fe(II)-catalyzed recrystallization of goethite by atom probe tomography," *Proceedings of the National Academy of Sciences,* vol. 116, no. 8, pp. 2866–2874, 2019, doi: 10.1073/pnas.1816620116.

[181] M. Bachhav, F. Danoix, B. Hannoyer, J. M. Bassat, and R. Danoix, "Investigation of O-18 enriched hematite (α-Fe2O3) by laser assisted atom probe tomography," *International Journal of Mass Spectrometry,* vol. 335, pp. 57–60, 2013, doi: 10.1016/j.ijms.2012.10.012.

[182] M. Bachhav, R. Danoix, F. Danoix, B. Hannoyer, S. Ogale, and F. Vurpillot, "Investigation of wüstite (Fe1−xO) by femtosecond laser assisted atom probe tomography," *Ultramicroscopy,* vol. 111, no. 6, pp. 584–588, 2011, doi: 10.1016/j.ultramic.2010.11.023.

[183] S. D. Taylor, J. Liu, B. W. Arey, D. K. Schreiber, D. E. Perea, and K. M. Rosso, "Resolving Iron(II) Sorption and Oxidative Growth on Hematite (001) Using Atom Probe Tomography," *The Journal of Physical Chemistry C,* vol. 122, no. 7, pp. 3903–3914, 2018, doi: 10.1021/acs.jpcc.7b11989.

[184] X. Zhao and D. Joester, "Characterization of mineralized tissues by atom probe tomography," *Journal of Materials Research,* pp. 1–12, 2024, doi: 10.1557/s43578-024-01472-9.

[185] J. Xu *et al.*, "Advanced materials for enamel remineralization," *Front. Bioeng. Biotechnol.,* vol. 10, p. 985881, 2022, doi: 10.3389/fbioe.2022.985881.

[186] J. Houard, A. Vella, F. Vurpillot, and B. Deconihout, "Three-dimensional thermal response of a metal subwavelength tip under femtosecond laser illumination," *Physical Review B,* vol. 84, no. 3, p. 033405, 2011, doi: 10.1103/physrevb.84.033405.

[187] M. Schiester *et al.*, "Effects of laser wavelength and pulse energy on the evaporation behavior of TiN coatings in atom probe tomography: A multi-instrument study," *Ultramicroscopy,* vol. 270, p. 114105, 2025, doi: 10.1016/j.ultramic.2025.114105.

[188] J. Tao *et al.*, "Energetic basis for the molecular-scale organization of bone," *Proceedings of the National Academy of Sciences,* vol. 112, no. 2, pp. 326–331, 2015, doi: 10.1073/pnas.1404481112.

[189] T. T. Tsong, "Pulsed-laser-stimulated field ion emission from metal and semiconductor surfaces: A time-of-flight study of the formation of atomic, molecular, and cluster ions," *Physical Review B,* vol. 30, no. 9, pp. 4946–4961, 1984, doi: 10.1103/physrevb.30.4946.

[190] C. Cappelli and A. Pérez-Huerta, "Testing the Influence of Laser Pulse Energy and Rate in the Atom Probe Tomography Analysis of Minerals," *Microscopy and Microanalysis,* vol. 29, no. 3, pp. 1137–1152, 2023, doi: 10.1093/micmic/ozad057.

[191] Cameca, "Appendix D," in *AP Suite 6.3.2C and IVAS 6 UserGuide*. Madison, WI, 2024, pp. D1–D28.

[192] T. J. Prosa, M. Holman, Y. Chen, and D. Reinhard, "Using Voltage-plus-Laser Mode to Characterize the Atom-Probe Field-Evaporation Properties of a Standard Silicon Specimen," *Microscopy and Microanalysis,* vol. 30, no. Supplement_1, p. ozae044.053, 2024, doi: 10.1093/mam/ozae044.053.

[193] D. J. Larson *et al.*, "Improving Analytical Capability via Simultaneous Voltage and Laser Pulsing in Atom Probe Tomography," *Microscopy and Microanalysis,* vol. 29, no. Supplement_1, pp. 609–610, 2023, doi: 10.1093/micmic/ozad067.295.

[194] D. W. Saxey, "Correlated ion analysis and the interpretation of atom probe mass spectra," *Ultramicroscopy,* vol. 111, no. 6, pp. 473–479, 2011, doi: 10.1016/j.ultramic.2010.11.021.

[195] S. Jin, H. Su, F. Qian, Y. Li, and G. Sha, "Effects of atom probe analysis parameters on composition measurement of precipitates in an Al-Mg-Si-Cu alloy," *Ultramicroscopy,* vol. 235, p. 113495, 2022, doi: 10.1016/j.ultramic.2022.113495.

[196] D. R. Diercks and B. P. Gorman, "Experimental Evaluation of the Interrelationships Between Laser Energy, Temperature, Applied Bias, and Measured Composition in Laser Pulsed Atom Probe Tomography," *Microscopy and Microanalysis,* vol. 22, no. S3, pp. 648–649, 2016, doi: 10.1017/s1431927616004098.

[197] R. J. H. Morris, R. Cuduvally, D. Melkonyan, M. Zhao, P. v. d. Heide, and W. Vandervorst, "Atom probe of GaN/AlGaN heterostructures: The role of electric field, sample crystallography and laser excitation on quantification," *Ultramicroscopy,* vol. 206, p. 112813, 2019, doi: 10.1016/j.ultramic.2019.112813.

[198] V. S. Bystrov *et al.*, "Computational and experimental studies of size and shape related physical properties of hydroxyapatite nanoparticles," *J. Phys.: Condens. Matter,* vol. 23, no. 6, p. 065302, 2011, doi: 10.1088/0953-8984/23/6/065302.

[199] T. S. d. Araujo, S. O. d. Souza, and E. M. B. d. Sousa, "Effect of Zn2+, Fe3+ and Cr3+ addition to hydroxyapatite for its application as an active constituent of sunscreens," *J. Phys.: Conf. Ser.,* vol. 249, no. 1, p. 012012, 2010, doi: 10.1088/1742-6596/249/1/012012.

[200] K. Keltoum, L. Edoha, DjouamaHanane, and LaacherLamia, "Coupled experimental and theoretical study of hydroxyapatite ceramic," *Bioinspired Biomim Nanobiomaterials,* vol. 12, no. 3, pp. 1–10, 2023, doi: 10.1680/jbibn.23.00007.

[201] F. G. Allen, "Work function and emission studies on clean silicon surfaces," *Journal of Physics and Chemistry of Solids,* vol. 8, pp. 119–120, 1959, doi: 10.1016/0022-3697(59)90291-4.

[202] H. B. Michaelson, "The work function of the elements and its periodicity," *Journal of Applied Physics,* vol. 48, no. 11, pp. 4729–4733, 1977, doi: 10.1063/1.323539.

[203] D. Fougerouse, D. W. Saxey, W. D. A. Rickard, S. M. Reddy, and R. Verberne, "Standardizing Spatial Reconstruction Parameters for the Atom Probe Analysis of Common Minerals," *Microscopy and Microanalysis,* vol. 28, no. 4, pp. 1221–1230, 2022, doi: 10.1017/s1431927621013714.

[204] A. Mikhalychev, S. Vlasenko, T. R. Payne, D. A. Reinhard, and A. Ulyanenkov, "Bayesian approach to automatic mass-spectrum peak identification in atom probe tomography," *Ultramicroscopy,* vol. 215, p. 113014, 2020, doi: 10.1016/j.ultramic.2020.113014.

[205] Cameca, "8.17.3.1 Local Range-Assisted Background Models," in *AP Suite 6.3 and IVAS 6 User Guide*. Madison, WI, 2022, pp. 8.58–59.

[206] J. Reyes-Gasga and E. F. Brès, "High Resolution STEM Images of the Human Tooth Enamel Crystals," *Applied Sciences,* vol. 11, no. 16, p. 7477, 2021, doi: 10.3390/app11167477.

[207] E. Klimuszko, K. Orywal, T. Sierpinska, J. Sidun, and M. Golebiewska, "Evaluation of calcium and magnesium contents in tooth enamel without any pathological changes: in vitro preliminary study," *Odontology,* vol. 106, no. 4, pp. 369–376, 2018, doi: 10.1007/s10266-018-0353-6.

[208] C. Robinson, J. A. Weatherell, and A. S. Hallsworth, "Distribution of Magnesium in Mature Human Enamel," *Caries Research,* vol. 15, no. 1, pp. 70–77, 1981, doi: 10.1159/000260502.

[209] V. K. Kis, A. Sulyok, M. Hegedűs, I. Kovács, N. Rózsa, and Z. Kovács, "Magnesium incorporation into primary dental enamel and its effect on mechanical properties," *Acta Biomaterialia,* 2020, doi: 10.1016/j.actbio.2020.08.035.

[210] K. A. Selvag and A. Halse, "Crystal growth in rat incisor enamel," *The Anatomical Record,* vol. 173, no. 4, pp. 453–468, 1972, doi: 10.1002/ar.1091730406.

[211] E. V. Woods *et al.*, "Mapping the Path to Cryogenic Atom Probe Tomography Analysis of Biomolecules," *Microscopy and Microanalysis,* vol. 31, no. 4, p. ozaf032, 2025, doi: 10.1093/mam/ozaf032.

[212] S. V. Dorozhkin, "Amorphous calcium (ortho)phosphates," *Acta Biomaterialia,* vol. 6, no. 12, pp. 4457–4475, 2010, doi: 10.1016/j.actbio.2010.06.031.

[213] A. A. El-Zoka, S. H. Kim, S. Deville, R. C. Newman, L. T. Stephenson, and B. Gault, "Enabling near-atomic–scale analysis of frozen water," *Science Advances,* vol. 6, no. 49, p. eabd6324, 2020, doi: 10.1126/sciadv.abd6324.

[214] T. M. Schwarz *et al.*, "Field evaporation and atom probe tomography of pure water tips," *Scientific Reports,* vol. 10, no. 1, p. 20271, 2020, doi: 10.1038/s41598-020-77130-x.

[215] D. M. Lyaruu *et al.*, "Barrier Formation: Potential Molecular Mechanism of Enamel Fluorosis," *Journal of Dental Research,* vol. 93, no. 1, pp. 96–102, 2013, doi: 10.1177/0022034513510944.

[216] H. E. Feki, J. M. Savariault, A. B. Salah, and M. Jemal, "Sodium and carbonate distribution in substituted calcium hydroxyapatite," *Solid State Sci.,* vol. 2, no. 5, pp. 577–586, 2000, doi: 10.1016/s1293-2558(00)01059-1.

[217] E. B. Wilson, "Probable Inference, the Law of Succession, and Statistical Inference," *J. Am. Stat. Assoc.,* vol. 22, no. 158, pp. 209–212, 1927, doi: 10.1080/01621459.1927.10502953.

[218] J. R. Famelton, C. A. Williams, C. Barbatti, P. A. J. Bagot, and M. P. Moody, "Point excess solute: A new metric for quantifying solute segregation in atom probe tomography datasets including application to naturally aged solute clusters in Al-Mg-Si-(Cu) alloys," *Materials Characterization,* vol. 206, p. 113402, 2023, doi: 10.1016/j.matchar.2023.113402.

[219] V. B. Vukkum *et al.*, "Insights from quasi-in situ cryogenic-transfer atom probe tomography for analyzing hydrogen diffusion in metallic alloys," *npj Materials Degradation,* vol. 9, no. 1, p. 85, 2025, doi: 10.1038/s41529-025-00626-2.

[220] M. S. Muthu, S. Vandana, G. Akila, M. Anusha, D. Kandaswamy, and M. B. A. Narayanan, "Global variations in eruption chronology of primary teeth: A systematic review and meta-analysis," *Archives of Oral Biology,* vol. 158, p. 105857, 2024, doi: 10.1016/j.archoralbio.2023.105857.

[221] P. Š. n. Uhrová, R. Beňuš, M. C. n. Kondeková, A. Vojtušová, M. Novotný, and A. Thurzo, "Use of third molar eruption based on Gambier's criteria in assessing dental age," *Int. J. Leg. Med.,* vol. 137, no. 3, pp. 691–699, 2023, doi: 10.1007/s00414-023-02953-y.

[222] J. P. Simmer and J. C. C. Hu, "Dental Enamel Formation and Its Impact on Clinical Dentistry," *J. Dent. Educ.,* vol. 65, no. 9, pp. 896–905, 2001, doi: 10.1002/j.0022-0337.2001.65.9.tb03438.x.

[223] W. F. Neuman, T. Y. Toribara, and B. J. Mulryan, "Synthetic hydroxyapatite crystals I. Sodium and potassium fixation," *Arch. Biochem. Biophys.,* vol. 98, no. 3, pp. 384–390, 1962, doi: 10.1016/0003-9861(62)90202-3.

[224] W. R. Stoll and W. F. Neuman, "The Uptake of Sodium and Potassium Ions by Hydrated Hydroxyapatite 1," *Journal of the American Chemical Society,* vol. 78, no. 8, pp. 1585–1588, 1956, doi: 10.1021/ja01589a022.

[225] J. Ngu, A. L. J. J. Bronckers, K. Katsura, Y. Zhang, and P. K. D. Besten, "Na+ and K+ transport and maturation stage ameloblast modulation," *Frontiers in Physiology,* vol. 14, p. 1124444, 2023, doi: 10.3389/fphys.2023.1124444.

[226] S. Habelitz, L. Pascual, and A. Durán, "Nitrogen-containing apatite," *Journal of the European Ceramic Society,* vol. 19, no. 15, pp. 2685–2694, 1999, doi: 10.1016/s0955-2219(99)00048-5.

[227] M. Gafurov *et al.*, "Nitrogen-containing species in the structure of the synthesized nano-hydroxyapatite," *JETP Lett.,* vol. 99, no. 4, pp. 196–203, 2014, doi: 10.1134/s0021364014040079.

[228] B. Kallapur, K. Ramalingam, Bastian, A. Mujib, A. Sarkar, and S. Sethuraman, "Quantitative estimation of sodium, potassium and total protein in saliva of diabetic smokers and nonsmokers: A novel study," *J. Nat. Sci., Biol., Med.,* vol. 4, no. 2, pp. 341–345, 2013, doi: 10.4103/0976-9668.117006.

[229] J. A. Bilbrey *et al.*, "Compositional Community Detection: Automated Identification of Chemical Segregation in Atom Probe Tomography Data," *Microscopy and Microanalysis,* vol. 31, no. 3, p. ozaf036, 2025, doi: 10.1093/mam/ozaf036.

[230] W. F. Neuman, T. Y. Toribara, and B. J. Mulryan, "The Surface Chemistry of Bone. VII. The Hydration Shell 1," *Journal of the American Chemical Society,* vol. 75, no. 17, pp. 4239–4242, 1953, doi: 10.1021/ja01113a028.

[231] A. S. Posner, A. Perloff, and A. F. Diorio, "Refinement of the hydroxyapatite structure," *Acta Crystallogr,* vol. 11, no. 4, pp. 308–309, 1958, doi: 10.1107/s0365110x58000815.

8. Appendices

8.1. (Chapter 2) Additional APT and TEM data from young and senior outer enamel

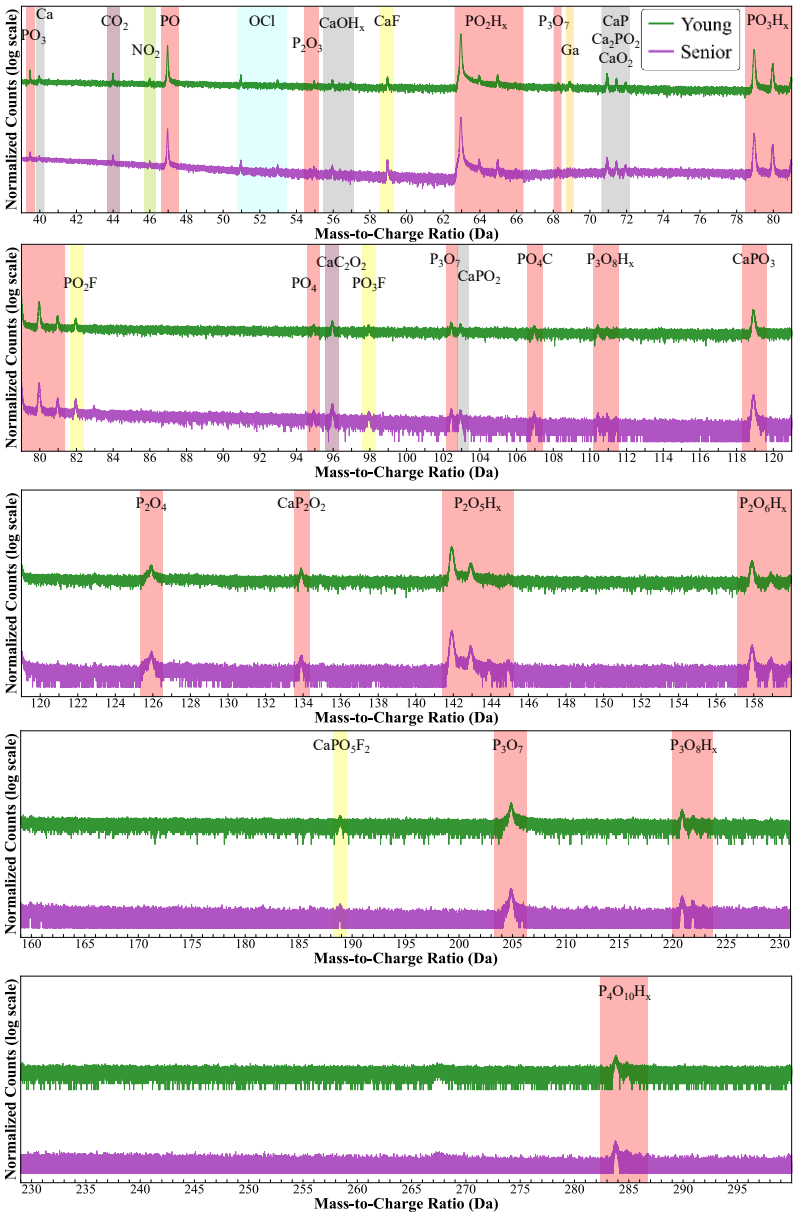

Supplementary Figure 1. Representative mass-to-charge spectra for young and senior enamel. *See Figure 2.1 in the main text for 0 – 40 Da. No peaks surpassing double the surrounding background were detected above 300 Da.*

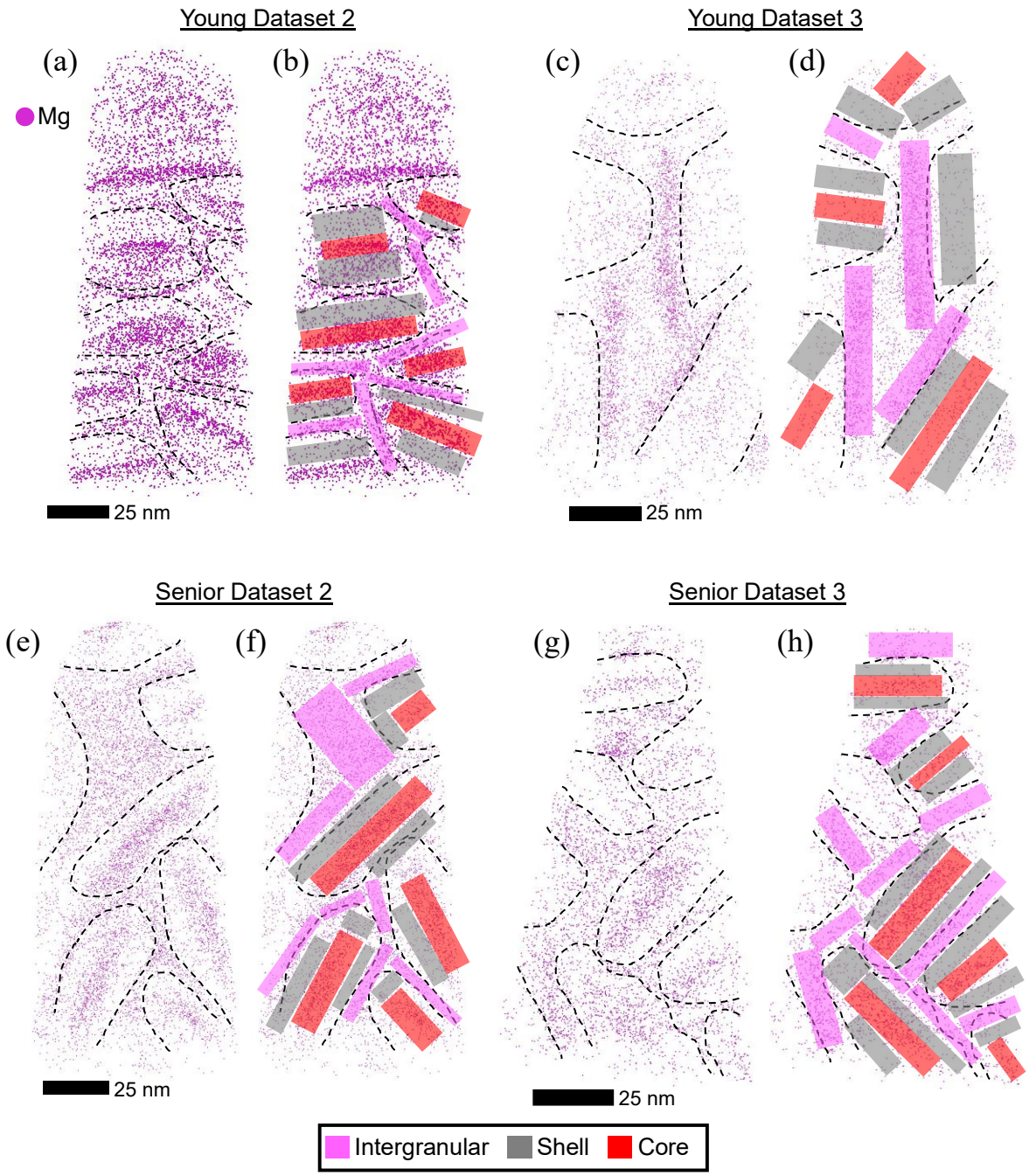

Supplementary Figure 2. APT reconstructions of young and senior enamel. *Young (a-b, e-f) and senior (c-d, g-h) datasets are presented. (a ,c, e, g) Only Mg ions are visualized to highlight the nanocrystal core and intergranular phases, with dashed lines outlining the nanocrystal boundaries. (b, d, f, h) Positions of ROIs used to segment the enamel into the intergranular, shell, and core phases.*

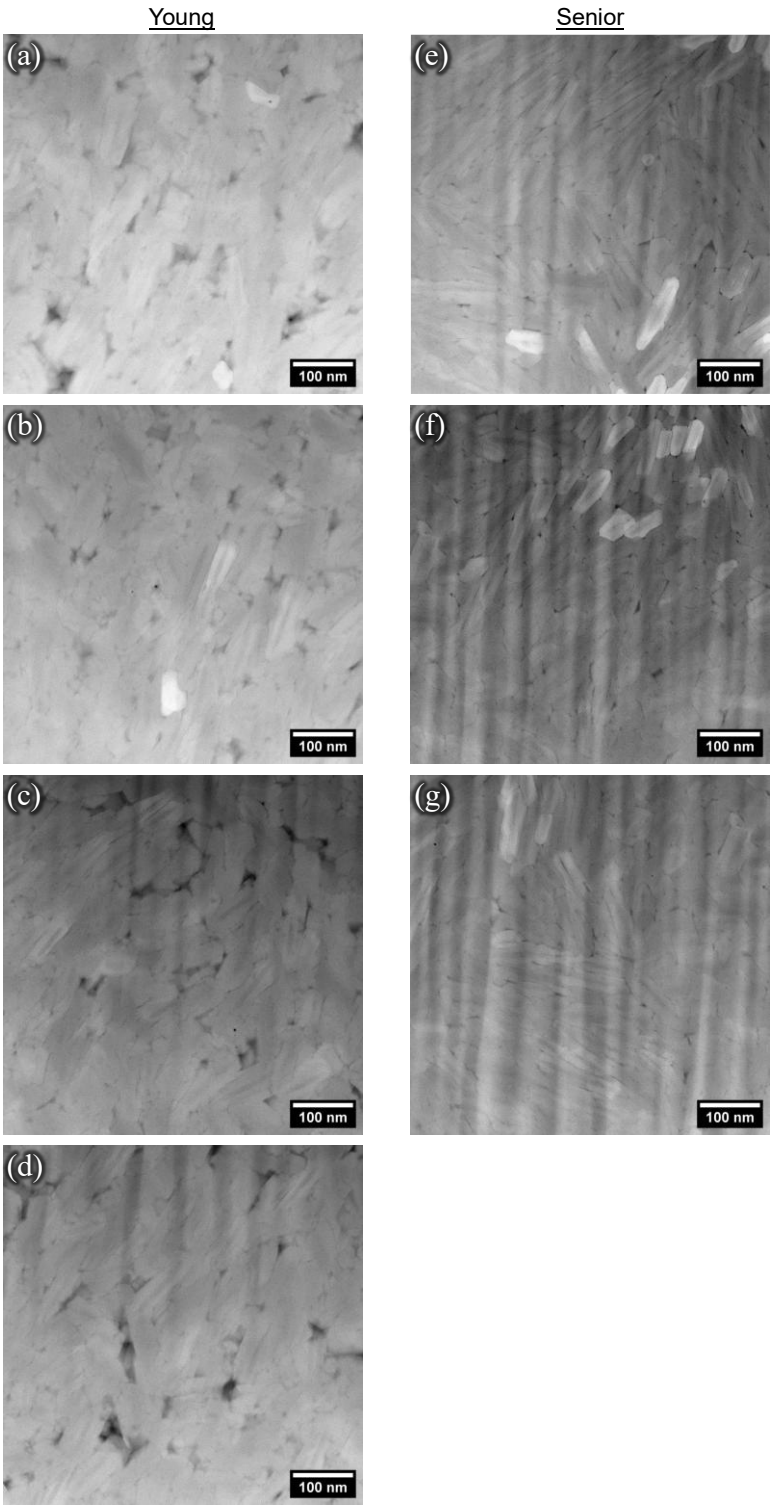

Supplementary Figure 3. Additional STEM HAADF micrographs at 165,000x magnification used for measuring nanocrystal dimensions. *(a-d) Young enamel. (e-g) Senior enamel.*

8.2. (Chapter 3) Location of APT liftouts from *Crocodylus porosus* enamel

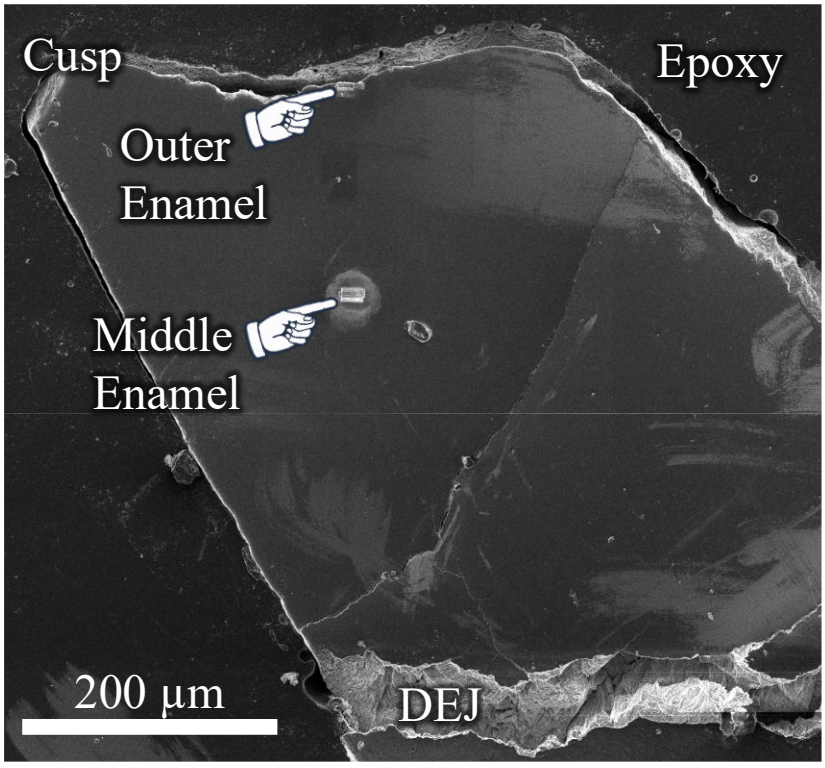

Supplementary Figure 4. Location of APT liftouts from *Crocodylus porosus* enamel. *Samples were taken from the cuspal portion of a molariform tooth sectioned buccal-lingually. The cross-section had been bisected from cusp to root before being mounted in epoxy, hence the straight edge on the left side. The enamel and dentin have significantly separated, potentially due to uneven dehydration shrinkage after mounting in epoxy.*

8.3. (Chapter 4) Additional details of sample preparation and data processing for synthetic HA samples

Liftout of samples in the PFIB or FIB was performed by first depositing a protective ~1 μm thick Pt cap with 5 kV 1.6 nA electron-beam followed by an additional 1 μm deposited with 30 kV 0.1 nA ion beam. Vertical trenches were then made on either side of the strip with 30 kV 0.3 nA regular cross section patterns, then the sample thinned to ~2 μm width with a 30 kV 0.3 nA ion beam cleaning cross section pattern. Undercuts were made with 30 kV 0.1 nA ion beam (Supplementary Figure 5a) with a 30° incident ion beam, then the liftout was attached to a nanomanipulator (Omniprobe, Oxford, Oxford Instruments, Concord, MA in Helios NanoLab 600i; EZLift, Thermo Fisher Scientific, Waltham, MA in Helios Hydra) with a Pt weld deposited at 30 kV 0.1 nA before being freed from the bulk crystal. The same Pt deposition was used to attach segments of the liftout to Si microposts (M22 array, Cameca, Madison, WI) (Supplementary Figure 5b).

Samples were sharpened for APT in the PFIB using a series of annular patterns (Supplementary Figure 5c). The size and duration of each pattern were the same for each sample in an effort to achieve more consistent specimen geometries. On occasion, a coarse (inner diameter ≥ 1 μm) pattern would need to be repeated or extended to eliminate nearby unwanted apexes. The typical process involved first using a 30 kV 0.3 nA Xe ion beam to mill a 4 × 1.2 μm (outer × inner diameter) annular pattern for 180 s. Then, the current was reduced to 0.1 nA for the following patterns: 4 × 1 μm for 60 s, 3.75 × 0.8 μm for 45 s, 3.75 × 0.6 μm for 30 s, 3.75 × 0.4 μm for 20 s, and 3.75 × 0.25 μm for 15 s. Any remaining Pt capping material and ~50 – 100 nm of HA were

removed with a 5 kV 16 – 47 pA Xe beam with no pattern (Supplementary Figure 5d-e). Similar patterns were used in the Helios, but the timing of each step was not recorded.

APT experiments were performed using the local electrode atom probe (LEAP) 4000 and 6000 systems to compare the influence of laser pulse energy (LPE) and pulse frequency. For all experiments on both systems, the base temperature was held at 40 K. On the LEAP 4000, the LPE was increased from 20 – 200 pJ while holding the pulse frequency constant at 200 kHz, all performed on the same needle during the same experiment. 4.5-5×10^5 ions were collected at each setting before changing to the next. On the LEAP 6000, the pulse frequency was held constant at 100 kHz while the LPE was varied from 5 – 15 pJ on one needle and 15 – 150 pJ on a separate needle. 1×10^6 ions were collected at each setting at a detection rate of 0.5%.

It is worth mentioning that using CSR as a control during data collection reliably is enabled by the Auto Pulse Energy Control and Live Calibration features of APSuite, which are only available for the LEAP 5000 and newer generations. Auto Pulse Energy Control continuously monitors the specified peak ratio (which can easily be set to the CSR) and adjusts the laser energy systematically to maintain that ratio throughout collection. In this study, we used ranges of [19.913, 20.065] Da for 40Ca2+ and [39.914, 40.077] Da for 40Ca+. Likewise, the Live Calibration adjusts the calibration file (e.g. voltage and bowl corrections and peak position fitting) to bring the live data during collection closer to what the final processed values would be. In this way, the range file developed from a completed experiment can be directly applied during collection of future datasets. That said, the ranges used for final analysis were adjusted based on the elbows of each peak for each individual experiment.

Peak fitting in the Live Calibration of APS and the reconstruction wizard of IVAS was performed using the following species: H^+ (at 1.007 Da), O^+/O_2^{++} (15.995), Ca^{++} (19.9815), O_2^+ (31.99), PO^+ (46.969), PO_2^+ (62.964), PO_3^+ (78.959), $CaPO_3^+$ (118.922), $P_2O_5^+$ (141.923), $P_2O_6^+$ (157.918), $P_3O_8^+$ (220.882), $P_4O_{10}^+$ (283.846). Note that for peaks above 100 Da, only peaks where the automatically detected range was approximately centered on the apex of the peak were used.

8.3.1. Supplementary Tables and Figures

Supplementary Table 1. Compositional measurements of hydroxyapatite from point measurements using energy dispersive spectroscopy.

	Ca	P	O	K	C	Si	Ca:P	(Ca+K):P
Average (at.%)	23.44	15.36	55.74	2.36	2.72	0.39	1.54	1.69
Standard Deviation (at.%)	1.19	1.30	1.99	2.15	0.28	0.39	0.20	0.09

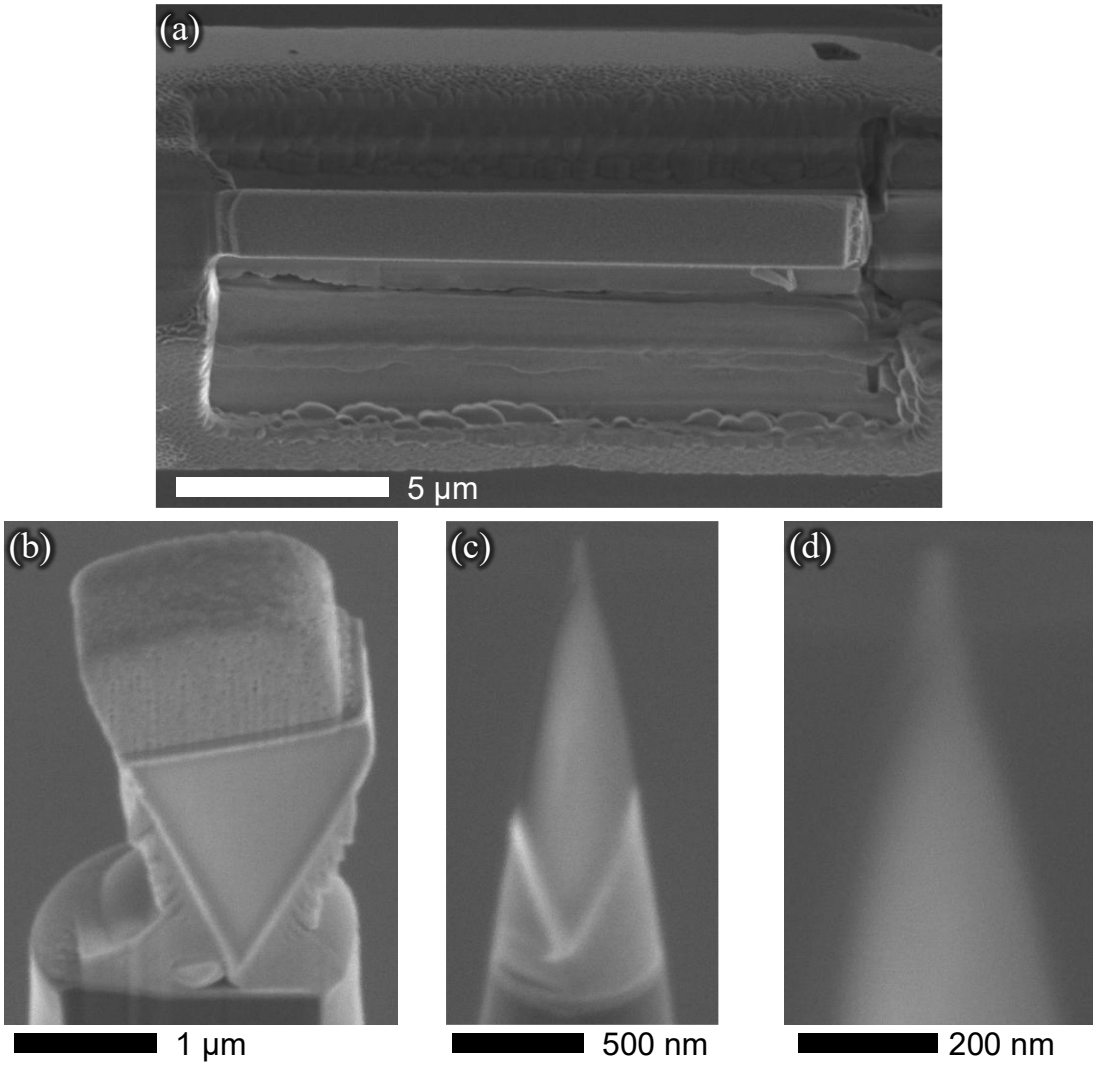

Supplementary Figure 5. Preparation of HA specimens for APT. *a) A Pt cap is put on one face of the HA crystal, then trenches milled on either side produce a triangular cantilever. B) The cantilever is freed and transferred via nanomanipulator to flat-top Si microposts and affixed by Pt welds. A cross section is performed to accurately monitor milling progress. c) A series of annular milling steps and subsequent low-kV ion beam are used to bring the needle to a final apex diameter < 150 nm. d) High magnification view of the specimen apex after sharpening.*

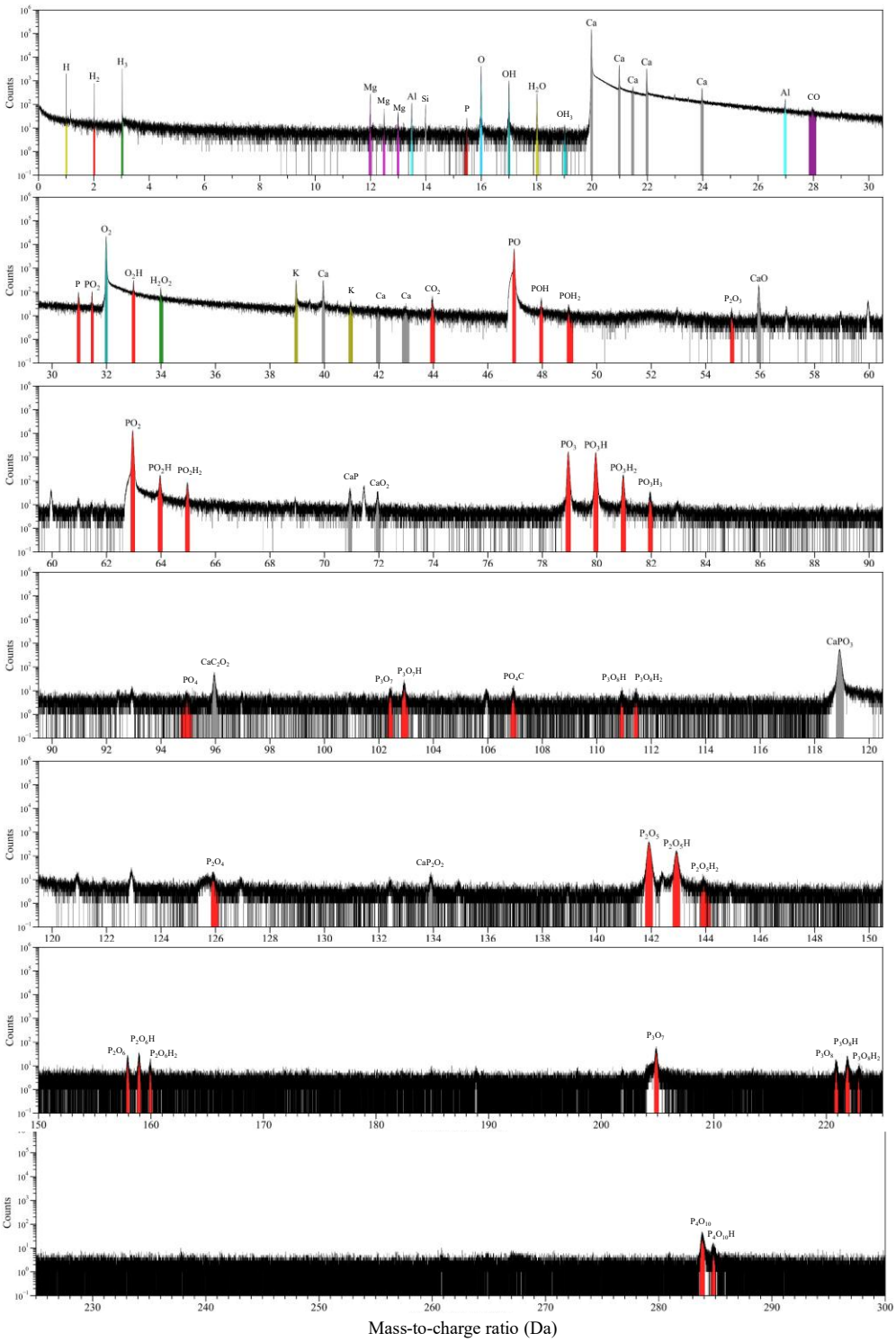

Supplementary Figure 6. Mass-to-charge spectrum of hydroxyapatite collected with a target $^{40}Ca^{2+}$:$^{40}Ca^{+}$ CSR of 200. *Elbow ranges are displayed.*

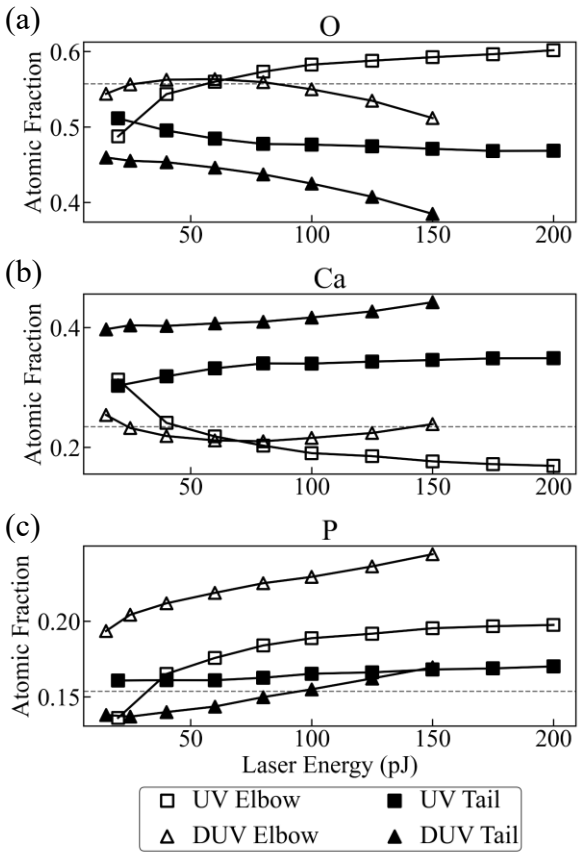

Supplementary Figure 7. Decomposed composition of (a) O, (b) Ca, and (c) P in HA on UV and DUV systems evaluated by tail- and elbow-ranging approaches as a function of LPE. *The horizontal dashed line in each reflects the expected atomic fraction from EDS measurements (Supplementary Table 1).*

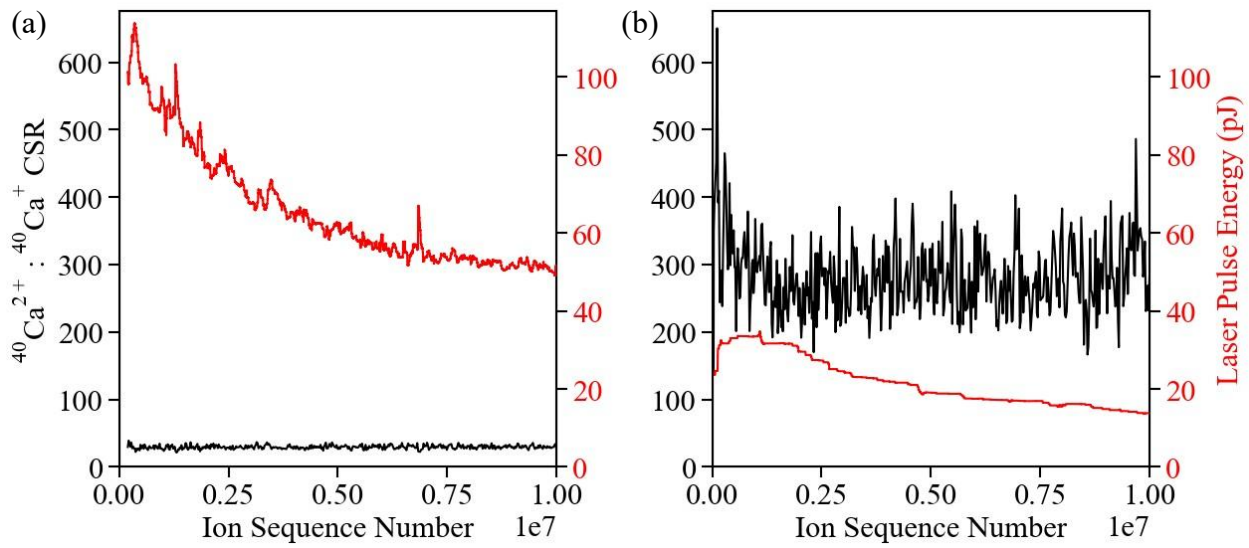

Supplementary Figure 8. Recorded $^{40}Ca^{2+}$:$^{40}Ca^{+}$ CSR (left axis, black line) and laser pulse energy (right axis, red line) as a function of ion sequence number during an experiment with a target CSR of (a) 30 and (b) 300 on the DUV laser system.

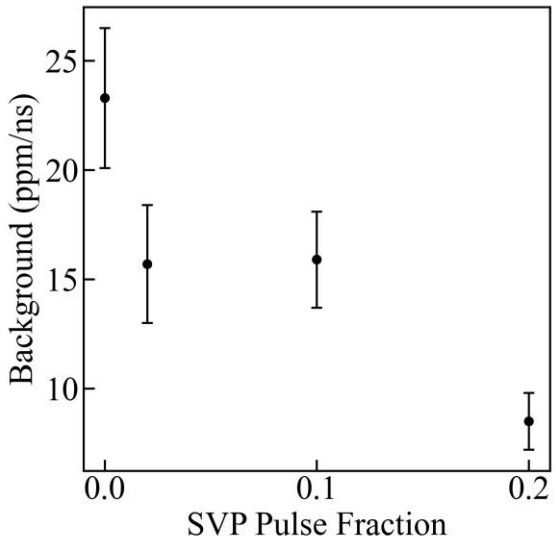

Supplementary Figure 9. Average and standard deviation of measured background during SVP experiments as a function of voltage pulse fraction.

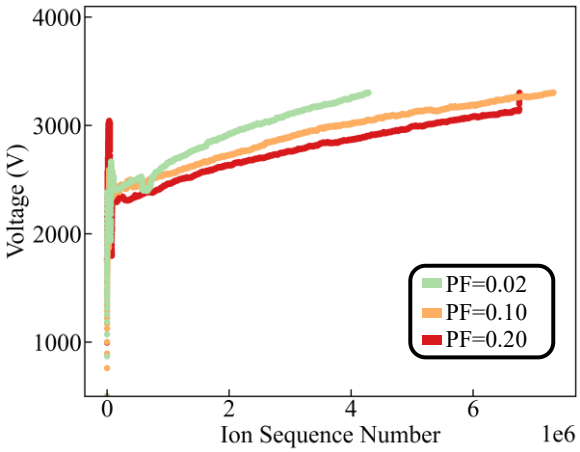

Supplementary Figure 10. Standing voltage versus ion sequence number for three SVP experiments with a target $^{40}Ca^{2+}$:$^{40}Ca^{+}$CSR of 200. *Prior to this data, each specimen had previously been run with an LPE of 20 pJ and target DR of 0.5%, ending at 2600 V. Each SVP experiment ended at a stop point set at 3300 V.*

8.4. (Chapter 5) Supplementary Information and Discussion

8.4.1. Uncertainty measurements in APT

APT is prone to instrumental limitations which limit the accuracy at very low counts. A commonly applied approximation of the error can be derived from Poisson counting statistics [18] using Equation (S1)

$$\boldsymbol{\sigma_i} = \boldsymbol{c_i}\sqrt{\boldsymbol{N_i^{-1}} + \boldsymbol{N_{total}^{-1}}} \quad \text{(S1)}$$

where σ_i and c_i are the uncertainty and composition (in ion%) for species *i*, N_i is the number of counts of species *i*, and N_{total} is the total number of ranged counts in the spectrum. Using as an example the spectrum from the PR phase of R6006_34095, after background subtraction, N_1 constituted 120 out of 249,207 counts for a concentration of 0.048 ion%. Using Equation (S1), Poisson counting statistics give an uncertainty in this measurement of ± 0.004 ion%, yielding an error interval of 0.044—0.052 ion%. However, it has been argued that a more realistic method to calculate uncertainty in the context of APT measurements, particularly for species with very low counts, is to use the Wilson score interval [217], defined using Equation (S2) [218]

$$\boldsymbol{p_i} = \frac{\boldsymbol{N_i + z_\alpha^2/2}}{\boldsymbol{N_{total} + z_\alpha^2}} \pm \frac{\boldsymbol{z_\alpha}}{\boldsymbol{N_{total} + z_\alpha^2}}\sqrt{\frac{\boldsymbol{N_i(N_{total} - N_i)}}{\boldsymbol{N_{total}}} + \frac{\boldsymbol{z_\alpha^2}}{\boldsymbol{4}}} \times \mathbf{100}\% \quad \text{(S2)}$$

where p_i is the error interval (in ion%) and z_α is the confidence score (e.g. 1.96 for a 95% confidence level). An advantage of the Wilson score interval is that the error interval can be asymmetric about c_i and cannot go below 0% for very small concentrations or above 100% for very high concentrations. Applying Equation (S2) to the N_1 counts stated above yields an interval of 0.040—0.058 ion% with a confidence level of 95%, a range of 0.018 ion%. This provides a more realistic understanding of the counting error associated with the measurement.

The counting uncertainty when averaging n measurements can be propagated using Equation (S3)

$$\boldsymbol{\sigma_{avg}} = \frac{\sqrt{\sum_{j=1}^{n}(r_j/2)^2}}{n} \quad \text{(S3)}$$

where r_j is the range of the Wilson confidence interval for measurement j. Applied to the example data of N_1 in young precipitates, this yields an uncertainty of 0.004 ion%, which is considerably smaller than the standard deviation of set of measurements at 0.013 ion%. A visualization of the Wilson 95% confidence interval for N_1 concentration in young enamel is provided in Supplementary Figure 11. Ultimately, we conclude that even for peaks with relatively small ion counts such as N_1, sufficient data was collected such that the standard deviation of multiple measurements is greater than the potential error from counting, and thus the statistical tests applied throughout this paper to determine significant differences are valid.

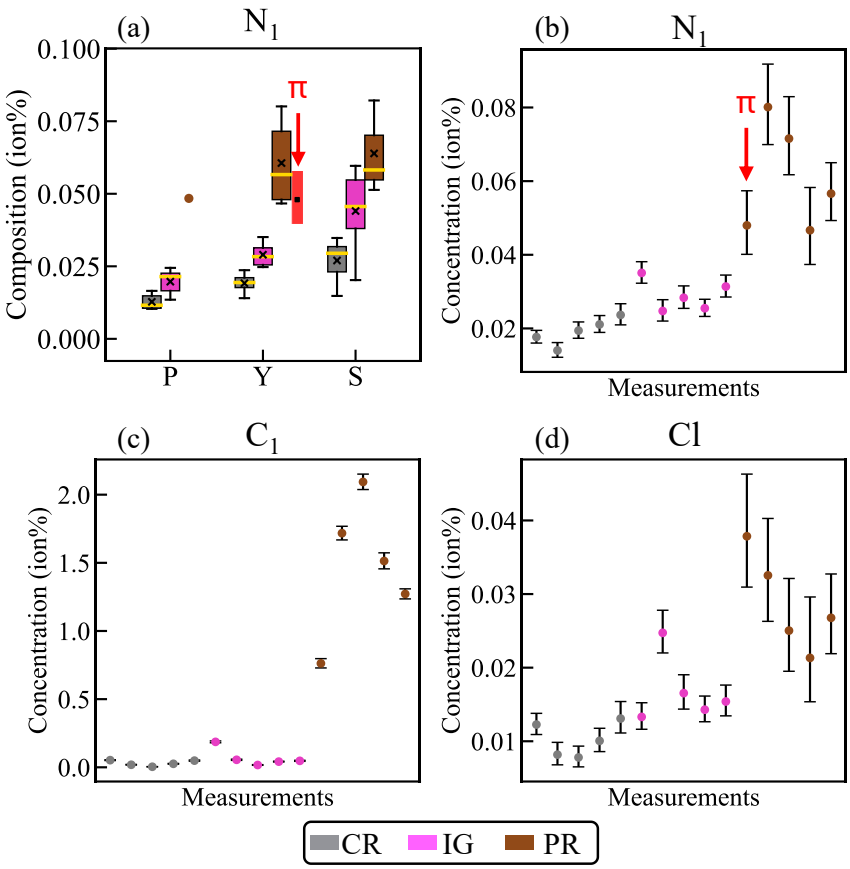

Supplementary Figure 11. Comparison of composition distribution and Wilson 95% confidence interval. *(a) Box plot of N_1 concentration reproduced from Figure 5.4 with the Wilson confidence interval for a* representative *precipitate measurement from young enamel "π" added as a red rectangle. The Wilson confidence intervals for the remaining phase measurements of N_1 are plotted in (b), grouped according to phase. Wilson interval plots are also presented as visual examples of the confidence intervals for (c) values very close to zero for C_1 and for (d) small concentrations of Cl associated with peaks with relatively high background levels due to the tail of the $^{40}Ca^{2+}$ peak.*

8.4.2. Estimation of Na concentration in hydration shell of hydroxyapatite

The total Na concentration of Na in saliva is taken to be 0.080 M, the average of the control group of n = 25 non-smoking non-diabetic individuals reported in [228]. A linear equation for the

amount of Na in the hydration shell of hydroxyapatite crystals ("y," in millimoles of Na per gram of HA) as a function of the concentration of Na in solution ("x," in millimoles per liter) at an ionic strength of 0.126 was derived from the data presented in Figure 3a of [224]: $y = 0.0013x + 0.0063$. The result was then multiplied by the molecular mass of hydroxyapatite (502.31 g/mol) to arrive at a fraction of moles of Na in the hydration shell to moles of HA, which can be multiplied by 100 at.% to yield an estimate of 6 at.%.

An important caveat to this estimation is that it ignores surface area, instead referencing the mass of hydroxyapatite. The specific surface area of the synthetic crystals in question is reported as 67.8 m^2/g [230]. To estimate the specific surface area of enamel nanocrystals, we can use an average nanocrystal area of 3200 nm^2 for young outer enamel reported in [35], or a more conservative 1590 nm^2 of a 32-plane crystal (developed crystal > 400 μm from the ameloblast) in fetal humane enamel [81]. The typical length of enamel nanocrystals is not well characterized, but for this case let us assume a generous length of 100 μm [30]. The unit cell of enamel has dimensions of a = b = 0.9432 nm, c = 0.6881 nm and has the stoichiometry of $Ca_{10}(PO_4)_6(OH)_2$ [231]. The a-b cross sectional area of the unit cell is thus 0.7704 nm^2, meaning the cross section of a crystal has between 2060 to 4150 unit cells, and the length (c-axis) has approximately 145000 unit cells, for a total of 3E8 to 6E8 unit cells per crystal. The mass per mole of unit cells is 1004.6 g, which can then be used to estimate the mass of a single crystal between 5-10E-12 g. Surface area estimates can be derived geometrically from the perimeter of the nanocrystals, resulting in a specific surface area estimate of 100 m^2/g from [81] and 48 m^2/g from [35]. These are of the same order of magnitude as the synthetic crystals used by [224], and thus the discrepancy in the concentration of Na that could be adsorbed in the HA must be explained by factors other than the hydration layer.

8.4.3. Supplementary Figures

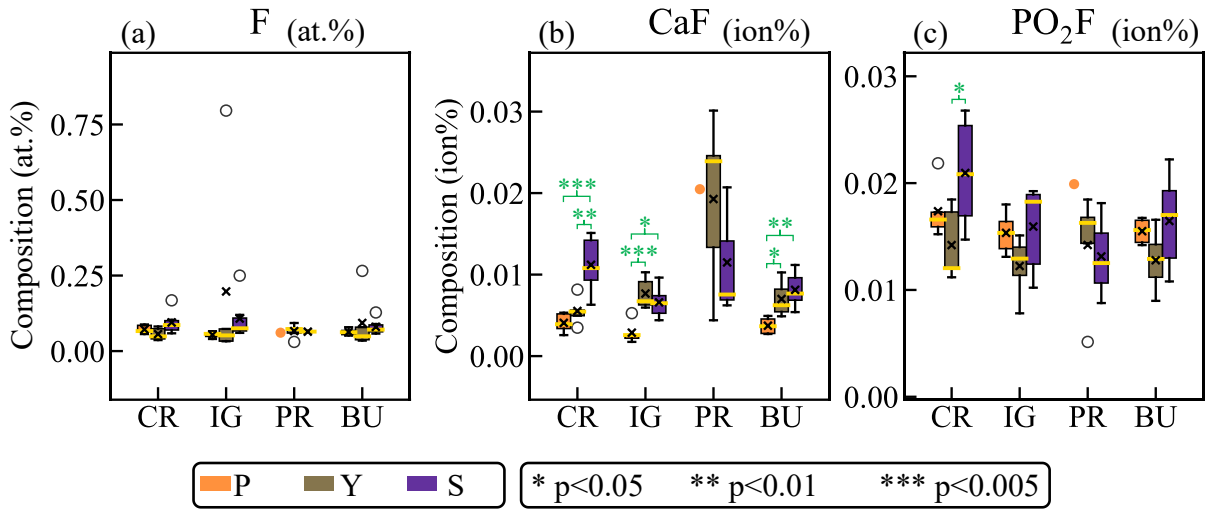

Supplementary Figure 12. Comparison of fluorine content in inner enamel by phase between teeth from different age groups. *Compositions are presented for molecular ions (a) CaF and (b) PO_2F in ion%, as well as for (c) the decomposed F composition in at.%. For each plot, the distribution of compositions for crystal (CR), intergranular (IG), and precipitate (PR) phases as well as bulk (BU) are* grouped *according to the tooth they came from: Primary (P), Young (Y), or Senior (S). When n > 2, "x" mark indicates the mean, yellow horizontal bar indicates the mean, the box indicates the interquartile range, whiskers indicate 1.5 times the interquartile range, and outliers are denoted by hollow circles. The level of statistical significance from Tukey post-hoc test is indicated with asterisks and a bracket connecting the two groups being compared. If n ≤ 2, individual data points are shown instead.*

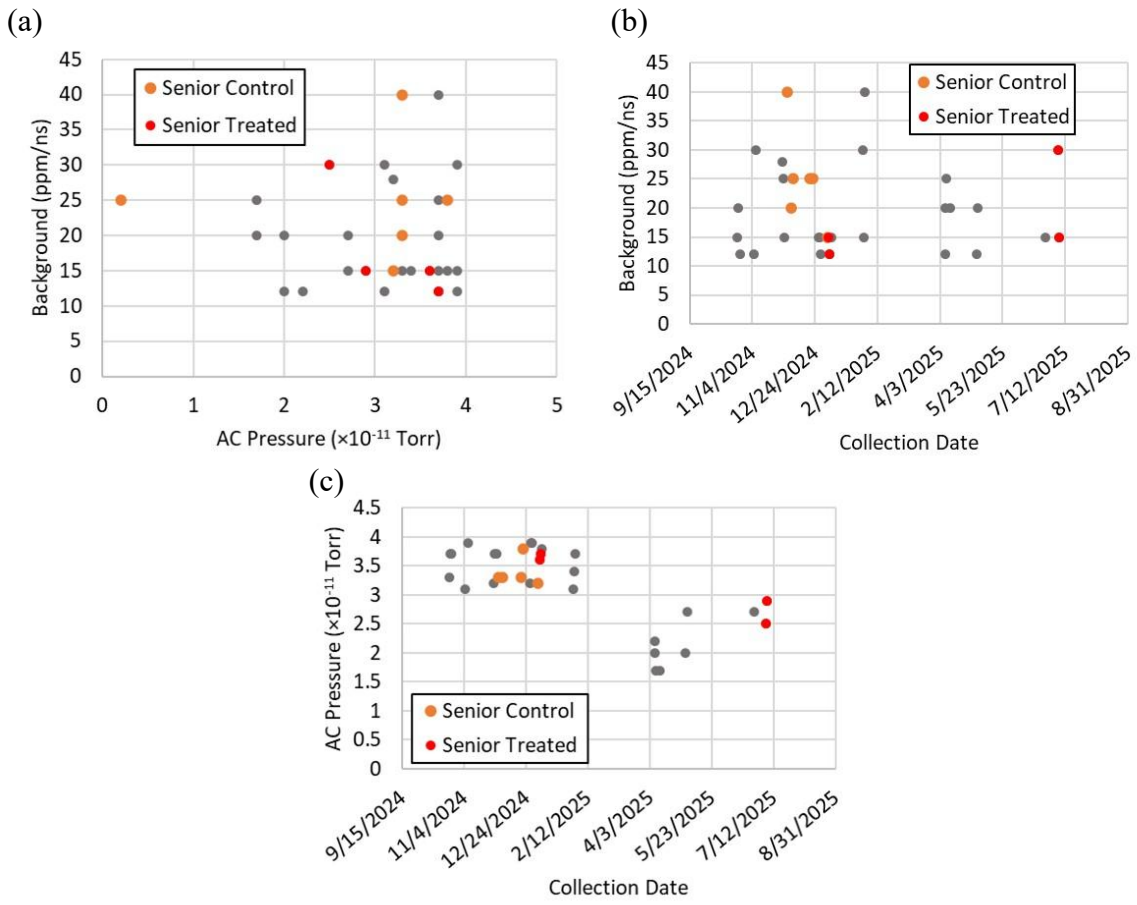

Supplementary Figure 13. Comparison of analysis chamber pressure, background level, and date of collection for senior data. (a) Background (in ppm/ns) versus analysis chamber (AC) pressure (units are multiplied by 10^{-11} Torr). (b) Background versus collection date. (c) AC pressure versus collection date. In each plot, data from primary and young are shown as gray points.

Supplementary Table 2. Elbow ranges used for a representative dataset. *Ranges are adjusted using the elbow approach for senior inner enamel run number R6006_34318.*

Name	Charge	Expected Da	Relative Abundance	Start (Da)	Stop (Da)	Volume (nm^3)
H	2	1.00705	0.000115	0.985	1.03	0
unknown1o15				1.128	1.189	0
H2	1	2.0156	0.9997	1.994	2.039	0
H3	1	3.0234	0.99955	3.002	3.048	0
C	2	6	0.9889	5.965	6.03	0.00878
N	2	7.0015	0.99636	6.971	7.163	0.02248
Mg-C				11.963	12.021	0
Mg	2	12.493	0.1	12.464	12.521	0.02325
Mg-CN				12.963	13.027	0
CNH	2	13.5054	0.985153	13.476	13.531	0.03127
N	1	14.003	0.99636	13.973	14.036	0.02248
N2H	2	14.5069	0.992584	14.471	14.531	0.02248
CH3	1	15.0234	0.988455	14.984	15.049	0.00878
P	2	15.487	1	15.436	15.495	0.02826
unknown15o5				15.499	15.545	0
O	1	15.995	0.99757	15.966	16.019	0.02883
CH4	1	16.0312	0.988307	16.023	16.064	0.00878
OH	1	17.0028	0.99742	16.972	17.031	0.02883
CH5	1	17.039	0.988159	17.035	17.065	0.00878
H2O	1	18.0106	0.997271	17.983	18.044	0.02883
OH3	1	19.0184	0.997121	18.991	19.052	0.02883
Ca	2	19.9815	0.96941	19.95	20.013	0.04351
PO2	3	20.988	0.995146	20.954	21.02	0.08592
Ca	2	21.4795	0.00135	21.443	21.534	0.04351
Ca	2	21.9775	0.02086	21.941	21.985	0.04351
CO2	2	21.995	0.9841	21.989	22.027	0.06644
Na	1	22.99	1	22.956	23.027	0.03949
Ca-Mg				23.938	24.025	0
Mg	1	24.986	0.1	24.947	25.033	0.02325
Mg	1	25.983	0.1101	25.943	26.038	0.02325
CO	1	27.995	0.986497	27.959	28.035	0.03761
CaOH2	2	28.9868	0.966764	28.944	28.993	0.07234
COH	1	29.0028	0.986349	28.997	29.045	0.03761
NO	1	29.998	0.993939	29.955	30.046	0.05131
P	1	30.974	1	30.938	31.023	0.02826
PO2	2	31.482	0.995146	31.431	31.513	0.08592
O2	1	31.99	0.995146	31.95	32.03	0.05766

Name	Charge	Expected Da	Relative Abundance	Start (Da)	Stop (Da)	Volume (nm^3)
O2H	1	32.9978	0.994997	32.953	33.033	0.05766
O2	1	33.994	0.00409	33.956	34.047	0.05766
Cl	1	34.969	0.7576	34.911	35.036	0.02888
PO4F	3	37.984	0.990315	37.939	38.029	0.16217
K	1	38.964	0.93258	38.919	39.01	0.0763
Ca	1	39.963	0.96941	39.914	40.011	0.04351
P2F	2	40.473	1	40.424	40.533	0.07513
CaH	1	40.9708	0.969265	40.929	41.022	0.04351
CaH2	1	41.9786	0.969119	41.928	42.033	0.04351
CO2	1	43.99	0.9841	43.943	44.04	0.06644
CO2H	1	44.9978	0.983952	44.948	45.044	0.06644
CO2H2	1	46.0056	0.983805	45.943	46.043	0.06644
PO	1	46.969	0.99757	46.919	47.023	0.05709
POH	1	47.9768	0.99742	47.901	48.03	0.05709
PO	1	48.973	0.00205	48.927	49.031	0.05709
KO	1	54.959	0.930314	54.892	55.058	0.10513
CaO	1	55.958	0.967054	55.899	56.022	0.07234
CaOH	1	56.9658	0.966909	56.91	57.031	0.07234
CaF	1	58.961	0.96941	58.896	59.021	0.06211
unknown60				59.868	60.04	0
PO2	1	62.964	0.995146	62.902	63.028	0.08592
PO2H	1	63.9718	0.994997	63.905	64.033	0.08592
PO2H2	1	64.9796	0.994847	64.907	65.045	0.08592
CaP	1	70.937	0.96941	70.876	71.003	0.07177
Ca2PO2	2	71.445	0.935194	71.392	71.452	0.17293
P2O5H	2	71.4654	0.987761	71.456	71.524	0.20067
CaO2	1	71.953	0.964704	71.882	72.018	0.10116
PO3	1	78.959	0.992728	78.886	79.034	0.11475
PO3H	1	79.9668	0.992579	79.893	80.043	0.11475
PO3H2	1	80.9746	0.99243	80.901	81.052	0.11475
PO2F	1	81.962	0.995146	81.883	81.981	0.10452
C3NO2	1	81.993	0.958871	81.985	82.051	0.10649
PO2FH	1	82.9698	0.994997	82.884	83.055	0.10452
PO4	1	94.954	0.990315	94.862	95.139	0.14358
PO4H	1	95.9618	0.990167	95.879	96.05	0.14358
PO4H2	1	96.9696	0.990018	96.888	97.054	0.14358
C3NO3	1	97.988	0.956541	97.9	98.077	0.13532
P3O7	2	102.4435	0.983114	102.333	102.546	0.28659
CaPO2	1	102.927	0.964704	102.84	103.042	0.12943
CaPO2H	1	103.9348	0.96456	103.853	104.057	0.12943
CaPO2H2	1	104.9426	0.964415	104.816	105.043	0.12943
PO4C	1	106.954	0.979323	106.852	107.038	0.15236

Name	Charge	Expected Da	Relative Abundance	Start (Da)	Stop (Da)	Volume (nm^3)
CaC2PO	1	110.932	0.945705	110.823	111.023	0.11817
P3O8H2	2	111.4488	0.98043	111.325	111.534	0.31541
P3O8H3	2	111.9527	0.980283	111.867	112.044	0.31541
CaPO3	1	118.922	0.96236	118.815	119.024	0.15826
CaPO3	1	120.926	0.005933	120.831	121.039	0.15826
CaPO3	1	122.926	0.006423	122.798	123.019	0.15826
P2O4	1	125.928	0.990315	125.802	126.059	0.17184
P2O4H	1	126.9358	0.990167	126.824	127.046	0.17184
P2O3F	1	128.931	0.992728	128.793	128.893	0.16161
CaCPO3	1	130.922	0.951678	130.861	131.066	0.16704
CaCPO3H	1	131.9298	0.951535	131.735	132.02	0.16704
CaP2O2	1	133.901	0.964704	133.779	134.004	0.15769
CaP2O2H	1	134.9088	0.96456	134.809	135.011	0.15769
CaP2O2H2	1	135.9166	0.964415	135.821	136.109	0.15769
CaP2OF	1	136.904	0.967054	136.808	136.904	0.14746
unknown137				136.908	137.033	0
P2O5	1	141.923	0.987909	141.805	142.043	0.20067
P4O10H	2	142.4269	0.975818	142.256	142.522	0.40133
P2O5H	1	142.9308	0.987761	142.816	143.046	0.20067
P2O5H2	1	143.9386	0.987613	143.818	144.06	0.20067
P2O4F	1	144.926	0.990315	144.787	145.073	0.19044
P4O11H2	2	150.9283	0.9733	150.76	151.025	0.43016
P4O10F	2	151.422	0.975964	151.296	151.553	0.41993
P2O6	1	157.918	0.985508	157.788	158.075	0.22949
P2O6H	1	158.9258	0.98536	158.797	159.068	0.22949
P2O6H2	1	159.9336	0.985213	159.821	160.065	0.22949
P2O5F	1	160.921	0.987909	160.805	160.931	0.21927
P2O6H3	1	160.9414	0.985065	160.935	161.06	0.22949
CaCPO5	1	162.912	0.947058	162.759	163.054	0.2247
CaC2P2O3	1	173.896	0.941114	173.735	173.971	0.20409
unknown178				177.785	178.083	0
CaP2O5	1	181.886	0.957689	181.784	182.024	0.24417
Ca2P5O8H2	2	182.3858	0.921365	182.302	182.57	0.45896
Ca2P5O7F	2	182.8795	0.923887	182.796	183.063	0.44873
P3O6	1	188.892	0.985508	188.804	189.038	0.25776
CaP2O6	1	197.881	0.955362	197.715	198.014	0.273
CaP2O6H	1	198.8888	0.955218	198.728	199.029	0.273
P3O7	1	204.887	0.983114	204.729	205.043	0.28659
P3O8	1	220.882	0.980725	220.746	221.03	0.31541
P3O8H	1	221.8898	0.980577	221.738	222.026	0.31541
P3O8H2	1	222.8976	0.98043	222.735	223.037	0.31541
P3O9H	1	237.8848	0.978195	237.689	238.084	0.34424

Name	Charge	Expected Da	Relative Abundance	Start (Da)	Stop (Da)	Volume (nm^3)
P3O9H2	1	238.8926	0.978048	238.75	239.024	0.34424
P3O8F	1	239.88	0.980725	239.774	240.07	0.33401
CaP3O8	1	260.845	0.950724	260.678	260.965	0.36399
unknown266o5				267.419	267.551	0
CaP3O9	1	276.84	0.948414	276.677	276.772	0.38775
CaP3O9H	1	277.8478	0.948272	277.655	277.894	0.38775
P4O10	1	283.846	0.975964	283.683	283.981	0.40133
P4O10H	1	284.8538	0.975818	284.619	285.062	0.40133
P4O10H2	1	285.8616	0.975671	285.576	286.058	0.40133
P4O11	1	299.841	0.973592	299.642	299.758	0.43016
P4O11H	1	300.8488	0.973446	300.682	300.834	0.43016
P4O11H2	1	301.8566	0.9733	301.631	301.781	0.43016
P4O10F	1	302.844	0.975964	302.675	302.732	0.41993
Ca2P5O8	1	362.756	0.921642	362.634	362.757	0.45896
Ca2P4O10	1	363.772	0.917168	363.654	363.75	0.48835